# Frontiers of Characterization and Metrology for Nanoelectronics 2024

**April 15-18, 2024**
**Monterey, California**

**fcmn2024.avs.org**

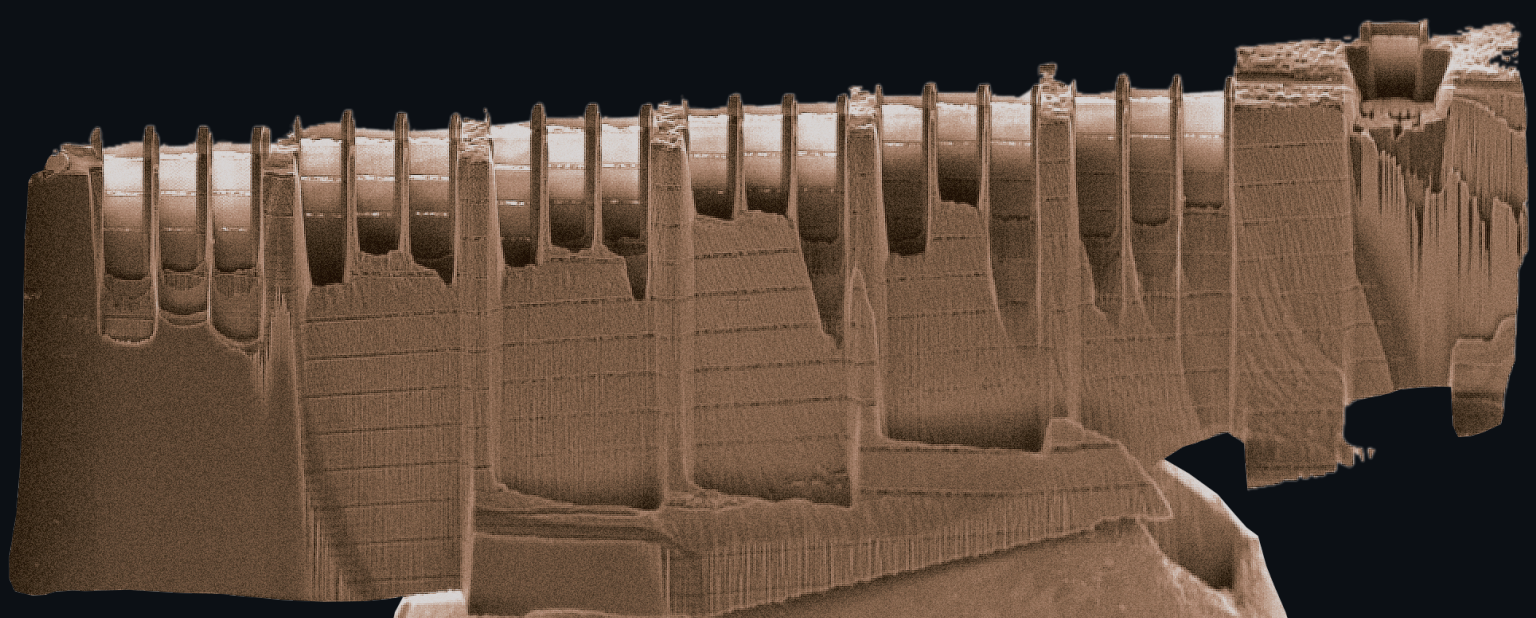

# Committee Co-Chairs

**J. Alexander Liddle**
National Institute of Standards and Technology

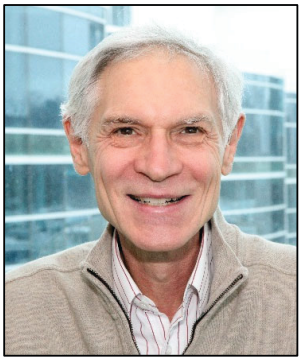

**Alain Diebold**
University at Albany

**Markus Kuhn**
Rigaku

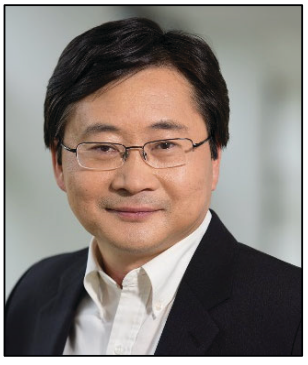

**Zhiyong Ma**
Intel

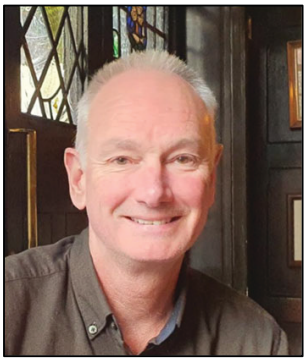

**Paul van der Heide**
imec

# Committee Members

- Ofer Adan, Applied Materials
- Jean-Paul Barnes, CEA-Leti
- Alan Brodie, KLA-Tencor
- Steve Consiglio, TEL Technology Center
- Michael Current, Current Scientific
- Frank de Jong, Thermo Fisher
- Ye Feng, Intel
- Christina Hacker, NIST
- Ajey Jacob, University of Southern California
- Shunsuke Koshihara, Hitachi High-Tech Corporation
- Bob McDonald, formerly of Intel (Treasurer)
- Baohua Niu, Intel TD Failure Analysis and Defect Metrology
- Shinichi Ogawa, AIST
- Erik Secula, NIST
- David Seiler, NIST
- Usha Varshney, NSF
- Jin Zhang, Lam Research
- Ehrenfried Zschech, Brandenburg University of Technology Cottbus – Senftenberg, Institute of Physics

**Cover Caption:** SEM image of a plan-view TEM sample showing 19 lamella at different layers in a 3D NAND device, made with an integrated fs-laser FIB-SEM. Credit: Carl Zeiss Microscopy

# 2024 International Conference on Frontiers of Characterization and Metrology for Nanoelectronics

Welcome to the 2024 International Conference on Frontiers of Characterization and Metrology for Nanoelectronics (FCMN)! Our goal is to bring together scientists and engineers interested in all aspects of the characterization technology needed for nanoelectronic materials and device research, development, integration, and manufacturing. All approaches are welcome: chemical, physical, electrical, magnetic, optical, *in situ*, and real-time control and monitoring. The semiconductor industry is evolving rapidly: the conference will highlight major issues and provide critical reviews of important materials and structure characterization and nearline/inline metrology methods, including hardware, data analysis, and AI and machine learning, as the industry both extends the technology deep into the nanoscale and increases the diversity of devices and systems. It is hoped that the invited talks, contributed posters, and informal discussions will be a stimulus to provide practical perspectives, breakthrough ideas for research and development, and a chance to explore collaborations and interactions on a world-wide basis.

We are pleased to have Rick Gottscho (LAM Research), Arie den Boef (ASML), and Dan Hutcheson (Techinsights), as keynote speakers for the event! Over thirty other invited talks will offer exciting overviews in the sessions that follow. Posters will supplement these overviews with the latest frontiers of metrology-based research results. These posters represent significant contributions to the latest developments in characterization and metrology technology, especially at the nanoscale.

The 2024 FCMN is the 14$^{th}$ in the series of conferences devoted to metrology frontiers for the semiconductor industry. It emphasizes the latest advances in characterization and metrology that are helping shape the future of the nanoelectronics revolution. The proceedings for many of the previous conferences in the series were published as hardcover volumes by the American Institute of Physics, New York. Most of these proceedings as well as many archived presentation slides are available to view for free on-line at www.nist.gov/pml/fcmn-publications-and-talks.

For the fourth time in a row, the committee is excited to bring the FCMN to Monterey, California! Monterey is a scenic California coastal city that rises from the pristine Monterey Bay to pine forested hillsides with sweeping bay views. We hope you enjoy your time here!

It is our sincere hope that you find this conference stimulating and enjoyable!

With best wishes from the Committee Co-Chairs,

**J. Alexander Liddle**, NIST;
**Alain Diebold**, University at Albany;
**Markus Kuhn**, Rigaku
**Zhiyong Ma**, Intel; and
**Paul van der Heide**, Imec

## Purpose and Goals

The FCMN brings together scientists and engineers interested in all aspects of the characterization technology needed for nanoelectronic materials and device research, development, integration, and manufacturing. The conference summarizes major issues and provides critical reviews of important semiconductor techniques needed in the semiconductor industry for advancing silicon nanoelectronics and beyond.

## Contributed Posters

One of the major emphases of this conference is on the contributed posters. These extended poster abstracts refereed by the committee represent significant contributions to the frontier, state-of-the-art materials, and device characterization.

Poster authors are responsible for setting up their displays, being present for the poster sessions on Tuesday and Wednesday afternoon, and removing their displays by the end of the conference on Thursday.

## Poster Sessions

The poster sessions with complimentary snacks and beverages are scheduled for 5:15 PM on Tuesday and 4:30 PM on Wednesday in San Carlos I and II at the Monterey Marriott.

## Banquet

A dinner banquet will be held on Tuesday, Apr. 16$^{th}$, at 7:00 PM in the Ferrante's Bay View Room on the 10$^{th}$ floor of the Monterey Marriott.

## Platinum Sponsors






## Gold Sponsors

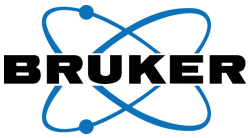


## Silver Sponsors




## Exhibitors

- CAMECA
- Covalent Metrology Services
- Malvern Panalytical
- Onto Innovation
- Photothermal Spectroscopy
- Rigaku
- Scienta Omicron
- SEMILAB
- Sigray, Inc.
- SPECS Surface Nano Analysis GmbH
- TESCAN
- Thermo Fisher Scientific
- Zeiss

## Partners

- American Vacuum Society
- National Science Foundation

Rigaku

*Leading with Innovation*

**Semiconductors have the power to change the world for the better**.

At Rigaku, we strive to make this a reality as the leading global supplier of X-ray metrology tools for semiconductor process R&D and high-volume manufacturing.

**THE WORLD OF SEMICONDUCTOR**
Metrology Tools From Lab to Fab

**TXRF | WD-XRF | ED-XRF | XRR | HR-XRD | CD-SAXS**


**METROLOGY TOOLS WITH PURPOSE**
Metrology Automation
Thin and Ultra-thin Film Characterization.
Wafer Contamination Monitoring
Ultra-thin single-layer films and multi-layer stacks
Non-Destructive 3D Measurement Technology
Structure properties of epitaxial layers
Inspection of epitaxial substrate defects
Inspection of transparent wafers
Line process control
Yield prediction
Semiconductor High-Volume Manufacturing Process Monitoring

**RIGAKU CORPORATION**
3-9-12, Matsubara-cho
Akishima-shi, Tokyo
196-8666, Japan
info-gsm@rigaku.co.jp
+81 3-3479-0618

**RIGAKU AMERICAS CORPORATION**
9009 New Trails Drive
The Woodlands, TX
77381-5209, USA
rsmd@rigaku.com
+1-281-362-2300

**RIGAKU EUROPE SE**
Hugenottenallee 167
Neu-Isenburg
63263 , Germany
semieurope@rigaku.com
+49 6102 77999 51

**RIGAKU.COM**

SIGRAY

Leaders in X-ray

## Introducing Two New Products


### EclipseXRM-900

Highest resolution (0.3 µm) x-ray microscope on the market for your Failure Analysis needs

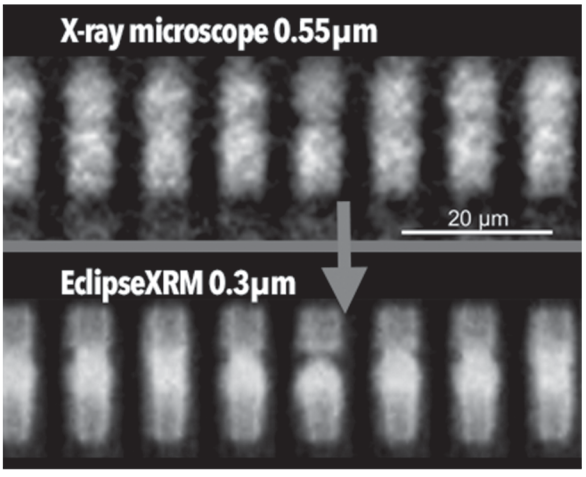


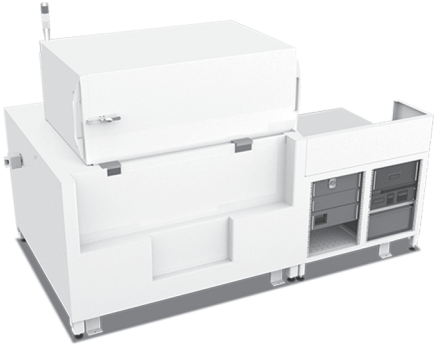

### XADA-200

X-ray circuit debugging for new Backside Power Distribution (BPD) devices

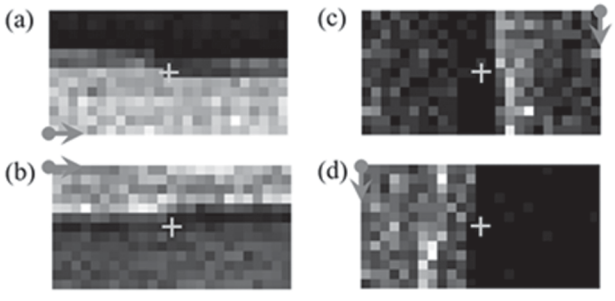


Localization of physical defect in SRAM (white pixels: more failing Schmoo tests)

# Accelerating next-generation devices through nanoscale insights.

## ZEISS Advanced Microscopy Solutions

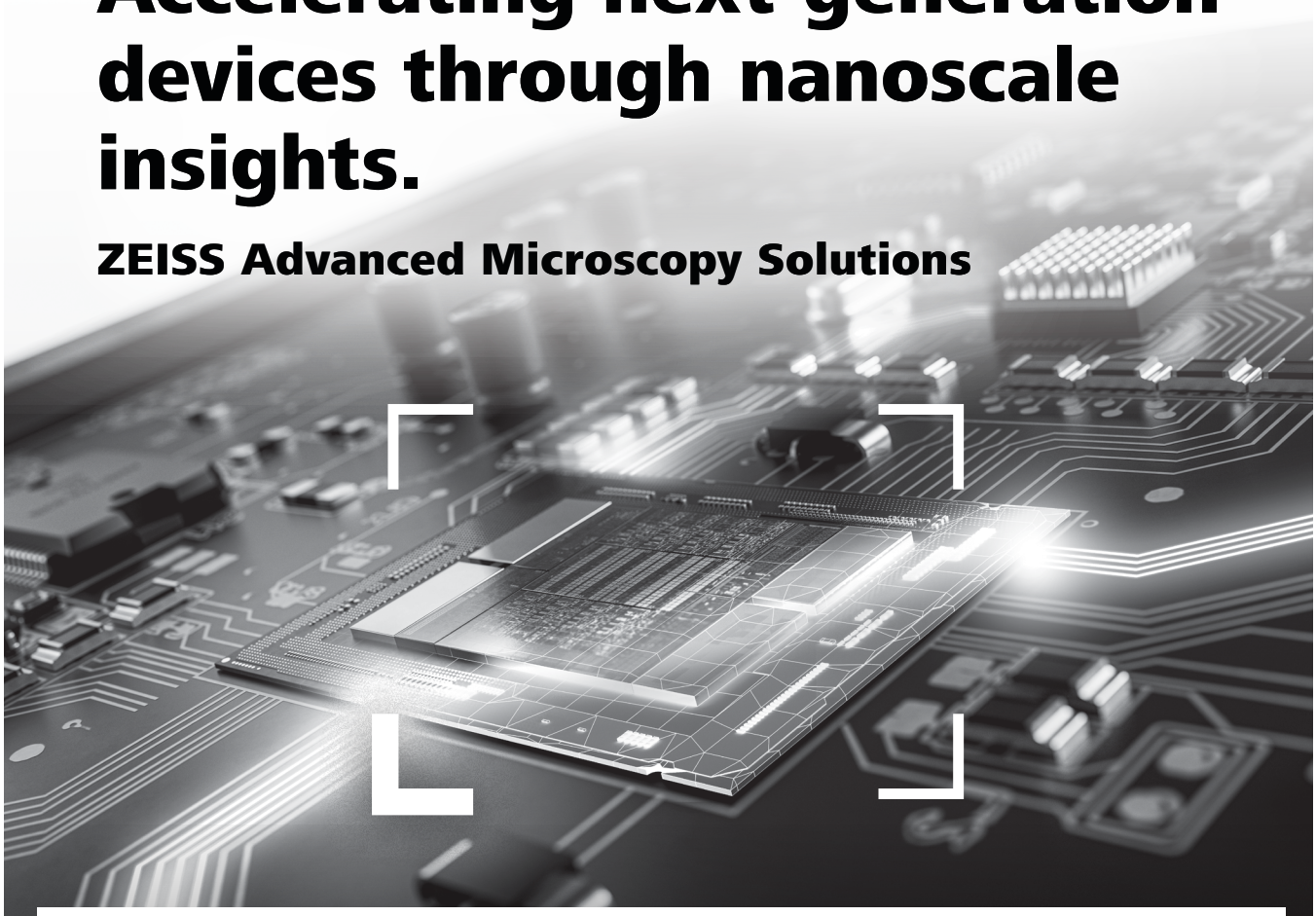

### ZEISS Versa 3D X-ray Microscope

AI-enabled fast, high-resolution 3D X-ray imaging

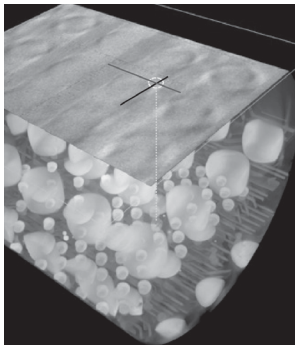

*Submicron 3D visualization of package interconnects and defects*

### ZEISS Crossbeam LaserFIB

From macro to nano in femtoseconds

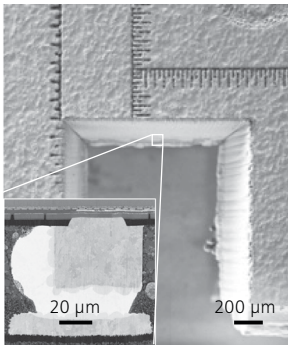


*Targeted sample prep and SEM imaging of microbump in PoP*

### ZEISS GeminiSEM Field-emission SEM

Nanoprobing of unperturbed sample states

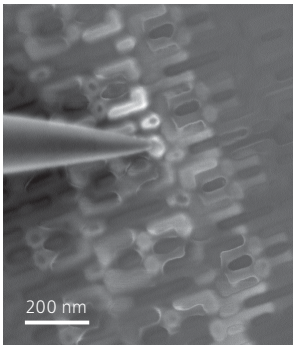


*Simultaneous sub-nm topographic and electrical characterization*

ZEISS

Seeing beyond




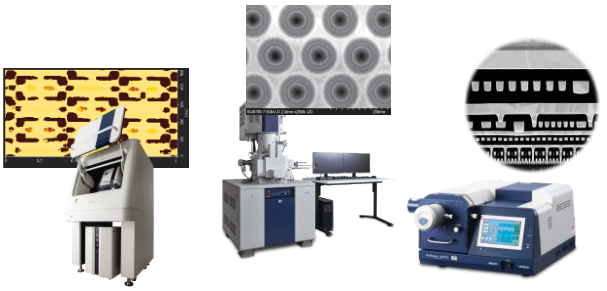



# Program at a Glance

| | Morning | AM Sessions | PM Sessions | Evening |
|---|---|---|---|---|
| **Tuesday** Apr. 16th | **7:00** Registration / Attendee Check-in | **9:00** Conference Opening **9:15** Plenary **11:15** Emerging Materials and Devices | **1:45** CHIPS Act & Industry Trends **3:45** Microscopies: New Developments in Chemical/Property Characterization | **5:15** Poster Session **7:00** Banquet |
| **Wednesday** Apr. 17th | **7:45** Registration / Attendee Check-in | **8:30** Advanced Packaging **10:30** New Developments in Chemical/ Electrical Characterization | **1:00** Patterning Metrology **3:00** Advanced Manufacturing Metrology – Defects | **4:30** Poster Session |
| **Thursday** Apr. 18th | **8:00** Registration / Attendee Check-in | **8:30** Plenary **9:15 AM** EUV and Advanced Patterning **11:15** Tomographies: New Developments in 3D Analysis | **2:45** Spintronics-Based Devices | |

# Monday, April 15

### Tutorials
**2:00 PM – 4:00 PM**

### Machine Learning and Its Application to Metrology
Dragan Djurdjanovic (UT Austin)

### Metrology Techniques
Alain Diebold (Univ. at Albany) and Paul van der Heide (Imec)

**4:30 – 6:30 PM**

### Advanced Packaging
Ofer Adan (Applied Materials)

### Reception and Registration
**7:00 – 9:00 PM**
Monterey Marriott

# Tuesday, April 16

### Registration
**7:00 AM – 8:30 AM**

### Conference Opening
**9:00 AM**
Conference Opening
J. Alexander Liddle, NIST, Conference Co-Chair

### 1. Plenary
Session Chairs: J. Alexander Liddle (NIST) and Alain Diebold (Univ. at Albany)

**9:15 AM ..... 25**
**Rick Gottscho**, *LAM Research*, Big Data, Little Data, and Virtual Twins: Accelerating Process Development for Semiconductor Device Fabrication

**10:00 AM**
Coffee Break and Poster/Exhibit Viewing

**10:30 AM..... 29**
**Arie den Boef**, *ASML*, Metrology Initiatives at ASML and ARCNL

## 2. Emerging Materials and Devices

Session Chairs: Ajey Jacob (Univ. of Southern CA), Usha Varshney (NSF), and Christina Hacker (NIST)

**11:15 AM..... 32**
**Xiaoqin (Elaine) Li**, *University of Texas-Austin*, Ultrafast Spectroscopy of/for Nanoelectronics

**11:45 AM..... 34**
**Daniel Schmidt**, *IBM*, In-Line Metrology for Sub-2nm Technology Nodes

**12:15 PM – 1:45 PM**
Lunch and Poster/Exhibit Viewing

## 3. CHIPS Act & Industry Trends

Session Chairs: Paul van der Heide (Imec) and Markus Kuhn (Rigaku)

**1:45 PM..... 37**
**Marla Dowell**, *National Institute of Standards and Technology*, Advancing Measurement Science for Microelectronics: CHIPS R&D Metrology Program

**2:15 PM..... 39**
**Zhenxin Zhong**, *TFS*, Latest Developments of Automated Transmission Electron Microscopy for Semiconductor Industry

**2:45 PM..... 42**
**Colin Ophus**, *Berkeley*, Applications of Machine Learning to STEM and 4DSTEM Characterization

**3:15 PM**
Coffee Break and Poster/Exhibit Viewing

## 4. Microscopies: New Developments in Chemical/Property Characterization

Session Chairs: Markus Kuhn (Rigaku) and Paul van der Heide (Imec)

**3:45 PM..... 45**
**Rudolf Haindl**, *Max Planck Institute*, Coulomb-correlated Electrons in a Transmission Electron Microscope

**4:15 PM..... 48**
**Umberto Celano**, *Imec*, Scanning Probe Microscopy: Pushing the Boundaries with Multi-Probes and Reverse Tip Sample Scanning

**4:45 PM..... 52**
**Kazuhiko Omote**, *Rigaku*, X-ray Metrology for Characterizing Advanced Nanoelectronics Structure

**5:15 – 6:45 PM**
**Poster Session (with Drinks and Hors d'oeuvres)**

**7:00 PM**
Banquet at Hotel

# Wednesday, April 17

### Registration
**7:45 AM – 8:30 AM**

### 5. Advanced Packaging
Session Chairs: Ehrenfried Zschech (Brandenburg University of Technology Cottbus – Senftenberg, Institute of Physics) and Baohua Niu (Intel)

**8:30 AM ..... 55**
**Yan Li**, *Samsung*, Fault Isolation Approaches for 3D IC Systems

**9:00 AM ..... 58**
**Matthew Andrew**, *ZEISS Innovation Center*, Advances in the Use of AI for X-ray Reconstruction: Applications in Electronics Packaging

**9:30 AM ..... 62**
**Pooya Tadayon**, *Intel*, Next Generation Metrologies & Fault Detection Methods in Support of Advanced Packaging

**10:00 AM**
Coffee Break and Poster/Exhibit Viewing

### 6. New Developments in Chemical/Electrical Characterization
Session Chairs: Paul van der Heide (Imec) and Shinichi Ogawa (AIST)

**10:30 AM..... 65**
**Claudia Fleischmann**, *Imec*, Advances in APT Quantification and Distortion Correction Approaches

**11:00 AM..... 68**
**Kento Sasaki**, *Univ. of Tokyo*, Arrangement of Nanosized hBN Quantum Sensor Spots by Helium Ion Microscope

**11:30 – 1:00 PM**
*Lunch and Poster/Exhibit Viewing*

### 7. Patterning Metrology
Session Chairs: Ofer Adan (Applied Materials), Alan Brodie (KLA-Tencor), and Shunsuke Koshihara (Hitachi High-Tech Corporation)

**1:00 PM..... 71**
**Jonghyeok Park**, Samsung Electronics, Wide-area Delayering Based 3D Tomography Solution as a Window into the Semiconductor Manufacturing

**1:30 PM..... 75**
**Eugen Foca**, *Carl Zeiss SMT GmbH*, 3D Metrology and Inspection of Advanced NAND and DRAM Devices Via Full 3D Characterization with FIB-SEM Tomography

**2:00 PM..... 78**
**Matt Hettermann**, *EUVTech*, Measuring the Complex Behavior of Phase in the EUV Regime and Implications for Phase Shift Masks

**2:30 PM**
Coffee Break and Poster/Exhibit Viewing

### 8. Advanced Manufacturing Metrology – Defects
Session Chairs: Tuyen Tran (Intel), Ye Feng (Intel), and Steve Consiglio (TEL Technology Center)

**3:00 PM..... 81**
**Byoungho Lee**, *Hitachi High-Tech Corporation*, MI(Metrology&Inspection)'s Deliverable Solutions for Next Journey

**3:30 PM..... 82**
**Shay Wolfling**, *Nova*, Advanced and Future Logic Device Architectures: Challenges and Solutions in Materials Metrology

**4:00 PM..... 85**
**Hamed Sadeghian**, Nearfield Instrument, Revolutionizing EUV Lithography Metrology for Sub-3nm Nodes: Validation of a Novel AFM System for Precise 3D Characterization in HVM

**4:30 – 6:00 PM**
Poster Session (with Drinks and Hors d'oeuvres)

## Thursday, April 18

### Registration
**8:00 AM – 8:30 PM**

### 9. Plenary
Session Chairs: J. Alexander Liddle (NIST) and Alain Diebold (Univ. at Albany)

**8:30 AM ..... 89**
**G. Dan Hutcheson**, *Techinsights*, The State of the Semiconductor Industry – Economics and Geopolitics

### 10. EUV and Advanced Patterning
Session Chairs: Alain Diebold (Univ. at Albany), Christina Hacker (NIST), Jin Zhang (Lam Research)

**9:15 AM ..... 92**
**Nigel Smith**, *Nanometrics*, New Directions for Optical Critical Dimension Metrology

**9:45 AM ..... 96**
**Christina Porter**, *ASML*, Soft X-Ray Scatterometry for 3D CD Metrology on Individual GAA Nanosheets

**10:15 AM**
Coffee Break and Poster/Exhibit Viewing

**10:45 AM..... 99**
**Guillaume Freychet**, *CEA Leti*, Overview Of Critical Dimension Small Angle X-ray Scattering (CD-SAXS)

## 11. Tomographies: New Developments in 3D Analysis

Session Chairs: Frank de Jong (Thermo Fisher) and Ehrenfried Zschech (Brandenburg University of Technology Cottbus – Senftenberg, Institute of Physics)

**11:15 AM..... 102**
**Michael Reisinger**, *KAI GmbH*, Understanding the Damage and Microstructural Evolution in Cu Metallizations During Thermomechanical-Fatigue

**11:45 AM..... 105**
**Nicolas Gauquelin**, *Univ. Antwerp EMAT*, Advances in 3D Tomography and 4DSTEM: Perspectives to Study Semiconductor Devices

**12:15 – 1:45 PM**
**Lunch and Poster/Exhibit Viewing**

**1:45 PM..... 108**
**Tony Levi**, *Univ. of Southern California*, Chip Scan: 3D X-ray Imaging of CMOS Circuits

**2:15 PM..... 111**
**Eric Van Cappellen**, *Thermo Fisher Scientific*, Integrating Atom Probe Tomography and Transmission Electron Microscopy into a Single Instrument

## 12. Spintronics-Based Devices

Session Chair: Jean-Paul Barnes (CEA-Leti)

**2:45 PM..... 114**
**Amanda Petford-Long**, *Argonne National Lab*, Advanced Electron Microscopy Based Metrology Approaches

**3:15 PM**
**Coffee Break and Poster/Exhibit Viewing**

**3:45 PM..... 117**
**Rafal Dunin-Borkowski**, *Ernst Ruska Centre for Microscopy and Spectroscopy with Electrons*, Characterization of Magnetic Textures in Materials for Spintronics-based Devices

**4:15 PM..... 118**
**Siamak Salimy**, *Hprobe*, MRAM End of Line Magnetic Testing: From Single Bit Properties to Full Memory Qualification

**4:45 PM**
**Conference End**

## Poster Presentations

# Accelerating Process Development for Semiconductor Device Fabrication

Richard A. Gottscho

*Lam Research, 4650 Cushing Pkwy, Fremont, CA 94538*

## INTRODUCTION

Although chips have been designed by computers for decades, the processes used to manufacture those chips have eluded design based on physics or data. Virtually all processes used to manufacture chips have been developed, not designed, by trial and error – a costly endeavor using highly trained and experienced process engineers searching for a combination of tool parameters that produce an acceptable result on the device. Out of more than a 100 trillion possibilities! Because the solution space dimensionality is so large and because process development is time-consuming and costly, machine learning approaches have been hampered by too little data. Physics based approaches suffer from large numbers of unknown parameters and complex equations that require excessive computational time to solve.

This talk will review results of a study,[1] which showed a "human first, computer last" approach could reach process engineering targets in half the time and half the cost compared to today's empirical approach. The results provide a path to leverage the strengths of human experts and their physics-based domain knowledge as well as the strengths of machine learning to deal with "little data" and accelerate the pace of innovation in semiconductor process engineering.

## THE VIRTUAL ENVIRONMENT

To provide a test bed on which different algorithms and methodologies could be compared, we built a virtual process environment based on known physical mechanisms for plasma etching (Fig. 1). The relationships between process recipe parameters and fluxes of reactive species to the wafer that govern the types and rate of surface reactions leading to etching were assembled from a survey of the literature as well as internal Lam Research engineering studies. We strived for a sufficiently realistic process environment that would enable us to reliably evaluate the merits of one methodology or one algorithm versus another. It is an open question as to how "accurate" this environment needs to be. We surveyed the human engineers who used the virtual environment to develop virtual process recipes that met virtual customer requirements. They unanimously described the experience as comparable to their real-world process development environment. Because the virtual environment is based on known physics and mechanisms and was designed to follow parameter trends, this wasn't too surprising; however, it is important for the environment to capture also the complexity and large dimensionality of the real processing environment and the engineers indicated that this was achieved.

## HUMAN MACHINE COLLABORATION

Once the virtual environment was created, we gave contestants a challenge problem: incoming material stack, range of recipe parameters, number of recipe parameters, and six output specs corresponding to mask remaining, top CD, middle CD, bottom CD, etched depth, and etch rate. Four groups of humans participated in the contest: senior engineers defined as having more than 7 years of experience in plasma etching plus a Ph.D. junior engineers defined as having a Ph.D. and less than1 year experience; non-technical professionals (such as from our human resources

department); and data scientists free to use whatever algorithmic approaches they preferred. The measure of success was the number of experiments to achieve the target specification, with the fewest number of experiments being the objective. The number of experiments can be expressed in terms of cost or time or both. Fewer experiments, less cost, less time.

One can immediately see the value in using a virtual environment that mimics the real environment (Fig. 2). The senior engineers consistently outperformed junior engineers by a factor of two. Both the non-technical and data scientist contestants performed poorly and with one exception did not converge on the virtual specification before spending about 10x the best senior engineer's performance. The value of experience is worth 2x education alone. One engineer's skills can be directly compared against another as well. It is important to note that the data scientists lacked domain knowledge, and this was reflected in the machine-based algorithms struggling to determine initial directions to pursue. That insight comes from technically trained and experienced engineers.

Each group displayed a characteristic learning curve as defined as the number of experiments or virtual dollars required to meet the virtual spec. For both the senior and junior engineers, initial learning was rapid (20% of the total time) such that within a few experiments, the output metrics were within 10-20% of the virtual specification. (Fig. 2). To close the gap to target, the engineers spent roughly 80% of their time (and cost) meandering around but above target until finally the right combination of the 11 input parameters enabled a solution within specification. This characteristic learning curve suggested an alternative solution strategy: let the humans start the experimental design and define a reduced set of recipe parameter ranges and share the results of those initial experiments and new parameter ranges with the data scientists. Thus, the data scientists now had domain knowledge and the algorithms had prior information on which they could make improvements with additional data. The design of experiments to generate additional data, for the winning algorithm, was influenced by how much uncertainty remained in the model. Each new experiment was designed by the algorithm to reduce uncertainty in the solution function. With this human first computer last (HF-CL) methodology, the Sr. Engineer and Data Scientist team could produce a result that was 2x faster or lower cost than the Sr. Engineer's baseline solution alone. (Fig 3)

## ADOPTION

### Culture

The learning curve of the HF-CL approach showed some interesting anomalies. Immediately after the transfer of knowledge and responsibility, the machine learning algorithm prioritized exploration over exploitation such that the experiments defined by computer initially produced recipes that produced results further from target. (Fig. 3) This behavior made our engineers nervous. As we transferred the methodology into the real-world, we encountered resistance partly because of the machine's learning trajectory. Humans do not like to produce a result that goes in the wrong direction even to learn; but machines do it without hesitation.

### Holistic Approach

The virtual environment provides a "sufficiently realistic" environment that can be used to compare human engineering skills, machine learning abilities, and hybrid combinations entailing human-machine collaboration. To facilitate collaboration between human and machine prospectively, we believe it is important to design experiments properly and archive data in such a way that they can be rapidly deployed in machine learning algorithms with minimal curation. Automated workflows that capture all data from an experiment and tailored to the human-machine collaborative environment will further accelerate time to solution.

## NEW METROLOGY WOULD BE DISRUPTIVE

Because plasma etch experiments require time-consuming and expensive metrologies to determine the result, data are limited, and machine learning techniques tailored to the small data world are most effective. Bayesian optimization approaches are well suited to this regime. Having said that, a metrology that provided real-time metrics of an etch profile as it evolves, or the electrical properties of a film as it is deposited and annealed would provide significant improvements in the pace of development.[2] Imagine a process engineer watching the etched structure evolve in real-time, turn a knob, and see immediately how they had influenced the etched profile. If such a metrology existed, it would not obviate the need for virtual environments nor the value of the Bayesian approach. Rather it

would accelerate learning and solution generation further by making use of known working methodologies and algorithms and suddenly providing them with far more information from which they can learn even faster.

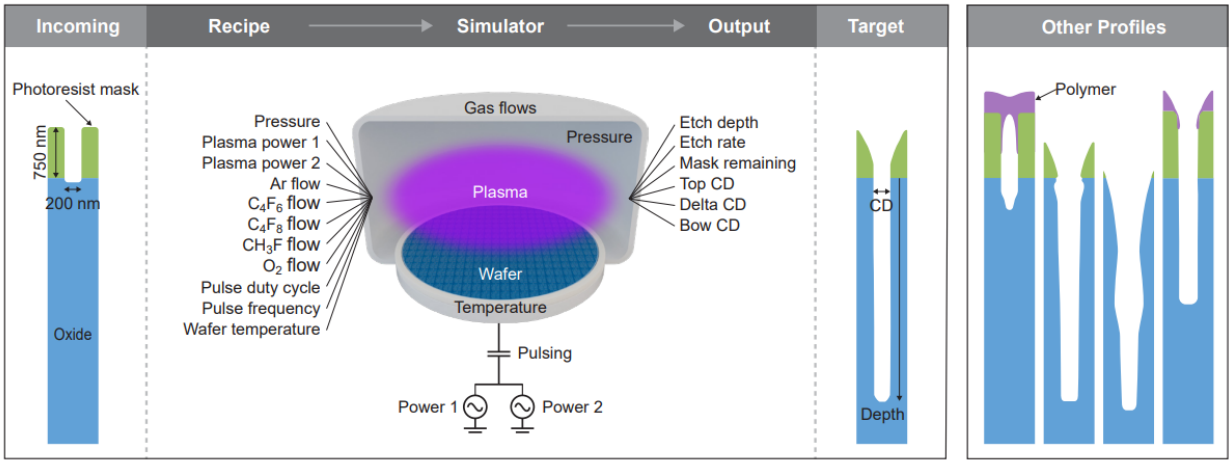


FIGURE 1. Schematic of the virtual process environment used in the contest. (Source: Figure 1 in Ref. 1)

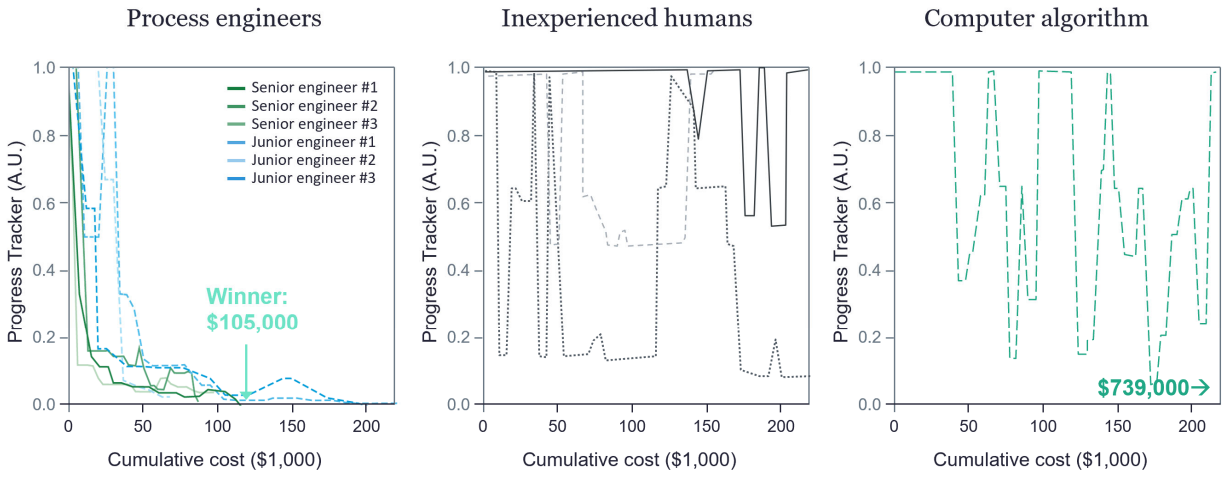


FIGURE 2. Results of the virtual process development efforts by senior engineers, junior engineers, non-technical personnel, and data scientists (computer algorithm). The senior engineers reached target using approximately half the experiments as junior engineers and less than 10 times the number of experiments required by non-technical or data scientist personnel without domain knowledge. The number of virtual experiments is proportional to virtual cost. (Source: Modified from Figure 2 in Ref. 1)

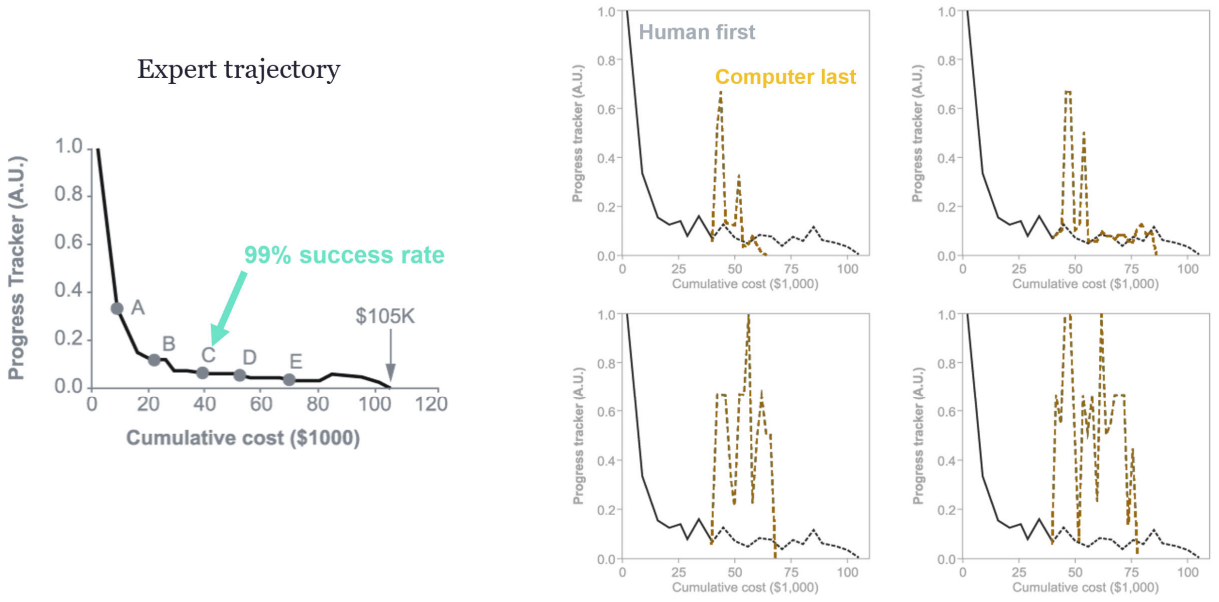


FIGURE 3. Senior, expert engineer learning trajectory on the left. The learning curves on the right are four separate instances of human-machine collaboration with the transfer point being C, which resulted in 99% of the HF-CL solutions being faster and lower cost than the expert baseline. On average, approximately 2x savings is observed. Also note that the computer algorithm initially generates recipes that result in greater distance from the desired target. But with that added information, they rapidly converge to a solution before the expert could do so. (Source: Modified from Ref. 1)

## REFERENCES

1. K. J. Kanarik, W. T. Osowiecki, Y. Lu, D. Talukder, N. Roschewsky, S. N. Park, M. Kamon, D. M. Fried and R. A. Gottscho, *Nature* **616**, 707–711 (2023).
2. R. A. Gottscho, "Bridging the “Valley of Death:” An Equipment Supplier’s Perspective, Lam RFI White paper NIST", (Posted by the National Institute of Standards and Technology on Dec 20, 2022, December 12, 2022).

## KEYWORDS

Semiconductor Processing, Plasma Etching, Machine Learning. Bayesian Optimization

# Metrology Initiatives At ASML And ARCNL

Arie den Boef[a,b,c], Paul Planken[b,d], Stefan Witte[b,c], Victor Calado[a]

a. *ASML Netherlands B.V., De Run 6501, 5504 DR Veldhoven, The Netherlands*
*b. ARCNL, Sciencepark 106, 1098 XG Amsterdam, The Netherlands*
*c. Vrije Universiteit, De Boelelaan 1105, 1081 HV Amsterdam, The Netherlands*
*d. University of Amsterdam, Sciencepark 904, 1098 XH Amsterdam The Netherlands*

## INTRODUCTION

Today, established metrology techniques are being pushed to their limits by the rapid innovations in the semiconductor device industry. For example, high-NA Extreme Ultra Violet (EUV) lithography enables a further reduction in device dimensions but this results in the need for even more robust and fast optical overlay (OV) metrology that needs to offer sub-nm precision on small metrology targets. Moreover, high-NA EUV lithography also leads to very thin resist resulting in low signals in applications like CD metrology and focus monitoring.

The use of Ruthenium (Ru) in Direct Metal Etch (DME)[1] and thick Carbon-based hardmasks in 3D-NAND manufacturing[2] pose additional challenges for optical overlay metrology and wafer alignment. These techniques usually use wavelengths where Ru and Carbon hardmasks are almost completely opaque. Extending the wavelength range towards the IR may be beneficial in a few cases but this is not sufficient to cover the entire application space. Another example is the progress in more complex device architectures. This trend was started by the replacement of the planer FET by the Fin FET. More complex devices like Gate All Around (GAA) transistors and complementary FET (cFET) transistors are being introduced leading to a desire to have fast and non-destructive high-resolution 3D-imaging of these devices.

All abovementioned challenges ask for significant innovations in existing metrology techniques and sometimes even more revolutionary metrology approaches need to be considered. This paper presents a concise overview of some metrology techniques that are being explored at ASML and the Advanced Research Center for Nano Lithography (ARCNL) in Amsterdam (www.arcnl.nl).

## DIGITAL HOLOGRAPHIC MICROSCOPY FOR OVERLAY METROLOGY

Optical OV metrology methods often use microscopy to image an OV target on an image sensor[3]. Optical OV metrology tools need to offer high throughput, a large wavelength range, high imaging quality and a low detection limit to cope with low diffraction efficiency from thin resist targets. Moreover, these requirements need to be realized at an acceptable cost. At ARCNL we explore Digital Holographic Microscopy (DHM) for OV metrology[4]. DHM can computationally correct imaging aberrations[5] and offers high imaging quality using only a few imaging lens elements. This enables a large wavelength coverage from visible to IR in a single sensor[6].

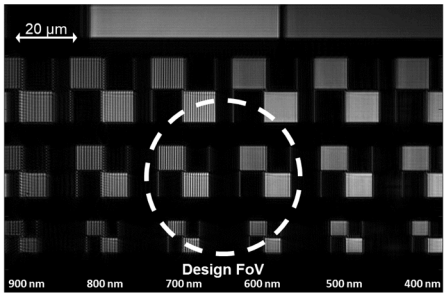


**FIGURE 1**. Aberration-corrected image of µDBO targets on a test wafer. The target size decreases from top-to-bottom and the target pitch decreases from left-to-right. The dashed circle indicates the Field-of-View (FoV) for which the optics designed.

Figure 1 shows an example of the aberration correction capabilities of a DHM test setup. With a very similar setup the first OV measurements from visible to near-IR wavelength were done as shown in Figure 2. These data show a so-called set-get OV measurement on a test wafer. These images have not yet been corrected for Tool Induced Shift (TIS) that explains the relatively large offset that is still present in, especially, the near-IR result.

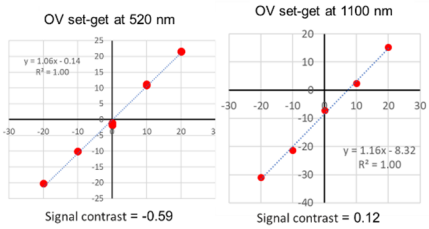


**FIGURE 2**. Measurement result that demonstrates the OV metrology capability of DHM from visible to near-IR wavelengths

## PHOTO-ACOUSTIC PUMP-PROBE IMAGING THROUGH OPAQUE LAYERS

Some materials are so opaque that even IR light cannot penetrate. Sometimes residual topography can "ripple" through the surface allowing the use of optical detection techniques. However, when the surface is perfectly planarized alternative methods are needed. ARCNL is therefore exploring photo-acoustic pump-probe techniques for detecting buried metrology targets[7]. In this technique a femto-second laser pulse ("pump") is incident on the opaque layer covering the buried target (Figure 3.A). This generates an acoustic wave that propagates towards the grating resulting in a backwards traveling diffracted acoustic wave that generates a perturbation at the surface that is optically detected with a probe pulse.

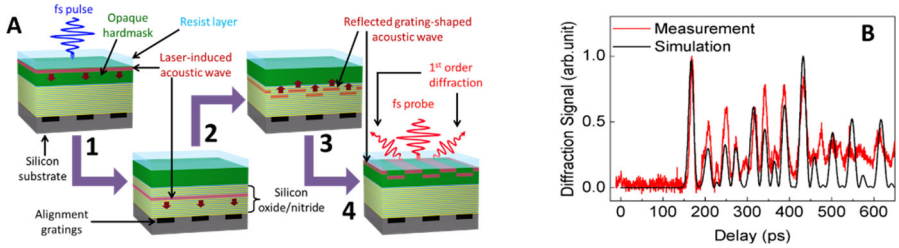


**FIGURE 3. (**A) Conceptual sketch of photo-acoustic detection of a buried grating underneath an opaque hardmask. (B) example of a measured (red curve) and simulated (black curve) signal from the probe beam.

Unfortunately, the detected signals shown in Figure 3.B are very weak leading to long acquisition times that are impractical for most applications. We are therefore investigating various options to increase the detected signal levels[8].

## SPECTRALLY-RESOLVED IMAGING OF DEVICE PATTERNS

There is a growing need for high-resolution imaging of complex devices like Gate-All-Around FET. TEM offers the resolution but is slow and destructive. Soft X-ray Scatterometry[9] also offers the required resolution and is fast but needs a periodic device array. ARCNL is exploring advanced Coherent Diffractive Imaging (CDI) techniques using a broadband soft X-ray source for spectrally-resolved imaging of non-periodic complex device structures[10].

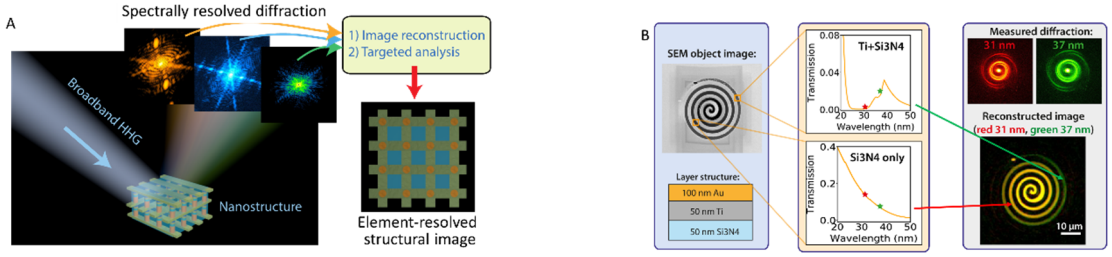


**FIGURE 4**. A: Conceptual drawing of a Coherent Diffractive Imaging setup for spectrally-resolved imaging. B: One of the first measured spectrally resolved images

The concept of CDI is schematically shown in Figure 4.A. A High Harmonic Generated (HHG) source illuminates a structure with high-brightness broadband soft X-ray light. The light diffracted by the structure is captured by an image sensor and sophisticated algorithms are used to reconstruct a spectrally resolved image of the structure. Different materials in the structure have a different wavelength-dependent response to the incident light which opens the path towards element-resolved imaging. Figure 4.B shows one of the first obtained measured results of an element-resolved image of a test structure. This measurement result was obtained in transmission.

These advanced imaging techniques can be extended to depth-resolved imaging and may open a path towards high-resolution depth resolved imaging of complex device structures.

## HIGH-NA EUV FOCUS SENSING OF ON-PRODUCT PATTERNS

The small depth of focus of high-NA EUV tools asks for robust focus metrology and possibly even focus control. Fast optical focus metrology is possible with dedicated focus-sensitive targets that make use of mask-3D effects. However, it is essential to connect these optical focus measurement to the focus behavior of actual device structures.

Focus errors of device structures can be determined by measuring Pattern Placement Errors (PPE) with e-beam since a focus error usually lead to a layout-dependent PPE[11]. By using a large field of view SEM we can capture a large variety of pattern layouts in 1 image acquisition. This large pattern variety creates a lot of diversity resulting in a robust "on-device" focus measurement.

As an example, Figure 5(a) shows a SEM image with irregular via patterns where some via's are color-coded by their pattern layouts corresponding in Figure 5(b,c,f). We found that many of these labeled via's show layout-dependent PPE and CD error that are sensitive to scanner focus and dose.

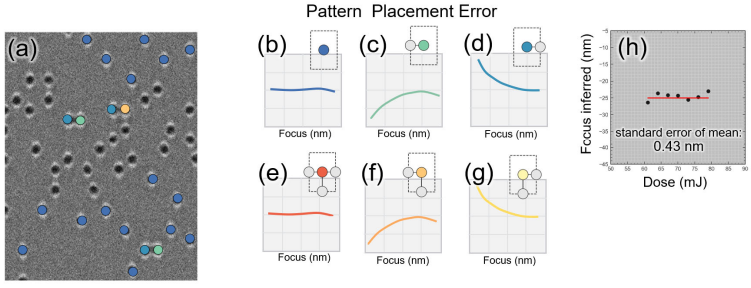


**FIGURE 5.** (a) SEM image of irregular via pattern, with some via's color labeled by their taxonomic class given in (b-g). (b-g) shows the pattern placement error as function of focus in a cartoon style. Each class has a specific relation to scanner focus (and dose) which allows a robust focus inference.

Using a dose-focus regression model the applied EUV focus on logic patterns is inferred with low dose crosstalk directly on device patterns. This is shown in Figure 5(h) by inferred focus as function of applied exposure dose. The focus inference is largely independent on the dose as we obtained a standard error not exceeding ~1 nm for various pattern types.

## REFERENCES


1. S, Paolillo, D. Wan, F. Lazzarino et al., *J. Vac. Sci. Technol.* **B 36**, 03E103 (2018); https://doi.org/10.1116/1.5022283
2. Z. Jiang, H. Zhu, and Q. Sun, *Electronics 2021*, **10**(12), 1374; https://doi.org/10.3390/electronics10121374
3. A. den Boef, *Surf. Topogr.: Metrol. Prop.* **4** (2016) 023001; doi:10.1088/2051-672X/4/2/023001
4. C. Messinis, *Ph.D. thesis*, https://ir.arcnl.nl/pub/296
5. T. van Gardingen-Cromwijk, S. Konijnenberg, W, Coene et al., *Light, Advanced Manufacturing*, accepted for publication
6. T. van Schaijk, C. Messinis et al., *J. Micro/Nanopattern. Mater. Metrol.*, **21** (1) 2022, doi: 10.1117/1.JMM.21.1.014001
7. S. Edward, Detection of hidden gratings using light and sound, *Ph.D. thesis,* June 18, 2020, https://ir.arcnl.nl/pub/114
8. T.J. van den Hooven, and P. C. M. Planken, *Photoacoustics* 31, 100497 (2023)
9. C. Porter et al., Metrology, Inspection, and Process Control XXXVII **12496**, 124961I (2023)
10. G.S.M. Jansen, A. de Beurs, X. Liu, K.S.E. Eikema, S. Witte, *Opt. Express* **26**, 12479 (2018)
11. V. Calado, S. Mathijssen, E. van Setten et al., *Proceedings SPIE*, to be published


## KEYWORDS

OV metrology, pump-probe, imaging, holography, soft X-ray imaging, lensless imaging

# Revealing Intrinsic Excited State Dynamics in Semiconductor Monolayers and Moiré Superlattices

Xiaoqin Elaine Li

*Physics Department at the University of Texas-Austin, Austin, Texas, U.S.A. 78759*

## INTRODUCTION

Exciton resonances dominate the optical spectra of van der Waals semiconductors, transition metal dichalcogenides (TMDs). When these layered materials are grown using chemical vapor deposition methods or exfoliated to the monolayer and bilayer thickness, the reduced Coulomb screening further enhances the binding energy of excitons to ~ 200-500 meV, making the fundamental excitations stable at room temperature and relevant for optoelectronic devices. Because of their large oscillator strength, their intrinsic dynamics occur on an ultrafast time scale of ~ 1 ps. There are many species of dark exciton resonances, especially in W-based TMDs. Understanding exciton and valley dynamics and their diffusion have been topics intensely investigated in the last few years.

## EXCITON DYNAMICS REVEALED BY ULTRAFAST SPECTROSCOPY

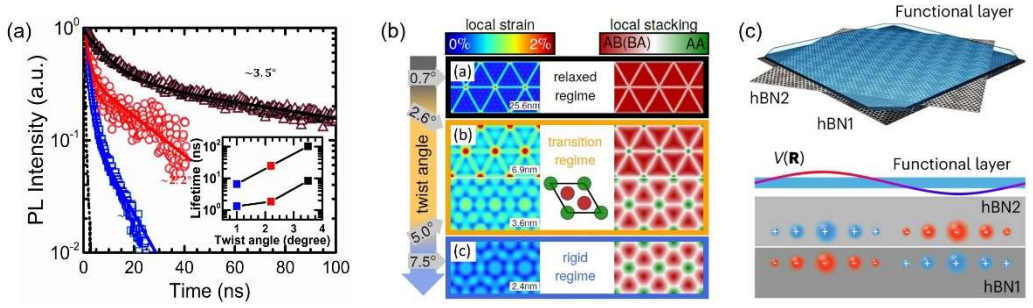


Fig. 1: (a) twisted angle-dependent interlayer exciton lifetime measured in MoSe2/WSe2 bilayers; (b) calculated lattice reconstructions; (c) moire engineering via twisted hBN substrate.

After a brief review of studies of exciton/valley dynamics TMD monolayers using a powerful spectroscopy tool called two-dimensional coherent electronic spectroscopy, I will discuss our newly developed understanding of moiré excitons. We show that the resonance energy and lifetimes of interlayer excitons all sensitively depend on the twist angle [1-2]. More importantly, I will discuss the limitations in our current understanding of excited states in these new semiconductor superlattices and the opportunities that may emerge.

First, I will discuss how the competition between strain and interlayer coupling leads to lattice reconstructions [3-4]. Such lattice reconstructions can be categorized into three different regimes: relaxed regime, transition regime, and rigid regime. These regimes can be optically characterized using Raman spectra. In different regimes, different excited states may form.

Secondly, I will discuss how one may construct a regular array of quantum dots using the moiré superlattice and why the commonly studied TMD bilayers may not be the best candidates. I will propose an alternative material platform [5] to realize a quantum emitter array based on moiré engineering.

Finally, I will discuss how spectroscopy methods we use in studying moiré superlattices may apply to wafer-scale characterizations of compound semiconductors.

## REFERENCES

[1] "Twist Angle-Dependent Interlayer Exciton Lifetimes in van der Waals Heterostructures", Junho Choi, et.al, Phys. Rev. Letters, 126, 047401, 2021
[2] "Excitons in semiconductor moiré superlattices", Di Huang, et.al., Nature Nanotechnology, 17, 227, 2022.

[3] "Phonon Renormalization in Reconstructed MoS2 Moire Superlattices", Jiamin Quan, et.al., Nature Materials, 20, 1100, 2021
[4] "Quantifying Strain in Moiré Superlattice" Jiamin Quan, et.al., Nano Lett. 2023, 23, 24, 11510–11516, 2023
[5] "Electrostatic moire potential from twisted-hBN layers" Dong Seob Kim, et.al., Nature Materials, 23, 65, 2024

## KEYWORDS

Semiconductor monolayers, moiré superlattice, exciton dynamics,

# In-Line Metrology for Sub-2nm Technology Nodes

Daniel Schmidt

*IBM Semiconductors Technology Research*
*257 Fuller Road, Albany, NY 12203*

## INTRODUCTION

In-line metrology is a key enabler for fast cycles of learning during development and for ensuring constant, optimum device performance during semiconductor manufacturing. Fast and non-destructive in-line techniques are required for dimensional and materials metrology – they are intended to capture process excursions in real-time (process monitoring) and can be used for advanced process control (feedback or feed-forward). Therefore, advanced metrology enables competitive and economical development as well as high-volume manufacturing.

As the industry keeps scaling to fulfill Moore's law, new architectures such as the nanosheet gate-all-around transistor have emerged and already transitioned into manufacturing at the 3 nm node.[1] The 3D nature of this device architecture with its stacked channels came with demanding process specifications and mandated a significant metrology leap.[2] The many new process steps, mostly related to the channel formation, require tight control and sheet-specific metrology to achieve and maintain desired device performance. Furthermore, the introduction of EUV lithography enabled further scaling and opened a large design space, which in turn requires additional metrology and novel concepts for future exposure tool mix and matching, for example.[3] Figure 1 depicts a simplified view on where the industry is headed: a backside power delivery network (BSPDN) has been demonstrated already for finFET technology[4] and is expected to be added next generation nanosheet devices. This requires wafer bonding to a carrier wafer, subsequent wafer thinning, and backside processing to electrically contact the devices. Monitoring the bonding process is critical as wafer warpage can have significant implications for backside overlay. The wafer thinning process must be precisely controlled and metrology from the backside will not be straightforward as the original frontside comprises full wafer device patterning. The next device evolution is projected to be stacking FETs on top of each other before the traditional Si or SiGe channels will be replaced by new 2D transition metal dichalcogenide semiconductors such as $MoS_2$ or $WSe_2$.[5] In any case, the stacked FET architecture will add significant complexity beyond nanosheet technology, especially to model-based techniques such as optical scatterometry. The introduction of 2D materials into semiconductor manufacturing will likely require another wave of lab-to-fab transitions related to metrology techniques. While one of the key techniques, Raman spectroscopy, has made its introduction into the fab just recently,[6] others are required for comprehensive process and materials characterization.

In addition to traditional transistor scaling, efforts are underway to monolithically integrate functional elements such as embedded magnetoresistive random-access memory (MRAM)[7] or phase-change memory (PCM) for analog AI applications.[8,9] These devices introduce new materials into the back-end-of-line (BEOL) processing and require dedicated and demanding metrology efforts.[10,11]

Besides traditional, monolithic integration, the industry is also moving towards heterogeneous integration and chiplet technology, which means that individual components (dies or chiplets) may be stacked on top of each other and/or are jointly placed on an interposer. The advanced packaging evolution has entirely different metrology requirements compared to the logic scaling ones discussed above. Through-silicon via (TSV) characterization from the front and backside, pre and post metrology for defect-free hybrid wafer bonding, large feature wafer level measurements, and die to die overlay all come along with a new set of challenges.[12,13]

Metrology developments are required for every process step, and techniques that have been introduced to semiconductor manufacturing only recently are expected to gain more importance as the industry continues the path to ever more powerful computational devices.

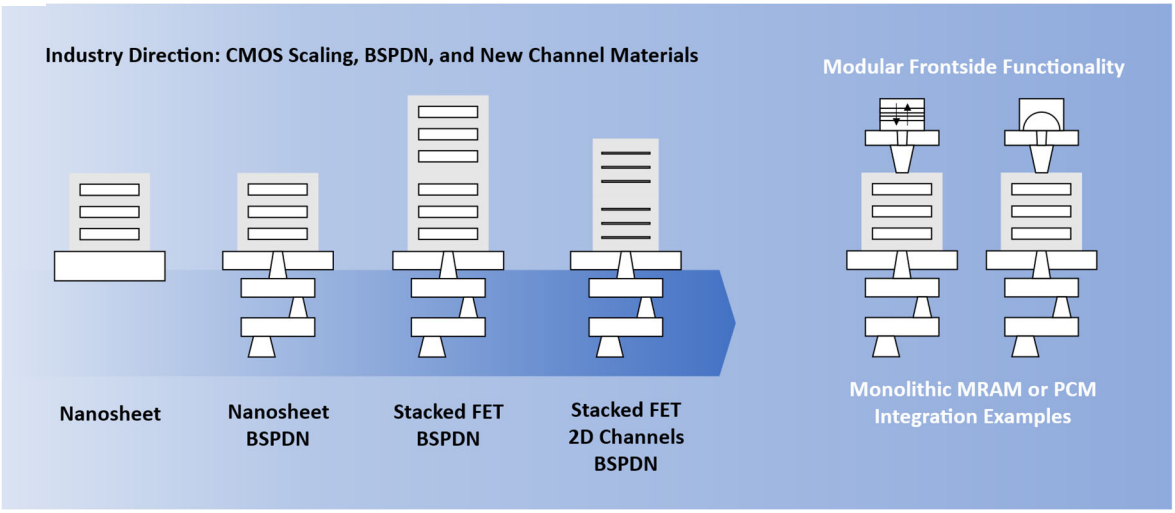


**FIGURE 1.** Simplified representation of the industry device scaling direction with backside power delivery network (BSPDN), stacking of nanosheet transistors, and 2-D channels: monolithic device complexity increases as scaling continues. Additionally, for every architecture, there is the option to embed magnetoresistive random-access memory (MRAM), phase-change memory (PCM), or other functional elements in the BEOL on the original frontside of the wafer.

## RECENT METROLOGY DEVELOPMENT EXAMPLES

One of the promising recent developments is vertical traveling scatterometry (VTS) enabled by absolute phase measurements through spectral interferometry.[10] The technique allows for data filtering related to spectral information from buried layers, which can then be ignored in the optical model. Selective analyses of the topmost part of an arbitrarily complex stack are possible within a single metrology step, which may enable solutions for application infeasible with traditional optical scatterometry. An example is presented in Fig. 2, where the first metal level (M1) is characterized with the same optical model on a target comprising only patterned M1 (not shown) and a more device-like target with a full FEOL build (Fig. 2a). In both cases, a good correlation to the transmission electron microscopy (TEM) reference is observed.[10]

Using design metrology co-optimization (DMCO), the MOL was omitted to simplify the metrology structure as much as possible with minimal impacts to the topography. Striking a balance between device-like and simplified architectures is the main goal of DMCO. Techniques like VTS will help to shift that balance toward device-like and simplify complex metrology tasks for BSPDN, stacked transistors, or embedded functional elements, which are all on the roadmap.

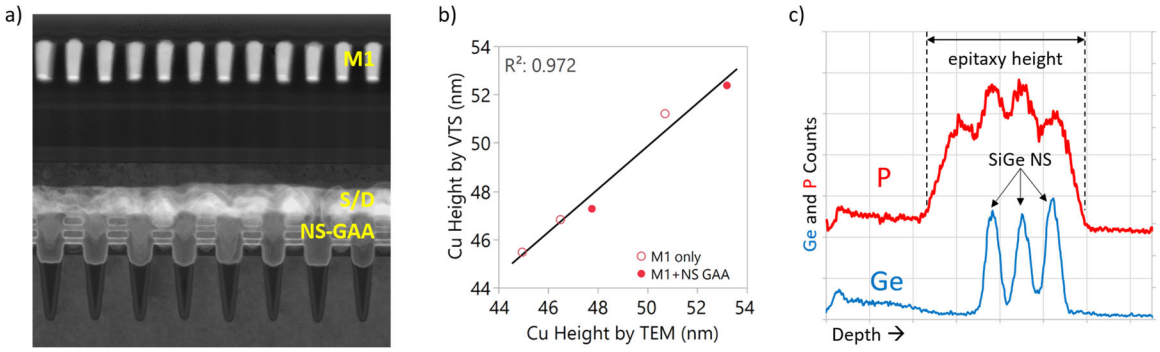


**FIGURE 2.** (a) TEM cross-section of a device-like metrology target comprising M1 on top of a full FEOL build with nanosheet gate-all-around (NS GAA) transistors including gate stack and source/drain epitaxy; MOL contacts are omitted in this design. (b) M1 Cu height determined by VTS in comparison to TEM reference; open symbols are referring to data from a target having no other patterning but M1, solid symbols depict values obtained from a target architecture as depicted in (a). (c) SIMS profile prior to sacrificial SiGe channel release showing Ge (SiGe NS) and P profiles from the source and drain epitaxy.

In recent years, sophisticated algorithms for data analyses and especially machine learning have given a boost to essentially all available metrology techniques. Specifically, model-based scatterometry benefitted significantly from such enhancements to increase sensitivity to smallest volume changes and enable sheet-specific measurements for nanosheet architectures.[14,15]

While x-ray photoelectron spectroscopy (XPS) has been used in the industry for years, Raman spectroscopy[6], and most recently the introduction of in-line secondary ion mass spectrometry (SIMS)[16] have added tremendous capabilities to the materials characterization portfolio. While traditionally not considered an in-line technique, SIMS has proven to be of significant value and, in certain cases, wafers can continue in the manufacturing line; therefore, it may be considered as a non-destructive technique to some extent. Measurements of doping profiles and material composition, especially on within fully integrated devices within nanometer-sized features and high aspect ratios are critical for process optimization toward highest device performance.

While there is already an impressive selection of in-line metrology tools available, further developments and the introduction of additional techniques are a necessity for metrology to match the needs arising from the scaling efforts that will not stop any time soon.

## REFERENCES


1. N. Loubet et al., "Stacked nanosheet gate-all-around transistor to enable scaling beyond FinFET," in *Symp. VLSI Technol*. 230–231, Kyoto, Japan (2017).
2. M. Breton, D. Schmidt, A. Greene, J. Frougier, N. Felix, *J. Micro/Nanopattern. Mats. Metro.* **21**, 021206 (2022).
3. R. Lallement, D. Schmidt, R. Johnson, J. Wong, C. Carr, M. Burkhardt, J. Morillo, A. Gabor, *Proc. SPIE* **12494**, 124940S (2023).
4. W. Hafez et al., "Intel PowerVia Technology: Backside Power Delivery for High Density and High-Performance Computing," in *Symp. VLSI Technol*, 1–2, Kyoto, Japan (2023).
5. K. P. O'Brien et al., *Nature Communications* **14**, 6400 (2023).
6. D. Schmidt, C. Durfee, J. Li, N. J Loubet, A. Cepler, L. Neeman, N. Meir, J. Ofek, Y. Oren, D. Fishman, *J. Micro/Nanopattern. Mats. Metro.* **21**, 021203 (2022).
7. D. Edelstein et al., "A 14 nm embedded STT-MRAM CMOS technology," in *IEEE Int. Electron. Devices Meeting (IEDM)*, San Francisco, CA, USA (2020).
8. S. Ambrogio et al., *Nature* **620**, 768 (2023).
9. M. Le Gallo et al., *Nature Electronics* **6**, 680 (2023).
10. D. Schmidt, M. Medikonda, M. Rizzolo, C. Silvestre, J. Frougier, A. Greene, M. A. Breton, A. Cepler, J. Ofek, I. Kaplan, R. Koret, I. Turovets, *J. Micro/Nanopattern. Mats. Metro.* **22**, 031203 (2023).
11. M. Medikonda, D. Schmidt, M. Rizzolo, M. A. Breton, A. Dutta, H. Wu, E. R. Evarts, A. Cepler, R. Koret, I. Turovets, D. Edelstein, *Proc. SPIE* **PC12053**, PC120530J (2022).
12. K. Sieg, C. Bottoms, C. J. Waskiewicz, A. Matos Mejia, J. Han, S. Butt, D. Schmidt, S. Schoeche, A. Hamer, A. Hubbard, *Proc. SPIE* **12955**, 12955-57 (2024).
13. S. Schoeche, D. Schmidt, J. Han, S. Butt, K. Sieg, M. Cheng, A. Cepler, S. Dror, J. Ofek, I. Osherov, I. Turovets, *Proc. SPIE* **12955**, 12955-56 (2024).
14. D. Schmidt, A. Cepler, C. Durfee, S. Pancharatnam, J. Frougier, M. Breton, A. Greene, M. Klare, R. Koret, I. Turovets, *IEEE Trans. Semicond. Manuf.* **35**, 412 (2022).
15. H. Chouaib, V. Dimastrodonato, A. Chou, A. Cangiano, A Cross, D. Shaughnessy, Z. Tan, D. Schmidt, C. Durfee, S. Pancharatnam, J. Frougier, A. Greene, M. Breton, *Proc. SPIE* **12955**, 12955-19 (2024).
16. S. Schoeche, K. Sieg, D. Schmidt, M. Nasseri, S. Mochizuki, M. Hopstaken, Y. Zhu, L. Xiang, J. Hoffman, D. Lewellyn, S. Okada, P. Isbester, *Proc. SPIE* **12955**, 12955-7 (2024).


## KEYWORDS

In-line Metrology, Semiconductors, Nanosheet, Gate-All-Around, Manufacturing, Characterization

# Advancing Measurement Science for Microelectronics: CHIPS R&D Metrology Program

M. L. Dowell*, H.H. Brown, G.R. Greene, P.D. Hale, S.L. Hughes, B.D. Hoskins, R.R. Keller, R.J. Kline, J.W. Lau, and J.M. Shainline

*National Institute of Standards and Technology*
*325 Broadway, Boulder, CO 80305*
*marla.dowell@chips.gov*

## INTRODUCTION

The CHIPS and Science Act of 2022 called for NIST to "carry out a microelectronics research program to enable advances and breakthroughs….that will accelerate the underlying R&D for metrology of next-generation microelectronics and ensure the competitiveness and leadership of the United States….", NIST is leveraging its measurement science expertise, standards development contributions, and stakeholder engagement practices to address the highest priority metrology challenges identified across industry, academia, and government agencies. The program expands upon NIST's strong track record of supporting the semiconductor technology and manufacturing ecosystem by developing, advancing, and deploying measurement technologies that are accurate, precise, and fit-for-purpose.

## KEY RESEARCH & DEVELOPMENT AREAS

In September 2022, NIST published a report titled Strategic Opportunities for U.S. Semiconductor Manufacturing, which identifies seven grand challenges that need critical attention from a metrology perspective to achieve the future state vision of a U.S.-led global semiconductor industry. [1] The CHIPS Metrology Program aligns its research and development portfolios based on the identified metrology needs of the seven grand challenges, which are listed here:

1. Metrology for Materials Purity, Properties, and Provenance
2. Advanced Metrology for Future Microelectronics Manufacturing
3. Enabling Metrology for Integrating Components in Advanced Packaging
4. Modeling and Simulating Semiconductor Materials, Designs, and Components
5. Modeling and Simulating Semiconductor Manufacturing Processes
6. Standardizing New Materials, Processes, and Equipment for Microelectronics
7. Metrology to Enhance Security and Provenance of Microelectronic-based Components and Products

The CHIPS R&D Office published Metrology Gaps in the Semiconductor Ecosystem in July 2023, outlining the Metrology Program's roadmap and its efforts to ensure that the research portfolio is aligned with CHIPS Act, external stakeholder needs, and NIST capabilities. [2]

In January 2024, NIST announced that over $109 million in funding had been provided to 29 approved NIST research projects. These current projects are helping to develop new measurement instruments, measurement methods, and measurement-informed models and simulations for advanced microelectronics design and manufacturing. NIST project teams have identified collaborative opportunities with industry and academic collaborators. Additional projects will be selected by the end of 2024.

## METROLOGY EXCHANGE TO INNOVATE IN SEMICONDUCTORS

The Metrology Exchange to Innovate in Semiconductors, or METIS, is a data exchange ecosystem being developed by NIST that will give stakeholders access to CHIPS Metrology research results and serve to catalyze innovative breakthroughs in U.S. semiconductor manufacturing. METIS will make research and data available in a manner that guards intellectual property, protects U.S. security interests, is aligned with the approach used by NIST for access to research results, and is self-sustaining to meet future needs. Establishing a data exchange ecosystem will meet that need, giving stakeholders access to CHIPS Metrology research results and serving to catalyze breakthroughs in U.S. semiconductor manufacturing. The METIS concept leverages and builds upon currently existing data management systems and processes at NIST, an organization uniquely qualified to both produce and manage leading metrology research and technical data products. By designing the data ecosystem around and for research needed by the public, industry, and the scientific community, METIS serves as a virtual platform for curation of microelectronics research data and tools with security and controls to enable the final products to reach their intended recipients. An initial draft of a publication describing METIS was released for public comment in December 2023. [3] The public comment phase of METIS allowed interested stakeholders to provide input on the design and implementation of METIS, the scenarios and use cases METIS will address, as well as other details.

## REFERENCES

1. Balachandra, A. , Gundlach, D. , Hale, P. , Jurrens, K. , Kline, R. , McBride, T. , Orji, N. , Rekhi, S. , Shyam-Sunder, S. and Seiler, D. (2022), Strategic Opportunities for U.S. Semiconductor Manufacturing, Special Publication (NIST SP), National Institute of Standards and Technology, Gaithersburg, MD, [online], https://doi.org/10.6028/nist.chips.1000, https://tsapps.nist.gov/publication/get_pdf.cfm?pub_id=936648 (Accessed February 12, 2024)
2. National Institute of Standards and Technology (2023) Metrology Gaps in the Semiconductor Ecosystem: First Steps Toward Establishing the CHIPS R&D Metrology Program. (Department of Commerce, Washington, D.C.) https://www.nist.gov/document/chips-rd-metrology-gaps-semiconductor-ecosystem
3. CHIPS for America (2023) Building a Metrology Exchange to Innovate in Semiconductors (METIS). (National Institute of Standards and Technology, Gaithersburg, MD), NIST Creating Helpful Incentives to Produce Semiconductors for America (NIST CHIPS) 1000-2 ipd. https://doi.org/10.6028/NIST.CHIPS.1000-2.ipd.

## KEYWORDS

Metrology, semiconductor, microelectronics, materials, standards, manufacturing

# Latest developments of automated transmission electron microscopy for semiconductor industry

Zhenxin Zhong*, Michael Strauss, Lin Jiang, Karthik Gnanasekaran, Xiaoting Gu

*Materials & Structural Analysis, Thermo Fisher Scientific, Inc.*
*5350 NE Dawson Creek Dr, Hillsboro, OR 97124-5793*
** Email:zhenxin.zhong@thermofisher.com*

## INTRODUCTION

With the recent transition to gate-all-around (GAA) transistor technology and complex 3D memory devices, critical process challenges are driving increasing demand for high quality (scanning) transmission electron microscopy ((S)TEM) reference metrology data.[1] Transmission electron microscopy (TEM) stands out as the preferred imaging technique for achieving the utmost spatial resolution. Automation provides necessary time to data, precision, and a high volume data with low cost of ownership.[2] The introduction of automated focused ion beam (FIB) sample preparation and (S)TEM analysis workflows were introduced about a decade ago for meeting the increasing demand of TEM dimensional analysis driven by FinFET technology advancement.[3] Automated Thermo Scientific™ FIB to Metrios™ (S)TEM workflow was reported to accelerate time to data (by over two times) with improved statistical significance by mitigating human errors.[4] (S)TEM automation has found widespread adoption across the semiconductor industry for research and development, failure analysis, and device fabrication process control. Nonetheless, (S)TEM automation also faces limitations, notably in the manual handling of TEM grids and holders. The construction of recipes for new use cases can pose significant time requirements and involves a steep learning curve.[4]

In this paper, we report the latest developments in automated (S)TEM in addressing these challenges. Recent innovations in TEM hardware and software have facilitated the realization of a fully automatic (S)TEM workflow. We introduce internal machine learning-based models designed for feature and region of interest (ROI) navigation, along with recipe-free (S)TEM automation. Development of sample tilt algorithms extends (S)TEM automation coverage for a wide range of semiconductor device types, including logic, DRAM, and 3D NAND.

## FULLY AUTOMATIC (S)TEM WORKFLOW

The need for high consistency and repeatability of data from an increasing volume of TEM samples, as well as a shortage of skilled labor, are making fully automated (S)TEM workflow a necessity for the industry. As illustrated in Figure 1, manual intervention of instrumentation, including loading/unloading of TEM sample holder, alignment of (S)TEM, and lamella info assignment, is still required for (S)TEM automation in prior generations of Metrios. Recent developments in (S)TEM automate these processes for a fully automatic (S)TEM workflow. A newly introduced stage (Smart Stage) in Metrios 6™ inserts and retracts the sample holder automatically in and out of the microscope column after user or robot places the holder in the parking position, eliminating manual handling and potential for human errors. The critical microscope alignments are maintained by Tool Readiness, an automated alignment workflow, for high quality data and robust (S)TEM automation. Critical wafer and sample information is passed from upstream FIB systems for automatic execution of (S)TEM imaging and analysis to obtain high volume TEM data. Fully automated TEM workflow reduces or removes the need for manual intervention and increases the accuracy and repeatability of results.

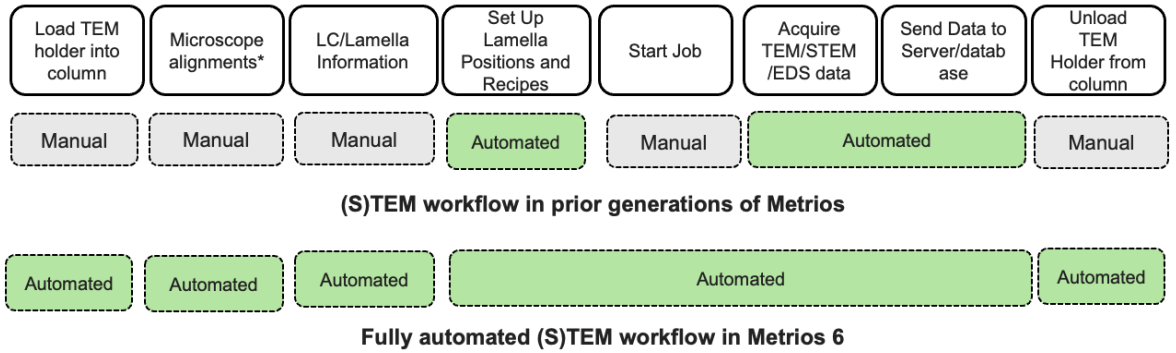


**Figure 1**. Road to fully automatic (S)TEM workflow

## RECIPE-FREE (S)TEM PROCESS FLOW AUTOMATION

Machine learning (ML) is driving a profound transformation in semiconductor manufacturing and metrology.[5] It plays a pivotal role in optimizing processes and significantly enhancing the throughput and precision of measurement techniques. Recent advancements in TEM techniques have facilitated the full automation of (S)TEM imaging and analysis processes through the employment of ML algorithms.[6] Figure 2a shows the major steps on the automated (S)TEM workflow in Metrios Smart Automation. Several of the navigation and lamella orientation steps are enabled by factory supplied ML models, including locating the lamella, tilting to the silicon zone axis, and determining the proper area of interest. Overview images of the features are acquired after the lamella is properly oriented. The user-trained ML model uniquely identifies each feature of interest. Feature positions are then recalled by the automated workflow for final image acquisition. The Metrios Smart Automation utilizes convolutional neural networks (CNN) for ML model training, allowing for wide variations in device processing and sample preparation. Different sample types from process steps can be trained into a single ML model, providing improved ease-of-use for the user. Figure 2b shows an example ML model trained for recognizing three GAA etch sample types. A new ML training method, object detection (OBD), has recently emerged, showcasing substantial reductions in model creation time. This advancement achieves a remarkable tenfold acceleration in time to build robust ML models compared to the previous CNN approach. Notably, a robust ML model development now demands less than 30 minutes. Figure 2c illustrates a comparison between CNN and OBD ML algorithms. CNN algorithm requires drawing polygons around the features of interest and the new OBJ algorithm employs bounding boxes for rapid feature segmentation. Recipe-free (S)TEM process flow automation utilizes ML algorithms to substantially reduce automation set-up time for each new process or sample type to provide ease-of-use and scalability.

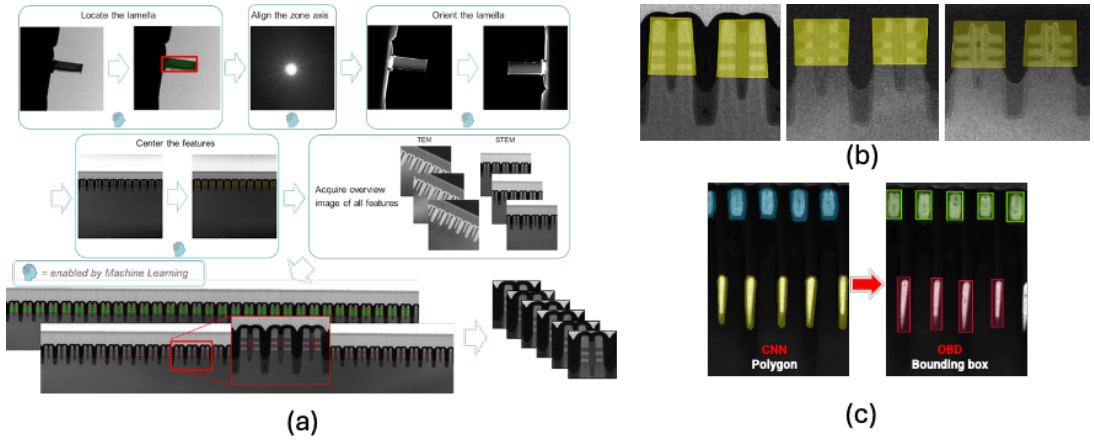


**Figure 2**. (a) A machine learning enabled automated (S)TEM workflow; (b) an example ML model for three GAA etch types; (c) CNN and OBD ML segmentation comparison (polygon vs bounding box annotation)

## (S)TEM WORKFLOWS ON VARIOUS DEVICE TYPES

Automatically orienting an electron-transparent specimen to the incident electron beam is an essential step for (S)TEM workflows and precise metrology analysis. Several specimen tilt alignment algorithms have been developed for extending (S)TEM automation workflows beyond samples with Si <110> substrates. Higher order zone axis alignment, e.g., Si<120>, Si<130>, are developed for advanced DRAM nodes with denser packing. Tilt alignment of non-crystalline specimens, including an ML-enabled algorithm for 3D NAND planar samples, will be discussed.

## SUMMARY

We introduce a fully automatic (S)TEM workflow, including automatic handling of holders, automatic tool alignment, and recipe-free (S)TEM process flow automation, specifically tailored for high volume reference TEM data. The integration of artificial intelligence and machine learning has been instrumental in enhancing (S)TEM automation workflows, broadening sample type coverage, and expediting the development time for ML models. Additionally, we will explore other advancements such as TEM hardware innovations aimed at accelerating data acquisition.

## REFERENCES

1. M. A. Breton, D. Schmidt, A. Greene, J. Frougier, and N. Felix, *J. Micro/Nanopattern. Mater. Metrol.,* **21(2)**, 021206 (2022)
2. O. Ugurlu, H. Johanesen, A. Kenslea, 2017 FCMN conf. proc. 48, (2017)
3. M. Kuhn, M. Zhou, Y. Johnson, K. 2017 FCMN conf. proc. 38, (2017)
4. P. v. Heide, E. Grieten, E. Vancoille, 2019 FCMN conf. proc. 35, (2019)
5. P. Leray, S. Halder, D. Cerbu, W. Verachtert, 2019 FCMN conf. proc. 28, (2019)
6. M. Strauss, C. Li, C. Hakala, X. Gu, A. Mani, Z. Zhong, Proceedings of the SPIE, **12496**, 1249639 (2023).

## KEYWORDS

Automated, TEM, process control, TEM metrology, Machine learning

## ACKNOWLEDGEMENTS

This project has received funding from the ECSEL Joint Undertaking (JU) under grant agreement No 826589. The JU receives support from the European Union's Horizon 2020 research and innovation program and Netherlands, Belgium, Germany, France, Italy, Austria, Hungary, Romania, Sweden and Israel.

The project leading to this application has received funding from the ECSEL Joint Undertaking (JU) under grant agreement No 826422. The JU receives support from the European Union's Horizon 2020 research and innovation program and Netherlands, Belgium, Germany, France, Romania, Israel.

The authors acknowledge IMEC for providing GAA samples under ECSEL JU grants. The authors also acknowledge the contribution from David Prentice and Jamie Gravell for GAA and 3D NAND TEM sample preparation.

# Applications of Machine Learning and Semi-Automated Workflows to 4D-STEM Characterization

Colin Ophus

*National Center for Electron Microscopy, Molecular Foundry, Lawrence Berkeley National Laboratory, 1 Cyclotron Road, Berkeley, CA, USA 94720*

## INTRODUCTION

Many materials science studies use scanning transmission electron microscopy (STEM) to characterize atomic-scale structure. Conventional STEM imaging experiments produce only a few intensity values at each probe position. However, modern high-speed detectors allow us to measure a full 2D diffraction pattern, over a grid of 2D probe positions, forming a four dimensional (4D)-STEM dataset [1]. These 4D-STEM datasets record information about the local phase, orientation, deformation, and other parameters, for both crystalline and amorphous materials [2]. However, 4D-STEM datasets can contain millions of images and therefore require highly automated and robust software codes to extract the target properties. In this talk, I will demonstrate some of the analysis tools developed to analyze data-intensive 4D-STEM studies of materials over functional length scales [3]. This includes measurements of macroscopic properties such as crystal phase, orientation, and local deformation maps [4], and microscopic properties such as atomic structures in 2D and 3D measured with ptychography and other phase contrast imaging modes [5]. I will also demonstrate some applications of machine learning tools, including inversion diffraction patterns where signals have been scrambled by multiple scattering of the electron beam [6], and performing automated classification of crystal systems and lattice parameters from diffraction patterns [7].

## SEMI-AUTOMATED 4D-STEM ANALYSIS WORKFLOWS

Figure 1a shows the geometry of a 4D-STEM experiment, where diffraction patterns are measured from many probe positions. Diffraction patterns generated by crystalline or semicrystalline materials contain Bragg peaks which encode the spacing the atomic lattice spacing and orientation [8]. The primary software tool we use to analyze these datasets is the open-source py4DSTEM toolkit developed by Savitzky et al. for 4D-STEM analysis [3]. Using py4DSTEM, we can preprocess the data, and then use template matching to measure the positions of each diffracted disk. We then apply calibrations the diffracted disks, including centering, removing ellipticity and determining pattern rotation. From these calibrated peak positions, we can reconstruct the morphology of a sample over functional length scales, for example the conductive polymers shown in Figure 1b. If the structure of the sample is known *a priori*, we can simulate a library of diffraction patterns, and compare this library to each pattern to determine the local crystalline phase and orientation [4]. py4DSTEM is also capable of generating complex visualizations, such as the overlapping orientation maps shown in Figures 1a and b.

We can also use 4D-STEM to image the structure of materials, down to the scale of individual atoms. We have implemented several 4D-STEM computational imaging methods in py4DSTEM, including differential phase contrast (DPC), parallax imaging, and ptychography [9]. DPC and parallax reconstructions are relatively straight-forward to apply, but there are many algorithms and regularizations that can be used for ptychography. In ptychographic reconstructions, we use iterative gradient descent and redundant information contained in overlapping STEM probe positions to reconstruct the phase shifts induced into the electron beam by the sample. We have focused on robustness and ease of use to facilitate widespread implementation. Ptychography can also be combined by with tilt series, to reconstruct sample structure in 3D. Figure 1c shows a ptychographic atomic electron tomography experiment, and the reconstruction of a complex Zr-Te nanowire structure encapsulated in a double-walled carbon nanotube [5]. These examples show the flexibility and power of 4D-STEM characterization.

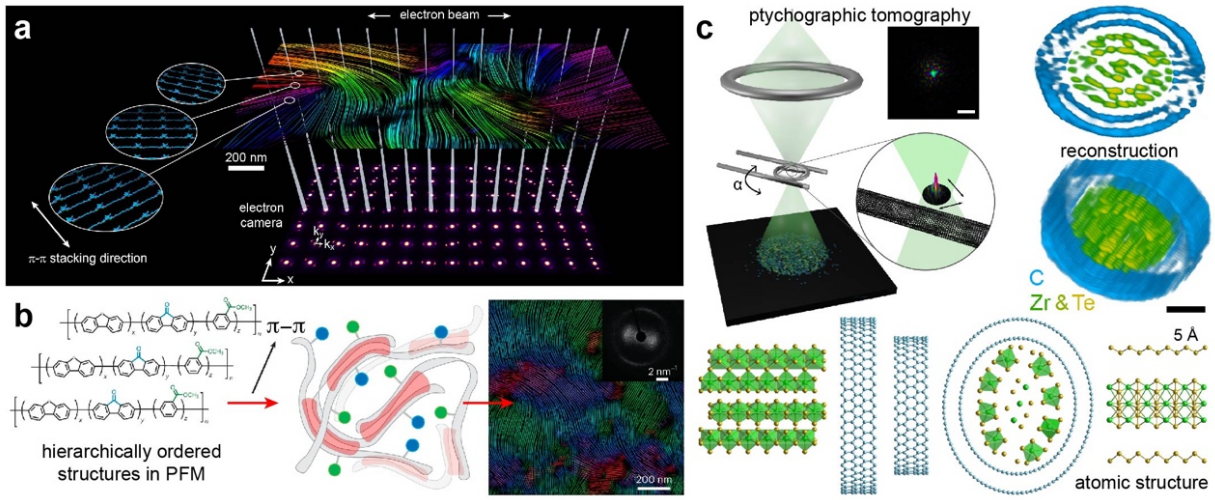


**FIGURE 1.** (a) 4D-STEM experimental geometry, with reconstructed orientation morphology shown above, adapted from [10]. (b) Orientation mapping of a polymer containing hierarchically ordered structures, adapted from [11]. (c) Ptychographic 3D tomography measurement of ZrTe nanowire in a double-walled carbon nanotube, adapted from [5].

## MACHINE LEARNING 4D-STEM ANALYSIS

One of the primary limitations of transmission electron microscopy is that the electron beam interacts very strongly with matter, and thus may scatter multiple times when passing through a specimen. This "dynamical diffraction" can reduce imaging contrast, blur our spectroscopic signals, and inject complex non-linear features into diffraction patterns. The 4D-STEM crystalline diffraction methods discussed above can be severely degraded by this multiple scattering. We have therefore developed a method to invert these complex diffraction patterns into simple structure factor representations, by using machine learning [6]. We first simulate hundreds of thousands of diffraction patterns from crystal structures taken from the materials project [12], which are then augmented with microscope errors such as pattern shifts and distortion, bad detect pixels and inelastic background. We then trained a network which we call FCU-Net, trained on the simulated diffraction patterns and the underlying ground truth structure factors. We have adapted U-Net to operate in the Fourier domain by using forward and inverse Fourier transforms at the input and output of the network respectively, and complex number activation functions. In this talk, I will show how this machine learning platform significantly outperforms conventional 4D-STEM analysis methods and show applications to strain mapping in both thick 2D materials and thick semiconductor samples.

As discussed above, 4D-STEM can be used to map crystal orientation and phases if we are analyzing known structures. However, in many cases we may not know all crystal phases contained in a sample, or the specimen might be contaminated with unknown secondary phases. We are therefore developing a machine learning approach for blind identification of both crystal families and space groups from diffraction patterns [7]. We start by using a Bloch wave method to simulate many millions of diffraction patterns from many orientations over multiple thicknesses [12]. We then encode these sets of vectors (Bragg disk 2D positions and intensities) into a vector representation by using a basis set which uses narrow radial bins and periodic annular weights. We then train a random forest classifier to estimate the crystal family and space groups from the annular and radial basis set and estimate the confidence of the prediction. Once the crystal family has been identified, further machine learning regression networks predict the lattice parameter(s) of the material from the spacing of the diffraction spots. We show that this approach can generate surprisingly robust predictions for simple crystal phases, though accuracy falls significantly for more complex crystalline structures.

All our simulated and experimental data is available online, adhering to FAIR data principles [13]. The simulated data can be freely used by any researchers to test their own machine learning approaches to 4D-STEM analysis. We have implemented our machine learning methods directly into py4DSTEM to make them more widely available. We also provide tutorials in the form of Jupyter notebooks to teach both our conventional and machine learning 4D-STEM analysis methods.

## REFERENCES


1. C. Ophus, Annual Review of Materials Research **53** (2023).
2. C. Ophus, Microscopy and Microanalysis **25**, 563-582 (2019).
3. B. Savitzky et al., Microscopy and Microanalysis **27**, 712-734 (2021).
4. C. Ophus et al., Microscopy and Microanalysis **28**, 390-403 (2022).
5. P. Pelz et al., Nature Communications **14**, 7906 (2023).
6. J. Munshi et al., npj Computational Materials **8**, 254 (2022).
7. S. Gleason et al., Microscopy and Microanalysis **29** S1, 698–699 (2023).
8. O Panova et al., Nature Materials **18**, 860-865 (2019).
9. G. Varnavides et al., arXiv:2309.05250 (2023).
10. K. Bustillo et al., Accounts of Chemical Research **54**, 2543-2551 (2021).
11. T. Zhu et al., Nature Energy **8**, 129-137 (2023).
12. M. de Graef, *Introduction to conventional transmission electron microscopy*, Cambridge University Press (2003).
13. M.D. Wilkinson et al., Scientific Data **3**, 1-9 (2016).


## KEYWORDS

Scanning Transmission Electron Microscopy, 4D-STEM, Open-Source Software, Machine Learning, Material Properties

# Coulomb-correlated Electrons in a Transmission Electron Microscope

Rudolf Haindl[1,2], Armin Feist[1,2], Till Domröse[1,2], Marcel Möller[1,2], John H. Gaida[1,2], Sergey V. Yalunin[1,2], Claus Ropers[1,2]

1. *Department of Ultrafast Dynamics, Max Planck Institute for Multidisciplinary Sciences, Göttingen, DE*
2. *IV. Physical Institute – Solids and Nanostructures, University of Göttingen, Göttingen, DE*

## INTRODUCTION

In contrast to possibilities arising from electron correlations in condensed matter systems, stochastic Coulomb interactions in free electron beams are usually considered detrimental. In electron microscopy, electron repulsion leads to stochastic longitudinal and transverse emittance growth [1, 2] and limits the brightness of state-of-the-art electron sources. However, in a regime where few-body interactions dominate, Coulomb interactions can also have predictable effects, such as antibunching in free-electron beams [3-5]. A powerful approach to induce strong electron-electron interactions is femtosecond-triggered photoemission from nanotips [6, 7]. Recently, femtosecond gating enabled strongly non-Poissonian beam statistics in free electron beams [5, 8, 9], with applications emerging in shot-noise-reduced electron microscopy and lithography.

In this work [9], we introduce event-based transmission electron microscopy to detect few-electron states from a laser-triggered nanoscale field emitter. We characterize the strong Coulomb correlations of few-electron states and show trajectory simulations describing the build-up of Coulomb-correlation between electrons. Finally, we discuss applications of beams of correlated electrons, including shot-noise reduction and electron heralding schemes.

## EXPERIMENT

The experimental work was carried out in transmission electron microscopes that are modified for photoexcitation of the electron source [8, 10] (see Fig. 1a). A laser pulse train with 2 MHz repetition rate and 160 fs pulse length generates ultrashort electron pulses by close-to-threshold laser-triggered Schottky emission. The photoelectrons are analyzed with a hybrid pixel electron detector, which is mounted behind the imaging energy filter (see Fig. 1a) and images the spectral and spatial properties of the electrons. The detected electrons are matched to the generating photoemission laser pulse, and the number of electrons detected per pulse $n$ = 1,2,3,4 is assigned (see Fig. 1b).

The power scaling of the few-electron states is shown in Fig. 1c. In accordance with close-to-threshold laser-assisted Schottky emission, the single-electron ($n$=1) rate scales linearly with laser power. The double-electron ($n$=2) and triple-electron rate ($n$=3) scale quadratically and cubically, respectively, giving evidence that few-electron states are generated by a n-photon, n-electron emission mechanism.

### Characteristic Spectral Features of Few-Electron States

The $n$=1-state spectrum exhibits a single peak at the beam energy $E_0 \simeq 200$ keV (see Figs. 1e). Strikingly, the electron pulses with $n$>1 exhibit a distinctive spectral shape with the number of peaks identical to the number of electrons in the pulse (see Fig. 1f-h), indicating a strong interaction between the electrons in the pulse. The $n$=2−4 -states are plotted with respect to the state-averaged energy $\overline{E}$. For $n$=2, a projection of the energies of electrons A and B onto a 2d-energy pair histogram (Fig 2a) shows the same feature as the $n$=2 spectrum: a strong dip at the central beam energy $E_0$. Therefore, two electrons almost never arrive at the detector with the same electron energy. Remarkably, two-dimensional energy correlations for number states $n$=3 and $n$=4 also reveal a regular arrangement (see Fig. 2b,c), in agreement with simulations.

A particle-tracing simulation gives a quantitative explanation of the experimental results. When two electrons are injected into a static electric field, the inter-particle Coulomb force is acceleration-enhanced. While the two electrons repel each other, both electrons are accelerated by the external field in the laboratory frame. The final kinetic energy difference is proportional to the mean velocity of the two electrons multiplied by their difference velocity, resulting in a final energy difference of around 2 eV (see Fig. 1i).

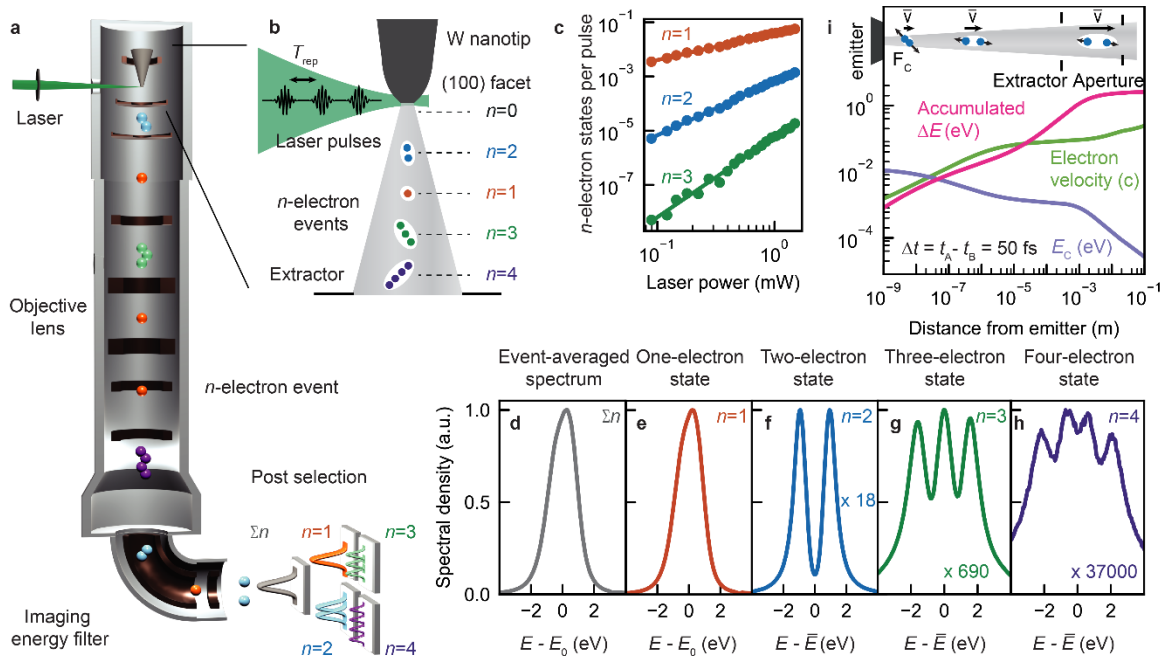


**FIGURE 1.** Few-electron states in a transmission electron microscope beam. a) The laser generates few-electron states via photoemission from a Schottky emitter (see panel b)). c) Power scaling of few electron states. d-h) Event-averaged (panel d) and event-resolved spectra with a distinctive spectral shape for $n$=1−4 (panels e-h). i) Particle trajectory simulation of the emitter geometry (sketch on top). The accumulated energy difference, electron velocity and coulomb energy are plotted against travel distance of electrons.

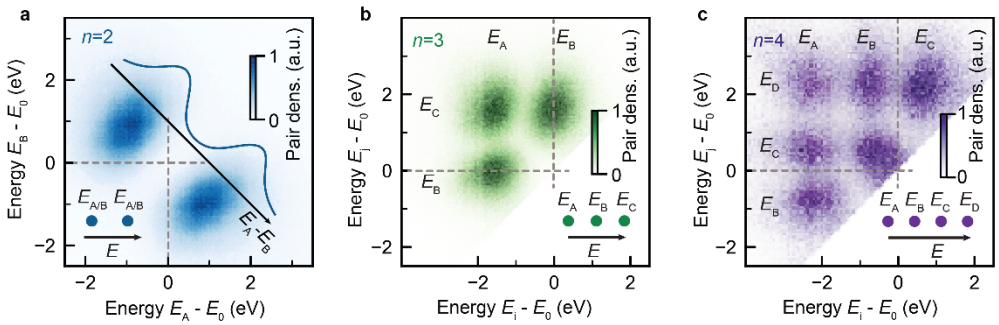


**FIGURE 2.** a) Energy histogram of $n$=2-states with electrons A and B. c&d) Sorted energy histogram for $n$=3 (panel b) and $n$=4 (panel c) with electrons A, B, C and D.

## Statistical Control over Electron Beams using Coulomb-correlations

Coulomb interactions affect longitudinal and transverse correlations and the electrostatic configuration shapes the ratio between the two components. Figure 3a shows the field dependence of the $n$=2-energy difference. For lower extraction fields, the correlation gap moves to lower difference energies, i.e., less correlation energy is accumulated during acceleration (see Fig. 3b). Rather, the Coulomb interaction is transferred preferably in transverse direction. As the electron beam passes beam limiting apertures, electron trajectories with higher transverse correlation are more

likely to be cut from the beam. This results in a reduced second-order correlation function $g_2(\tau=0)$ of electrons in the same pulse (see Fig. 3b). Hence, the electric field can be used to suppress higher order number states.

Other opportunities for statistical control of few-electron states arise from tailoring their spatial and spectral properties. For example, an aperture placed in a beam crossover reduces the number of transmitted higher number states, thereby reducing the shot-noise in electron beams. Alternatively, sub-Poissonian statistics can be generated by spectral filtering with a slit in a spectrally dispersed plane, where mostly $n$=1-states are transmitted (see Fig. 3c). Conversely, replacing the energy slit with a beam stop will mostly stop $n$=1-states, facilitating super-Poissonian beam statistics (see Fig. 3d).

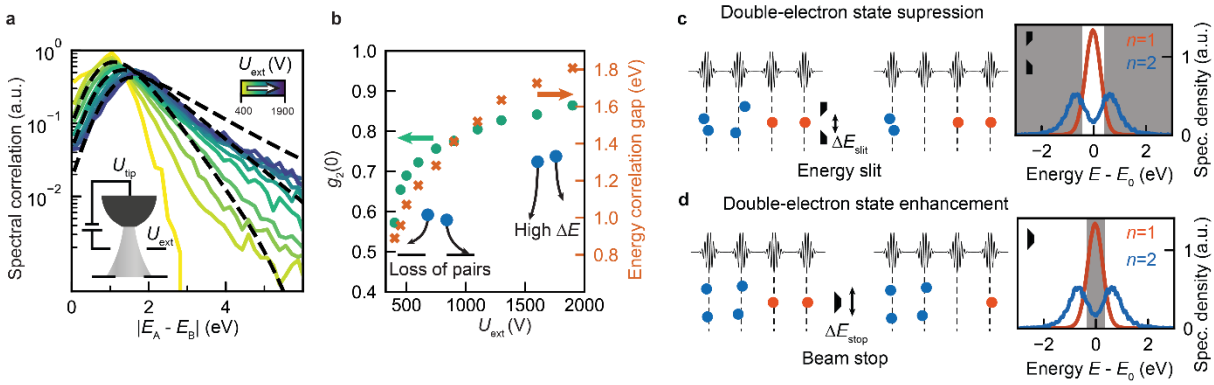


**FIGURE 3.** a) Electron pair correlation functions for various extraction fields. b) A decrease in extraction field reduces the correlation gap (red) and the second order correlation function at zero delay $g_2(0)$. c, An energy slit enhances the ratio of transmitted one-electron states over two-electron states. d, A beam stop suppresses the two-electron state number. c&d right: Experimental spectra with a digital slit/beam stop filtering energies shown in gray.

## CONCLUSION

We introduced electron number states that enable new experimental schemes, such as correlated probing with multiple electrons. Furthermore, a manifold of applications arises from manipulating the beam statistics. While already a shot-noise reduced ($n$=1-state enhanced) beam has great potential, a $n$=2 electron beam can serve as a source of heralded electrons. In this application, one of the two electrons is measured on a detector and thereby heralds the second electron, which interacts with a sample. This scheme allows to precisely count the number of electrons that interacted with a sample. In summary, Coulomb-correlated electron sources allow for a multitude of applications for electron microscopy and lithography.

## REFERENCES

1. H. Boersch, *Z. Phys.* **139**, 115-146 (1954).
2. K.H. Loeffler, *Z. Angew. Phys.* **27**, 145 (1969).
3. H. Kiesel, A. Renz, and F. Hasselbach, *Nature* **418**, 392–394 (2002).
4. M. Kuwahara, et al., *Phys. Rev. Lett.* **126**, 125501 (2021).
5. S. Keramati, W. Brunner, T.J. Gay, and H. Batelaan, *Phys. Rev. Lett.* **127**, 180602 (2021).
6. P. Hommelhoff, Y. Sortais, A. Aghajani-Talesh, and M. A. Kasevich, *Phys. Rev. Lett.* **96**, 077401 (2006).
7. C. Ropers, et al., *Phys. Rev. Lett.* **98**, 043907 (2007).
8. R. Haindl, et al., *Nat. Phys.* **19**, 1410–1417 (2023).
9. S. Meier, J. Heimerl and P. Hommelhoff, *Nat. Phys.* **19**, 1402–1409 (2023).
10. A. Feist, et al., *Ultramicroscopy* **176**, 63–73 (2017).

## KEYWORDS

Electron emitters, Electron correlations, Coulomb interactions, Electron microscopy, Electron lithography, Non-Poissonian electron beams

# Scanning Probe Microscopy: Pushing the Boundaries with Multi-Probes and Reverse Tip Sample Scanning

Umberto Celano* and Thomas Hantschel

*imec, 3001 Leuven, Belgium*
**Corresponding author: Umberto Celano, email: umberto.celano@imec.be*

## INTRODUCTION

The rapid pace of introduction of new three-dimensional (3D) architectures in nanoelectronics has created a solid demand for customized physical characterization and metrology solutions. At present, the evolution from finFET towards nanosheet (NS)-FET and the upcoming introduction of complex 3D interconnections to support heterogeneous integration is setting a high bar for analytical solutions required for failure analysis (FA) and metrology. Among other techniques, we provide here an update in two main areas of development for atomic for microscopy (AFM), arguably one of the most attracting methodologies in terms of flexibility in the type of information generated, with resolution, speed, throughput, and access to data. First, we report on recent advancements in multi-probe sensing schemes and the development of a tomographic AFM tool for materials research and FA. This area of development is currently considered a promising pathway for the automation of tomographic data generation and artifact-free data collection for various electrical AFM modes. Second, we review reverse tip sample (RTS) scanning probe microscopy (SPM), a method focusing on the idea of decoupling the actions of tip selection and replacement from sensing. This area of development for the field is considered as a powerful pathway for shorter time-to-data (<10x), enhanced dataset statistics with no compromise for nm-precise resolution.

## METHODS

Compared to existing AFM solutions both concepts reported here require major hardware modifications. These are described in detail elsewhere1,2 and are summarized here in the following section. For tomographic sensing our focus is on synchronized multi-probe sensing methods for the accurate control of material removal. To this end we leveraged the rapid switching capabilities of our multi-probe head scanner, the Rapid Probe Microscope (RPM-3D), a tool where a tiltable axis of the scanner allows for the rapid interchange between up to 3 different, and customizable probe tips (Figure 1a). To ensure that the optimal probe is used for each tier of a slice and sense of the tomographic dataset, we designed a dedicated clip cassette (Fig. 1). The RTS SPM sensing scheme is designed and implemented by mounting the sample on an AFM cantilever and providing a probe chip containing arrays of individual tip structures against which the sample is scanned (Fig. 1b). The concept is clearly the opposite to that of standard AFM probing where a single probe is scanning against the sample surface. To this end, we had to address key issues in the analysis flow, with the majority of the hardware modifications impacting the cantilever (here, hosting the sample) and the probe chip, i.e., a dense array of tip structures mounted on the AFM stage and to be ready to probe the sample as this is brought down from the AFM scanner. In this way, hundreds of probe tips can be contained in the array, including various kinds of tips for different analysis purposes (Fig. 1b). Among other advantages we highlight, the seamless tip exchange whenever required, the fast data acquisition from multiple tips (for enhanced throughput and statistics), the easy combination of analysis methods (e.g.,

tapping, and electrical modes) by pure sample reposition, and the possibility to reduce contact-induced sources of variability in various measurement modes.

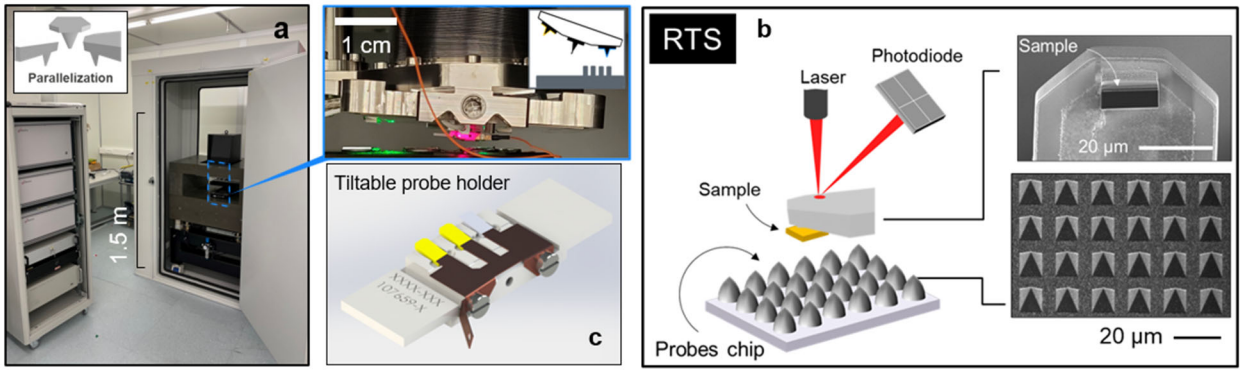


**FIGURE 1.** (a) Three-dimensional rendering of the customized RPM-3D system. Optical image of the custom probe cassette used to enable the probe switching, and schematic of mode of operation of the RPM-3D head. (b) Proposed RTS SPM configuration where the sample is mounted at the cantilever end and hundreds of tips are placed onto a probe chip and are instantly available for scanning the sample. (c) 3D rendering of the custom probe cassette.

## RESULTS AND DISCUSSION

The RPM-3D has been designed to allow for a fully automated switching and alignment routine, capable of switching, aligning, and compensating for any tip-to-tip variation to ensure the landing accuracy as reported elsewhere. At the foundation of tomographic sensing with AFM lies the possibility to control the atomically precise material removal induced by a sliding diamond tip. Paired with the self-adjusting capability of removal rate (RR) by dynamically varying the load force, every single scan improves the quality and speed of data acquisition, automation, high dimensional data handling, and extended volumetric sensitivity (range $10^7$-$10^{12}$ $nm^3$) offering volumetric mapping of electrical properties in the area of interest. Figure 2a shows that the RPM-3D can provide material removal in the range of 3–10 nm/scan in various materials. Moreover, the ability to automate the material removal allows us to set a target value for the removal rate (nm/scan), that the system will try to maintain automatically. This is shown in Fig. 2b where the 'scalpel-switch-sense' flow is reported for the self-extraction of the removal rate (RR) that is auto-tuning the tip-sample load force depending on the user's request, thus obtaining a good control over the RR for tens of scans. Fig. 2b shows a schematic view of the block diagram used in the control of RR during multiple read-out scans used in the Scalpel SPM. Note that the RPM-3D can be used to automate the depth sensing process, by alternating in between machining and sensing scans with probe switching. The tool can automatically modify the load force to maintain a constant RR.

Finally, another important advantage offered by probe alternation in tomographic sensing for electrical AFM, is the mitigation of tip-induced reconstruction artefacts in the secondary sensing channel (i.e., current, resistance, etc.). In a recent work reported by Sharma et al.,1 two electrical profiles are acquired in a location with a high density of dot cells effectively removing the TiN top-electrode. Both profiles are collected at the same location at the depth of 40 nm. This ensures that it is positioned well below the top-electrode in the oxide layer. By alternating the probes while maintaining the sample location, we can compare the data acquired for two different conductive probes, namely a diamond probe (CDT-NCHR, k = 92 N/m) and a Pt/Ir coated Si probe (ATEC-CONTPt, k = 7 N/m). Note that here the diamond probe is deliberately used at the same high-pressure conditions applied during the process of material removal, while the Pt/Ir probe is scanned at low force, i.e., the minimum force needed to obtain a good electrical contrast. The results (not shown here) indicate striking differences for the same structures when measured with the two probes. For the case of the high-pressure scan with the diamond probe, multiple shape and conductive artifacts can be identified. Similarly, the electrical contrast presented blurred features with the presence of double-tip artifacts.

In contrast, the measurement obtained with the Pt/Ir coated Si probe, measuring at a low pressure in the exact same location of the sample is free from these artifacts.

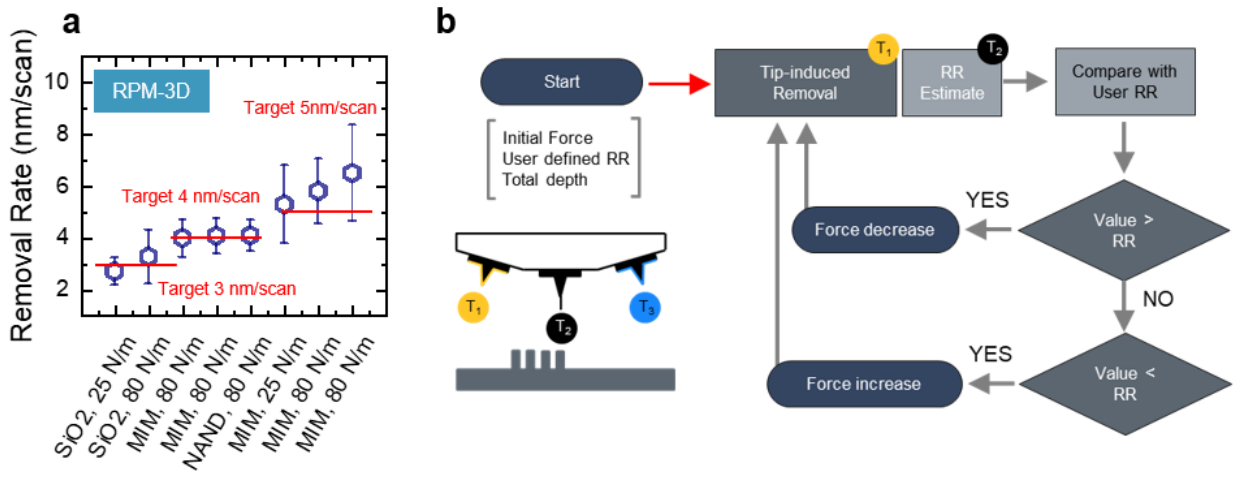


**FIGURE 2.** (a) RR control targeting three, four, and five nm of material erosion per scan. The plot shows a comparison between different samples ($SiO_2$ blanket, metal-insulator-metal MIM, and 3D NAND dummies). Note, each datapoint represents ten scans obtained on the sample described in the x-axis and a new probe is used for every datapoint. (b) Schematic view of the block diagram used in the control of RR during continuous scans used in the Scalpel SPM.

For RTS SPM, its successful implementation critically depends on the availability of suitable probe chips with integrated tip arrays. Therefore, we designed, fabricated, and evaluated first prototype probe chips using two well established methods for standard SPM probes: tip molding, and tip etching. Tip molding was used to make pyramidal doped diamond tip structures (Fig. 1b) with a low aspect ratio which are preferred for high-pressure electrical SPM applications such as scanning spreading resistance microscopy (SSRM). Hereby, inverted pyramids were first anisotropically etched into (100)-Si using KOH, then the etch pits were filled with boron doped microcrystalline diamond (MCD) using hot-filament chemical vapor deposition (HFCVD), and finally the Si mold material was etched away in KOH. The fabricated diamond tip prototype arrays were successfully tested in contact mode topography AFM measurements on nanostructured surfaces and in SSRM for carrier profiling on Si device structures. The obtained results in terms of resolution, conductivity, and wear resistance compared well to the performance of standard full diamond tips (FDTs). Tip etching was utilized to fabricate the first Si tip array prototypes; note that such Si tips have the advantage that they can be made with a high degree of freedom with respect to their shape, aspect ratio and dimensions. Moreover, functional coatings such as thin metal coatings can be easily applied to them. Fig. 3a illustrates schematically that Si tip structures were arranged in rows and are composed of a pedestal (8-15 µm high) with a nanoscopic tip structure on top (several hundreds of nanometers high). The inter-tip distance is 25 µm. Fig. 3b shows a fabricated Si tip prototype structure made by inductive coupled plasma (ICP) reactive ion etching (RIE). Fig. 3c shows optical images of a metal cantilever coated with nanoparticles (acting as sample to be measured) approached to the Si tips and scanning on them in intermittent contact mode. The resulting topography images are displayed in Fig. 3d; each Si tip scanned an area of 3x3 and 1x1 $\mu m^2$ and then then the cantilever was seamlessly moved to another Si tip (switching time of a few seconds only) and the scan sequence was repeated (in total 9 tips were used). This measurement illustrates the potential of RTS SPM for improved measurement quality and statistics by scanning the area of interest with several tips (compared single-tip scanning for conventional SPM).

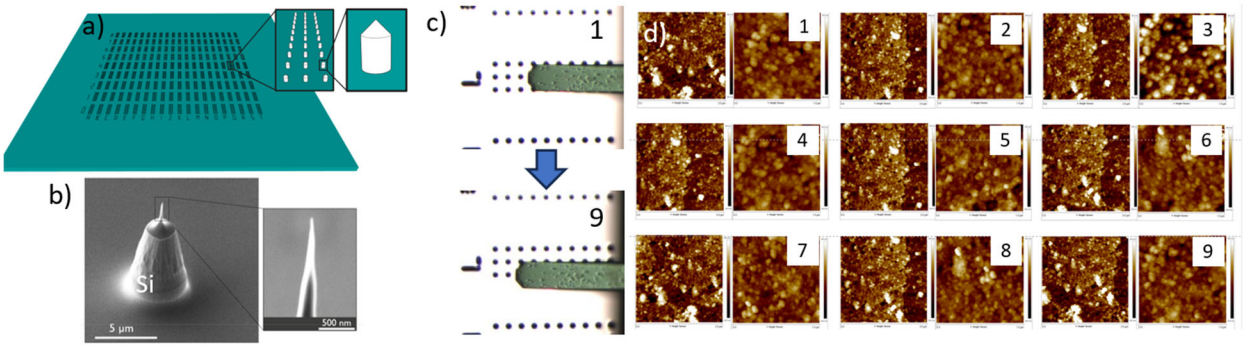


**FIGURE 3.** (a) Scheme of Si tip array design; (b) prototype of etched Si tip structure inspected by scanning electron microscopy; (c) optical image of nanoparticles coated metal cantilever engaged to Si tip and scanning it in intermittent contact mode; (d) 3x3 and 1x1 $\mu m^2$ scans performed on 9 different tips recorded after each other by swift tip switching.

## REFERENCES

1. Sharma, D., et al., EDFA Technical Articles **2023**, 25 (4), 20-26.
2. Celano, U., et al., 2019 IEEE International Electron Devices Meeting (IEDM), **2019**, 0163

## KEYWORDS

Scanning Probe Microscopy; Atomic Force Microscopy, Multi-probes SPM; Tomographic AFM; Reverse Tip Sample Scanning

# Non-destructive Metrology for Semiconductor Materials and Devices by X-rays

Kazuhiko OMOTE

*X-Ray Research Laboratory, Rigaku Corporation, Akishima, Tokyo, 196-8666, Japan*

## INTRODUCTION

Nowadays, X-ray metrologies are indispensable for evaluating material properties of semiconductor devices and their manufacturing processes. For example, SiGe is a key material for improving performance of logic devices through strain engineering. X-ray diffraction (XRD) is a unique technique to investigate the stacking structure and crystal quality. X-ray reflectivity (XRR) measurements can give absolute values of the layer thicknesses from sub nanometer to several hundred nanometers. Crystal defects, which are critical for the device performance, of various substrate wafers can be scanned by X-ray topography (XRT). Nanometer-scale surface device structures are observed precisely using glazing incidence small angle X-ray scattering (GI-SAXS). High aspect ratio hole structures, such as 3D flash memories can be analyzed by transmission small angle X-ray scattering (T-SAXS). X-ray imaging techniques are becoming critical for inspecting defects of advanced packaging devices. All those X-ray metrologies are nondestructive as is and do not require any prior sample treatment. In this paper, we will review state of the art applications of these X-ray metrology methods for advanced semiconductor technologies.

## EXAMPLES OF APPLICATIONS

For investigating patterned SiGe films and film stack structures, high-resolution XRD utilizing a crystal collimator is required. However, it is difficult to maintain high intensity by using a conventional flat crystal to focus on the small area of measurement pads. To overcome this, we have developed a high-resolution small-spot optic combined with a Johansson crystal and focusing multilayer mirror (hybrid optic) as shown in Fig. 1. This enables the measurement of rocking curves of patterned SiGe on Si and the ability to obtain thicknesses and Ge content of epitaxial SiGe films and film stacks at small pad dimensions. Those key parameters are simultaneously evaluated as shown in the same figure.

Crystal perfection of the substrate wafer is critical for performance of devices, which are fabricated on it. X-ray topography can scan whole wafer to investigate crystal defects, such as misorientation, dislocations, stacking faults,

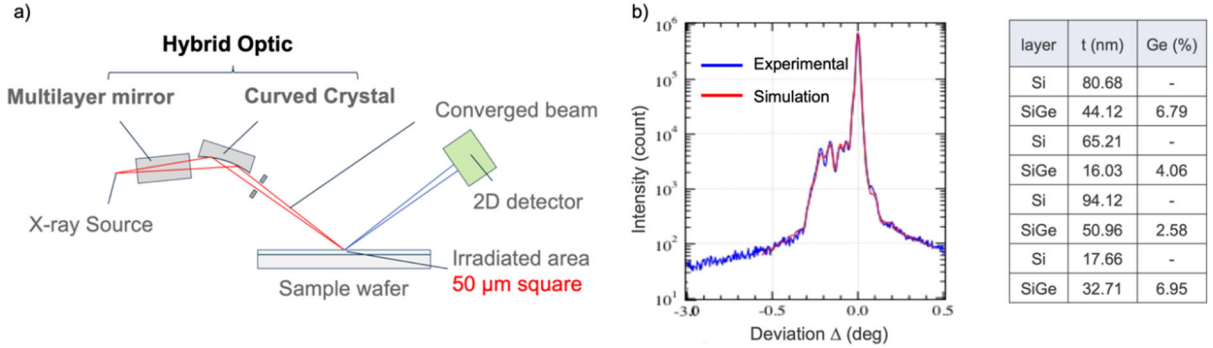


| layer | t (nm) | Ge (%) |
|---|---|---|
| Si | 80.68 | - |
| SiGe | 44.12 | 6.79 |
| Si | 65.21 | - |
| SiGe | 16.03 | 4.06 |
| Si | 94.12 | - |
| SiGe | 50.96 | 2.58 |
| Si | 17.66 | - |
| SiGe | 32.71 | 6.95 |

Fig. 1. a) Measurement geometry for the 50μm high-resolution XRD measurement. b) Multilayer SiGe measurement result is analyzed by the simulation with the layer structure listed in the table.

and so on. Many of those can manifest as killer defects for the fabricated devices. Fig. 2 shows an X-ray topography image of a SiC wafer, a substrate that is being rapidly developed for high-efficiency power devices. We can observe numerous dislocations are present, even for device production wafers, and therefore inspection for the crystal quality is indispensable.

To increase memory capacity, flash memory has adopted a 3-dimensional structure, in which memory cells are formed around a deep memory hole. The fabrication process is facing a lot of challenges in manufacturing such high aspect ratio (HAR) holes and creating consistent memory cells. For investigating such memory hole structures, we have developed a transmission X-ray small angle scattering (T-SAXS) instrument. Incident X-rays penetrate through both the device area and Si substrate and scattered X-ray are detected by a 2D-detector as shown in Fig. 3. The scattering intensity of each spot changes in accordance with the scattering vector $\boldsymbol{Q} = (Q_X, Q_Y, Q_Z)$, through a rotating angle $\omega$ and scattering angle $2\theta$. By analying $\boldsymbol{Q}$ dependence of the scattering intensity, we can determine the precise three-dimensional shape of the HAR holes. The observed structure agrees very well with the STEM result as shown in Fig. 4.

Not discussed here, but additional X-ray metrology methods include XRR for thin film thickness and density measurements and the application of GI-SAXS to analyze the dimensional properties of surface structures such as EUV resists. The adoption of X-ray methods for semiconductor development and manufacturing has significantly increased and a robust roadmap for advanced sources, optics and detectors will further enhance the capabilities of these increasingly critical methods.

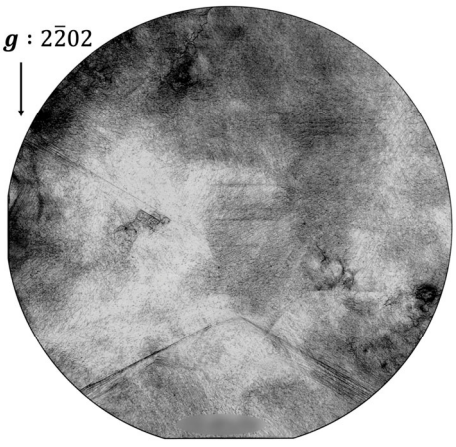


Fig. 2. X-ray topography image of a 4 inch 4H SiC wafer.

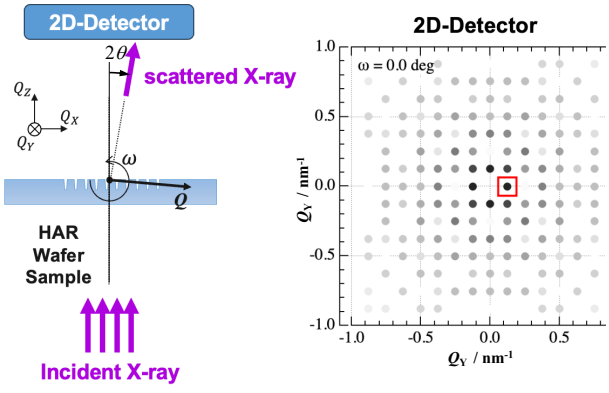


Fig. 3. Measurement geometry of T-SAXS and typical scattering pattern on the two-dimensional detector.

## KEYWORDS

X-ray diffraction, X-ray topography, small angle X-ray scattering, SiGe, SiC, 3D flash memory.

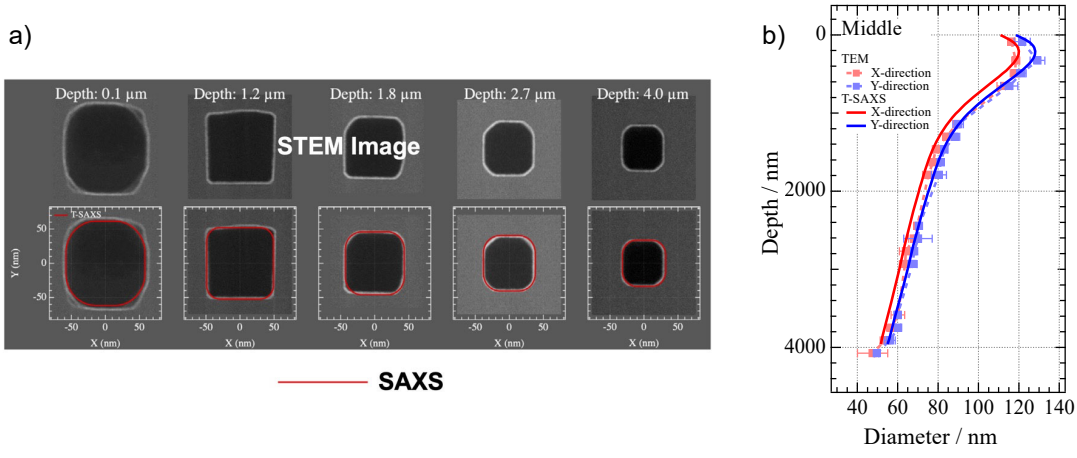


Fig. 3. a) The result of non-destructive T-SAXS (red line) is superimposed on the STEM image at depths of 0.1 μm, 1.2 μm, 1.8 μm, 2.7 μm, and 4.0 μm. b) Comparison of the CD profile obtained by SAXS (solid line) and TEM (squares). The SAXS results agree very well with that of TEM for both CD-profile and XY cross-sections sections.

# Fault Isolation and Failure Analysis Approaches for Advanced Packaging

Yan Li

*Samsung Semiconductor Inc. San Jose, California, USA*



## INTRODUCTION

With the recent advance in Artificial Intelligence (AI) technology, high performance computers (HPC) with better performance, more functionality, low latency, wider bandwidth, less power consumption, and lower cost are getting more and more imperative. The traditional method of increasing the number of microprocessor transistors in a microelectronic device by reducing transistor size through lithography is getting more and more costly. Advanced Packaging techniques can assemble multiple chiplet technology nodes with different functions into the same compacted package by enabling dense Die to Die (D2D) interconnecting, 2.5D die embedding, and 3D die stacking. By leveraging the best available chiplets having smaller die size, advanced packaging technique can maximize device performance with much faster product development cycle, lower cost, and higher yield [1], [2].

Fault isolation and failure analysis of advanced packaging are crucial, especially during the packaging technology development. Identifying defects in the failed units at either End of Line (EOL) or post reliability test, fundamental failure mechanism study, and root cause investigation can provide valuable data feedbacks to the technology development and potential solution paths to resolve problems. As the 2.5D or 3D packages are getting bigger and more complicated, there are significant fault isolation and failure analysis challenges. It is hard to non-destructively locate each defect in a complex 3D package with multiple failing structures. Non-destructive and high-resolution imaging techniques with large field of view could be used for defect identification. Artifact free sample preparation techniques, which could reveal fine features in a large area, are often needed during physical failure analysis. High-resolution defect imaging techniques revealing nm scale defects, and material analysis techniques for ppm level contamination and sub-micron scale organic material identification are usually adopted into the failure analysis flow. Meanwhile, the advanced packaging business needs of short product development cycle, high volume manufactory, and cost-saving request that the failure analysis techniques for advanced packaging to be low coast, having short Through Put Time (TPT) and high success rate. Fault isolation and failure analysis approaches for advanced packaging will be discussed in this presentation to address current challenges, as well as future development trends [1], [2].

## FAULT ISOLATION APPROACHES FOR ADVANCED PACKAGING

Non-destructive investigation of the entire Area of Interest (AOI), which could be related to the failures, is typically performed to detect gross failures. Non-destructive imaging techniques with large field of view, such as optical microscopy, Infrared Imaging, Scanning Acoustic Microscopy (SAM), and X-ray microscopy, are widely used to detect package damage, die cracking, delamination between layers, and interconnect defects.

If the failed units do not show gross defects, fault Isolation (FI) techniques are needed to locate tiny defects in advanced packages, which are very complicated electrical systems. For parametric failures, FI tools, such as Time-domain reflectometry (TDR), Lock-In Thermography (LIT), Magnetic Field Imaging (MFI), Micron or sub-micron probing, are typically used. TDR, LIT, and MFI could provide defect location non-destructively, with the assistance

of reference units or modeling. TDR analysis typically needs reference units, and is good for open or high resistance failures, while LIT and MFI are efficient for short failures. Micron or sub-micron probing is used to probe units during manual de-layering. The failed structure can be probed layer by layer, until the failure location is identified. For functional failures, which typically happen at transistor level, optical FI tools, E-beam imaging and probing, as well as nanoprobing are utilized.

For the die to die connections through embedded bridge dies, routings to package pins are through the top two dies with transistor level connection. If the die to die connection has parametric failures, it is hard to identify the failure location non-destructively by using the conventional package FI techniques. It would be great to have a test programs, which could help isolate the die to die connection failures to either of the top two dies, the bridge die, and the interconnects between the bridge die through electrical tests. Additionally, various virtual metrologies and AI applications could also be developed to help identify the failure locations through simulation, clustering and pattern recognition [2].

## FAILURE ANALYSIS APPROACHES FOR ADVANCED PACKAGING

Once the failure locations are defined by fault isolation, non-destructive and high-resolution imaging techniques, such as 3D X-ray Computed Tomography (CT), SAM, and IR imaging can be used to reveal defects in a relatively smaller AOI. This would save TPT for units with known failure mechanisms.

For units with unknown failure mechanisms, Physical Failure Analysis (PFA), utilizing techniques of sample preparation, defect imaging, and material analysis, is needed to disclose the details of defects for root cause investigation. Sample preparation techniques, such as mechanical polishing, laser ablation, Focused Ion Beam (FIB), Plasma-FIB, and broad-beam ion milling, can be selected based on the cost, TPT, and resolution requirements. Once the defects are revealed by sample preparation, high resolution defect imaging techniques, for example Scanning Electron Microscopy (SEM) and Transmission Electron Microscopy (TEM), are used to expose subtle details of the defects for root cause understanding. Additionally, material analysis tools, such as Energy-dispersive X-ray spectroscopy (EDX), Electron Backscatter Diffraction (EBSD), X-ray Photoelectron Spectroscopy (XPS), Time-of-Flight Secondary Ion Mass Spectrometry (TOF-SIMS), Fourier Transform Infrared Spectroscopy (FTIR), Atomic Force Microscopy based Infrared Spectroscopy (AFM-IR), and Optical Photothermal Infrared micro Spectroscopy (O-PTIR), can be employed to investigate the detailed information of the defects, for example chemical elements, crystallographic orientation, surface or interface ppm level contamination, chemical state, organic material identification etc. The comprehensive material analysis sometimes is crucial for failure mechanism hypothesis, validation, and solution path identification. Additionally, failure location commonality analysis, progressive or in-situ observation of failures can also provide important information for root cause understanding [1].

The application of automation and AI in defect imaging techniques, such as optical microscopy and IR imaging is efficient for defect detection and classification, especially for high volume or in-line inspection. AI adoptions in SEM, TEM, SAM, and X-ray microscopy image improvement are very promising. Additionally, the implantation of AI in failure analysis report classification and failure mode prediction could help reduce FA queue and improve efficiency [3]-[5].

## CONCLUSIONS

Advanced packaging is the industry trend to provide microelectronic devices with better performance and lower cost. Fault isolation and failure analysis in advanced packaging is crucial for the technology development, because it can provide valuable feedback data for yield and reliability improvement. However, enormous technical challenges along with demanding business requirements could occur. Approaches of the fault isolation and failure analysis in advanced packaging is reviewed in this presentation to address these challenges. Additionally, future development trends in this field, including automation, AI, and other innovative techniques, are discussed.

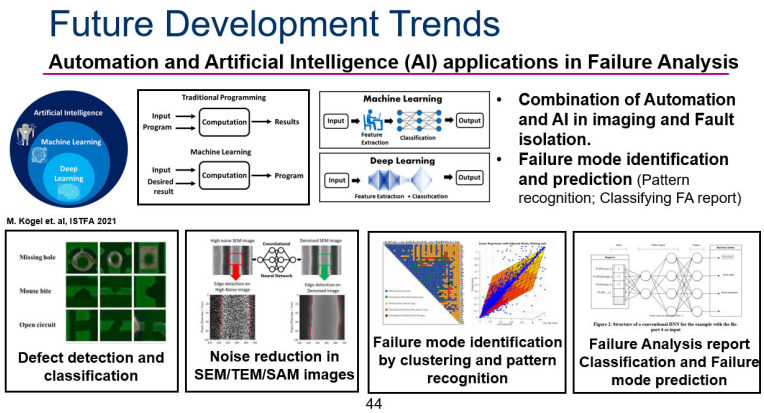


44

**FIGURE 1.** Automation and AI applications in advanced packaging FA [2].

## REFERENCES


1. Y. Li, and D. Goyal, *3D Microelectronic Packaging, From Architectures to Applications*, *2nd edition*, Springer, 2021.
2. C. Schmidt, Y. Li, B. Zee, R. Agny, R. Parente, S. Brand, M. Kögel, and F. Altmann, *Package Innovation Roadmap in Electronic Device Failure Analysis Technology Roadmap*, Electronic Device Failure Analysis Society, 2023, https://doi.org/10.31399/asm.tb.edfatr.t56090131
3. M. Kögel, S. Brand, F. Altmann, "*Machine learning based data and signal analysis methods for the application in failure analysis*," Proceedings from the 47th International Symposium for Testing and Failure Analysis (ISTFA, ASM International), (2021).
4. T. Ishida, I. Nitta, D. Fukuda, and Y. Kanazawa, *"Deep Learning-Based Wafer-Map Failure Pattern Recognition Framework,"* 20th International Symposium on Quality Electronic Design (ISQED), 2019, pp. 291–297, doi: 10.1109/ISQED.2019.8697407.
5. P. Frederik, A. Safont-Andreu, C. Burmer, and K. Schekotihin, *"Report Classification for Semiconductor Failure Analysis."* Proceedings from the 47th International Symposium for Testing and Failure Analysis (ISTFA, ASM International), (2021).


## KEYWORDS

Advanced packaging, 2.5D packaging, 3D packaging, FI, FA, AI, ML, DL

# Advances in the Use of AI for X-ray Reconstruction: Applications in Electronics Packaging

Matthew Andrew, Moran Xu, Andriy Andreyev

*Carl Zeiss X-ray Microscopy, 5300 Central Pkwy, Dublin, CA 94568*

## INTRODUCTION

3D XRM has become the preferred solution for non-destructive structural and failure analysis over 2D X-ray imaging techniques because it provides rich volumetric information on a specimen, and it now plays a crucial role in fueling the advances of IC package development and failure analysis [1], however while much progress has been made, significant challenges remain. X-ray imaging suffers from arrange of artifacts and imaging issues, including noise [2], sparse sampling artifacts [3], beam hardening [4], missing angle artifacts [5], and other issues. many of these issues have historically been dealt with using a combination of specialized 3D reconstruction technology [6], [7], and post processing filters [8]. While these techniques remain the state-of-the-art often they give suboptimal imaging results and can introduce new artifacts or biases in the results that should be avoided if possible.

In this investigation we introduce a general framework for performing image restoration that we call the synthetic prior, and show how it can be applied to the issue of noise and artefact removal in X-ray reconstruction. We then show how this technique can be used with an application in electronics packaging to improve image quality or reduce acquisition time, both compared to traditional X-ray reconstruction techniques and compared to state-of-the-art deep learning reconstruction (DeepRecon).

## IMAGE RESTORATION USING A SYNTHETIC PRIOR

Let us consider a generic imaging operator $G$ that transforms some structure function $S$ to some image $I$. The task of any generic image restoration task is to come up an inverse operator that perfectly restores the structure function based on the (measured) image function.

$$I = G(S) \qquad (1)$$

$$\boldsymbol{S = G^{-1}(I)} \quad (2)$$

The development of this inverse imaging operator is often extremely challenging, application specific, and may introduce sub-optimal artefacts or imperfect image restoration into the resulting estimate of $S$. The past 10 years have seen an explosion in the availability of open-source machine learning and computer vision tools, revolutionizing the way we examine X-ray reconstruction in specific (e.g. [9], [10], [11], [12]) and computer vision / computational imaging in general (e.g. [13]). Deep learning methods present a robust and powerful method to create generic inverse operators, given the right training data using direct image regression (e.g. [14], [15]). In the terms of equations 1 & 2 we would generally need a matched $I$ and $S$ functions to train a network. This presents an obvious challenge in its practical use for imaging a broad array of samples with diverse feature distributions for whom we do not have "ground truth" structure estimates.

Here we introduce a new concept – the use of an intermediate "synthetic prior" – that marries these two concepts – that of the generic utility of deep learning approaches to solving inverse problems, given sufficient training data, and the tractability of forward problem relative to its inverse. This initial corrected version of the data constitutes a first estimate of the structure function, termed the "synthetic prior". The synthetic prior is then degraded through a forward imaging operator, creating a secondary image function. This well-structured image pair can be used in the optimization of hyperparameters for any inverse operator, but particular interest is the training of an inverse deep convolutional network-based operator. A final estimate of the structure function is then created by passing the initial image data through the newly determined function $G_I^{-1}$.

$$\boldsymbol{S = G_1^{-1}(I)} \quad (3)$$

$G_1^{-1}$ has many advantages over $G_0^{-1}$. Firstly it is trained on data that approximates the feature distributions in the structure function $S$, $S'$, so the resulting networks are optimized to the sample structures being examined. Secondly any errors in the synthetic prior $S'$, are correlated to errors in the image intermediate $I'$, so the resulting network will tend to ignore them. Finally the described workflow can be applied to many different image restoration tasks, some of which do not have solutions that are of high enough quality for scientific tasks. This bar (of scientific utility) is not necessarily present for the synthetic prior intermediate $S'$, only for the final prediction $S$. As such algorithms can be designed to maximize the utility of $S'$ as a synthetic prior, without the constraint that the resulting datasets be used for analysis.

## Application to X-ray Tomography Noise Reduction and Artefact Removal

One of the biggest challenges in X-ray imaging is the tradeoff between imaging, resolution, and throughput. To achieve high resolutions, laboratory X-ray sources are relatively low flux, and high resolution X-ray detectors are relatively low efficiency. This introduces an overlapping source of artefacts, both true image noise and spatially correlated spurious signal arising from sparse angular sampling (i.e. limited projection numbers) [3]. This limits the application of high-resolution imaging within the electronics industry generally, as the time required for high-quality high-resolution X-ray imaging are often impractical for inline or near-line applications. In this case we have several potential candidate algorithms to use for our initial correction function $G_0^{-1}$, however for this study we use state-of-the-art deep learning based X-ray reconstruction ZEISS DeepRecon Pro [3], [21], [22], www.zeiss.com. This uses a modified Noise2Noise [15] based approach where both artefacts and noise are decorrelated between training datasets, however can over-smooth datasets. To consider the output of this initial reconstruction as a synthetic prior intermediate we need a way of re-creating the image $I'$. In this study we use novel heuristic data-driven forward modelling of the noise and artefact functions which are then added back to the synthetic prior to create a synthetic image dataset. An inverse model ($G_1^{-1}$) is then trained to map this synthetic image dataset back to the synthetic prior. This model is then applied on the original image data ($I$) to create the final recovered structure.

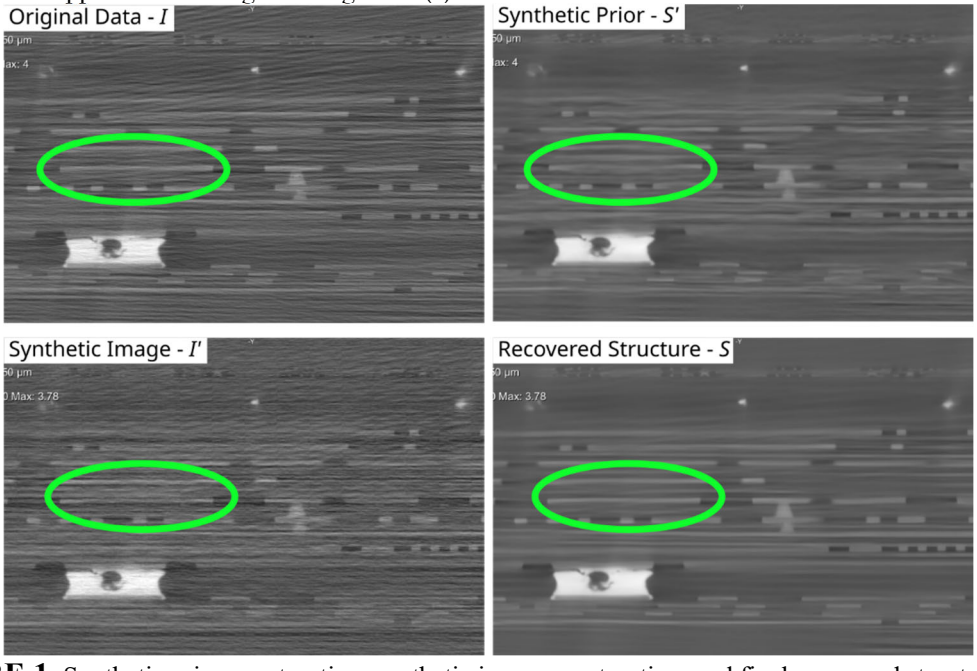


**FIGURE 1**: Synthetic prior construction, synthetic image construction, and final recovered structure from a reconstruction of a commercially acquired electronics compute package, acquired using the conditions described below and 400 projections.

## APPLICATION TO ELECTRONICS PACKAGING

This technique was applied to a commercially acquired electronics compute package. This was imaged using a Zeiss Context micro-CT, with the below conditions. This creates an image with a reconstructed voxel size of

1.73µm with a reconstructed volume geometry of 3064 x 3064 x 1936 voxels. The entire projection dataset was reconstructed using both the existing commercial traditional reconstruction (FDK [23]), DeepRecon pro software state-of-the-art deep learning reconstruction, and synthetic prior based reconstruction. Comparative results are shown below in figure 2.

**TABLE 1.** Image acquisition conditions

| Projection number | Voltage (kV) | Power (W) | Detector | Exposure (s) | Filter (proprietary) | Source – RA distance (mm) | Detector – RA distance (mm) | Detector dimension |
|---|---|---|---|---|---|---|---|---|
| 2401 | 120 | 10 | Flat Panel | 2.5 | HE2 | 13 | 550 | 3064 x 1936 |

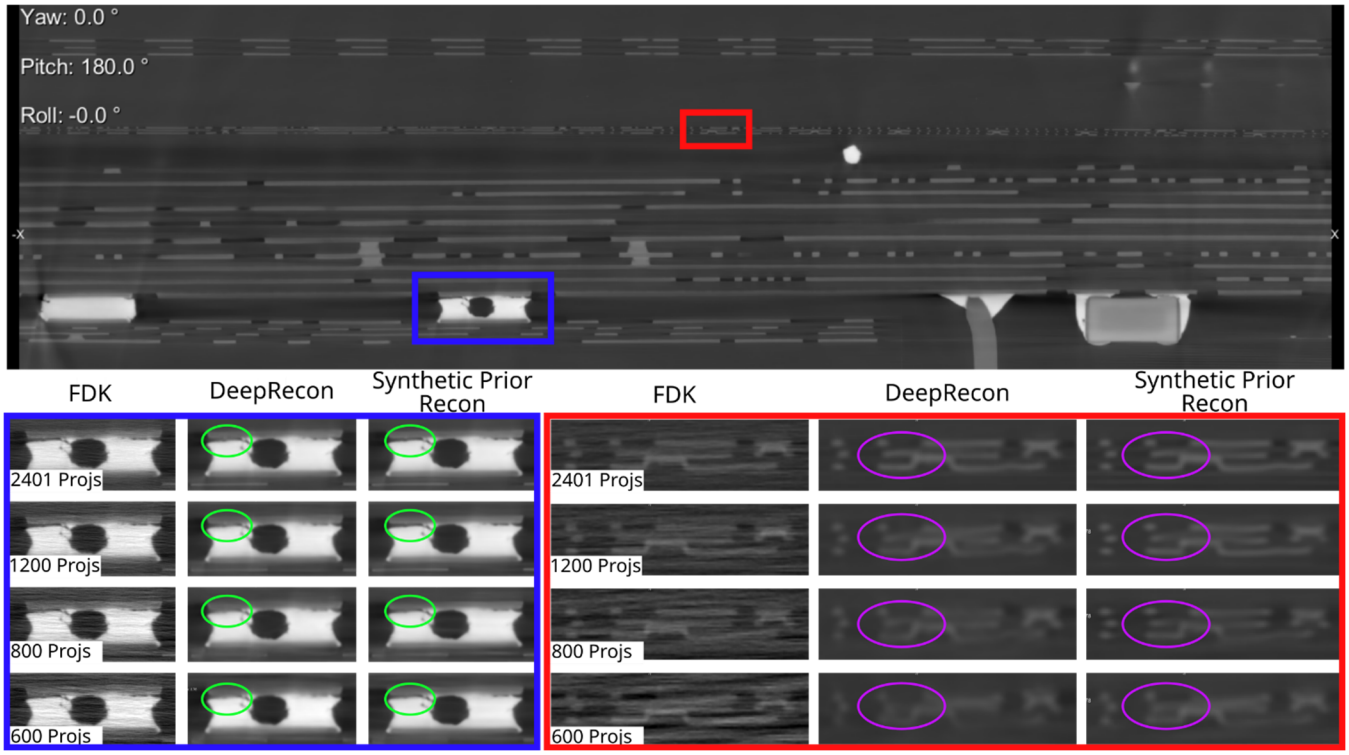


**FIGURE 2**: Comparative results from reconstruction using FDK, DeepRecon and Synthetic Prior reconstruction.

Subset of the dataset were passed through the entire reconstruction workflow - the full projection set (2401 projections), a 50% subsampled projection set (1200 projections), 33% subsampled projection set (800 projections) and a 25% subsampled projection set (600 projections). Different features are highlighted to showcase the differential performance of synthetic prior reconstruction relative to both traditional (FDK) reconstruction and state-of-the-art reconstruction (DeepRecon). Different regions of interest are highlighted, including a solder micro-bump (blue) and a redistribution layer (red). The solder bump has a crack in it, highlighted in green, and the re-distribution layer has complex structure highlighted in purple. All three reconstruction techniques show the difficult to recover features when using the full projection set (2401 projections), however the structure of the lower contrast redistribution layer and subtle solder bump cracks are much more easily distinguishable when using synthetic prior reconstruction than either legacy (FDK) reconstruction or state-of-the-art Deep Learning reconstruction.

## CONCLUSIONS

In this paper we introduce a new technique for image restoration, with application to X-ray reconstruction and artefact removal – the synthetic prior intermediate. This technique is then applied to reconstructing a sample of a commercially acquired X-ray package, showing significantly improved results relative to traditional reconstruction and state-of-the-art deep learning reconstruction (DeepRecon), showing significantly improved recovery of challenging faint features, which would typically take a significantly larger number of projections to recover.

## REFERENCES


[1] A. Gu, M. Terada, H. Stegmann, T. Rodgers, C. Fu, and Y. Yang, "From System to Package to Interconnect: An Artificial Intelligence Powered 3D X-ray Imaging Solution for Semiconductor Package Structural Analysis and Correlative Microscopic Failure Analysis," in *Proceedings of the International Symposium on the Physical and Failure Analysis of Integrated Circuits, IPFA*, 2022. doi: 10.1109/IPFA55383.2022.9915756.

[2] V. Davidoiu, L. Hadjilucas, I. Teh, N. P. Smith, J. E. Schneider, and J. Lee, "Evaluation of noise removal algorithms for imaging and reconstruction of vascular networks using micro-CT," *Biomed. Phys. Eng. Express*, vol. 2, no. 4, p. 045015, Aug. 2016, doi: 10.1088/2057-1976/2/4/045015.

[3] M. Andrew, L. Omlor, A. Andreyev, ravikumar Sanapala, and M. Samadi Khoshkhoo, "New technologies for x-ray microscopy: phase correction and fully automated deep learning based tomographic reconstruction," 2021. doi: 10.1117/12.2596592.

[4] R. A. Brooks and G. Di Chiro, "Beam hardening in X-ray reconstructive tomography," *Phys. Med. Biol.*, vol. 21, no. 3, 1976, doi: 10.1088/0031-9155/21/3/004.

[5] Y. Huang, S. Wang, Y. Guan, and A. Maier, "Limited angle tomography for transmission X-ray microscopy using deep learning," *J. Synchrotron Radiat.*, vol. 27, 2020, doi: 10.1107/S160057752000017X.

[6] Q. Lin, M. Andrew, W. Thompson, M. J. Blunt, and B. Bijeljic, "Optimization of image quality and acquisition time for lab-based X-ray microtomography using an iterative reconstruction algorithm," *Adv. Water Resour.*, vol. 115, pp. 112–124, 2018, doi: 10.1016/j.advwatres.2018.03.007.

[7] D. Rückert, Y. Wang, R. Li, R. Idoughi, and W. Heidrich, "NeAT: Neural Adaptive Tomography," *ACM Trans. Graph.*, vol. 41, no. 4, 2022, doi: 10.1145/3528223.3530121.

[8] A. Buades, B. Coll, and J.-M. Morel, "Nonlocal Image and Movie Denoising," *Int. J. Comput. Vis.*, vol. 76, no. 2, pp. 123–139, 2008, doi: 10.1007/s11263-007-0052-1.

[9] J. Dong, J. Fu, and Z. He, "A deep learning reconstruction framework for X-ray computed tomography with incomplete data," *PLoS One*, vol. 14, no. 11, 2019, doi: 10.1371/journal.pone.0224426.

[10] M. Andrew *et al.*, "Fully automated deep-learning-based resolution recovery," 2022. doi: 10.1117/12.2647272.

[11] G. Wang, J. C. Ye, and B. De Man, "Deep learning for tomographic image reconstruction," *Nature Machine Intelligence*, vol. 2, no. 12. 2020. doi: 10.1038/s42256-020-00273-z.

[12] F. Cognigni, M. E. E. Temporiti, L. Nicola, N. Gueninchault, S. Tosi, and M. Rossi, "Exploring the infiltrative and degradative ability of Fusarium oxysporum on polyethylene terephthalate (PET) using correlative microscopy and deep learning," *Sci. Rep.*, vol. 13, no. 1, p. 22987, 2023, doi: 10.1038/s41598-023-50199-w.

[13] G. Barbastathis, A. Ozcan, and G. Situ, "On the use of deep learning for computational imaging," *Optica*, vol. 6, no. 8, 2019, doi: 10.1364/optica.6.000921.

[14] A. Migga *et al.*, "Comparative hard x-ray tomography for virtual histology of zebrafish larva, human tooth cementum, and porcine nerve," *J. Med. Imaging*, vol. 9, no. 03, 2022, doi: 10.1117/1.jmi.9.3.031507.

[15] J. Lehtinen *et al.*, "Noise2Noise: Learning image restoration without clean data," in *35th International Conference on Machine Learning, ICML 2018*, 2018.

[16] S. Beckouche, J. L. Starck, and J. Fadili, "Astronomical image denoising using dictionary learning," *Astron. Astrophys.*, vol. 556, 2013, doi: 10.1051/0004-6361/201220752.

[17] A. Krull, T. O. Buchholz, and F. Jug, "Noise2void-Learning denoising from single noisy images," in *Proceedings of the IEEE Computer Society Conference on Computer Vision and Pattern Recognition*, 2019. doi: 10.1109/CVPR.2019.00223.

[18] C. Tian, L. Fei, W. Zheng, Y. Xu, W. Zuo, and C. W. Lin, "Deep learning on image denoising: An overview," *Neural Networks*, vol. 131. 2020. doi: 10.1016/j.neunet.2020.07.025.

[19] A. Mohammad-Djafari, *Inverse Problems in Vision and 3D Tomography*. 2013. doi: 10.1002/9781118603864.

[20] D. P. Kingma and J. L. Ba, "Adam: A method for stochastic optimization," in *3rd International Conference on Learning Representations, ICLR 2015 - Conference Track Proceedings*, 2015.

[21] M. Andrew, L. Omlor, A. Andreyev, and C. H. G. VOM HAGEN, "Accessible neural network image processing workflow," 17 / 372,019, Jan. 12, 2023

[22] H. Villarraga-Gómez *et al.*, "Improving throughput and image quality of high-resolution 3D X-ray microscopes using deep learning reconstruction techniques," in *11th Conference on Industrial Computed Tomography (iCT)*, 2022, pp. 8–11.

[23] L. A. Feldkamp, L. C. Davis, and J. W. Kress, "Practical cone-beam algorithm," *J. Opt. Soc. Am. A*, vol. 1, no. 6, p. 612, 1984, doi: 10.1364/JOSAA.1.000612.


## KEYWORDS

AI, X-ray Reconstruction, Image restoration

# Next Generation Metrologies & Fault Detection Methods in Support of Advanced Packaging

Pooya Tadayon

*Intel Fellow, Direction of Assembly & Test Pathfinding*
*Intel Corporation*
*Assembly Test Technology Development*
*Hillsboro, Oregon*

## INTRODUCTION

The evolution of advanced packaging technologies, such as 3D integration and multi-chip modules, has driven aggressive reduction in dimensions of interconnects, such as traces, solder joints, substrate vias, through-silicon vias, and hybrid bonding interconnects (HBI) [1]. These advancements call for the deployment of sophisticated electric fault isolation tools and methods to enhance the (X, Y, Z) localization of defects to characterize and root cause failures.

For instance, a key challenge in electric fault isolation is multi-stacked structures requiring sub-micron isolation accuracy of defects to determine the metal layer in the stack where the defect is located [Figure 1]. As the industry drives further aggressive scaling and HBI becomes more mainstream, techniques are needed to isolate electrical open failures in structures requiring (X, Y, Z) localization accuracy of better than 1 micron. Currently, the resolution of non-destructive isolation methodologies based on thermal signals generated by defects is greater than 5 microns. In addition, HBI feature-to-feature interaction at the nanometer scale over large areas makes dimensional measurement a very slow and expensive process. Ideally, much faster dimensional metrology systems with sub-micron (Z) resolution are needed to allow mapping of parts pre and post bond.

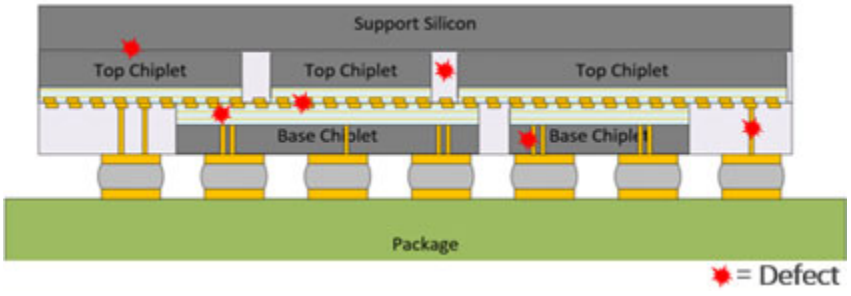


**FIGURE 1.** Cartoon image of a hypothetical 3D integrated circuit built using HBI, with the red stars designating potential location of defects. Due to aggressive scaling of feature sizes, future metrologies require sub-micron spatial accuracy in all three dimensions to pinpoint location of defects.

Non-destructive imaging (NDI) has become a critical tool for failure root cause analysis. NDI helps analyze multiple potential failure locations of the device under test (DUT) to conclusively identify and pinpoint a defect without introducing sample preparation artifacts that could have damaged or altered it. This is especially important when the number of failing devices is limited. NDI is also critical to enable progressive reliability testing when the DUTs are non-destructively analyzed at time zero and at multiple additional times to generate a map of failures as a function of time. NDI also helps in reducing failure analysis time-to-

data by avoiding tedious and time-consuming sample preparation steps required by destructive failure analysis methodologies.

There are, however, critical challenges in enabling NDI for next generation advanced packaging. For example, detection of single non-contact open HBI requires a spatial resolution better than 1 micron in (X, Y) and 10 nanometers in (Z). In this case, conventional 2D and 3D x-ray methodologies cannot achieve such a resolution, particularly in the (Z) axis. Another challenge is the detection of subtle delamination, smaller than 10 microns in the (X, Y) plane near the die edge, with a die thickness larger than 200 microns and stacked dies at the top. The imaging capability of conventional C-mode Scanning Acoustic Microscopy (CSAM) methodologies suffers significant deterioration due to the die sidewall and acoustic scattering caused by the multi-stack layers.

Device validation and physical debug are also dependent on new innovations in the era of advanced packaging. The current state-of-the-art for simple 2D devices is to use Infrared Ray Emission (IREM) in conjunction with Focused Ion Beams (FIB) and a host of other tools to enable circuit edit [2]. In the era of 3D integration, however, access to the buried die in the stack is blocked and new innovations in debug hardware and methodology are required to overcome this challenge [Figure 2].

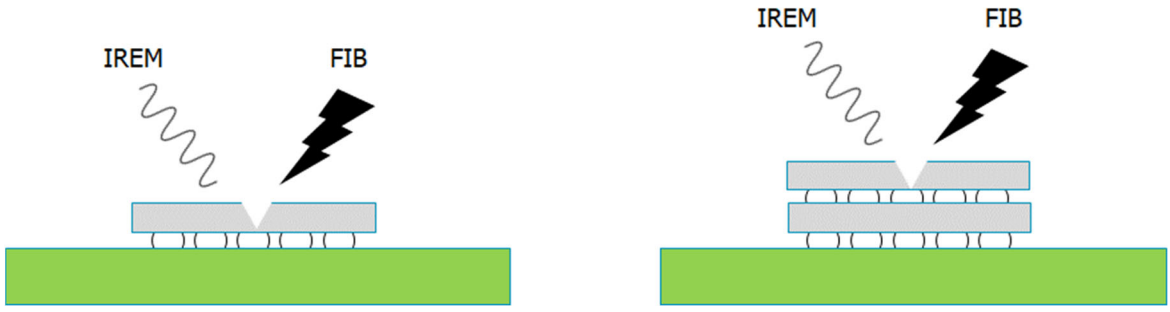


**FIGURE 2.** Image on the left shows an existing 2D device with all the circuitry accessible for current state-of-the-art physical debug tools. Image on the right shows a 3D device where the circuitry in the bottom die is no longer accessible. Physical debug challenges will continue to grow as architects build more complex devices with a larger number of chiplets in the stack.

Advanced packaging is also driving fundamental changes to materials used in packaging. A key inflection point in the future is replacement of the organic core in package substrates with a glass core which offers better thermal, electrical, and mechanical properties [3-4]. There are, however, significant gaps in metrologies to detect defects in glass core substrates. For example, detection of cracking defects in fully assembled glass core packages remains an open problem, with no existing non-destructive methodology available.

Glass also has unique optical properties which open the door to delivering highly compelling solutions for co-package photonics [5]. Use of glass in optical applications, however, poses unique challenges including design for manufacture, design for inspection and the need for new technologies for nondestructive index of refraction mapping in three dimensions when waveguides are integrated within the glass structure [Figure 3]. To minimize insertion loss between mating parts, glass components must be manufactured – and verified – with both high accuracy and precision. The surfaces that control alignment must also be designed such that measurement uncertainty for critical features is acceptable using off the shelf systems. High-speed and high accuracy metrologies are required that are capable of micron level resolution through a transparent sample.

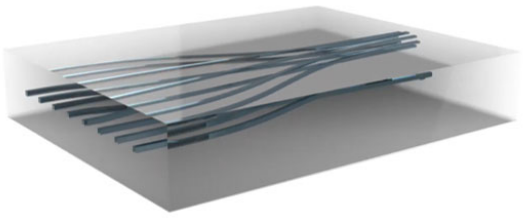

**FIGURE 3.** Example of a glass component with integrated waveguides within the interior of the glass substrate. These components are a critical building block for optical applications and need to be measured ahead of time to validate the fidelity of the waveguides prior to attaching them to high-value silicon.

A fundamental problem that needs to be solved is integration of metrology and inspection solutions within processing tools, with the end goal of enabling real-time, actionable process feedback for quicker optimization and adjustments, leading to a more robust process with higher yield. Examples include enabling overlay and gross void detection measurements within bonder tools to induce offset correction or enabling integrated pad recess metrology in CMP tools for real-time platen adjustments aimed at process uniformity. Such capabilities would lead to a reduction in wafer transfer overhead, thus minimizing cycle time and leading to fewer opportunities for contamination issues and yield loss related to handling. In addition to faster time to data and reduced risk of yield loss, integration of metrologies into production tools results in significant cost as well as space savings.

The primary challenge to enabling this vision is limited space within process equipment to introduce bulky inspection capabilities. Innovative solutions are needed by metrology suppliers to reduce the size of inspection modules while equipment suppliers need to think differently about integration schemes to accommodate these modules (for example, replacing a loadport with a metrology solution, as has been demonstrated in some CMP equipment).

The challenges highlighted in this brief review are daunting, but not insurmountable. A model based on strong collaboration between academia and industry to deliver innovative technologies that can be brought to market quickly is key to lowering cost and time-to-market, thus making advanced packaging more affordable for a larger segment of the market.

## REFERENCES


1. G. Gao et al., "Scaling Package Interconnects Below 20µm Pitch with Hybrid Bonding," 2018 IEEE 68th Electronic Components and Technology Conference (ECTC), San Diego, CA, USA, 2018, pp. 314-322, doi: 10.1109/ECTC.2018.00055.

2. Giacobbe, John A., et al. "Circuit Edit and Optical Probe Development and Validation for Next Generation Process Nodes." ISTFA 2011. ASM International, 2011.

3. A. B. Shorey and R. Lu, "Progress and application of through glass via (TGV) technology," 2016 Pan Pacific Microelectronics Symposium (Pan Pacific), Big Island, HI, USA, 2016, pp. 1-6, doi: 10.1109/PanPacific.2016.7428424.

4. T. Iwai et al., "A Novel Inorganic Substrate by Three Dimensionally Stacked Glass Core Technology," 2018 IEEE 68th Electronic Components and Technology Conference (ECTC), San Diego, CA, USA, 2018, pp. 1987-1992, doi: 10.1109/ECTC.2018.00298.

5. N. Psaila, S. Nekkanty, D. Shia and P. Tadayon, "Detachable Optical Chiplet Connector for Co-Packaged Photonics," in Journal of Lightwave Technology, vol. 41, no. 19, pp. 6315-6323, 1 Oct.1, 2023, doi: 10.1109/JLT.2023.3285149.


## KEYWORDS

Advanced packaging, metrology, inspection, fault detection, fault isolation, physical debug.

# Advances in APT Quantification and Distortion Correction Approaches

C. Fleischmann[1,2], M. Dialameh[1], V. V. Krasnov[1,2], J. Lüken[3], R. J. H. Morris[1], J. E. Scheerder[1], Y. Tu[1,2], J. Sijbers[3], J. De Beenhouwer[3]

[1]*Imec, Kapeldreef 75, 3001 Heverlee, Belgium*
[2]*Quantum Solid State Physics, KU Leuven, Celestijnenlaan 200D, 3001 Heverlee, Belgium*
[3]*Imec-Vision Lab, University of Antwerp, Universiteitsplein 1, 2610 Antwerp, Belgium*



## INTRODUCTION

Accurate compositional analysis has always been key in the semiconductor industry given the intricate interplay between the chemical composition and the performance of a device. With the expansion of the materials library in semiconductor processing, the aggressive scaling, and the transition from planar to 3-dimensional (3D) device architectures, compositional analysis faces some demanding challenges. Nowadays, we need to detect etch residues, verify chemical uniformity, or quantify material composition within buried, ultra-thin layers in high-aspect ratio 3D nanostructures (Fig. 1). The need for spatially resolved compositional mapping has drawn attention to Atom Probe Tomography (APT), a high-resolution mass spectrometry technique that delivers a 3D atomic map of the analyzed sample volume. In the last decade, APT has revealed unique insights into semiconductor structures[1-3]. The APT community has made considerable progress in understanding the underlying physical mechanisms[4] and instrumental developments such as automation[5,6], excitation sources[7], field-of-view[8], etc. Opportunities remain in view of the quantification uncertainty when analyzing multi-component material systems, for which industry requirements are not met yet. It is also highly desirable to improve the data reconstruction protocol to minimize (or eliminate) distortions in the 3D reconstructed dataset. Ultimately, this would yield an improved spatial resolution thereby achieving more accurate analytical tomography of heterogeneous 3D nanostructures. The present work will discuss how we can leverage APT to address the characterization challenges in the semiconductor industry. Showcasing curated application examples, we will highlight aspects on quantification accuracy and will briefly outline our initiatives towards improved data reconstruction.

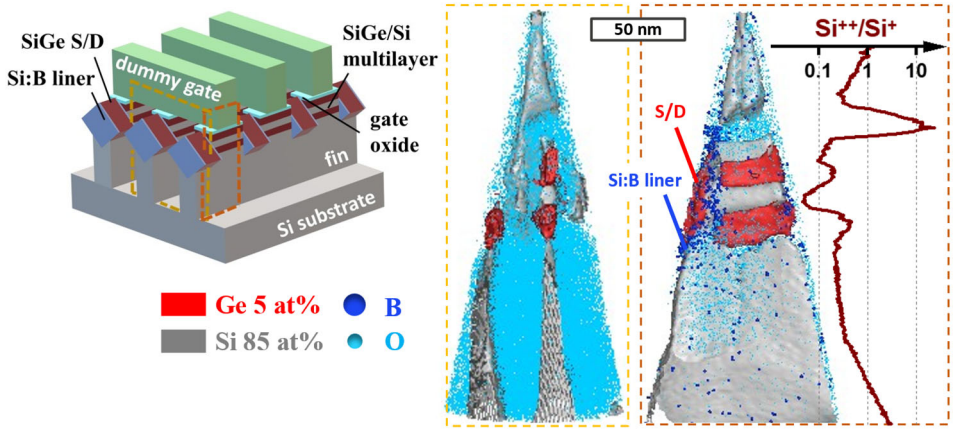


**FIGURE 1.** Sketch of a gate-all-around nanosheet transistor (not fully processed) and APT data acquired on an Invizo®6000 on such a structure. Shown are a reconstructed point cloud and iso-concentration surfaces, as viewed along (yellow square) and perpendicular (orange square) to the fin structures, with the corresponding charge-state-ratio evolution extracted within the fin.

## TOWARDS ACCURATE QUANTIFICATION IN 3D NANOSTRUCTURES

In an atom probe, quantification is achieved by identifying and counting each single atom that hits the detector, with an element-independent detection efficiency up to 80%[4]. Despite this simplicity, quantification inaccuracies are commonly observed, albeit not fully understood, for B in Si, $Si_xGe_{1-x}$, nitrides, oxides, etc. Often the measured composition shows a non-linear trend with the analysis conditions (Fig. 2). When analyzing heterogeneous nanostructures there is, however, a trade-off to be made between the set experimental conditions and the analysis yield, limiting the flexibility to perform measurements optimized for most accurate quantification (Fig. 1). In addition, the heterogeneity of such structures can cause local curvature at the tip surface, resulting in localized electric field gradients and related changes in the accuracy. To overcome these bottlenecks, we proposed a correction scheme, here exemplified on a SiGe multilayer from a gate-all-around transistor architecture. In this approach, a calibration curve is established on a reference sample (Fig. 2). Based on this, a voxel-by-voxel correction of the measured Ge composition within the nanostructure is performed to remedy potential quantification biases originating from the deviation to the optimum charge-state-ratio during the analysis. The following boundary conditions apply: the calibration curve is recorded on a homogeneous, stable reference sample of similar composition, on the same instrument, using the same excitation wavelength and base temperature, and the quantification inaccuracy to correct for is larger than any additional uncertainty (e.g. counting statistics). The latter assumption starts, however, to break down for voxel dimensions below 5 x 5 x 5 $nm^3$, i.e. when one needs to detect local compositional fluctuations within the plane and the thickness of a single nanosheet. In such small volumes, one must also account for the statistical inhomogeneity inherent to random alloys (Fig. 2), in which the element distribution is binomial in nature[9].

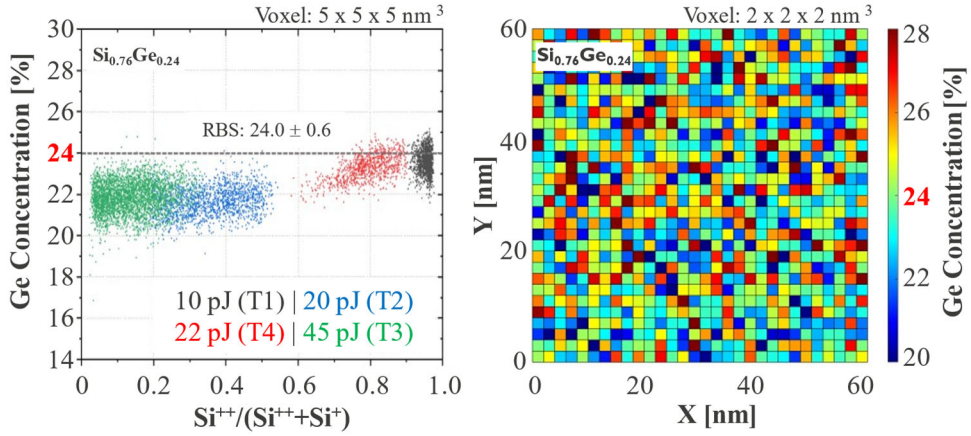


**FIGURE 2.** (left) Experimental calibration curve for a $Si_{0.76}Ge_{0.24}$ reference sample where each dot represents the information extracted from a 5 x 5 x 5 $nm^3$ voxel, sub-sampled within each tip for 4 different tips/measurement conditions (color code). (right) Compositional inhomogeneity of a random $Si_{0.76}Ge_{0.24}$ alloy (numerical simulation) with a probing voxel size of 2 x 2 x 2 $nm^3$.

## INITIATIVES TO IMPROVE DATA RECONSTRUCTION

In tomographic methods, 3D reconstruction forms an essential and critical step in the workflow that determines spatial resolution and even analytical performance. Current standards for APT data reconstruction (Bas protocol[4]) describe the tip geometry and ion trajectories insufficiently well, thereby misplacing the atoms in the reconstructed volume, causing faulty dimensions and distorted shapes (Fig. 1). Efforts are being made to replace the unphysical assumptions in these quasi-stereographic projection-based models by more realistic ion trajectories solved by electrostatic field simulation from the actual tip geometry. Knowledge about the tip geometry (evolution) is therefore key, which led us to develop two experimental tip shape imaging routes. Relying on Atomic Force Microscopy (AFM), the 3D topography of an atom probe tip can be determined in a fast, contact-less, and accurate manner (Fig. 3). AFM tip imaging should not obstruct continuation of data acquisition in the atom probe, potentially allowing iterative *in-situ* cycling (APT-AFM-APT-AFM...) using a transfer system or in a hybrid AFM-APT tool. In a proof-of-concept study, such AFM images have successfully informed a trajectory-based reconstruction protocol, yielding reduced density fluctuations in the reconstructed data.

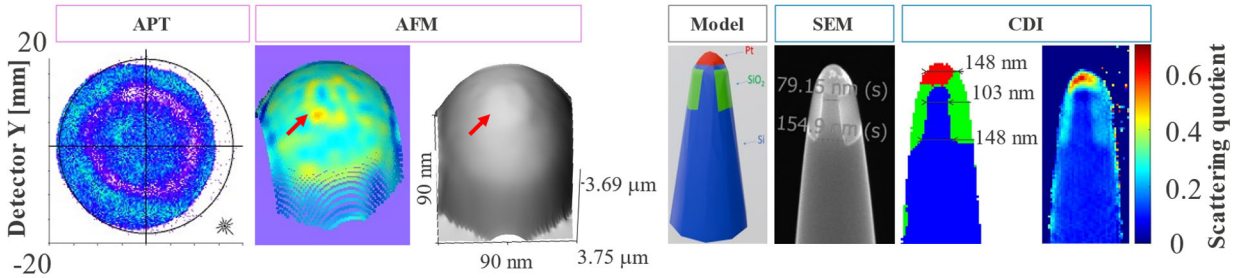


**FIGURE 3.** (left panel) APT hit map showing density variations resulting from the local curvature at the tip surface (red arrow) indicated in the corresponding AFM images (local curvature and topography) of that same tip. (right panel) SEM and scanning CDI image (chemical map and scattering quotient) of the same APT tip. The chemical map is retrieved from the scattering quotient, the Si fin, $SiO_2$ and Pt contamination are shown in blue, green and red color, respectively.

Ptychography or scanning coherent diffractive imaging (CDI) is an alternative, contact-less imaging method[10] that could use the same table-top EUV light source that triggered field evaporation in the EUV-APT setup described in[7]. Compared to AFM imaging, CDI provides a larger field-of-view along the tip axis, at a lower spatial resolution (Fig. 3). While our proof-of-concept yields a 2D projection of the APT tip, 3D information could in principle be obtained by tomographic CDI[10]. If the different materials in an atom probe tip exhibit sufficient optical contrast, CDI can be chemically sensitive and visualizes embedded nanostructures (Fig. 3). Such structural/chemical information, combined with the tip geometry might for example feed the model initialization step in a model-driven reconstruction workflow as developed by Fletcher *et al.*[11].

At present, most alternative reconstruction frameworks achieve a (quantifiable) reduction in density fluctuations and image distortions. However, computational efficient methods do not offer the accuracy (spatial resolution) required for semiconductor applications[11] and still undermine the true potential of APT. On the other hand, physically motivated methods that consider atomic-scale effects are too slow for industry standards. The challenge lies in developing a method that reconstructs realistic volumes of heterogenous structures with a (sub)-nanometer scale accuracy at a reasonable timescale (<several hours). The first obstacle is the creation of an efficient forward operator model, which heavily depends on mesh generation capability. We are therefore investigating a unique strategy to generate a high-quality mesh for a modular and full-scale volumetric finite element simulation using a state-of-the-art finite element solver to numerically determine the electric potential and field. A fast and accurate solution of the involved partial differential equations could be achieved through a low concentration of vertices in the vacuum, which still cover a relevant length scale while preserving accuracy in the near field, therefore requiring a highly variable density. We believe that this could be a crucial stepping-stone towards fast and accurate 3D data reconstruction addressing the characterization needs of the semiconductor industry.

## REFERENCES

1. W. Vandervorst *et al*., *Mater. Sci. Semicon. Process*. **62** 31–48 (2017).
2. A. D. Giddings *et al*., *Scr. Mater.* **148**, 82-90 (2018).
3. J. P. Barnes *et al*., *Scr. Mater.* **148**, 91-97 (2018).
4. B. Gault *et al*., *Nat Rev Methods Primers* **1**, 51 (2021).
5. J. Uzuhashi *et al*., *Ultramicroscopy* **247**, 113704, (2023).
6. K. P. Rice *et al.*, *Microsc. Microanal*. **28**, 726 (2022).
7. B. W. Caplins *et al*., *Rev. Sci. Instrum*. **94**, 093704 (2023)
8. Y. Chen *et al*., *Microsc. Microanal*. **29**, 813-814, (2023)
9. M. P. Moody *et al., Microsc Res Tech* **71**, 542 (2008).
10. M. Dierolf *et al., Nature*, 467, 436–439, (2010)
11. C. Fletcher *et al., J. Phys. D: Appl. Phys*. *55*, 375301 (2022)

## KEYWORDS

3D APT, compositional analysis, quantification uncertainty, data reconstruction, tip geometry, AFM, CDI, mesh generation

# Arrangement of Nanosized hBN Quantum Sensor Spots using Helium Ion Microscope

Kento Sasaki

*Department of Physics, The University of Tokyo, Bunkyo-ku, Tokyo 113-0033, Japan*

## INTRODUCTION

There are point defects in wide bandgap semiconductors, whose electron spin states can be optically initialized and readout even at room temperature. Quantum sensing of physical quantities such as magnetic field and temperature using discrete levels of point defects has been studied since 2008 [1,2,3]. This sub-nanometer-sized quantum defect sensor can be very close to the measurement target and thus has the potential for high spatial resolution and the ability to detect small magnetic material. For example, it is used to investigate the local conduction characteristics of microwiring and the magnetization of micromagnets [4,5,6].

In this talk, we will introduce the principle of quantum sensing using boron vacancy defects ($V_B$) in hexagonal boron nitride (hBN), which was first reported in 2020 [7], and our work toward higher spatial resolution and sensitivity [8,9,10].

## BORON VACANCY IN HEXAGONAL BORON NITRIDE

First, we will explain the properties of $V_B$ in hBN and the principle of the quantum sensing. $V_B$ is a defect in which a single boron atom is replaced by a vacancy [Fig. 1(a)]. Each of the nearest nitrogen atoms supplies $sp^2$ and $2p_z$ dangling bonds and three electrons, and thus, there are six orbitals and nine electrons at the vacancy. The negatively charged state ($V_B^-$) with 10 electrons exhibits an electron spin $S = 1$ [11]. This $V_B^-$ can be used as a quantum sensor.

The energy levels and optical transitions of $V_B^-$ are shown in Fig. 1(b). Upon irradiation of green light, $V_B^-$ transitions from the ground state to the excited state while keeping its electron spin state. There are two main pathways for relaxation from the excited state to the ground state [7]. One is the direct relaxation from the excited state to the ground state. It is a radiative relaxation pathway that keeps the electron spin state. The other is a non-radiative pathway that relaxes indirectly to the ground state via a metastable state. In this pathway, the $m_S = \pm 1$ of the excited state selectively relaxes to the $m_S = 0$ of the ground state. Therefore, the $m_S = \pm 1$ states exhibit less photoluminescence (PL) intensities than the $m_S = 0$ state. In addition, continuous optical excitation polarizes the electron spin to the $m_S = 0$ state. These properties allow optical initialization and readout of the electron spin state [8].

These properties are used for optically detected magnetic resonance. By measuring the PL intensity while continuously irradiating excitation green light and microwaves, the transition from the $m_S = 0$ state to the $m_S = \pm 1$ states by magnetic resonance can be observed. The typical results are shown in Fig. 1(c). The PL intensity decreases around a microwave frequency of about 3500 MHz in a zero magnetic field. This resonance corresponds to the energy gap between $m_S = 0$ and $m_S = \pm 1$ of the ground state. When an external magnetic field is applied, the splitting between the resonance frequencies increases. It is due to an increase in the energy difference between the $m_S = +1$ and -1 states, reflecting the Zeeman effect. Therefore, the magnetic field can be quantitatively estimated from these resonance frequencies. In addition, temperature and pressure can also be estimated by detecting energy changes due to crystal lattice deformation.

This quantum sensor works even when the hBN flakes are less than 100 nm thick. It provides nanometer proximity to measurement targets with the van der Waals forces. This proximity is essential to take advantage of quantum defect sensors' sub-nanometer size.

## ARRANGEMENT OF QUANTUM SENSORS

$V_B$ can be created by damaging hBN crystals with ions, neutrons, or electron beams. Their irradiations are usually uniform, producing quantum sensors uniformly throughout the flake. In this case, the spatial resolution of the magnetic field measurement is limited to the optical resolution. It is typically about 1 μm, which is more significant than the hBN flake thickness; even if the sensors can adhere to the measurement target, the static stray magnetic field may be averaged out due to its large field gradient. In this case, the excellent adhesion property of the hBN quantum sensor cannot be fully utilized.

To mitigate this issue, we attempted to arrange defect spots using focused ion beams [8]. We used a helium ion microscope to narrow the ion beam size to a sub-nanometer to achieve highly precise arrangement. We devised an array of sensor spots to enable high sampling/spatial resolution magnetic field imaging even with optical resolution measurements. The proof-of-principle of this method was demonstrated by measuring the stray magnetic field distribution from the current flowing through the Au wire.

The proof-of-principle measurement was done with a 66 nm thick hBN flake on a silicon substrate with an Au wire 3.2 μm wide and 100 nm thick. The irradiation pattern was designed so that the size of each irradiation spot (100 nm)$^2$ was sufficiently smaller than the optical resolution, and the spacing between irradiation spots (>1 μm) was sufficiently farther apart than the optical resolution. Each irradiation spot is shifted slightly by the same size as the irradiation spot so that the quantum sensors can be placed entirely in the direction across the Au wire.

Figure 2(a) shows the PL intensity distribution of the fabricated device. The bright spots are located at the irradiated spots. It is due to the creation of $V_B$ by the ion irradiation. The spots on the Au wire have higher PL intensity. The steep increase in PL intensity on the Au wire is consistent with the fact that $V_B$ is produced only in a small spot about the same size as the irradiation spot. Such an increase in the PL intensity on Au has been observed in previous studies and is thought to be caused by plasmon effects [12].

Figure 2(b) shows the result of imaging the stray field of the current in the Au wire. The vertical axis is the field normalized per unit current. A maximum current of about 8 mA was used in the measurement. The magnetic field in the out-of-plane direction is positive at the right edge of the Au wire and negative at the left edge. It is qualitatively consistent with Ampère's circuital law. Simulations considering the device structure quantitatively reproduce the obtained experimental results. It is essential to note that the steep change of the field near the edges is reproduced. It indicates that quantitative magnetic field imaging can be performed with higher spatial resolution than conventional optical resolution in specific axial directions. In addition, we also confirmed that individual sensor spots on the Au are sensitive enough to detect about 70 μT in 1 second.

## SUMMARY

The $V_B$ in hBN is sub-nanometer-sized quantitative magnetic field sensor. Nanospots of hBN quantum sensors can be precisely arranged using helium ion microscope. We used them for high spatial resolution magnetic field imaging. This technique would be applied to 0-dimensional objects, such as quantum dots, and symmetric or periodic structures, such as magnetic domains and superconducting vortices.

## ACKNOWLEDGEMENT

This talk is mainly based on Ref. 8, and we thank its collaborators. We thank Mr. Tomohiko Iijima (AIST) for the usage of AIST SCR HIM for the helium ion irradiations.

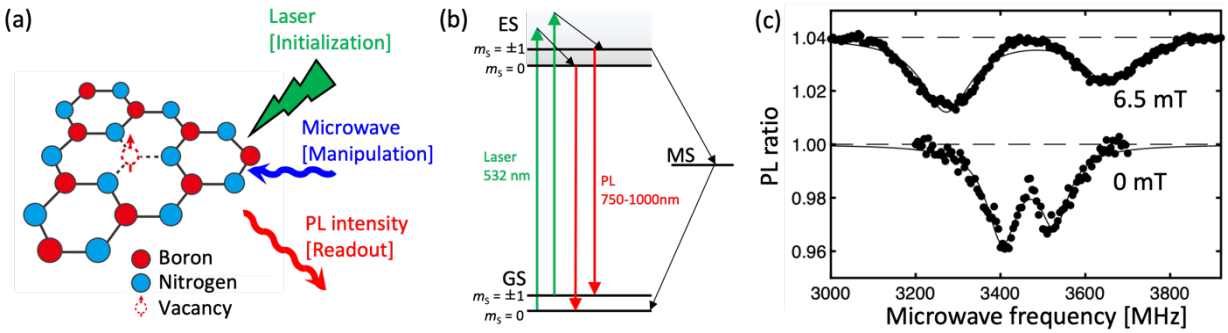


**FIGURE 1.** (a) Structure of a boron vacancy defect. (b) Energy levels and optical transitions of the defect. GS: ground state, ES: excited state, and MS: metastable state. (c) Optically detected magnetic resonance spectrum. Vertical axis is the ratio of PL intensity with and without microwaves.

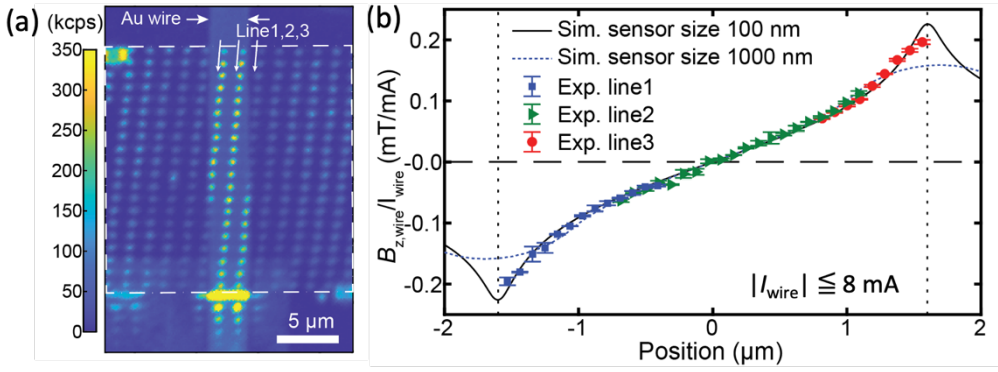


**FIGURE 2.** (a) PL intensity distribution of hBN quantum sensor nanospots created using helium ion microscope. (b) Imaging of stray magnetic fields from currents in the Au wire.

## REFERENCES

1. J. M. Taylor *et al.*, *Nat. Phys.* **4**, 810-816 (2008).
2. G. Kucsko *et al.*, *Nature* **500**, 54-58 (2013).
3. C. L. Degen, *Rev. Mod. Phys.* **89**, 035002 (2017).
4. M. J. H. Ku, *Nature* **583**, 537-541 (2020).
5. A. Laraoui and K. Ambal, *Appl. Phys. Lett.* **121**, 060502 (2022).
6. F. Casola *et al.*, *Nat. Rev. Mater.* **3**, 17088 (2018).
7. A. Gottscholl *et al.*, *Nat. Meter.* **19**, 540-545 (2020).
8. K. Sasaki *et al.*, *Appl. Phys. Lett.* **122**, 244003 (2023).
9. K. Sasaki *et al.*, *Appl. Phys. Express* **16**, 095003 (2023).
10. H. Gu *et al.*, *Appl. Phys. Express* **16**, 055003 (2023).
11. J. R. Reimers *et al.*, *Phys. Rev. B* **102**, 144105 (2020).
12. X. Gao *et al.*, *Nano Lett.* **21**, 7708 (2021).

## KEYWORDS

Quantum sensing, hexagonal boron nitride, helium ion microscope, magnetic resonance, magnetometry

# Wide-area Delayering Based 3D Tomography Solution as a Window into the Semiconductor Manufacturing

Jonghyeok Park[1], Jubok Lee[1], Yunje Cho[1], Junghee Cho[1], Jeonghyeon Wang[1], Hyenok Park[1], Jeongwoo Yu[1], Jiwoong Kim[1], Yun Hwang[1], Heesu Chung[1], Kwangrak Kim[1], Taeyong Jo[1], Hansaem Park[1], Junghee Yun[2], Yongwoon Han[2], Seongjun Cho[2], Subin Oh[3], Jungmo Sung[3], Jin Choi[3], Sungho Lee[3] and Myungjun Lee[1]

*[1]MI Equipment R&D Team, Mechatronics R&D Center, Samsung Electronics Co., Ltd.*
*(1-1, Samsungjeonja-ro, Hwaseong-si, Gyeonggi-do, 18448, Korea)*
*[2]Foundry Analysis Science & Engineering Team, Samsung Electronics Co., Ltd*
*(42-24, Samsung-2ro, Giheung-gu, Yongin-si, Gyeonggi-do, 17114, Korea)*
*[3]Advanced Analysis Science&Engineering Team, Semiconductor Research, Samsung Electronics Co., Ltd.*
*(1, Samsungjeonja-ro, Hwaseong-si, Gyeonggi-do, 18448, Korea)*

*Jonghyeok Park, jh_86.park@samsung.com ; Myungjun Lee, myung01.lee@samsung.com*



## INTRODUCTION

In this study, we explore a wide-area delayering-based 3D tomography solution essential for the device manufacturing process. The trend towards miniaturization and three-dimensional device structures has significantly heightened the complexity of manufacturing process control. This miniaturization is making it increasingly difficult to detect defects and physical failure analysis (pFA). With the emergence of devices like V-NAND, which require etching techniques for features with high aspect ratios (HAR), such as channel holes or metal contacts, there are growing needs for precise measurements of in-depth etch profiles, including characteristics like bending or tilting [1].

Current inline measurements are insufficient to meet these new challenges, often necessitating destructive analysis in analytical laboratories. However, laboratory analyses are limited by their localized field of view, paralleled cross-sectional analysis and the capacity constraints of manual techniques, typically employing tools like Focused Ion Beam (FIB)[2,3]. To address these limitations, we propose an automated solution using wide-area delayering for 3D Tomography analysis. This top-down delayering approach significantly expands the analysis area compared to traditional FIB, providing a new dimension of measurement areas through 3D tomography that traditional cross-sectional analysis cannot offer. The practicality and benefits of this method will be demonstrated through various device study examples in the latter part of this paper.

## AUTOMATED 3D TOMOGRAPHY SOLUTION

Here, we introduce the hardware components and operation methodology of the system designed to acquire a serial image set for automated 3D tomography, and the data processing methodology for generating and analyzing 3D volumes from the acquired serial images.

First, we describe the system configuration of the developed Wide-area Top-down Delayering System (W-TDS) (Fig.1(a)). One of the major objectives of the system is to acquire serial images while delayering the sample in the direction perpendicular to the surface. Determining the slice thickness is another crucial objective, essential for expanding from a 2D image-based data set to 3D tomographic analysis. A key engineering aspect of the system is configuring all these main functionalities, which are (i) delayering, (ii) high-resolution imaging, and (iii) depth measurement on same platform. The Ar+ ion beam method is used for wide-area delayering of the device surface. The ion source with modified ion optics (with focusing and scanning) is employed. Such ion optics enable the focusing and scanning of the ion beam, achieving highly uniform delayering over large areas (< Φ10mm, uniformity

< 2%) controlling ion dose along the sample areas through the manipulations of beam scan range and profile. For high-resolution secondary electron (SE) imaging, Zeiss Gemini SEM 460 system is integrated. The WLSI technique (Zygo, Newview-9000 OEM) was employed to evaluate the delayering depth in a wide area after the milling process (repeatability < 2.5 nm). The three main process modules are located in parallel, centered around a transfer module with a robotic transfer mechanism. Once the sample holder is loaded, the holder is transferred into each process module and serial section imaging is carried out by each process according to a user-defined recipe (see Figure 1(b)). The developed system allows for a fully automated analytical process including automated SEM optimization[4] and imaging operation without human intervention or air exposure of the sample.

Given a set of SEM images, we present a sequence to reconstruct a 3D tomographic volume (Fig.1(f)). The 3D volume was reconstructed without misalignment or discontinuities between the slices by applying registration and interpolation algorithm. To classify the structure based on the device's structural features, we employ the AI based segmentation using 3D U-Net[5] where our dataset includes a set of SEM images of adjacent layers so that it can reduce the effect of interaction volume artifact, therefore material and structure can be clearly distinguished. As a result of the series of data processing, we can obtain a 3D volume data, which is segmented and classified according to the material composition (i.e. metal/oxide) and also to the structural characteristics of the device (i.e. line/via). With 3D tomography, the device structure can be comprehensively investigated.

## DEVICE ANALYSIS CASE STUDIES

Finally, we validate our approach with several case of device analysis. Through examples of analysis in logic and memory components, the advantages of proposed methodology over conventional techniques will be discussed.

### pFA of Logic BEOL Metal Layers

We demonstrate the pFA process for logic devices with electrical faults. Utilizing the proposed method, we carry out the 3D volume analysis on a logic BEOL metal faults, and the results are summarized in Figure 1(a-d). 3D structural were displayed on the ROI areas of suspected failing net and corresponding layers for samples where open or short faults were inferred by the electrical die sorting (EDS) test. Serial images (10-20 slices) of the inferred location and layer of the defect were acquired. In the 3D volume, the suspected failing net inferred (plotted as cyan in the graphical design image, Fig. 1(b)) is also highlighted in red (Fig.1 (a)). It is clearly confirmed that a single-line open (SLO) defect in disconnected metal line by the 3Dand section image (Fig. 1(a, c)). Similarly, when examining the short case, we can infer that a conducting fault caused by the formation of a bridge between adjacent metal lines on two separated nets from the magnified 3D view (Fig. 1(d)).

The results indicate its potential to a high level troubleshooting process of complex device failures, providing a more comprehensive understanding of device 3D structures, thus improving the overall efficiency and reliability of semiconductor manufacturing processes is expected.

### 3D Structural Analysis in HAR Structure of Memory Device

Next, 3D-based advanced device structure analysis cases on HAR structure is demonstrated. Figure 1(e-i) summarizes the results of 3D analysis of a HAR contact structure. In addition to the conventional depth profiling analysis, analysis technique through 3D volume data has great advantages in terms of improved freedom of structure analysis and visualization. First, using volume processing and design information, a specific target structure can be segmented, thus conspicuous visualization, coloring target structure, is enabled (Fig. 1(e)). Plus, only the segmented structure can be extracted (Fig. 1(f)), eliminating unnecessary regions or structures, precise 3D observation of the buried structure becomes possible. Furthermore, since 3D volume allows free extraction of a cross-section with various direction (Fig. 1(g)), it is expected that the cross-section analysis case can be greatly expanded, combining with the existing 2D image analysis algorithms.

Finally, utilizing the advantages of 3D analysis, we examined the evaluation for the 3D banding analysis of HAR contact. Single contact structure is extracted, and its detailed shape is displayed (Fig. 1(h)). In the image, the Z scale has been scaled down to eight times smaller for better visualization. In the result, cross-sectional images of XZ-plane were extracted, and the edge and center positions of metal structures are displayed. (blue plot for the metal structure, and red plot for its center position) The bending behavior of structure through the downward profile can be visualized. In addition, the change in the hole center position in XY plane toward in-depth direction is displayed with a color plot (Fig. 1(i)). Through this, the direction and magnitude of bending according to the in-depth direction can be quantitatively evaluated.

## CONCLUSIONS

In this work, we introduced a fully-automated 3D tomography solution to satisfy the increasing requirements of defect analysis and dimensional measurements in the device manufacturing process.

We have devised the automated system that, based on large-area milling technique, precisely delayering the sample surface to acquire high-resolution serial images. In addition, we have introduced the data processing sequence and technique that allows for the reconstruction of 3D volumes from the image set, and facilitates specialized segmentation tailored for device analysis.

The series of device case studies were conducted to validate the potential of proposed method in advanced analysis. In the case of pFA of logic devices, through the 3D visualization of the suspected failing net and detailed 3D view analysis, it was shown that structural vulnerabilities that causes defects can be detected more effectively. This enriched information is particularly valuable in identifying and diagnosing failure issues that are often challenging with conventional 2D analysis. Plus, the results from the case of HAR structures, such as those found in V-NAND, our 3D volumetric approach allowed us to obtain in-depth profiles and bending characteristics—insights often elusive to alternative analytical methods.

## REFERENCES

1. Lee, G. H. et al. S. L., *App. Sci.* **11** (15), 6703 (2021).
2. Song, H.S. et al., *ISTFA 2018 Proceedings*. 133-137 (2018).
3. Wang, D. D. et al., *AIP Advances* **5** (12), 127101, (2015).
4. Yunje, C. et al., *Proc. SPIE PC12053, Metrology, Inspection, and Process Control XXXVI*, doi: 10.1117/12.2612446 (2022)
5. Çiçek, Ö. et al., *Medical Image Computing and Computer-Assisted Intervention (MICCAI)*, 9901, 424-432. (2016)

## KEYWORDS

Wide-area top-down delayering system (W-TDS), 3D tomography, logic BEOL, pFA automation, 3D structure analysis.

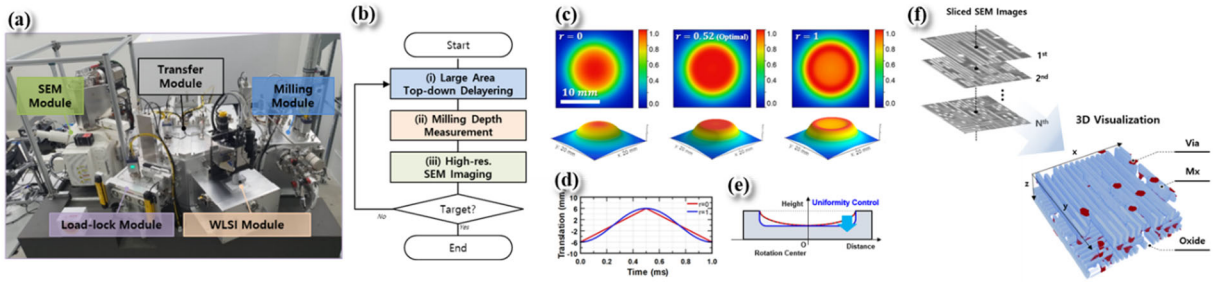


**FIGURE 1.** (a) Photograph of the automated W-TDS process modules. (b) Functional process flow to acquire serial images. Ion milling dose map is simulated by accumulating ion beam with linear and rotational motion (r is cos/tri. ratio). (c) Simulated ion beam dose map with different motion profile. (d) Scan profile for the ion beam with different cos/tri. ratio. (e) Schematic diagram of milling profile with r=0 (red) and r=1 (blue). (f) Input (SEM images), output (3D visualization).

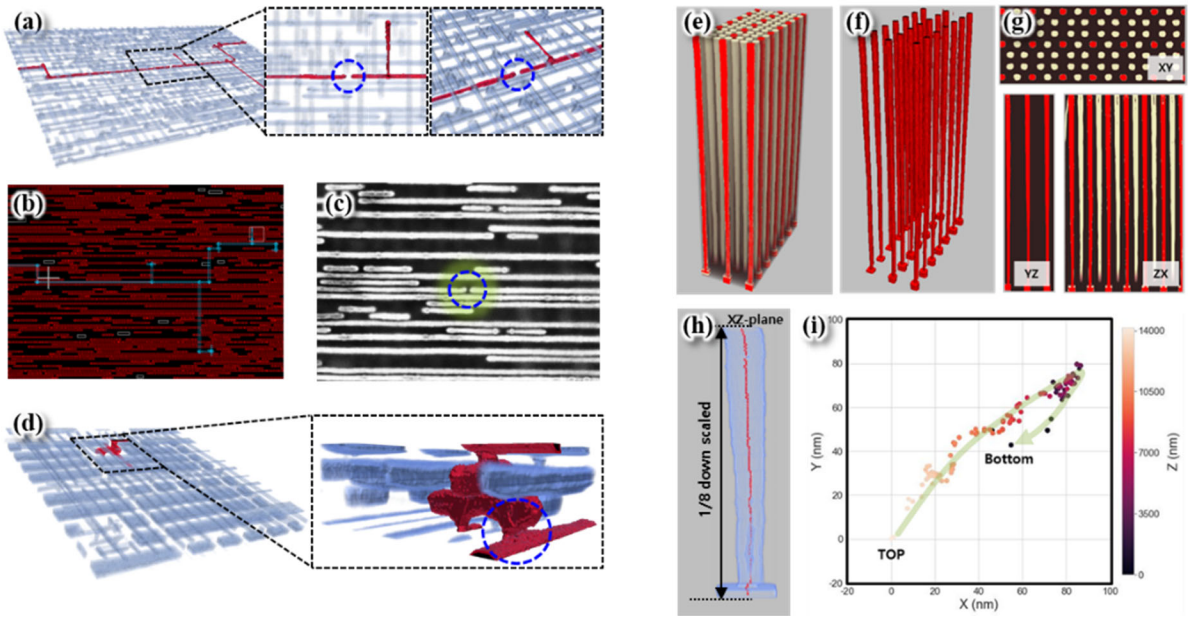


**FIGURE 2.** (a) Reconstructed 3D volume with open defective sample. The suspected failing net is highlighted in red. (b) Graphical design image with suspected failing net (cyan) from EDS test. (c) The section image of the suspected fault location. (d) 3D volume for the sample with short defective sample. Magnified images of suspected bridge defect is displayed. (e) Reconstructed 3D volume of HAR contact structures (f) Segmented extracted target contacts with landing pads. (g) plane cut images for XY-, YZ- and ZX-planes, respectively. (h) XZ-plane cut image of single contact structure where a center of its hole position is denoted with red dot and (i) relative changes in center position of contact hole from top to bottom.

# 3D Metrology And Inspection Of Advanced NAND And DRAM Devices Via Full 3D Characterization With FIB-SEM Tomography

D. Klochkov[1], T. Korb[1], K. Lee[2], H. Kim[1], R. Pichumani[2], L. Mantha[1], P. Hüthwohl[1], E. Foca[1]

[1]*Carl Zeiss SMT GmbH, ZEISS Gruppe, Rudolf-Eber-Straße 2, 73447 Oberkochen, Germany*
[2]*Carl Zeiss SMT Inc., 5300 Central Parkway, Dublin 94568, USA*



## INTRODUCTION

The ongoing growth of memory devices – 3D-NAND and DRAM – into the third dimension as well as the shrinkage of the individual memory cells continue to challenge the manufacturing technology, especially the etching and deposition steps. The 3D-NAND memory stacks which are currently under development exceed a few tens of microns in height and are fabricated with several hundred bi-layers. For current DRAM devices, the diameter shrink of capacitors combined with an increase of their height boosts the aspect ratio to more than 100:1. To ensure a high yield in the manufacturing of these devices, new modes of metrology are needed, leading to unavoidable paradigm shift in established process control solutions. In particular, efficient control of the manufacturing processes demands full 3D characterization of the memory channels, cells, bi-layers, as well as of the logic arrays above, below and around the storage arrays ([1]). At the same time, a new metrology approach needs to provide flexibility for an efficient tradeoff between the data density and information richness on the one hand, and throughput or time-to-data on the other.

FIB-SEM tools, consisting of a focused ion beam (FIB) device for cutting and a SEM for imaging, operated in a "slice-and-view" mode have been utilized to generate 3D volume data in various areas of science and engineering. However, adoption of such techniques in the semiconductor manufacturing domain requires overcoming several challenges. To generate distortion- and artefact-free data volumes, the images of the single slices need to be arranged correctly with respect to each other in 3D space with sub-nanometer accuracy. The total time spent for slicing, imaging, and for the final numerical 3D volume reconstruction and subsequent analysis is limited by tight throughput requirements in semiconductor fabs and labs. We provide an overview of the challenges that had to be overcome to perform 3D-tomography and metrology of 3D-NAND and DRAM devices. We demonstrate the resulting 3D reconstructions and dedicated metrology of such devices performed with ZEISS FIB-SEM tomography tool where the described challenges have been successfully addressed.

## 3D-CHARACTERIZATION OF 3D MEMORY DEVICES WITH FIB-SEM TOMOGRAPHY

Storage areas of the memory devices essentially consist of densely packed high-aspect-ratio (HAR) structures – "pillars" formed by GAA-transistors in 3D-NAND or by capacitors in DRAM. Numerical characterization of the HAR structures can be divided into (i) measurements of their lateral cross-sections at different depths/heights and (ii) measurements of the structures shape in 3D such as tilt or twist. The lateral cross-section measurements include CDs of the structures in different direction, shapes, thickness of the transistor films, proximity of the cells or capacitors to each other etc. (Fig. 1). All of these characteristics are computed in a dense grid of depths/heights (for 3D-NAND, the measurements can be performed in every layer of the bi-layer stack or even denser) giving a high-resolution

height/depth-profile of the respective characteristic [2]. Figure 2 provides two examples of the "integral" measurements of the HAR-structures in 3D – total depths of DRAM capacitors (left) and relative tilts of the 3D-NAND "pillars" (right). These measurements characterize each HAR structure individually and can only be obtained using a full-scale 3D-tomography [3]. An essential feature of the ZEISS FIB-SEM 3D-Tomography solution is full de-coupling of the lateral image quality and resolution from the resolution in the vertical direction. It is a tradeoff between resolution / data density along the vertical axis and throughput.

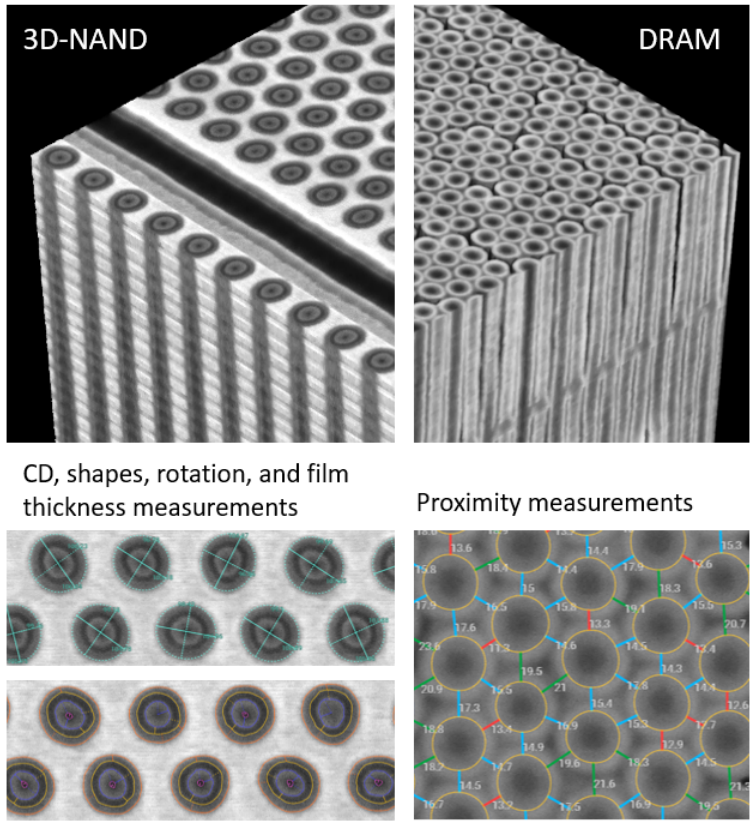


**FIGURE 1.** Examples of the reconstructed 3D-volumes of 3D-NAND and DRAM devices (top) and of lateral cross-section measurements of the 3D-NAND cells and DRAM capacitors (bottom).

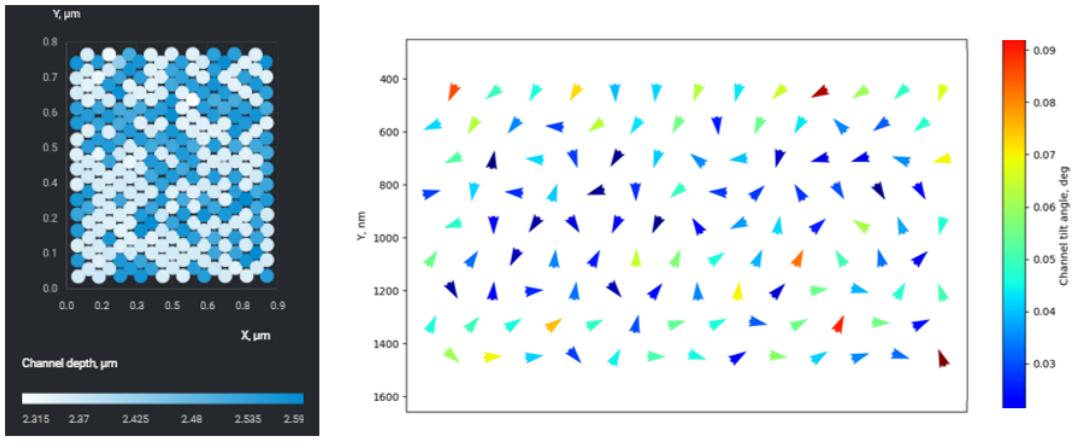


**FIGURE 2.** *Left:* Examples of measured individual DRAM capacitor height/depth (color coded). *Right:* Examples of measured relative tilt of the individual 3D-NAND "pillars". The color of the triangles indicates the amount of the tilt angle while their direction corresponds to the direction of the tilt.

# MAIN EFFECTS OF SLICE-AND-IMAGING IMPERFECTIONS ON THE RECONSTRUCTED VOLUME AND MEASUREMENTS

To make FIB-SEM 3D-tomography useful for the analysis of semiconductor devices, a series of technical challenges need to be addressed.
Majority of the metrology tasks imply data analysis on planes parallel or orthogonal to the wafer surface. However, in most FIB – SEM systems the arrangement of the columns does not allow for cutting of slices orthogonal to the SEM column. Instead, the images are rather generated at an angle with respect to the SEM column. As a result, a stack of planar top-down images needs to be generated numerically out of angled slices without distortions, artefacts, or loss of resolution.
Variable image distortion not only affects the results of the measurements but also makes it impossible to align slices in a 3D-stack. The amplitude of the residual mismatch between the slices caused by this effect is usually proportional to the size of the FoV. Such mismatch leads to artefacts in the reconstructed shapes such as short length-scale glitches or "jumps" of the imaged structures.
The separation of adjacent slices i.e., slice thickness, needs to remain stable to within nm-precision during the entire acquisition in order to achieve a homogeneous spatial resolution inside the reconstructed data volume. The local variations of the slice thickness need to be precisely measured and properly accounted for during the volume reconstructions. A failure to do so leads to similar artefacts as in the previous case.
Non-planarity and variable topography of the individual slice surfaces can be considered as a local lateral variation of the slice thickness and is exceptionally challenging for precise volume reconstruction. Usually, a combination of prior knowledge about the device design and precise slice thickness control during the acquisition are used for a proper accounting for this effect in the reconstruction.
We demonstrate 3D-tomography of memory devices where all of the above listed challenges have been addressed by a set of sophisticated techniques related to acquisition and data evaluation which are implemented in the ZEISS FIB-SEM tomography tool.



## REFERENCES

[1] L. Tu, J. Mi, H. Fan, et al., *Proceedings Volume 11325, Metrology, Inspection, and Process Control for Microlithography XXXIV; 113250L (2020)* https://doi.org/10.1117/12.2551610*, SPIE Advanced Lithography, 2020*
[2] J. T. Neumann, D. Klochkov, T. Korb et al., *Proceedings Volume 11325, Metrology, Inspection, and Process Control for Microlithography XXXIV, 113250M (2020)* *https://doi.org/10.1117/12.2552006*, *SPIE Advanced Lithography, 2020*
[3] P. Gin, M. Wormington, Y. Amasay et al., Journal of Micro/Nanopatterning, Materials, and Metrology, Vol. 22, Issue 3, 031205 (March 2023), *https://doi.org/10.1117/1.JMM.22.3.031205*

## KEYWORDS

3D metrology, inspection, 3D tomography, scanning electron microscopy, focused ion beam, metrology, 3D-NAND, DRAM, HAR

# Measuring the Complex Behavior of Phase in the EUV Regime and Implications for Phase Shift Masks

Patrick Naulleau, Seth Cousins, Feng Dong, Matt Hettermann, Dave Houser, Stuart Sherwin

*EUV Tech Inc., Martinez, CA, 94553, USA*

## INTRODUCTION

Enabling the short and long term scaling of extreme ultraviolet (EUV) lithography patterning dimensions, depends on the availability and utilization of actinic (at-wavelength) metrology and characterization techniques. Continuing EUV patterning shrink is limited by our understanding and control of materials, including both mask materials as well as patterning materials. To date, EUV patterning in high volume production has not yet achieved the same low k1 typically accessible in the DUV regime. Phase shift masks are being actively pursued as a pathway to further reduction of k1 in the EUV regime by way of improved image log slope and/or improved photon efficiency. To this end, actinic characterization of phase shift materials and phase shift masks is essential. Phase in the EUV regime is extremely sensitive to even subtle changes in material characteristics as well as thin-film interference effects. Additionally, although the phase of a mask is often referred to as a single scalar term, in EUV, the reality is quite different with substantial and non-linear dependence on both angle and in-band wavelength demanding more thorough representation of the phase.

## DISPERSION IN THE EUV REGIME

To date, the role of dispersion in EUV lithography has generally been ignored. While this is not really a concern for imaging optics and binary masks, the emergence of phase shift masks has elevated the importance of this effect. The complex index of refraction in the EUV regime can readily be measured using variable angle reflectometry [1]. Figure 1 shows an example of such a measurement for TaN, a typical EUV mask absorber material. The impact of dispersion is clearly visible as observed by the substantive difference in reflectance behavior as a function of small wavelength change near 13.5 nm. While the data shows results over a total wavelength range of 2 nm, we note that the typical bandwidth of a single EUV Mo/Si multilayer is on the order 0.5 nm, so the dispersion impacts within an EUV lithography system will be approximately 4 times smaller than observed in Fig. 1.

Although TaN is commonly used as an EUV mask absorber and does exhibit significant phase shift at EUV, it is in fact not well suited for use as a phase shift mask material as a result of its strong absorption characteristics. Effective application of phase shift mask technology requires the absorber to be *leaky* enough to support destructive interference between the light reflecting from the absorber and clear regions of the mask, respectively. Figure 2 shows the measured [2-4] wavelength dependent n and k (the real and imaginary parts of the complex index of refraction, respectively) for three different materials better suited to use in phase shift masks. The non-linear dispersive effects are clearly evident in the data.

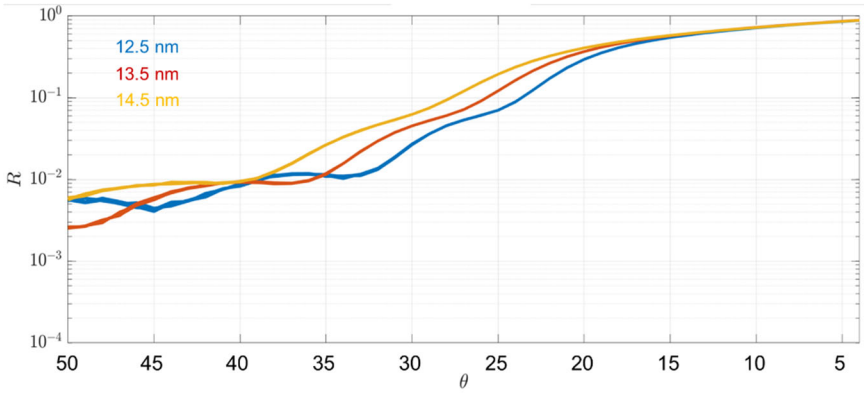


**FIGURE 1.** Variable angle reflectance of TaN in the EUV regime. The x axis represents angle from glancing and the y axis represents the intensity ratio of the reflected light to the illuminating light. The measurements were performed using the EUV Tech ENK Tool, a laser-produced plasma based variable angle spectroscopic scatterometer [2-4].

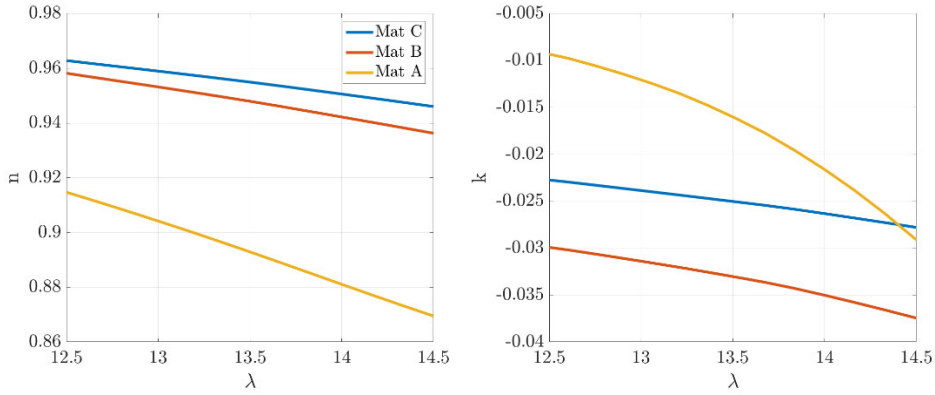


**FIGURE 2.** Measured wavelength dependent real (n) and imaginary (k) parts of the complex index of refraction of three different EUV phase shift mask materials. The measurements were performed using the EUV Tech ENK Tool [2-4].

## PHASE ON EUV MASKS

Due to the reflective nature of EUV masks, controlling the phase is significantly more complicated than for transmission masks used in the DUV regime, where phase is dominated by refractive effects. The phase of an EUV mask will depend on reflectance from the individual layers making up the absorber stack as well as refraction through those layers and the multilayer reflectance phase. In light of the dispersion described above, the reflection and refraction terms will show significant wavelength dependence, moreover, the reflectance terms will be highly dependent on incident angle as is the phase of the underlying multilayer reflectance. Figure 3 shows the computed phase as a function of wavelength and angle for a standard Mo/Si multilayer. As expected from a Bragg reflector, the phase evolves rapidly across the reflectance peaks in wavelength and angle. The highlighted regions depict the lithography system wavelength and angular bandwidths. Across the relevant wavelength range we see 50 degrees of phase change from the multilayer and the relevant angular band shows 80 degrees of phase change.

As described above, the phase on an EUV mask will exhibit significant dependence on wavelength and angle and thus cannot be well represented by a single value, but rather the full wavelength and angle response must be characterized in order to accurately predict imaging performance. Spectroscopic, angle resolved reflectometry intrinsically encompassing these wavelength and angle parameters is thus ideally suited to the lithographic relevant measurement of EUV mask phase [3]. Figure 4 shows an example of such a measurement [4] for an EUV phase shift mask. The results show up to 30-degrees phase shift across the spectral passband and up to 15-degrees phase shift across a typical illumination angle range. We note that the angles of 2 and 10 degrees are representative of what might be used in a dipole illumination setting. With this amount of phase diversity, it is evident that simply

characterizing the phase at the nominal value of 13.5-nm wavelength and 6-degree illumination would in fact not be adequately representative of the true as used phase of the system.

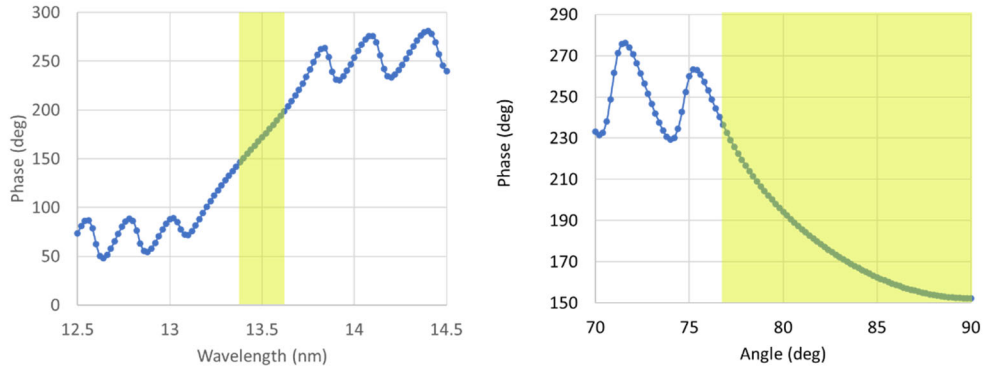


**FIGURE 3.** Computed phase response of Mo/Si multilayer mirror. The highlighted regions depict the lithography system wavelength and angular bandwidths.

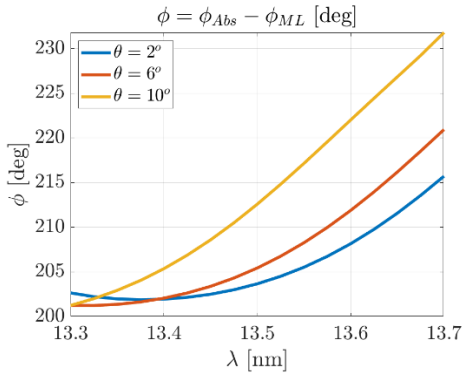


**FIGURE 4.** Measured [4] phase response of an EUV phase shift mask as a function of wavelength and at 3 different illumination angles. The measurements were performed using the EUV Tech ENK Tool [2-4].

## REFERENCES

1. B.L. Henke, E.M. Gullikson, and J.C. Davis, X-ray interactions: photoabsorption, scattering, transmission, and reflection at E=50-30000 eV, Z=1-92, Atomic Data and Nuclear Data Tables **54** no.2, 181-342 (July 1993).
2. S. Sherwin, Actinic EUV reflectometry and scatterometry: from national lab to commercial applications," Proc. SPIE **PC12292**, International Conference on Extreme Ultraviolet Lithography 2022, PC122920P (11 November 2022); https://doi.org/10.1117/12.2643550.
3. E. Gomar-Nadal, M. Tavassoli, K. Bijjula, S. Sherwin, M. Hettermann, C. Wilson, F. Dong, D. Houser, A. Khodarev, C. Perera, P. Naulleau, "Development of EUV phase shift mask metrology," Proc. SPIE **12751**, Photomask Technology 2023, 127510O (21 November 2023); https://doi.org/10.1117/12.2688453
4. S. Sherwin, M. Hettermann, D. Houser, C. Perera, P. Naulleau, "EUV actinic scatterometry for in-pattern phase metrology," Proc. SPIE PC12751, Photomask Technology 2023, PC127510P (22 November 2023); https://doi.org/10.1117/12.2688099

## KEYWORDS

Extreme ultraviolet, phase metrology, photomask, spectroscopy, reflectometry, lithography

# MI(Metrology&Inspection)’s deliverable solutions for next journey

Byoung-Ho Lee

*Hitachi High-Tech Corporation*
*Toranomon Hills Business Tower, 1-17-1 Toranomon, Minatoku, Tokyo, 105-6409, Japan*



## INTRODUCTION

From the time semiconductors were first created, processes such as lithography, dry etching, wet etching, CMP, thin film, and diffusion have been essential because they are the basic processes for making semiconductors. However, although it is helpful in the case of metrology and inspection, it is not a necessary process for the receiving process. Rather, the MI(Metrology&Inspection) process was often perceived as a time-consuming process for rapid production. However, as semiconductor technology progressed and several competitors emerged, speed of development became important, and MI took center stage. Through MI, quick feedback and feedforward on processes’ qualities have become essential elements for improving yield and are also key to shortening the development period for new products. Several organizations, including imec and IRDS (International Roadmap for Device and Systems), are presenting roadmaps for future semiconductor technology. Until recently, reduction of design rules has been the core of the semiconductor process, but it shows many limitations in semiconductor development through shrinkage, so the 3Dization of semiconductors is accelerating further. Let's look at past, present, and future trends in semiconductor development and review how the development of MI technology has changed accordingly. We will also predict what MI technology will be needed for future semicindutor development.

## KEYWORDS

Metrology & Inspection, 3D devices, Semiconductor’s tech direction, MI’s tech direction

# Advanced and Future Logic Device Architectures: Challenges and Solutions in Materials Metrology

Shay Wolfling

*Nova LTD,*
*5 David Fikes St, Rehovot Israel 761020*

## INTRODUCTION

Since the inception of the semiconductor industry, traditional scaling has played a pivotal role in the consistent decrease in cost per transistor with each successive technology node. This process initially focused on shrinking gate oxide thickness and optimizing the doping profile of the source, drain, and channel. However, to sustain the momentum of cost reduction and density enhancement, modern scaling strategies over the last two decades have shifted towards the adoption of innovative materials and device architectures, including strained channels, high-k metal gates (HKMG), and fin field-effect transistors (FinFETs). Some of these key scaling strategies are depicted in Figure 1. The latest updates from the International Roadmap for Devices and Systems (IRDS) suggest that scaling below 5-nm technology nodes will encounter significant hurdles, amplifying the significance of materials research [1,2]. The integration of novel materials, reduction of feature sizes, introduction of new device architectures, implementation of low-temperature processing, and the shift towards 3D complex structures fabrication all pose substantial challenges to materials characterization and contamination analysis, which are crucial for process development and quality assurance.

As the industry moves toward the architecture of future logic devices, including Gate All Around (GAA) and beyond, material-related challenges are set to intensify [3,4]. The selection of materials is guided by multiple factors, including matching electrical properties, ensuring adequate isolation, etch selectivity, and simplifying processing requirements. With the advancement of technology nodes, the demand for characterization accuracy increases, pushing towards tighter error margins for metrics such as layer thickness, elemental concentration, and other material properties. To satisfy such demands, it becomes imperative to advance characterization techniques, including those that are predominantly “lab-techniques” [5], towards a high-volume manufacturing, fully automated wafer-compatible methodologies.

Advanced material metrology tools that are currently employed in laboratory settings to characterize and monitor process excursions, are instrumental in identifying process deviations and their underlying causes by mapping physical and material parameters. For the evolution and refinement of process control, it is imperative that such tools are transitioned to inline applications. Consequently, there is an observable trend toward integrating laboratory-grade process control and metrology solutions within the fabrication environment.

This paper offers a new view on material metrology solutions in the fab, enabling chip makers to achieve high yield and reliability in semiconductor device manufacturing**.**

## GATE-ALL-AROUND MATERIAL CHALLENGES

The advanced logic architecture of GAA is clearly a significant evolutionary leap from FinFETs, offering enhanced performance and cost per transistor. However, the manufacturing complexity and cost of such an architecture pose considerable challenges, accompanied by an increased complexity of measurement processes.

A typical 3D structure of GAA in the Inner Spacer manufacturing step, as well as some of the typical material metrology challenges are depicted in Figure 2. Uniform thickness, material composition, and Silicon: Silicon-Germanium (Si:SiGe) superlattice quality are vital for the device's electrical performance and need to be controlled throughout the manufacturing process. Any variation can lead to poor device performance and significant yield loss.

The transition from GAA to monolithic Complementary Field-Effect Transistors (CFET), where transistors are placed in a 3D architecture (NMOS transistor on top of the PMOS transistor) [6], will further enhance these challenges.

## FROM LAB TO FAB INLINE SOLUTIONS

In order to control the manufacturing process of advanced nodes, chip manufacturers depend on various metrology tools, some of which are predominantly laboratory technologies. Present-day laboratory-based solid-state characterization revolves around imaging methodologies such as Scanning Electron Microscopy (SEM), Transmission Electron Microscopy (TEM), and the array of techniques within the Scanning Probe Microscopy (SPM) family, including Atomic Force Microscopy (AFM). However, the variety of utilized technologies and capabilities is significant, and includes a wide range of spectroscopic techniques, encompassing Infrared (IR), Raman Spectroscopy, X-ray Photoelectron Spectroscopy (XPS), Rutherford Back Scattering (RBS), Secondary Ion Mass Spectrometry (SIMS), Electron Energy Loss Spectroscopy (EELS), Atom Probe Tomography (APT), and more.

It should be noted that taking a Lab technology into the Fab is a development process, which is quite challenging and requires many innovations and modifications. First, one needs to automate the technology in all software and hardware aspects. Secondly, the developed solution must have Fab connectivity, layers of process control, tool matching and a high up-time. Last but not least, such a transition is typically accompanied by enhancing the performance of the technology for the challenging needs of advanced nodes and by additional layers of data-analysis algorithms. In evaluating new technologies for metrology in high-volume manufacturing (HVM), it is essential to consider not only their performance metrics such as resolution, precision, and sensitivity, but also their potential for throughput enhancements and advanced algorithms; comprehensive data analysis suites are crucial for converting raw data into actionable insights, facilitating detailed analysis and informed decision-making processes.

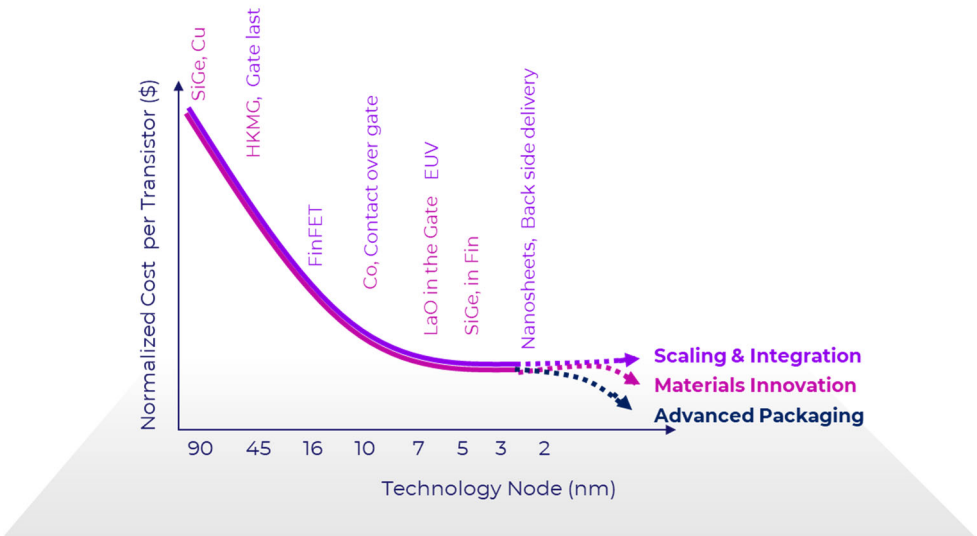


**FIGURE 1.** Key scaling strategies of the last decades.

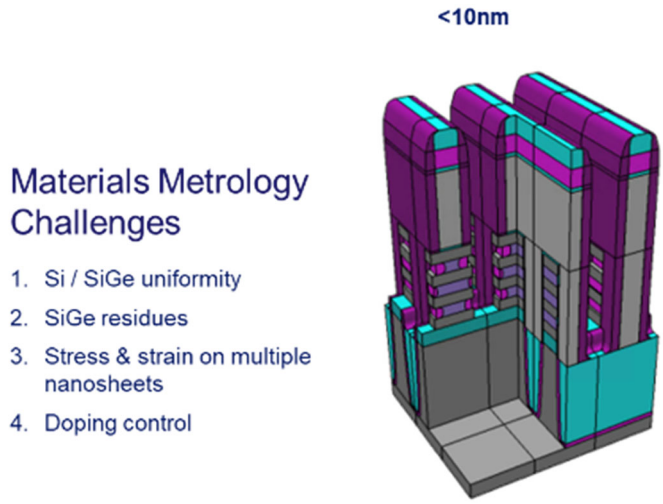


**FIGURE 2.** Examples of materials metrology challenges in GAA inner spacer manufacturing step.

## REFERENCES

1. IRDS™ 2023: Metrology https://irds.ieee.org/editions/2023/20-roadmap-2023-edition/123-irds%E2%84%A2-2023-metrology.
2. IRDS™ 2023: Beyond CMOS and Emerging Materials Integration https://irds.ieee.org/editions/2023/20-roadmap-2023-edition/126-irds%E2%84%A2-2023-beyond-cmos-and-emerging-materials-integration.
3. Y. Sohn, “Diversifying the role of MI in semiconductor manufacturing through new technologies and innovations”, SPIE 2022.
4. M.A. Breton et al., “Review of nanosheet metrology opportunities for technology readiness”. J. Micro/Nanopattern. Mater. Metrol. 021206-1 Apr–Jun 2022, Vol. 21(2).
5. P. Wong, “Semiconductors: New Lab-to-Fab Solutions and the Future of Semiconductor Technology”, US Department of State, FPC BRIEFING Apr 2022.
6. R. Marko, “Demonstration of a Stacked CMOS Inverter at 60nm Gate Pitch with Power Via and Direct Backside Device Contacts”, Paper 29.2, IDEM (2023).

## KEYWORDS

Inline metrology, Materials metrology, Gate-All-Around, Nanosheets, Lab-to-Fab

# Revolutionizing EUV Lithography Metrology for Sub-3nm Nodes: Validation of a Novel AFM System for Precise 3D Characterization in HVM

Nelda Antonovaite, ShihWei Yu, Khalid Elsayed, Erik Simons, Hokyun Chin, Arseniy Kalinin, Irene Battisti, Helda Pahlavani, Seokhan Kim, Artem Khachaturiants, Niranjan Saikumar, Rudolf Wilhelm, Hamed Sadeghian

*Nearfield Instruments, B.V. (The Netherlands)*
*Vareseweg 5, 3047 AT Rotterdam, The Netherlands*



## INTRODUCTION

EUV lithography enables continued scaling beyond 3 nm nodes and allows the employment of single patterning methods with improved resolution and reduced edge placement error (EPE) benefits. Thinner photoresist layers with shrinking feature sizes consequently make stochastic errors such as micro-bridges, breaks, scum, footing, and line edge roughness, worse during the lithography step. Furthermore, the low-contrast nature of the photo-resist materials poses serious metrology challenges for traditional metrology systems like OCD or CD-SEM, where for the latter, the photoresist damage due to an increased number of electrons is a serious issue. Therefore, a nondestructive metrology solution with sub-nanometer resolution and with information in the third dimension (full profile shape) is required to optimize the lithography process. Atomic force microscopy (AFM), a topography imaging technique, can achieve the required precision to capture critical dimensions of photoresist patterns in 3 dimensions, but it is generally limited by the ability to fully resolve deep and narrow structures, can be destructive and suffer from low throughput. Here, we show validation of a novel in-line AFM system, QUADRA, that overcomes these challenges. Details on precision, non-destructiveness, probe lifetime, throughput, and parameter extraction including a new footing detection algorithm are reported for photoresist Line/Space patterns (32 nm pitch) that meet the requirements for cost-effective use in high-volume manufacturing (HVM) environment.

## METHODS

QUADRA is a high-throughput fully automated metrology tool[1] equipped with 4 independently positioned miniaturized high-bandwidth AFM heads[2]. Wafers are measured upside-down to shorten the mechanical measurement loop and together with an active vibration isolation system[1] to ensure an unprecedented noise floor of 50 pm at high scanning speeds in the HVM fabs with typically high environmental noise. QUADRA uses the proprietary Feed Forward Trajectory Planning (FFTP) scan mode designed to reach the bottom of deep and narrow trenches or holes (typical dimensions of EUV patterns for < 3 nm nodes) at much higher scanning speeds than any other AFM tools[3]. The tip shape and trajectory are optimized to lower tip-wafer interaction forces, achieving fully non-destructive measurement on sensitive photoresists.

## RESULTS

### QUADRA performance on Line/Space photoresist patterns

For EUV metrology, TEM is used to obtain several cross-sections of the wafer from which the profile of the line and space patterns can be evaluated, and critical dimensions (CD) extracted but it does not have enough sampling to report shot and wafer level uniformity. On the other hand, CD-SEM is a top-down imaging technique used to extract

line width (LW), line width roughness (LWR), and line edge roughness (LER) with sufficient sampling for local CD uniformity (LCDU) but it lacks reliable information in the third dimension, depth. QUADRA has the benefit of being able to measure the 3D shape of the line and space patterns and reconstruct the real shape by correcting for tip-shape effects with sampling similar to CD-SEM. As a result, all parameters of interest such as CDs (depth, width, sidewall angle), LCDUs (LWR, LER), and surface roughness (top and bottom of the line) are extracted using an on-tool automatic data processing workflow (see Figure 1). In contrast to CD-SEM, QUADRA extracts LW and LCDUs as a function of depth where typically LCDUs (3σ) at the bottom is lower and increases at the top of the line while LW is larger at the bottom and decreases by several nm at the top (see Figure 2, a). Furthermore, we report the standard deviation (STD) of 10 repeated measurements of typical parameters of interest which demonstrates the high precision of QUADRA for lateral and vertical measurements (Table 1).

Generally, for probe-based techniques, the main concerns in metrology are tip-to-tip matching (TTTM), tip wear, and sample damage. Here we show that for selected probe type, measurements of variations such as LWR, LER, top-line and bottom-trench roughness, as well as depth, are independent of sub-nm differences in probe dimensions (Table 1) since STD of a single probe and difference in mean values of two probes (TTTM) are in the same order of magnitude. Only LW requires removing tip-shape effects through a deconvolution algorithm to compensate for tip-to-tip differences (Table 1). Furthermore, we also show that the same parameters are stable over 200 images proving a long probe lifetime (Figure 2, b). The non-destructiveness of FFTP scanning mode is shown by measuring the same location 12 times followed by a larger scan where damage is not observed (Figure 2, c).

The throughput of QUADRA is 30 WPH for a typical sampling of 20 shots per wafer which is at least 10 times higher than any other AFM system, > 100 times higher than TEM, and similar to CD-SEM although the latter lacks precise vertical information.

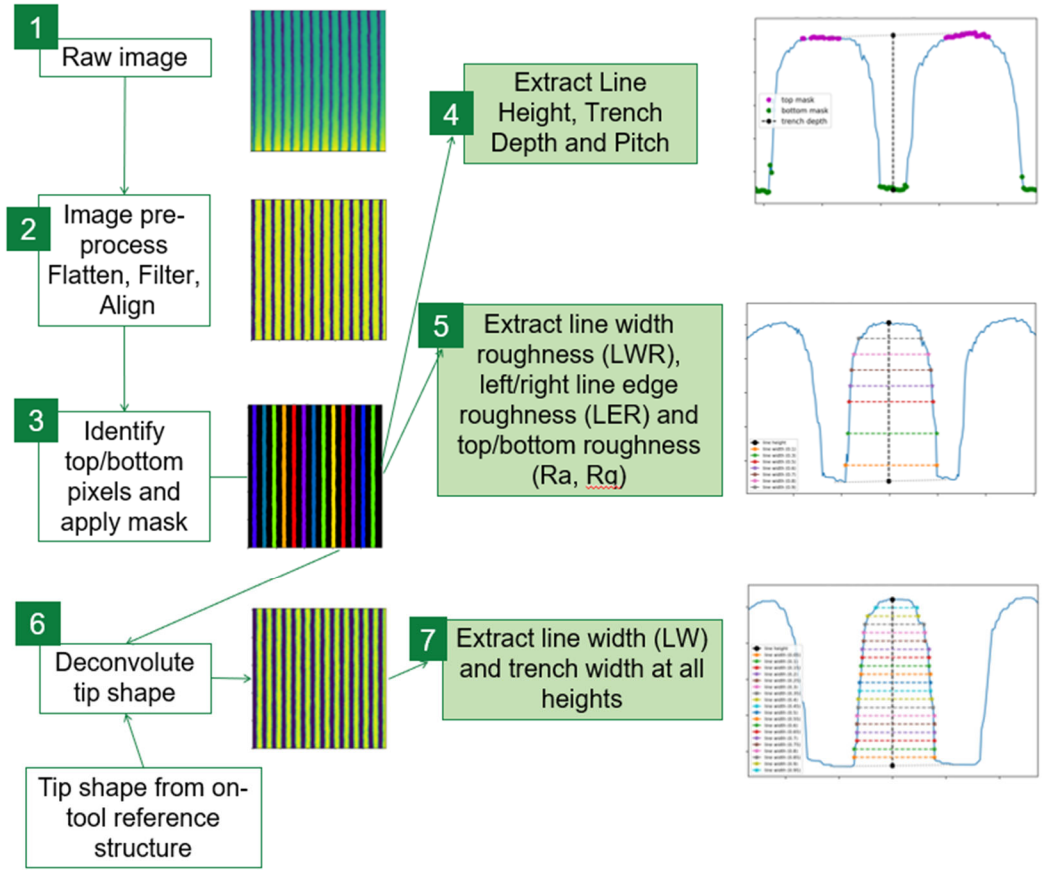


**FIGURE 1.** Automated data processing workflow: 1) raw image is 2) preprocessed to flatten, filter, and align image followed by 3) identification of top and bottom pixels and creation of masks that are used to 4) extract Line Height, Trench Depth and Pitch as well as 5) LWR, LER, and top/bottom roughness. For lateral dimension extraction, the image needs to be 6) deconvoluted using tip shape which is previously defined by measuring on-tool reference structure followed by 7) extraction of LW and trench width from bottom to the top of the line.

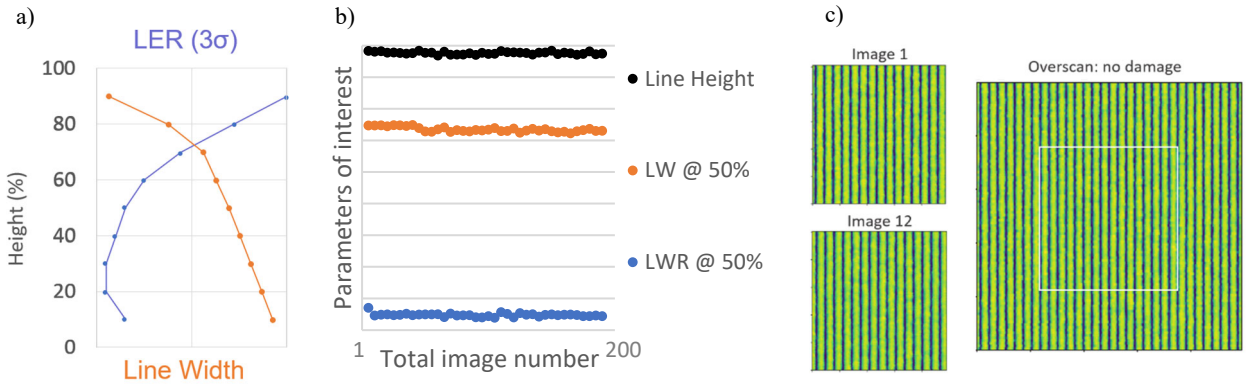


**FIGURE 2.** QUADRA performance on photoresist patterns: a) mean LW and LER as a function of the percentage of height; b) LW and LWR at 50% height, and line height as a function of total image number on a test shot (not all images were taken on the same shot); c) first and last repeated images and overscan (lower resolution) with white square indicating repeated measurement location.

**TABLE 1.** Precision (STD of 10 repeats) and tip-to-tip matching (TTTM) of QUADRA for different parameters on Line/Space EUV photoresist patterns.

| Parameters of interest | STD (nm) | TTTM (nm) |
|---|---|---|
| **Line Height (1σ)** | <0.10 | 0.10 |
| **Pitch 50% (1σ)** | <0.005 | 0.01 |
| **Top line Rq (1σ)** | <0.02 | 0.005 |
| **Bottom trench Rq (1σ)** | <0.10 | 0.02 |
| **LW 10% - 90% (1σ)** | <0.20 | 0.60/0.20* |
| **LWR/LER 10% - 90% (3σ)** | <0.10 | 0.03 |

* Before/After deconvolution

## Scum and Footing Detection Algorithm

Besides previously reported microbridges and breaks, there are smaller defects such as footing and scum that are relevant to detect for EUV process control. Scum is an under-developed photoresist at the bottom of the trench connecting two lines while footing is a wider line at the bottom of the line (Figure 3, a). Since QUADRA measures 3D shape, we developed a contour-based algorithm that can discriminate between LER variation along the depth and defects (scum/footing):

1. Contours are defined along the sidewall at different levels of heights (Figure 3, b).
2. Differences in contours (x) at low and high levels are calculated and if it is larger than the threshold, pixels are marked as defects (Figure 3, c).
3. X threshold and height level selection are based on mean LW and LER curves (e.g. Figure 2, a) from scan areas with no defects.
4. Defects can be classified based on length and width set by $X_{thr}$ and $Y_{thr}$ (Figure 3, d). The number of defects $N$ and the percentage of defected pixels to a total number of image pixels *def (%)* can be calculated as an alternative to the 2-dimensional pixNOK method of CD-SEM. These parameters can be used to compare the defectivity of different types of photoresists and their processing conditions (Figure 3, e).

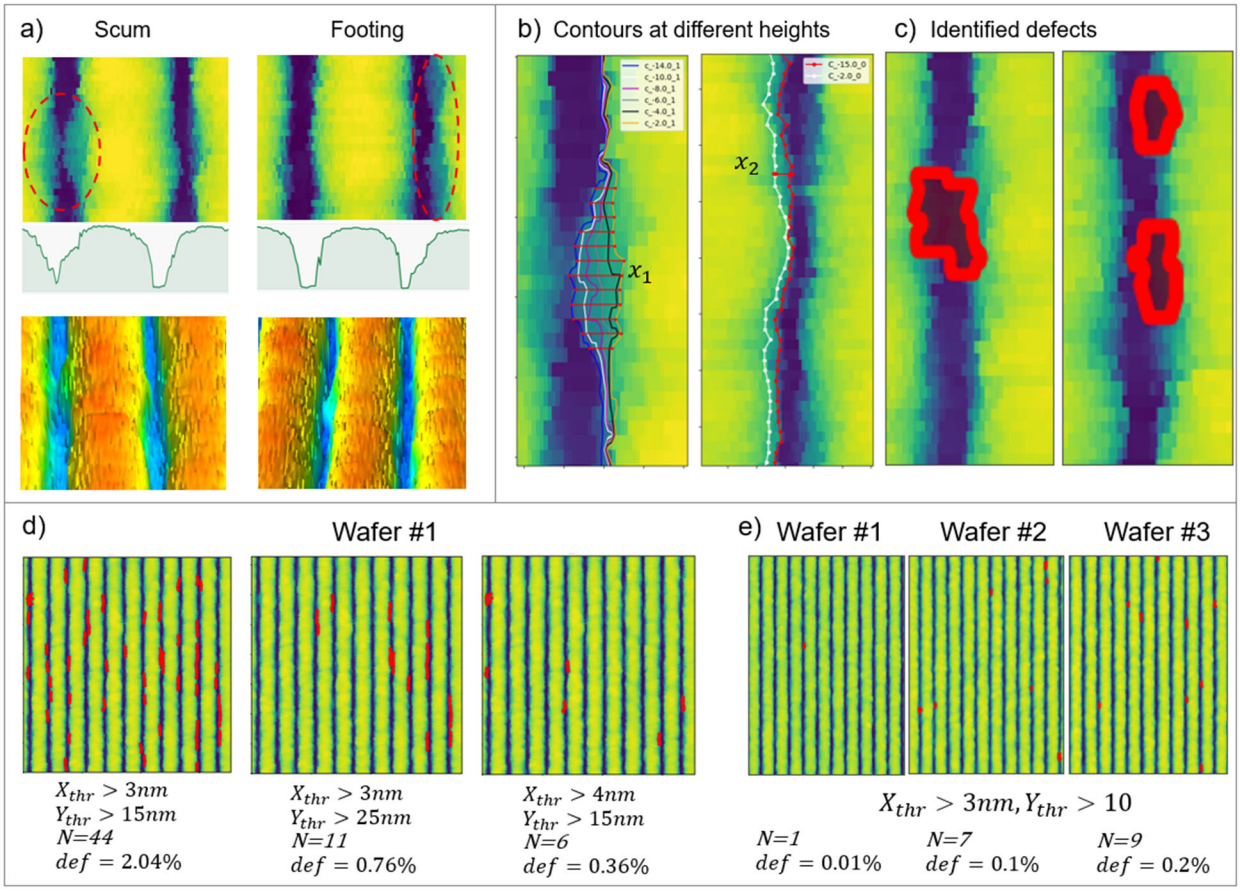


**FIGURE 3.** Scum and footing detection algorithm: a) examples of two types of defects, scum and footing, in photoresist patterns measured by QUADRA; b) contours at different levels of heights with large (left) and small (right) differences, $x_1$ and $x_2$, respectively; c) identified defects of images in a); d) defect classification based on thresholds in the vertical and horizontal size (X and Y); e) comparison of defectivity of 3 types of wafers.

## REFERENCES

1. Sadeghian, H., Herfst, R., Dekker, B., Winters, J., Bijnagte, T., & Rijnbeek, R. (2017). High-throughput atomic force microscopes operating in parallel. Review of Scientific Instruments, 88(3), 033703. https://doi.org/10.1063/1.4978285
2. Herfst, R., Dekker, B., Witvoet, G., Crowcombe, W., de Lange, D., & Sadeghian, H. (2015). A miniaturized, high-frequency mechanical scanner for high-speed atomic force microscope using suspension on dynamically determined points. Review of Scientific Instruments, 86(11), 113703. https://doi.org/10.1063/1.4935584
3. Mucientes, M., Khachaturiants, A., Trussell, R., Kalinin, A., Guo, Y., Simons, E. C., Kim, S., Nadyarnykh, O., Moussa, A., Bogdanowicz, J., Severi, J., Lorusso, G., Simone, D. D., Charley, A.-L., Leray, P., Reijzen, M. E. van, Bozdog, C., & Sadeghian, H. (2022). High-NA EUV photoresist metrology using high-throughput scanning probe microscopy. Photomask Japan 2022: XXVIII Symposium on Photomask and Next-Generation Lithography Mask Technology, 12325, 189–198. https://doi.org/10.1117/12.2641698

## KEYWORDS

Semiconductor metrology techniques, lithography process control, stochastic defects, critical dimension measurement, LWR measurement, atomic force microscopy

# The State of the Semiconductor Industry – Economics and Geopolitics

G. Dan Hutcheson

*TechInsights Inc.*
*2025 Gateway Place, Suite 370*
*San Jose, CA 95110*

## INTRODUCTION

This is the standard font and layout for the individual paragraphs. The style is called "Paragraph." Replace this text with your text. The "Enter" key will take you to a new paragraph. If you need to insert a hard line break within the paragraph, please use Shift+Enter, rather than just tapping the "Enter" key.

Once 2023 was over, it was clear most got it wrong in what was a year of odd contradictions. When it came to the macro picture, most economists predicted we were headed into a downturn and consumers – according to surveys – thought we were in one. Instead, macroeconomic growth was strong. It wasn't even a soft landing. It turned out not to matter what consumers thought, as they opened their wallets and continued to spend with the good-savings tailwind from the COVID days. Auto sales in the US were their best in four years. However, China's ending its lockdown did not bring the economic bonus many expected. Instead, the economic health was U.S. centric.

What about the mega-dip that many feared? Last year at this time, things looked dark with chip inventories through the roof and fears of government spending causing a glut. Yes, there was a glut, which I had reported on in June of 2022. But it was the result of the shift from Just-In-Time to Just-In-Case during the Great Shortage of 2021, causing chip companies – memory in particular – to lose visibility in the demand side of their supply chains.

Yet, I was more optimistic last year, writing, "This question has moved to the center of worries around the industry. I still believe there is more upside potential than downside to the forecasts that are out there based on lower volatility seen since 2012." As it turned out, there was no megalodon lurking in the depths below to swallow us up. By last January, most of the damage was behind us. For ICs, 2023's deceleration would turn out to be near the moderated average and equipment was hardly down at all, thanks to geopolitical drivers.

Moore's Law: dead AND alive? At the start of 2023, general sentiment had it that Moore's Law was dying as some saw Pat Gelsinger as its last holdout. But as the year came to a close, The Economist magazine declared Moore's Law was "like Schrödinger's hypothetical cat—at once dead and alive," based on what they saw at IEDM. They pitted Gelsinger against Jensen Huang and essentially ruled Pat the winner. The funny thing is, Jensen's own chart of transistor density growth for GPUs shows that if Nvidia is not benefiting from Moore's Law, he has a Secret Santa that's packing ever-more transistors into their chips. Just that Jensen's Santa is not from the North Pole. Its home is in Northern Taiwan.

Nvidia had been in the driver's seat for more than a year. Intel was seen by many as being in a classic tech fail-whale dive. Yet by the end of the year, Intel's stock had outperformed all foundries. At IEDM, Intel's and imec's presentations showed there still plenty of life to be had by shrinking transistor footprints.

So what does The Economist know? After all, they are a general publication with little technical depth. But I think they're on to something with the Schrödinger's hypothetical cat simile, because if one parses what Moore's Law believers and deniers say, one finds they use alternative readings and extrapolations from Moore's paper to make their case. I prefer to use the version from the man who coined the term Moore's Law, Carver Mead, which boils down to: What Moore's paper means is that if we all continue to innovate as a community, our industry will grow. I don't think anyone would argue we have stopped innovating.

Geopolitical: Here's what I wrote last year, "Don't expect the geopolitical issues over semiconductors to abate in 2023. What will happen is a continued move by the big-3 chip companies to re-globalize wafer fab production." This was something most everyone expected, with China's response to Nancy Pelosi's Taiwan visit in August of 2022 including more Aerial encounters and China shutting down military communications with the US. Then in February, America shot down a spy balloon from China that had entered its airspace. This crashed diplomatic relations between the two countries.

In September, there was Huawei-gate. TechInsights had uncovered a 7nm chip made by SMIC in the new Mate 60 Pro smartphone. This was a shock to the world, who believed it was impossible to make 7nm without EUV. The shock to anyone in the litho-world was that anyone was shocked by this, as both TSMC and Intel had done 7nm without EUV five years earlier. A more important shock to some was its demonstration that sanctions don't stop progress … Sanctions only slow progress.

Then a big surprise came in November when Presidents Xi and Biden met in San Francisco. Even with Huawei-gate, geopolitical tensions started to cool. Executives I talked to who had had dinner with Xi just after, said the man looked more relaxed than in years. Since then, the military communications line has reopened and aerial intercepts are down.

Surprises: As for last year's predictions of surprises with a better-than-even chance of occurring before the end of the year:

- The American Chips Act will get bogged down over who is a true American company deserving of an award. Will it be American-based companies or global companies who produce in America?
  - It was bogged down more by bureaucracy than this. Though the bureaucracy put enough rules and regulations to be off-putting to non-American and even American companies.
- India will make a credible effort to launch in-country wafer fabrication.
  - Two important things happened: Micron's $1B investment in a test and assembly facility in Gujarat and Vedanta's doubling down on its plan to build a 300mm 28nm fab in the state after the deal with Foxconn went comatose in 2022 and then revived itself in early 2023. Executives at Vedanta do seem committed. SEMI will host a SEMICON event in the country this year, another sign that India is moving beyond the aspirational stage.
- TSMC will announce a leading-edge fab in Europe.
  - They chose Dresden.
- The Auto chip shortage will abate as demand for cars drops.
  - The Auto chip shortage did abate, however, the Auto market was strong. The expected impact of high-interest rates and low consumer confidence did not result in the macroeconomic recession as many had predicted. Even the UAW strike did little to hinder auto sales growth. However, high interest rates and sticker shock did hit the EV market, which along with Elon Musk's comments about reducing SiC content, sent a shockwave through power semiconductors.

2024: What's worrisome about the coming year is there is such a wide divergence of forecasts. At the macroeconomic level, there are those who got the downturn wrong and are just pushing the dip into 2024. There are those who have adopted firm- or soft-landing projections (i.e. something like the ex-Navy or ex-Air Force pilot landings you've experienced on airlines … in both cases you are safe). Then there a those who forecast a return from this year's strong growth to something more normal in the two-to-three percent range. Instead of adjusting to 2023's results, they are seeing a Fed that's done with interest rate hikes and may even lower them. Though this will be confounded by their seeking to not be seen as influencing the Presidential election in the United States. It's not just the US. With over 60 countries holding major elections, it's been called the biggest election year in history. Economies tend to do well in election years. So, I put myself in this Goldilocks camp, for the same reasons, plus there's not a debt ceiling crisis to worry about like last year.

Still, the worry wall to climb is that this lack of consensus is the result of far higher levels of uncertainty and hence a greater chance for the unexpected to change things. 2024 is not a year to show caution to the wind like we all did in 2021. And remember where that got us: Chips became the new toilet paper, with a glut emerging in mid-2022 and deceleration in 2023. If we play our cards right, growth in 2024 should extend into 2025.

AI will continue to be the big driver, as it breaks out of training camps in the data center and deploys in devices around the edge. The resulting volume of silicon processed and sold will be far greater than training-GPUs in the datacenter, as deployment (inference) spurs a replacement cycle in Autos, Industrial Electronics, PCs and smartphones. This will drive a macroeconomic tailwind of productivity demand. In this environment, tech works because it's the only way to drive meaningful productivity.

Geopolitical: My sense is that geopolitical tensions will ease this year because China's economy is in the doldrums. This is in part because its attempt to turn the post-WWII Western Order into a new China Order in a game of Go that surrounded the US, has instead resulted in its being surrounded by the countries around it. So drivers like Foreign Direct Investment have dried up as global capital finds friendlier places to invest, while its own consumers fail to take up the slack as they lack confidence in their social safety net. Thus, China will be kept busy by the internal fires it needs to tend to.

For semiconductors, one thing is certain: the fires driving its re-globalization beyond Taiwan and South Korea will continue. I also expect these fires to break out of the leading edge and head towards essential technologies in fab, test, and packaging.

Surprises: As for my prediction of surprises with a better-than-even chance of occurring between now and the end of the year:

- Metaverse: will 2024 be the year? It's certainly set to be a great conflict between Apple's Vision Pro and Meta's Quest 3. It's definitely a big question for the most valued company in the universe: Can it change a dead market without Steve Jobs' vision? I don't think so, because the barrier to it being a large silicon-demand driver like the smartphone is competition for screen-time share. Smartphones and tablets grew timeshare because screens were systematically smaller and unplugged. While they took time from plugged-in screens, they grew the screen-time pie by displacing print media. You hardly ever see anyone reading paper media anymore and the paper media publishers are attempting to push you to subscribe online. So where's the time to play in metaverse going to come from? Most likely the time will be taken from other screens. Then it's likely like tablets, where at first we'll see them in the wild a lot. Then people will get tired of carrying them around and revert to pocketable smartphones like they did when they displaced books and magazines with phones. So AR/VR will remain a niche this year.
- EV growth will continue to be slower than expected, which will weaken power semiconductor demand. It's a combination of price, interest rates, range anxiety, and lack of charging infrastructure.

## REFERENCES

1. M. P. Brown and K. Austin, *The New Physique*, Publisher City: Publisher Name, 2005, pp. 25-30.
2. M. P. Brown and K. Austin, *Appl. Phys. Letters* **85**, 2503-2504 (2004).

# New Directions For Optical Critical Dimension Metrology

Nigel Smith, Alex Boosalis, Mark Carr, Yiliang Liu, Pedro Vagos & G. Andrew Antonelli

*Onto Innovation*
*9025 NE Von Neumann Drive*
*Hillsboro, OR 971 USA*
*e-mail: Nigel.Smith@ontoinnovation.com*

## INTRODUCTION

Scatterometry offers non-destructive optical measurement of many dimensional parameters of interest for semiconductor process control. For brevity these techniques are referred to as “Optical Critical Dimension” or “OCD” and are commonly based on either single-wavelength or spectral ellipsometers with a very narrow range of incident angles. The probe beam in these instruments is relatively large and has indistinct edges, and as the dimensions of patterned arrays within devices inevitably shrinks it becomes necessary to reduce the probe region to avoid overlap with the array edges and resulting measurement error. Reducing the probe diameter of these instruments below 20µm to match the array dimensions without compromising other essential instrument properties is very difficult, and it becomes necessary to consider different approaches.

## INSTRUMENT DESCRIPTION

An imaging system provides a simple means of achieving a small probe region. In a microscope, the size of the illuminated region is controlled by the field stop and the magnification of the objective, unless limited by the resolution of the lens system. The smallest probe is achieved by using the highest illumination numerical aperture (NA). If the NA is close to 1, then the diffraction-limited spot size is of the same order as the wavelength of the incident light. Limiting the field size to at least twice the diffraction limit avoids variation of probe size with wavelength and so probe dimensions as small as 2µm are feasible with visible light operation. In the current instrument (figure 1(a)) the probe size is 4.9µm. A small probe allows measurement inside arrays and investigation of the variation of pattern dimensions close to the array edges (figure 1(b)).

A high NA microscope generates a very wide range of incident angles at the sample, whereas ellipsometers have a very narrow range. In the image plane, the microscope mixes the incident and reflected angles together making analysis at the very least difficult. Reflected light at each angle of incidence and azimuth angle is directed to a single point in the objective pupil plane. However, rather than the single pair of angles detected by an ellipsometer, the pupil plane contains all incidence angles up to the aperture stop in the illumination path, and all azimuth angles. The available data is therefore much richer than that from even multiple angle ellipsometers.

Detection of the signal intensity in the pupil plane when a narrow bandwidth light source is used is a well-known technique [1]. The data can be extended to multiple wavelengths at the expense of increased measurement time by tuning the light source to multiple different wavelengths. Combining the method with interferometry gives access to the amplitude and phase of the reflected signal and advantageously increases the amount of information obtained.

Interference can be introduced externally to the imaging path [1] or within it. If a broad bandwidth light source is used, then spectral information can be extracted by frequency analysis of the signal change as the path difference is varied [2]. In a high NA optical system, the diameter of the probe region changes rapidly with defocus and so any path difference scanning must be achieved while at constant focus, dictating use of an interferometer configuration such as Linnik rather than Mirau (figure 2).

## SIGNAL ANALYSIS

Fourier analysis of the pupil intensity with interferometer path difference allows extraction of the sample spectral reflectance, as shown in figure 3. The standard method for performing critical dimension measurement using scatterometry finds the best fit between a rigorous electromagnetic model of light scattering at the sample and the experimental data (figure 4). The model must be calculated at each wavelength, azimuth and angle of incidence and must allow for the influence of the instrument on the signal, typically by dividing the signal by a reference signal obtained from a well-controlled film sample, such as a thin film of silicon dioxide. The model may be pre-calculated or determined on demand.

The pupil image diameter is approximately 200 pixels and, depending on scan length, there are 100 or more wavelength samples, so that the complete data set contains millions of points (figure 5(a)) rather than the 200-1000 points used by conventional ellipsometers. Reducing the number of data points speeds up analysis. Reduction selects the points contributing most to result quality, defined for example as the best measurement precision and sensitivity, generating the set of points shown in figure 5(b). This data set includes points from many different wavelengths and angles that would not be available to traditional instruments.

## RESULTS

An example showing correlation between measurements and CD-SEM values for a simple structure is shown in figure 6. The measurement precision (3 times standard deviation) of the scatterometry measurement is indicated. The uncertainty of the SEM measurement is unknown.

Measurement precision for a range of measurement parameters is shown in figure 7. Currently, experimental data is available for only some parameters. There is a large range in both the experimental results and in the corresponding simulated values, which assume only random noise in the measurement signals. Hardware noise such as light source fluctuation and vibration will be present in the experimental results, so that the simulated values are guides only.

## CONCLUSION

Performing scatterometry measurements in the back focal plane of a white light interferometer has been shown to be a viable OCD technique, using familiar model fitting techniques, and with a much smaller probe diameter than other means. Improvements in measurement uncertainty are desirable. The need to operate with a limited number of data points because of the time required to simulate signals undermines the advantage of having data at a very wide range of azimuth and incident angles. Leveraging this rich data is desirable and will be achieved through improvements in the methods used for signal analysis.

### REFERENCES

[1] J. T. Fanton, J. Opsal, D. L. Willenborg, S. M. Kelso and A. Resenwaig, "Multiparameter measurements of thin films using beam-profile reflectometry," *J. Apply. Phys.,* vol. 73, no. 11, pp. 7035-7040, 1993.

[2] J. Jung, Y. Hidaka, J. Kim, M. Numata, W. Kim, S. Ueyama and M. Lee, "A breakthrough on throughput and accuracy limitation in ellipsometry using self-interference holographic analysis," in *Proc. SPIE 11611, Metrology, Inspection, and Process Control for Semiconductor Manufacturing XXXV*, 2021.

[3] X. Colonna de Lega, M. Fay, P. de Groot, B. Kamenev, J. R. Kruse, M. Haller, M. Davidson, L. Miloslavsky and D. Mills, "Multi-purpose optical profiler for characterization of materials, film stacks, and for absolute topography measurement," in *Proc. SPIE 7272*, 2009.

### KEYWORDS

Optics, Metrology, Interferometry, Ellipsometry, Scatterometry, Semiconductor

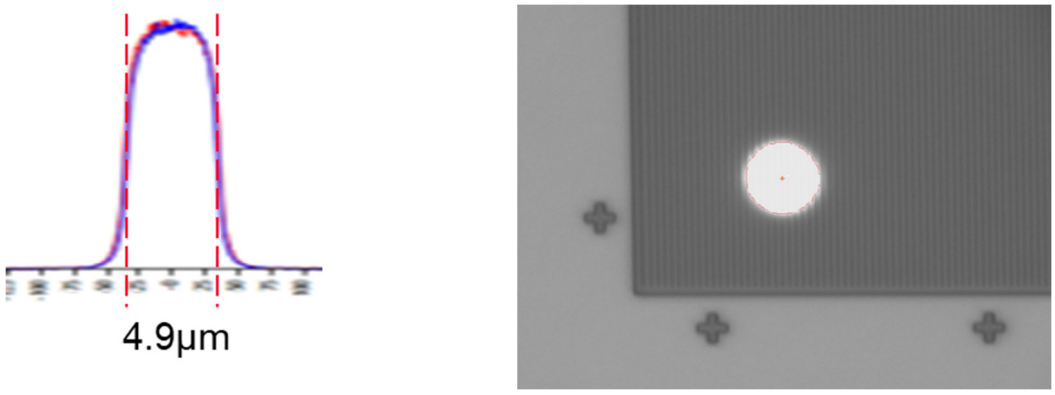


(a) intensity cross-section (b) superimposed on 360nm pitch grating target

**FIGURE 1.** Probe spot and sample image.

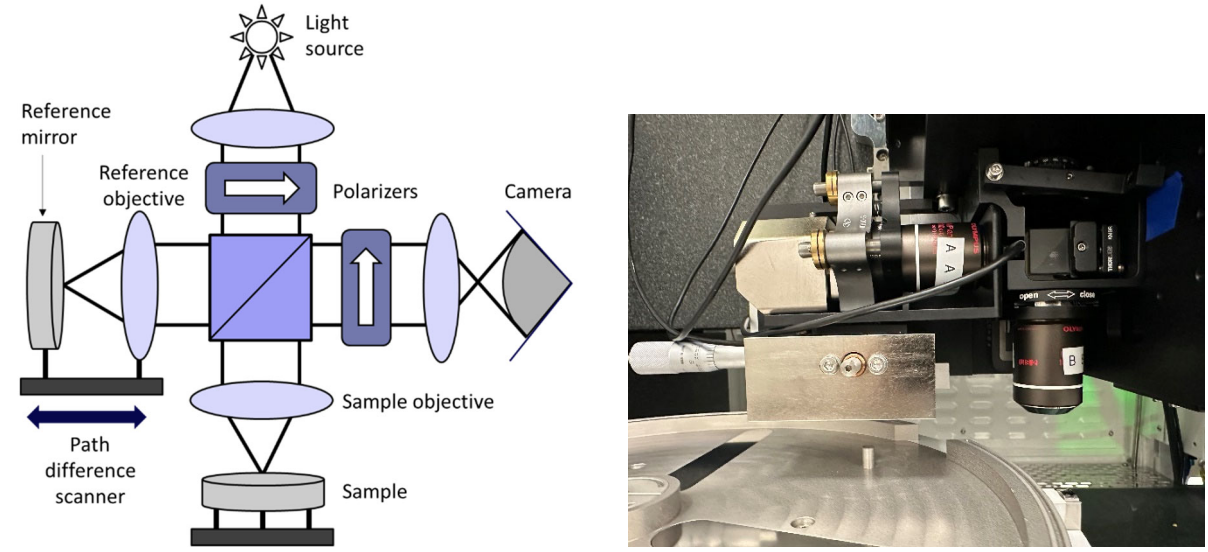


(a) Instrument layout with Linnik interferometer. (b) The Linnik assembly with the reference arm scanner at the bottom

**FIGURE 2.** The instrument.

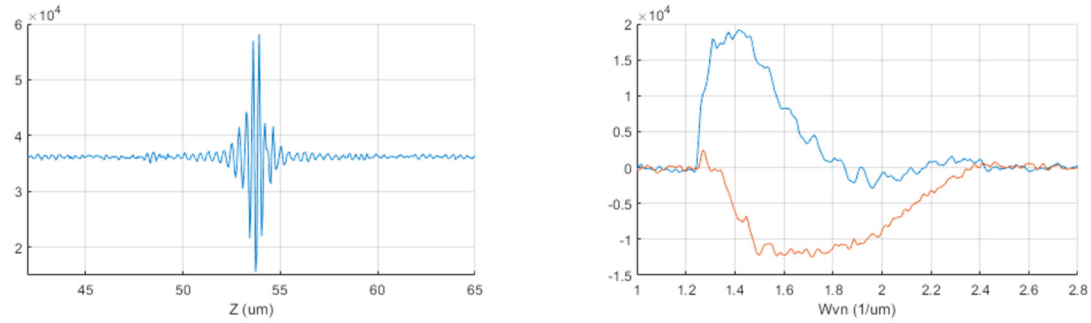


(a) Signal vs. path difference at one pixel in the pupil plane (b) Real and imaginary components of reflectance vs. wavenumber at the same pixel

**FIGURE 3.** Interference signal and complex reflectance at one pixel.

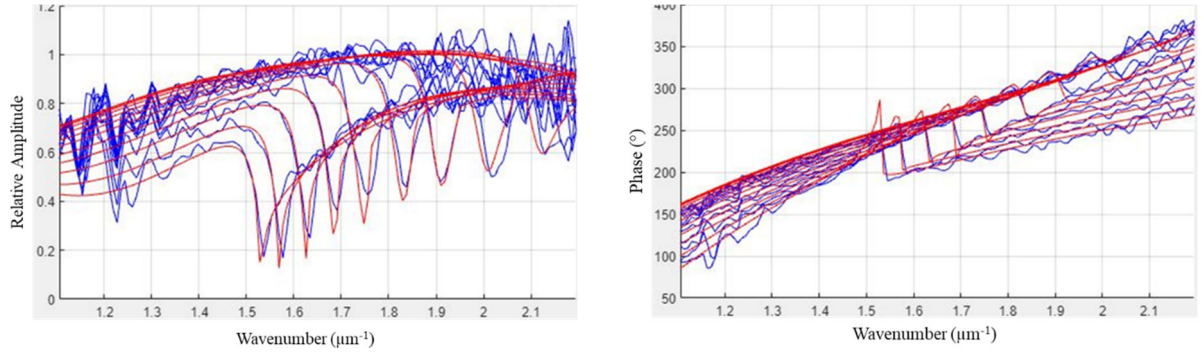


(a) Signal and model amplitude. (b) Signal and model phase.

**FIGURE 4.** Signal and model at one pixel.

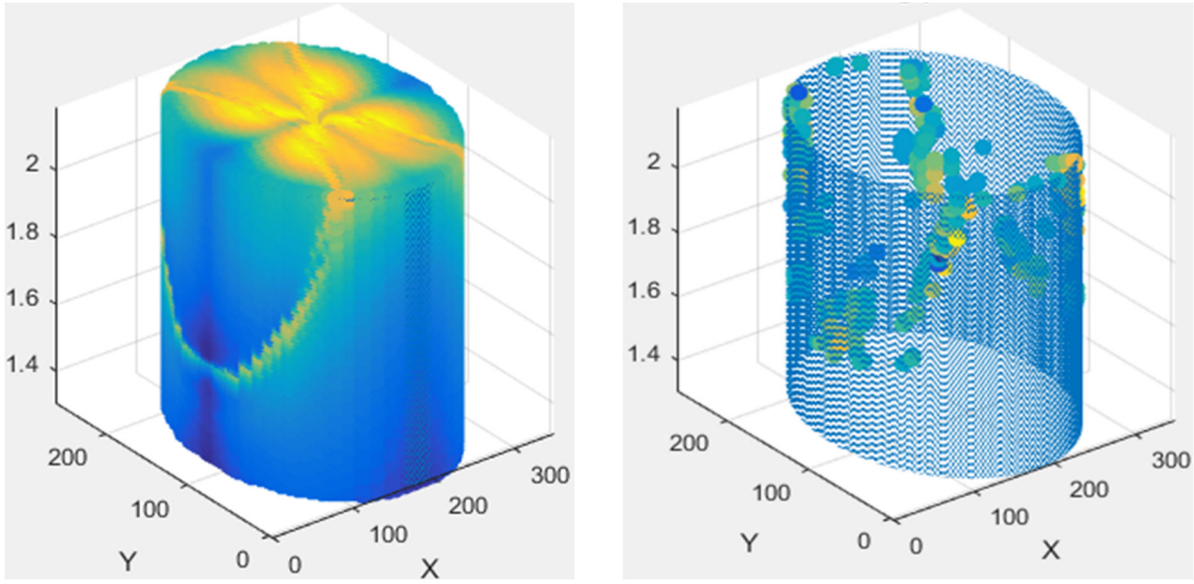


(a) All data points (b) After selecting the best 300 data points

**FIGURE 5.** Reducing the total number of data points. The vertical axis is wavenumber (μm$^{-1}$) and color represents sensitivity to parameter change.

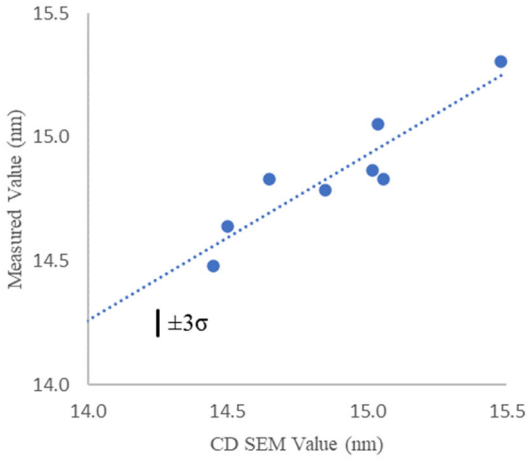


**FIGURE 6. M**easurement correlation to CD-SEM.

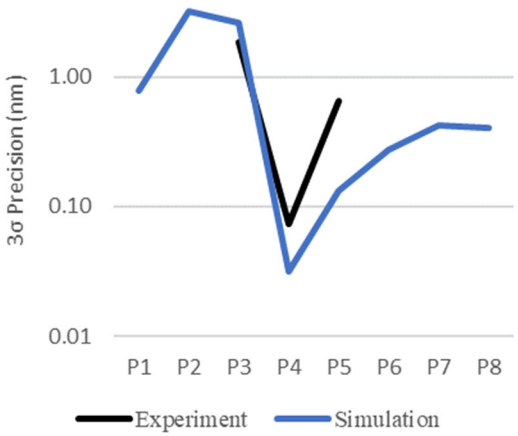


**FIGURE 7.** Precision (log scale) for eight parameters**.**

# Soft X-Ray scatterometry for 3D CD metrology on individual GAA nanosheets

Christina Porter[1], Teis Coenen[1], Loes van Rijswijk[1], Sandy Scholz[1], Jeroen Ploegmakers[1], Deepak Nayak[1], Sumin Lim[1], Juliane Reinhardt[1], Ricarda Wohrwag[1], Niels Geypen[1], Rafael Peretti Pezzi[1], Arjen Vermeer[1], Rik van Laarhoven[1], Argyri Giakoumaki[1], Victoria Flint[1], Spike Cai[1], Axel von Sydow[1]

1. *ASML, De Run 6501, 5504 DR, Veldhoven, The Netherlands*

Aritra Mandal[2], Andre Miller[2], Ayan Das[2], Navnit Agarwal[2], Tuyen Tran[2]

2. *Intel, 2501 NE Century Blvd., Hillsboro, Oregon 97124 USA*

## INTRODUCTION

Nanoscale devices have increasingly complex 3D geometries which require revolutionary metrology techniques. Upcoming gate all around (GAA) devices (i.e. nanosheets, forksheets, and CFETs) pose new profile metrology challenges for which there is not yet any established HVM metrology solution due to their complex 3D profiles. Also in DRAM, as feature sizes shrink, it is becoming increasingly difficult to measure the profiles of features with adequate precision. Traditional inline metrology techniques such as optical critical dimension (OCD) metrology face significant challenges characterizing these devices, suffering from low sensitivity and increasingly difficult parameter correlations, particularly when individual nanosheet parameters are of interest as opposed to average properties of all sheets. Transmission electron microscopy can provide accurate and useful information, but it is destructive and slow, making it undesirable in HVM. Thus, a variety of emerging technologies and hybrid combinations of multiple techniques such as OCD, AFM, CD/HV-SEM, XRD, and Raman spectroscopy are under investigation in the semiconductor industry [1].

Soft x-ray (SXR) scatterometry using 10-20 nm wavelength light is a promising next-generation metrology technique for 3D CD metrology and edge placement error (EPE) applications, with the outlook to have sufficient throughput for HVM. [2] This wavelength regime offers unique benefits over existing optical metrology tools today:

(a) It enables measurement of fully design rule compliant features.

(b) SXR provides optimal material contrast, with strong enough scattering to detect small features in devices and weak enough scattering to lessen the crosstalk due to material dispersion with respect to optical CD metrology.

(c) SXR provides 3D capability, with stack heights of up to several hundred nanometers supported and depth information collected in a single shot due to the use of a broadband source and sensor.

(d) SXR gives strong decorrelation between parameters, allowing many parameters of interest to be extracted accurately and simultaneously (such as individual nanosheet CDs and layer thicknesses, grating tilts, and edge placement errors).

In this work, we explore SXR metrology in simulation as well as on an experimental system. We present simulation and measurement results showing strong sensitivity to individual nanosheet parameters of interest, focusing here on sheet and gap heights at the nanosheet release step of an upcoming Intel gate all around process.

# 3D PROFILE METROLOGY ON GAA DEVICES

A unique benefit of SXR metrology is excellent parameter decorrelation as compared to visible light. We simulate a realistic SXR source, illuminator and sensor with shot noise and ideal parameter inference. We find 3σ <0.1nm static reproducibility should be achievable for individual nanosheet and gap heights at nanosheet release with 0.5 sec exposure at current SXR source power levels. This is due to the excellent decorrelation in the signal, visible in the correlation matrix in the center panel of Figure 1. Note that here a diagonal matrix is ideal, and pale colors off diagonal indicate low correlation between parameters. This matrix compares very favorably to metrology using visible wavelengths, where many elements would be expected to take on values much closer to ±1, indicating undesirably high crosstalk between parameters of interest.

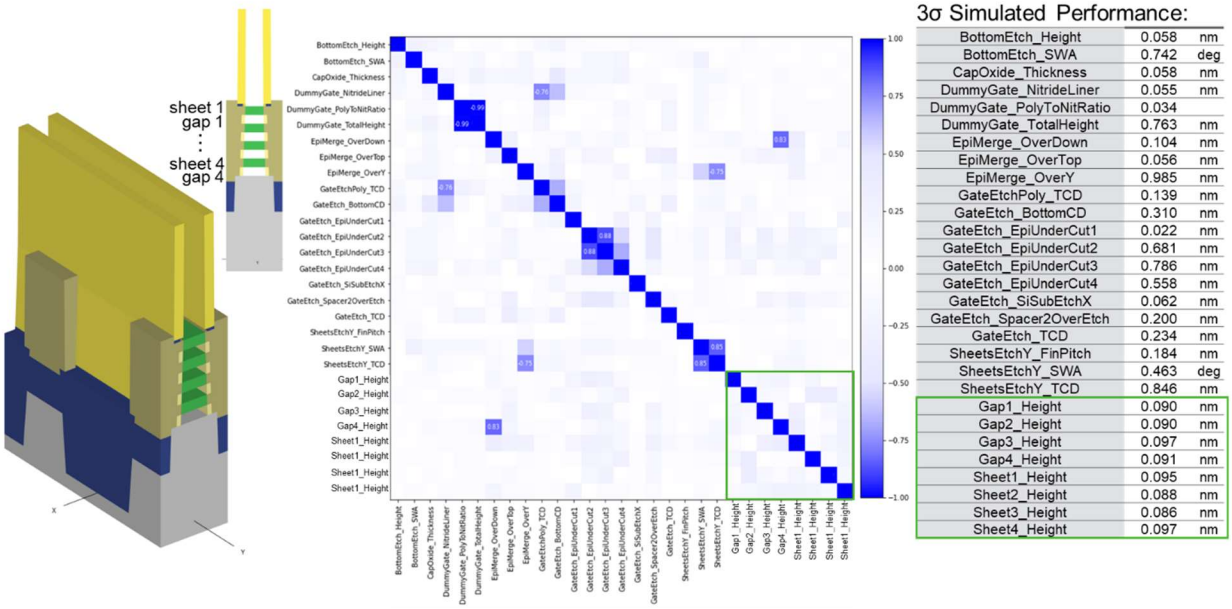


3σ Simulated Performance:

| | | |
|---|---|---|
| BottomEtch_Height | 0.058 | nm |
| BottomEtch_SWA | 0.742 | deg |
| CapOxide_Thickness | 0.058 | nm |
| DummyGate_NitrideLiner | 0.055 | nm |
| DummyGate_PolyToNitRatio | 0.034 | |
| DummyGate_TotalHeight | 0.763 | nm |
| EpiMerge_OverDown | 0.104 | nm |
| EpiMerge_OverTop | 0.056 | nm |
| EpiMerge_OverY | 0.985 | nm |
| GateEtchPoly_TCD | 0.139 | nm |
| GateEtch_BottomCD | 0.310 | nm |
| GateEtch_EpiUnderCut1 | 0.022 | nm |
| GateEtch_EpiUnderCut2 | 0.681 | nm |
| GateEtch_EpiUnderCut3 | 0.786 | nm |
| GateEtch_EpiUnderCut4 | 0.558 | nm |
| GateEtch_SiSubEtchX | 0.062 | nm |
| GateEtch_Spacer2OverEtch | 0.200 | nm |
| GateEtch_TCD | 0.234 | nm |
| SheetsEtchY_FinPitch | 0.184 | nm |
| SheetsEtchY_SWA | 0.463 | deg |
| SheetsEtchY_TCD | 0.846 | nm |
| Gap1_Height | 0.090 | nm |
| Gap2_Height | 0.090 | nm |
| Gap3_Height | 0.097 | nm |
| Gap4_Height | 0.091 | nm |
| Sheet1_Height | 0.095 | nm |
| Sheet2_Height | 0.088 | nm |
| Sheet3_Height | 0.086 | nm |
| Sheet4_Height | 0.097 | nm |

**FIGURE 1.** Left: Simulated GAA stack at nanosheet release. Middle: Parameter correlation matrix showing decorrelation between the nanosheet parameters of interest (darker color indicates stronger crosstalk between parameters in off-diagonal elements). Individual sheet and gap heights are in the green box. Right: Simulated SXR performance (3σ) due to photon shot noise, with 0.5 sec exposure time at current power levels, assuming ideal tool calibration.

We additionally present measurement results from Intel devices as shown in Figure 2. Figure 2 (left) shows a diffraction pattern measured on our soft x-ray testbench. Figure 2 (right) shows set-get response on the individual nanosheet and gap heights. We build a data driven inference model from measurements of 18 fields on 6 wafers with individual nanosheet heights perturbed during the deposition of the mandrel, then processed up to the nanosheet release step. We additionally train on one wafer with an unperturbed mandrel deposition, but an increased etch time at nanosheet release (the real control case for this layer). We find good sensitivity to the sheet and gap heights for all sheets and gaps, with an average $R^2$ and slope >0.85 on non-edge fields, on 4 measured target types with varying pitch, fin CD, and presence or absence of epi.

Finally, though we do not yet have TEM data from these wafers and are thus only training to the programmed *nominal* set values per wafer, we can investigate the get delta from set as a function of wafer position, where we expect that a significant portion of our get error should be due to wafer fingerprint. As shown in Figure 3, we see wafer fingerprints that appear consistent for different target types. Set-get accuracy of the inference model will be further verified with TEM references in the follow-up of the current work.

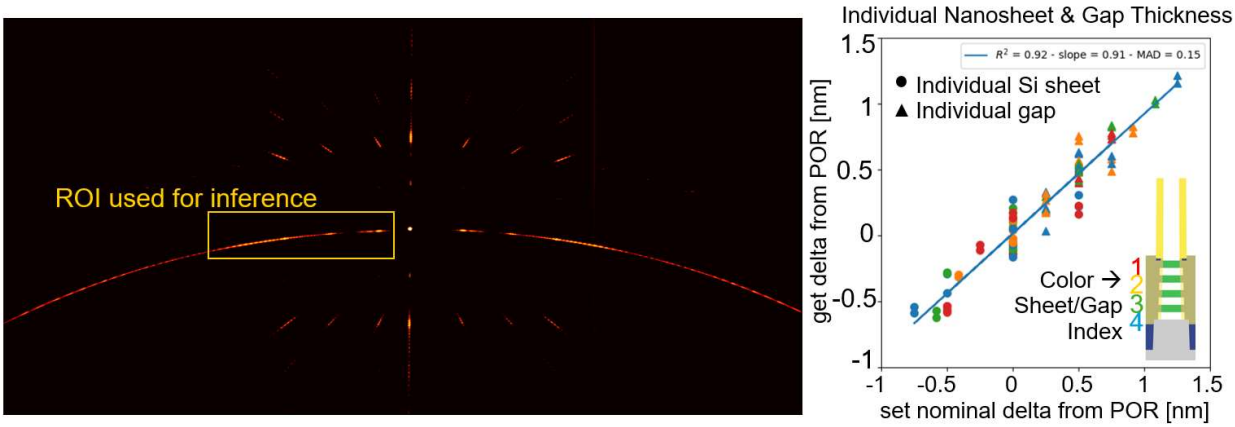


**FIGURE 2.** Left: Measured HDR diffraction image from GAA stack at nanosheet release. Right: Set-get inference results on individual nanosheet and gap heights. Model is trained on measurements of 17 fields on 6 wafers with programmed sheet and gap height variations, then tested on an 18th field on all wafers.

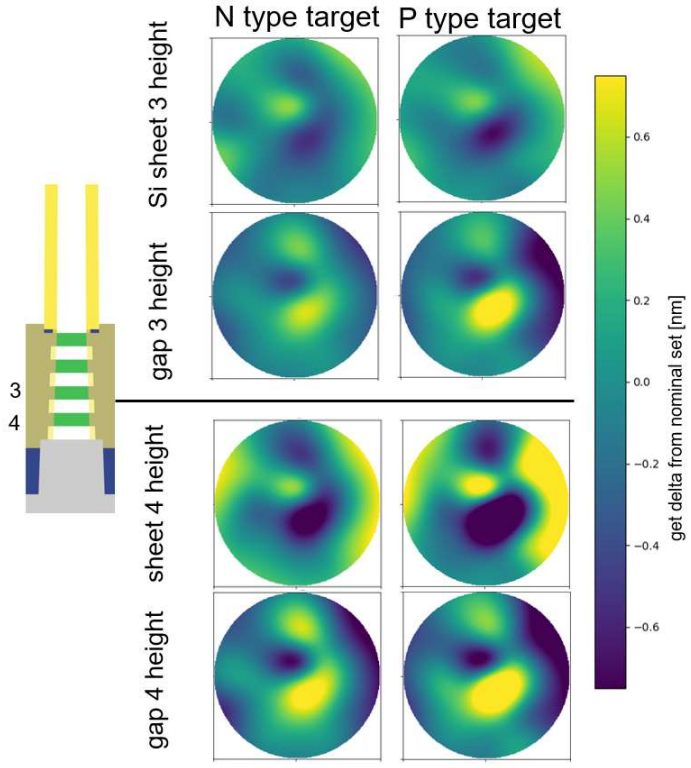


**FIGURE 3.** Interpolated wafer fingerprints for the POR wafer (based on the 18 measured fields), with small mean get error subtracted per plot such that intra-wafer variations can be easily compared. N and P type targets show consistent fingerprints for both sheet 3 and 4, in this example. A strong anti-correlation between the fingerprints for gap and sheet heights can be observed.

## REFERENCES

1. M. A. Breton *et al.*, *Proc. SPIE 11611, Metrology, Inspection and Process Control XXXV,* 116111R (2021).
2. C. Porter *et al.*, *Proc. SPIE 12496, Metrology, Inspection and Process Control XXXVII, 1249611 (2023).*

## KEYWORDS

Metrology, Scatterometry, EUV, OCD, Profilometry, 3D CD Metrology

# Overview Of Critical Dimension Small Angle X-ray Scattering (CD-SAXS)

G. Freychet[1]

[1]*Univ. Grenoble Alpes, CEA, Leti, F-38000 Grenoble, France*

## INTRODUCTION

Critical Dimension Small Angle X-ray Scattering (CD-SAXS) have been explored for more than two decades. Starting with the need of new characterization methods with sub-nm resolution to accompany the component size reduction produced by the semiconductor industry over the year, Jones et al. performed the first CD-SAXS experiment at the synchrotron in the early 2000s [1]. The promising results combined with the potential high resolution of the technique and the constantly search for new metrologies capable of a non-destructive evaluation of three-dimensional (3D) nanoscale patterns lead to the first apparition of CD-SAXS in the International Technology Roadmap for Semiconductors roadmap (ITRS) in 2007 [2]. It was first listed as a candidate next generation CD metrology tool for future nodes. Over the past 17 years, scientists have explored experimental measurement with different sources from synchrotron to lab source, to meet industry clean room standard [3-4]. Different x-ray energy ranges were tested, from hard X-ray to soft X-ray explore new material generations such as Block copolymers or Extreme Ultra-Violet (EUV) resist [5-8]. In addition, various geometries were explored, from transmission to grazing-incidence (GI) and grazing-transmission (GT) geometries [9-10]. The main effort over the years was to enable CD-SAXS measurement in laboratories. The main constrain was around the x-ray source and more specifically the need to go through a standard 700 µm-thick Silicon wafer. Widely spread Cu-Kα x-ray sources (8.047 keV) have too low energy/flux to be used in the transmission configuration with more of 99.9% of the x-rays absorbed by the substrate. New laboratory high-energy sources, such as liquid-metal jet, were developed to improve brightness in compact electron-impact x-ray sources [3]. These developments have enable the commercialization of CD-SAXS instruments and CD-SAXS is now routinely used to characterizer structures such as 3D NAND and DRAM. These tall nanostructures give strong scattering which helps overcoming the still limited flux of the current x-ray sources and further development are still needed to enable the study of finFETS at the lab.

## CRITICAL DIMENSION SMALL ANGLE X-RAY SCATTERING

CDSAXS experiments consist of collecting scattering pattern at various angles in order to access the in-depth information of the lines. As illustrated on figure 1a, the sample is mounted on a rotation stage, with line gratings aligned parallel to the axis of rotation, y. The data collected at various φ angles (usually ranging from -60 to 60 degrees with 1 deg step) are then converted to a reciprocal space map (RSM). Figure 1b shows an example of RSM where several peak orders can be observed, the horizontal intense line on figure 1b. These peaks come from the periodic spacing, also named pitch, between lines (the $q_x$-spacing being equal to $2\pi/\text{pitch}$). In this example, the pitch is equal to 112 nm. The intensity profiles of the eleven first orders are presented in figure 1c. The intensity modulations are coming from the Fourier Transform of the in-depth profile of the lines. The CD-SAXS is an inverse method, meaning you do not image directly your object but only collect information on the amplitude of its Fourier Transform. The procedure to extract the in-depth profile of the line is to use an inverse iterative approach. The in-depth line profile can be approximated using a set of parameters and will be iterated until a satisfactory match between the simulated and measured diffraction intensities is obtained.

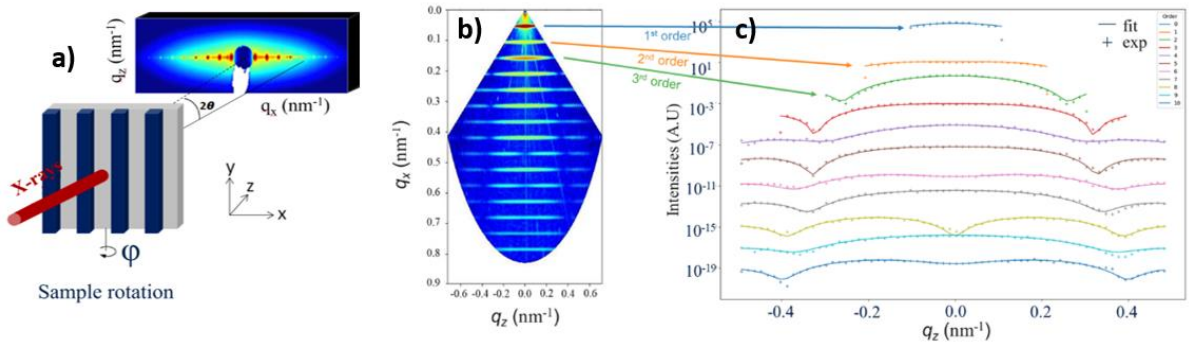


Figure 1: a) CD-SAXS geometry with the grating oriented parallel to the y-axis; b) Reciprocal space map obtained from a rotation of the samples from -60 to 60 degrees with 1-degree step; c) The intensity profiles along $q_z$ for the different Bragg orders. The crosses represent the experimental data points and the plain line the results of simulations (credit to [11]).

The in-depth profile of patterned line gratings can vary significantly depending on the patterning process, with for example very asymmetric profiles in the case of multiple patterning processes. However, a generic description of the profile as a stack of trapezoids enable to describe a wide range of shapes. As illustrated on figure 2a, each trapezoid is described by a left sidewall angle $\beta_l$, a right sidewall $\beta_r$, a height h, and a bottom width $\omega_0$. By varying the number of trapezoids and these combinations of parameters, this model enable to reproduce a wide range of shape. The Fourier transform of a trapezoid can be expressed as:

$$F(q_x, q_z) = \frac{1}{q_x}\left[-\frac{m_1}{t_1}\, e^{-i\,q_x\left(\frac{\omega_0}{2}\right)}\left(1 - e^{-i\,h\left(\frac{q_x}{m_1}+q_z\right)}\right) + \frac{m_2}{t_2}\, e^{-i\,q_x\left(\frac{\omega_0}{2}\right)}\left(1 - e^{-i\,h\left(\frac{q_x}{m_2}+q_z\right)}\right)\right] \qquad (1)$$

With $m_1 = \tan(\beta_l)$, $m_2 = \tan(\pi - \beta_r)$, $\omega_0$ is the bottom linewidth and $h$ is the height. With this efficient methodology to calculate the expected signal of the CD-SAXS, the approach is to use the $q_x$, $q_z$ and intensity values extracted from the experimental data as an input and run a minimization process between the simulated and experimental data. While the first CD-SAXS models used very basic shape, the CD-SAXS methodology have benefited from the improvement of algorithms and computing resources to become more robust and converge more efficiently and with more certainty toward the best line profile. Hanon *et al.* demonstrated that a covariance matrix adaptation is the most efficient combination of algorithm and goodness of fit criterion for finding structures with little foreknowledge of the grating [12, 13]. Coupled with a Monte Carlo Markov chain algorithm to extract the uncertainty of each parameter of the model, CD-SAXS methodology enable a robust extraction of the in-depth profile that can be correlated to direct imaging such as cross-section TEM to validate the extracted model, as illustrated on figure 2b.

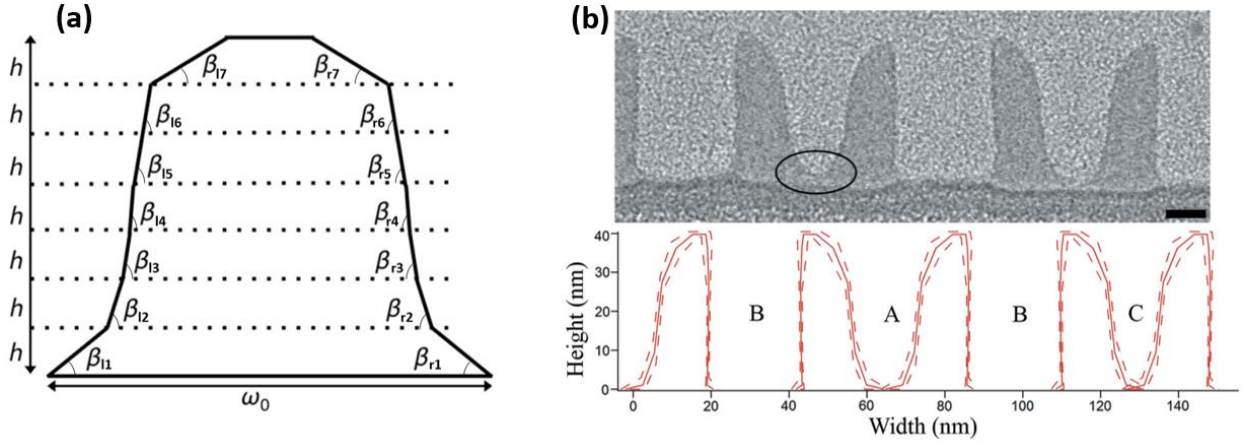

Figure 2: a) (credit [10]) CD-SAXS geometry with the grating oriented parallel to the y-axis; b) (credit [4]) On top, a epresentative cross-sectional TEM image of a line grating patterned using the pitch quartering scheme, showing the asymmetric structure and variable spacing between lines. The ellipse highlights the extra material between the line pair separated by narrower spacing. The scale bar indicates 10 nm. At the bottom, the corresponding best fits to the scattering profile.

## PERSPECTIVES

While significant progress were made over the last two decades, remaining challenges for CD-SAXS are remaining. The first one is the development a of CD-SAXS laboratory equipment enabling the study of few nanometers tall objects. Two directions are currently explored: the development of brighter compact x-ray sources with an increase of an order of magnitude more photons required; the exploration of the use of soft x-ray sources to enable the reflection geometry with a relatively high incident angle (several degrees) to keep the footprint of the beam small in the samples. Both approached present significant challenges that will need to be tackled in the coming year to enable the CD-SAXS to be really integrated to control different stages of lithography process. Moreover, there is a need to continue the exploration of CD-SAXS capabilities to obtain information on line roughness, overlay as well as positioning the role and ability of CD-SAXS to help answering future challenges of metrology for the future nodes [14].

## REFERENCES


1. R. L. Jones, T. Hu, E. K. Lin, W.-L. Wu, R. Kolb, D. M. Casa, P. J. Bolton,G. G. Barclay, Appl. Phys. Lett., 83, 19, 4059–4061 (2003).
2. ITRS, International Technology Roadmap for Semiconductors, https://www.itrs.net/ (2013).
3. R.J. Kline, D.F. Sunday, D. Windover, B.D. Bunday, *J. MicroNanolithography MEMS MOEMS*, **16**, 014001 (2017).
4. D. F. Sunday, S. List, J. S. Chawla, and R. J. Kline, J. Appl. Crystallogr., 48, 5, 1355–1363 (2015).
5. D.F. Sunday, M.R., Hammond, C., Wang, W., Wu, D. Delongchamp, M., Tjio, J.Y., Cheng, J.W., Pitera and R.J. Kline, *ACS Nano*, **8**, 8426–8437 (2014).
6. D.F. Sunday, F. Delachat, A. Gharbi, G. Freychet, C.D. Liman, R. Tiron and R.J. Kline, *J. Appl. Crystallogr.*, **52**, 106–114 (2019).
7. G. Freychet, I.A. Cordova, T. McAfee, D. Kumar, R.J. Pandolfi, C. Anderson, S.D. Dhuey, P. Naulleau, C. Wang and A. Hexemer, *J. MicroNanolithography MEMS MOEMS*, **18**, 2 (2019)
8. W-L. Wu, R.J. Kline, R.L. Jones, H-J. Lee, E.K. Lin, D.F. Sunday, C. Wang, T. Hu, C.L. Soles, *J. MicroNanolithography MEMS MOEMS*, **22**, 3, 031206 (2023).
9. X. Lu, K. G. Yager, D. Johnston, C. T. Black and B. M. Ocko, *J. Appl. Cryst.*, **46**, 165-172 (2013).
10. G. Freychet, D. Kumar, R.J. Pandolfi, P. Naulleau, I. Cordova, P. Ercius, C. Song, J. Strzalka and A. Hexemer, *Phys. Rev. Appl.*, **12**, 044026 (2019).
11. T. Choisnet, A. Hammouti, V. Gagneur, J. Reche, G. Rademaker, G. Freychet, G. Jullien, J. Ducote, P. Gergaud and D. Le Cunff, Robinson, *Metrol. Insp. Process Control XXXVII, SPIE*, 52 (2023).
12. F. Hannon, D. F. Sunday, D. Windover, and R. Joseph Kline, *J. MicroNanolithography MEMS MOEMS*, **15**, 3, 034001 (2016).
13. D.F. Sunday, S. List, J.S. Chawla, R.J. Kline, *J. Micro/Nanolith. MEMS MOEMS*, **15** (1), 014001 (2016).
14. J. Reche, P. Gergaud, Y. Blancquaert, M. Besacier and G. Freychet, *IEEE Trans. Semicond. Manuf.*, **35**, 425–431 (2022).


## KEYWORDS

Critical-Dimension small angle x-ray scattering (CD-SAXS), GISAXS, Nanostructure, Compact x-ray sources, Synchrotron

# Understanding The Damage And Microstructural Evolution In Cu Metallizations During Thermo-mechanical Fatigue

Michael Reisinger[a], Laura Neumann[b], Tobias Ziegelwanger[c], Sebastian Moser[a], Kristina Kutukova[d], Bartlomiej Lechowski[d], Jozef Keckes[c], Ehrenfried Zschech[d,e]

[a]*KAI Kompetenzzentrum für Automobil und Industrieelektronik GmbH, Europastrasse 8, 9524 Villach, Austria*
[b]*Institute for Ceramic Technologies and Systems FhG, Dresden, Maria-Reiche-Strasse 2, 01109 Dresden, Germany*
[c]*Department of Materials Physics, Montanuniversität Leoben, Jahnstrasse 12, 8700 Leoben, Austria*
[d]*deepXscan GmbH, Zeppelin street 1, 01324, Dresden, Germany*
[e]*Brandenburg University of Technology Cottbus-Senftenberg, Konrad-Zuse-Str. 1, 03046 Cottbus, Germany*

## INTRODUCTION

In the power semiconductor industry, the increasing demands on performance and reliability require the development of novel test concepts, to understand fatigue mechanisms that govern device lifetime. Such devices are complex heterostructures, consisting of different materials with different material properties. In power applications, the thermo-mechanical fatigue of metallization layers is a significant factor for device reliability. During short circuit events, the electric power is mostly dissipated in the semiconductor device. Consequently, the device's junction temperature will rise dramatically, resulting in high thermo-mechanical stresses caused by the mismatches of the thermal expansion coefficients (CTE) of the different sublayers. These stresses can lead to plastic deformation within the metallization layer and ultimately cause material fatigue and a degradation of the functional properties [1].

A known challenge for the development of new technologies is the decrease of the device footprint, which leads to a reduction of the device area and consequently to an increased power density [1]. Hence, the basic understanding of the thermo-mechanical behavior of the power metallization layer is crucial, to improve the lifetime modeling and guarantee product reliability. Therefore, thermo-mechanical fatigue tests at application relevant conditions are needed to investigate the degradation behavior of the metallic interconnects.

In this contribution, the thermo-mechanical fatigue of Cu on Si was studied. Dedicated test chips (polyheater) were developed, to enable cyclic loading via heating pulses with heating rates up to $10^6$ K/s. Critical parameters such as maximum temperature, base temperature, heating rate as well as pulsing frequency were varied, to change the loading conditions and active degradation mechanism. Moser et al. found, that depending on the heating rate the dominant degradation mechanism switches from pore and crack formation at grain boundaries, towards dislocation-driven plastic deformation [2]. According to Kleinbichler et al, the material fatigue via pore and crack formation can be divided into 3 different substages: (I) initial pore nucleation, (II) pore growth followed by the pore coalescence to microcracks and (III) crack growth [3].

For lifetime modeling it is crucial to understand the underlying physical mechanism. This input is required to link the kinetics of the individual substages with specific loading conditions in order to achieve the goal of damage prediction. Therefore, a thermo-mechanical fatigue test concept will be presented, including cyclic loading via polyheater test chips. Synchrotron-radiation based X-ray diffraction (XRD) experiments reveal the thermo-mechanical stress within Cu metallization layers during ultra-fast heating. The material degradation was quantified using in-situ and ex-situ scanning electron microscopy (SEM). Laboratory transmission X-ray microscopy (TXM) and nano X-ray computed tomography (nano-XCT) techniques at multiple photon energies are used to visualize changes of the Cu microstructure at several cycling stages nondestructively with a resolution down to sub-100 nm in 2D and 3D.

# EXPERIMENTS AND RESULTS

## Test Structure and applied thermo-mechanical stress

Polyheater test chips are simplified microelectronic devices, to study the thermo-mechanical fatigue of Cu on Si structures (Figure 1a). The specific design enables fast cyclic heating of a Cu structure, indicated as the region of interest (ROI) using electric power pulsing. When applying voltage to the power pads (A), the electrical power is dissipated in a high resistive polysilicon layer, which heats the chip center (B) including the ROI. The temperature can be determined by resistance measurements via the sensing pads (C). Figure 1b shows a representative heating pulse, applied in the course of thermo-mechanical fatigue tests. Major pulse parameters such as base temperature ($T_{Base}$), maximum temperature ($T_{max}$), pulse length, and waiting time between two pulses are independent of each other and can be individually adjusted [4].

The thermo-mechanical stress during a heating pulse was investigated via 20 kHz XRD at the Synchrotron Radiation Facility at Paul Scherrer Institute. Using polyheater test chips, the Cu metallization was thermo-mechanically stressed and an X-ray diffraction pattern of the Cu metallization was acquired every 50 µs through the course of a single heating pulse. Subsequently, the residual stress within the Cu metallization was evaluated and linked with the corresponding temperature (Figure 1c). These measurements reveal the yield point, the maximum thermo-mechanical stress as well as the plastic deformation causing Cu metallization degradation. A comparison with standard laboratory scale wafer curvature measurements with heating rates of $10^{-1}$ K/sec show the heating rate dependency of Cu metallizations.

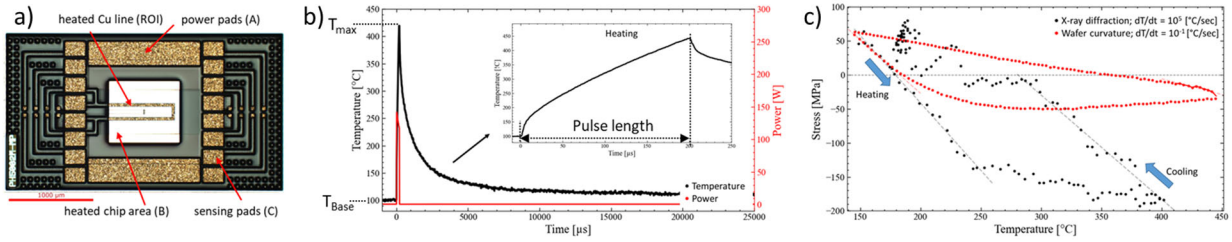


**FIGURE 1.** a) Polyheater chip used for fatigue experiments and nano-XCT. b) A representative heating and power pulse, which is cyclically applied during thermo-mechanical fatigue test. c) Evolving of the thermo-mechanical stress at different temperature during slow and fast heating experiments.

## Damage detection using 2D and 3D techniques

The microstructure changes and the damage evolution during Cu metallization fatigue was studied using SEM. A dedicated in-situ setup enables the electric contacting and testing of polyheater chips within the vacuum chamber of a SEM. In-situ image acquisition reveals changes at the surface through the course of thermo-mechanical testing (Figure 2a) [5]. Depending on the loading conditions, both described degradation mechanisms were observed. To investigate the Cu metallization interior, few micrometers of the top surface were removed using electrochemical polishing. Subsequently, the smooth surface reveals the generated damage features in 2D. Computer vision-based algorithms were used to classify these features into pores and cracks. Both defect classes are quantified and correlated with the number of applied loading cycles in order to distinguish between the three stages of the metallization fatigue (Figure 2b).

The thermo-mechanical ageing and degradation including defect evolution, e.g. microcrack propagation in polyheaters with different geometries of Cu and Si, were studied at 8.0 keV and 9.2 keV photon energies (Cu-Kα and Ga-Kα radiation, respectively). The use of Ga-Kα radiation generated from a Ga-containing target of a laboratory X-ray source applying the liquid metal-jet technology results in a significantly higher image contrast of Cu/dielectrics structures compared to the use of Cu-Kα radiation from a rotating anode X-ray source, caused by the fact that the energy of the Ga-Kα emission line is slightly higher than that of the Cu-K absorption edge (9.0 keV photon energy) [6]. Nano XCT of the selected regions of interest (ROIs) allows to visualize defects in Cu interconnects as a function of fatigue cycling. This 3D information reveals damage hot spots and provides input for the understanding of the

interaction of neighbored damage features. The vertical alignment of pores and cracks indicates the formation of complex damage networks (Figure 2c).

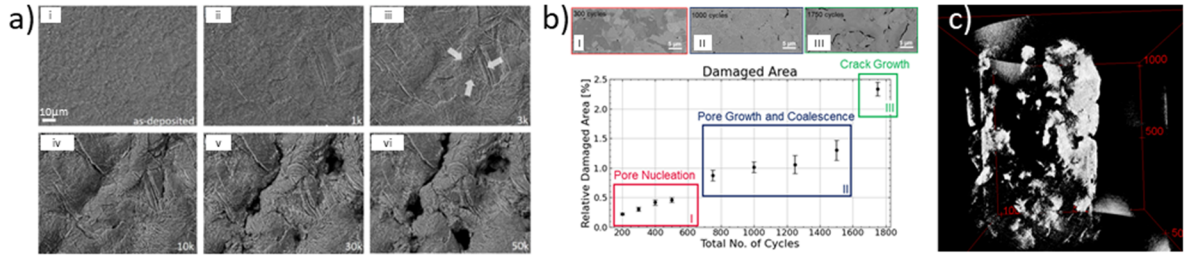


**FIGURE 2.** a) In-situ SEM images acquired through the course of a polyheater test are showing changes at the Cu metallization surface (i – vi). b) Statistical evaluation of damage features at polished Cu surfaces show sequential degradation stages (I – III). c) 3D tomography of a metallization reveals complex damage networks within the metallization volume.

## CONCLUSION

Polyheater chips are a versatile test vehicle to investigate and to understand the thermo-mechanical fatigue behavior of Cu metallizations. Due to the high thermo-mechanical stresses caused by fast heating, damage features such as pores and cracks are formed through the course of cyclic loading. The presented experimental concept shows, that a workflow requires to combine several experimental techniques to cover all aspects needed as an input to damage modeling. High-contrast laboratory nano-XCT using Ga-Kα radiation has a high potential for defect inspection and for the study of degradation processes. This knowledge is needed for the understanding of thermo-mechanical fatigue in Cu structures. Particularly, degraded Cu metallization at stage II (pore growth and coalescence) as well as stage III (crack growth) was studied with this technique with about 100nm resolution. Because of the nondestructive nature of X-ray imaging, damage networks within still functional chips can be revealed and monitored in in-situ experiments. One unique application will be the early detection of future critical defects. These kinetic studies will help to understand the defect evolution. Today, this concept is limited to simplified polyheaters with dedicated design. The recently demonstrated proof of concept of the extension of laboratory TXM in the high photon energy regime will allow to image damage in thicker Cu and Si 3D structures nondestructively [7]. Future developments of laboratory X-ray imaging techniques are targeted on defect inspection and fault isolation in semiconductor industry. Combined with in-situ attachments, degradation kinetics in and eventually failure of microelectronic products can be studied to provide valuable information to reliability engineering.

## REFERENCES

1. M. Nelhiebel, R. Illing, C. Schreiber, S. Wöhlert, S. Lanzerstorfer, M. Ladurner, C. Kadow, S. Decker, D. Dibra, H. Unterwalcher, M. Rogalli, W. Robl, T. Herzig, M. Poschgan, M. Inselsbacher, M. Glavanovics, S. Fraissé, *Microelectronics Reliability* **51**, 1927–1932 (2011).
2. S. Moser, M. Kleinbichler, J. Zechner, M. Reisinger, M. Nelhiebel, M. J. Cordill, *Microelectronics Reliability* **137**, (2022).
3. M. Kleinbichler, C. Kofler, M. Stabentheiner, M. Reisinger, S. Moser, J. Zechner, M. Nelhiebel, E. Kozeschnik, *Microelectronics Reliability* **127**, (2021).
4. S. Moser, G. Zernatto, M. Kleinbichler, M. Nelhiebel, J. Zechner, M. J. Cordill, R. Pippan, *JOM* **71**, 3399-3406 (2019).
5. K. Hlushko, T. Ziegelwanger, M. Reisinger, J. Todt, M. Meindlhumer, S. Beuer, M. Rommel, I. Greving, S. Flenner, J. Kopecek, J. Keckes, C. Detlefs, C. Yildirim, *Acta Materialia* **253**, (2023).
6. K. Kutukova, B. Lechowski, J. Grenzer, P. Krueger, A. Clausner and E. Zschech, *JEM,* submitted (2024).
7. B. Lechowski, K. Kutukova, J. Grenzer, P. Krueger, I. Panchenko, A. Clausner and E. Zschech*, Nanomaterials* 2024, **14**, accepted.

## KEYWORDS

Thermo-mechanical fatigue, X-ray microscopy, X-ray computed tomography, Cu metallization, Defect detection

# Advances In 3D Tomography And 4DSTEM: Perspectives To Study Semiconductor Devices

Nicolas Gauquelin, Daniel Arenas Esteban, Mikhail Mychinko, Andrey Orekhov, Daen Jannis, Evgenii Vlasov, Sandra van Aert, Johan Verbeeck, Sara Bals

*Electron Microscopy for Materials Research (EMAT), University of Antwerp, 2020 Antwerp, Belgium*

## INTRODUCTION

The semiconductor industry continues to produce oh smaller devices that are increasingly complex in shape and composition. The ultimate sizes and functionality of these new devices will be affected by fundamental and engineering limits such as heat dissipation, carrier mobility and fault tolerance thresholds. At present, it is unclear which are the best measurement methods required to evaluate the nanometer-scale features of such devices and how the fundamental limits will affect the required metrology. In this talk, I will review advances made to 3D electron tomography which enables morphology and composition investigations of nanostructures in 3D, even at atomic resolution. I will furthermore discuss the use of 4DSTEM, which is a method to record information in real space and reciprocal space simultaneously with atomic resolution. I will then give an example where both techniques were combined and try to give a view towards the possibilities offered by combining the two for future characterization of devices.

## ADVANCES IN 3D ELECTRON TOMOGRAPHY

Electron tomography (ET) has become an indispensable technique for the 3D characterization of nanomaterials during the last decade and has primarily been used to understand surface faceting or to accurately quantify anisotropic morphologies for nanomaterials that cannot be properly understood when using 2D imaging only.[1] In fact, even spherical morphologies cannot always be correctly interpreted from a 2D projection, as they may have a preferential orientation on a TEM grid due to some asperities. Although we ideally would like to image a NP in 3D in an angular range of 180°, within an electron microscope there is limited space above and below the sample that restrict rotation. Such a restricted rotation represents another significant challenge in ET: the so-called “missing wedge. There are several practical techniques applied to the mitigation or minimization of missing wedge artifacts for conventional ET, as well as the development of advanced reconstruction algorithms that mitigate those artifacts towards a clever interpretation of the tilt series datasets.[2] Alternatively, ET using on-axis holder has been developed to entirely remove missing wedge artifact contributions, using a precisely prepared rotation holder stub by FIB milling. This last approach has the potential to become the method of choice for understanding the ever more complex 3D structure of semiconductor device architectures when getting into the 2nm technology.[3]

Over the last decade, Multimode tomography (MMT), as the name itself implies, uses at least two different TEM techniques or “modes” to obtain projections of a specimen in 2D, which can be subsequently reconstructed to achieve a 3D multimode tomogram. Unfortunately, not every signal that can be measured within an electron microscope can be used for ET. Indeed, the collected signals must satisfy the projection requirement, meaning that the intensity of acquired images must be a monotonic function of a certain property of the sample under investigation, usually the thickness.

HRSTEM imaging combined with advanced data alignment and 3D reconstruction techniques has enabled to achieve the goal of reconstructing nanoparticle at the atomic scale, allowing for detailed analysis of crystal structure of nanomaterials and their surface faceting. The modern state of atomic resolution tomography allows for the

investigation of complex nanomaterials, e.g. where the presence of facets of high order can be carefully determined.[4] Atomic resolution tomography has been made much more straightforward by fast tomography which circumvented the significant limitation of conventional ET as it reduces the time required for acquisition of a full tilt series (≈40 min to several hours, depending on the angular increment needed) to less than a minute. [5]

Recently, an alternative technique that allows for high-resolution characterization of the surface structure without the need to acquire a full tilt series was proposed. It is based on the detection of secondary electrons in STEM that naturally convey information about the surface morphology. Given the general unavailability of SE imaging in STEM, the detection of SEs was implemented using electron beam-induced current (SEEBIC) [6]. The suggested methodology allowed to retrieve topographical information from a single image allowing a time-efficient investigation of the nanoparticles

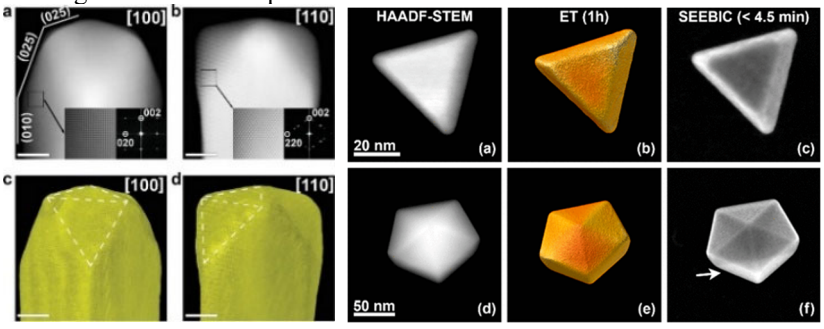


(left) Atomic resolution tomographic analysis of a gold nanorod (reproduced from ref 4) (right) HAADF stem 2D image, 3D reconstruction from ET and SEEBIC imaging of a gold nanoparticle (reproduced from ref 6)

## ADVANCES IN 4DSTEM

Recent advances in detector technology and computational methods have enabled many experiments that record a full image of the STEM probe for many probe positions, either in diffraction space or real space. These methods are commonly denominated as 4DSTEM.

We have applied those methods to 2Dmaterials to determine their orientations over mm fields of view with the SEM as well as the number of layers and presence of folds and twists.[7] For transition metal dichalcogenides (TMD) focusing on MoS2 and we have shown the possibility to determine stacking and twist angles [8-9]. These 4DSTEM analysis can even be used during in-situ measurements to retrieve structural evolution of materials as a function of electric [10] or through a phase transition with temperature [11]

The study of amorphous materials by 4DSTEM has been the subject of a lot of attention more recently as NBED-based 4DSTEM, also called fluctuation microscopy can give insights into the local order in glass materials[12]

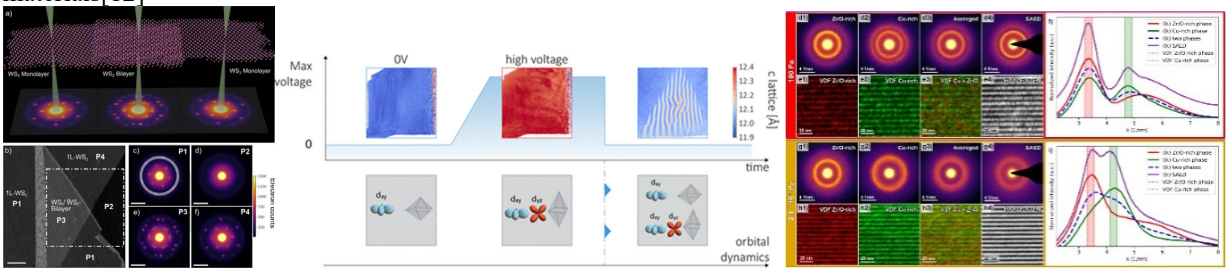


(left) Determination of twist angle between 2 WS2 layers by 4DSTEM (reproduced from ref 9) (center) structural phase transition and pattern formation by electric-field quenching in Ca2RuO4 single crystal (reproduced from ref 10) (right) 4D-STEM diffraction data for local crystal structure analysis of nanolaminated ZrCu films deposited at 100Pa and 2.1x10$^{-3}$ Pa

## 4DSTEM TOMOGRAPHY

The 4D STEM acquisition provides an entire list of possibilities for data acquisition. Classically, this technique has been used to analyze several aspect of 2D samples, from crystal structure maps to holography. The potential of implement a third spatial dimension is of tremendous interest. With the advances in high-resolution tomography, the implementation of 4D STEM dataset can potentially allow crystal analysis at the voxel level. This combined approach is even more helpful for samples composed of different elements that provide different signals. As an example, figure XX shows a recent study of a Metal Organic Framework encapsulating a gold nanoparticle for drug delivery propose. The 4D STEM approach can be used to efficiently separate the information recorded in the reciprocal space to evaluate the two sample components separately.

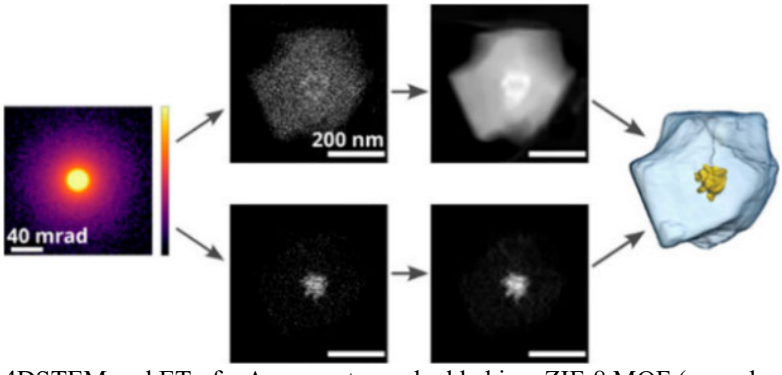


4DSTEM and ET of a Au nanostar embedded in a ZIF-8 MOF (reproduced from ref 13)

## REFERENCES

1. K. Jenkinson, L. M. Liz-Marzán, S. Bals, Adv. Mater. 34, 211039 (2022)
2. B. Goris, T. Roelandts, K.J. Batenburg, H. Heidari Mezerji, S. Bals, Ultramicroscopy 127, 40-47 (2013)
3. International Roadmap for Devices and Systems (2023)
4. B. Ni, M. Mychinko, et al., Adv. Mater. 35, 2208299 (2023)
5. W. Albrecht and S. Bals, J. Phys. Chem. C 2020, 124, 50, 27276–27286 (2020)
6. E. Vlasov, A. Skorokov, A. Sanchew-Iglesias, L. Liz-Marzan, et al., ACS Materials Lett. 5, 7, 1916–1921 (2023)
7. A. Orekhov, D. Jannis, N. Gauquelin et al., https://doi.org/10.48550/arXiv.2011.01875
8. A. Nalin Mehta, N. Gauquelin, et al., Nanotechnology 31 (44), 445702 (2020)
9. S. Psilodimitrakopoulos, …, N. Gauquelin et al., npj2D Materials and Applications, 5, 77 (2021)
10. N. Gauquelin, F. Forte, D. Jannis, et al., Nano Lett. 23, 17, 7782–7789 (2023)
11. N. Gauquelin, et al., in preparation
12. M. Ghidelli, A. Orekhov, …, N. Gauquelin, et al. Acta Mater. 213 (2021), 116955.
13. M. Hugenschmidt , D. Jannis, A. Anil Kadu, L. Grunewald et al., ACS Materials Lett. 6, 1, 165–173 (2024)

## KEYWORDS

Electron tomography, nanoparticles, 4DSTEM, 2D materials, phase transition

# Chip Scan: 3D X-ray Imaging of CMOS Circuits

A. F. J. Levi[1], Mirko Holler[2], Manuel Guizar-Sicairos[2], Tomas Aidukas[2], Walter Unglaub[1], and Gabriel Aeppli[2]

[1]*ECE, University of Southern California, Los Angeles, CA 90089-2533, USA. E-mail: alevi@usc.edu*
[2]*Paul Scherrer Institut, CH-5232 Villigen PSI, Switzerland.*

## INTRODUCTION

In the past few years there have been several advances in use of coherent X-rays for *non-destructive* three-dimensional (3D) imaging and analysis of integrated circuits. In principle, billions of CMOS transistors and their metal interconnects can be imaged using this chip scan technique. The method allows reinspection of areas of interest at different levels of resolution in 3D. Not only is this of potential interest for metrology, identification of manufacturing defects and counterfeit products, and non-destructive reverse engineering of integrated circuits, but it also enables a path to a certified trust service to ensure integrated circuits are manufactured to customer design.

Here, we review status of our work and report on a number of possible future directions for the technology.

## VIRTUAL DELAYERING OF METAL INTERCONNECTS

Electrical interconnects in integrated circuits are usually complex and hierarchical. Patterned metal layers and vias define electrical connection and they are critical to enabling circuit function. Electrical interconnect is, in effect, a static connectome. Typically, in today's commercially relevant circuits, metal layers closest to transistors fabricated near the surface of a silicon substrate are a few tens of nanometers thick and have the smallest lateral feature sizes. Circuits can be manufactured that make use of many metal interconnect layers embedded in an insulating dielectric. A typical stack from the lowest transistor layers in a silicon substrate to the top-most metal layer is more than 4 microns high and a typical chip dimension is 1 cm on a side. 3D X-ray imaging of chips with this aspect ratio is best achieved using a microscope configured in a laminographic geometry with appropriate depth of field and zoom capability. [1]

Figure 1(a) illustrates the complexity of electrical interconnect in a CMOS integrated circuit. The figure shows a 3D X-ray image of a small portion of an Intel Pentium G3260 processor manufactured in a 22 nm FinFET technology. [2]

Typical back-end-of-line fabrication processes use photolithography to define metal layers. The photolithographic masks that enable this are described using a standard GDS-II format. The masks contain circuit interconnect design information and can be mapped back to the circuit schematic. While actual manufacture of metal interconnects can deviate considerably from the GDS-II mask pattern, the topology of the intended design must be respected to remain faithful to the circuit schematic.

If the resolution and quality of the 3D X-ray image reconstruction is of sufficient fidelity, it is possible to create a topologically correct representation of a given manufactured metal layer by use of a cut through the image and appropriate image-processing. This virtual delayering process is illustrated in Fig. 1(b) and may be used to identify manufacturing errors by comparing intended design with measured X-ray images.

Advanced Gate-All-Around (GAA) nano-sheet devices are expected to have digital transistor densities in excess of 400 per square micron of substrate area. The volume taken up by each transistor *and* its local interconnect will be less than 50 x 50 x 325 $nm^3$ and detailed 3D imaging of these GAA devices will require nm resolution.

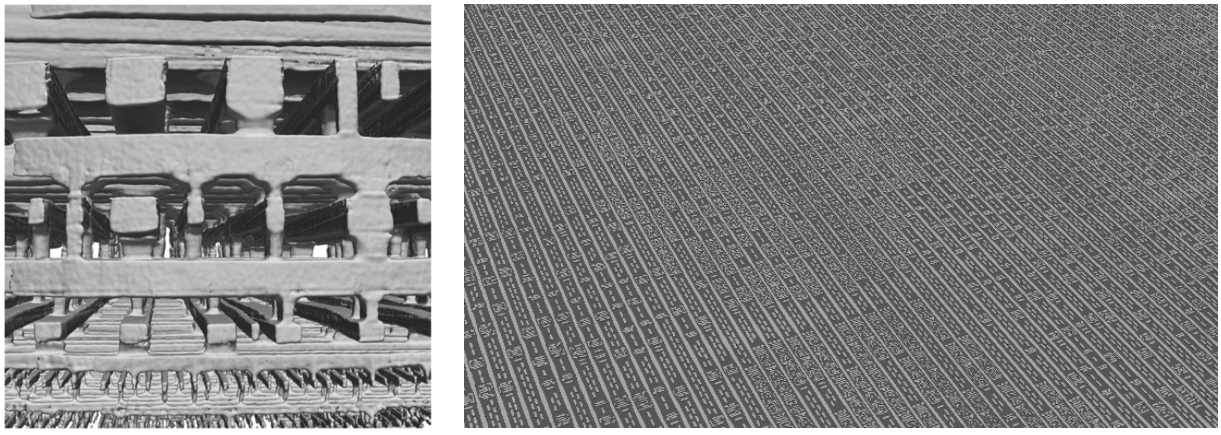

(a) (b)

**FIGURE 1.** (a) 3D-image created from coherent X-ray scattering data shows a small portion of an Intel Pentium G3260 processor manufactured in a 22 nm FinFET technology. [2] Patterned metal layers connected by vias and metal interconnect closest to transistors fabricated on the silicon substrate have smallest lateral feature size. (b) Example of a virtually delayered integrated circuit image obtained using a ptychographic X-ray laminography microscopy. The 3D aerial-view image shows metal interconnect layer M1 that is part of general-purpose logic circuitry implemented in a 16 nm CMOS FinFET technology. Pitch of the long metal lines is 576 nm.

## RESOLUTION AND SCAN TIME

3-D X-ray image resolution and the time it takes to complete a chip scan are not unrelated. Achievable resolution depends on X-ray flux and so a given flux and resolution will limit scan time. At high values of flux the physical circuit structure can be damaged and so it is important not to operate in a regime where such radiation damage impacts imaging fidelity.

An upgrade of the synchrotron at the Paul Scherrer Institut, similar to that pioneered by the Swedish MAXLAB, [3] is expected to increase X-ray brilliance available to our existing ptychographic X-ray laminography microscope by a factor of 100 and new X-ray optics will increase flux by another factor of 100. Since achievable resolution scales as the X-ray dose to the inverse fourth power [4] the increased flux may be used to improve resolution by a factor of 10. Changing the way data is acquired using the X-ray detector array and modifying the algorithms used to reconstruct 3D images from X-ray diffraction data can further increase resolution *and* depth of field. Resolution can be traded-off against scan time and reducing the number of high-flux images taken has the effect of both mitigating risk of radiation damage and reducing scan time. This combination of hardware and algorithmic improvements, including the use of priors and machine learning techniques, [5] promises realization of an X-ray laminography microscope with zoom capability that is able to image cm-sized chips in 3D at sub-nm resolution.

## X-RAY FLUORESCENCE

Adding X-ray fluorescence (XRF) to an X-ray laminography microscope can be used to extract useful information about material composition - even if imaging is performed with a modest resolution of around 50 nm. Since, in principle, XRF can detect better than a part per million concentrations of atom species in a solid, it can be used to provide information on trace quantities of elements, including detection of n-type dopants such as As. [6] Identification of atomic composition of the materials used in the manufacture of circuits can contribute to metrology, failure analysis, and could be used to simplify extraction of circuit schematics from X-ray imaging data. It can also support 3D image reconstruction.

Multi-modal X-ray imaging of chips is not new. For example, Maria Scholz wrote a thesis at the University of Hamburg on multi-modal imaging of integrated circuits in 2020. [7] The experiments were performed using a conventional ptychography nano-probe microscope with a cylindrical sample 5 to 8 micrometer in diameter that was cut out of an integrated circuit using a focused ion beam.

The integration of XRF detection into our existing high-resolution coherent X-ray laminography microscope to detect material composition in integrated circuits supported on a planar substrate has a number of potential advantages. This additional imaging capability for planar substrates may extend non-destructive metrology, provide new ways to approach chip failure analysis, and increase efficiency of reverse engineering. For example, typical contemporary chips use many materials, including silica, silicides, and nitrides. If, along with the electrical connectome, a measure of the elements present can be mapped across the chip it may be possible to use this information to more efficiently establish and verify the circuit schematic and the circuit function. XRF can also be used to improve efficiency and accuracy of 3D image reconstruction since fluorescence is isotropic and so does not suffer from the missing cone in coherent X-ray diffraction in the laminography geometry.

The idea to use XRF to analyze integrated circuit composition has also motivated further study of detector technology. For example, XRF Silicon Drift Detectors [8] are limited by the statistical fluctuation of the generated charge in the active volume while an alternative superconducting Transition Edge Sensor has ten times better spectral resolution [9] but suffers from a count rate that is limited to just a few counts per second per pixel.

## CONCLUSION

A ptychographic X-ray laminography microscope with zoom capability can be used to non-destructively image CMOS integrated circuits in 3D. This chip-scan imaging capability may be of interest for non-destructive reverse engineering of integrated circuits, metrology for advanced technology nodes, the efficient identification of manufacturing defects and counterfeit products, as well as enabling a certified trust service that ensures integrated circuits are manufactured to customer design.

## REFERENCES


1. M. Holler, M. Odstrcil, M. Guizar-Sicairos, M. Lebugle, E. Müller, S. Finizio, G. Tinti, C. David, J. Zusman, W. Unglaub, O. Bunk, J. Raabe, A. F. J. Levi and G. Aeppli, *Nature Electronics* **2**, 464–470 (2019).
2. M. Holler, M. Guizar-Sicairos, E. H. R. Tsai, R. Dinapoli, E. Müller, O. Bunk, J. Raabe and G.Aeppli, *Nature*, **543**, 402–406 (2017).
3. M. Eriksson, L.-J. Lindgren, M. Sjöström, E. Wallén, L. Rivkin and A. Streun, *Nucl. Instrum. Methods Phys. Res. A* **587**, 221–226 (2008).
4. M. R. Howells, T. Beetz, H. N. Chapman, C. Cui, J. M. Holton, C. J. Jacobsen, J. Kirz, E. Lima, S.Marchesini, H.Miao, D. Sayre, D. A. Shapiro, J. C. H. Spence and D. Starodub, *J. of Elect. Spect. Related Phenom.* **170**, 4–12 (2009).
5. I. Kang, Y. Jiang, M. Holler, M. Guizar-Sicairos, A. F. J. Levi, J. Klug, S. Vogt, and G. Barbastathis, *Optica* **10**, 1000-1008 (2023).
6. N. D'Anna, D. Ferreira Sanchez, G. Matmon, J. Bragg, P. C. Constantinou, T. J. Stock, S. Fearn, S. R. Schofield, N. J. Curson, M. Bartkowiak, Y. Soh, D. Grolimund, S. Gerber and G. Aeppli, *Adv. Electron. Mater.* **9**, 2201212 (2023).
7. *3D multimodal X-ray imaging of a microchip: Correlating structure, composition and orientation at the nanoscale.* M. Scholz, Thesis, University of Hamburg (2020).
8. G. Utica1, E. Fabbrica1, M. Carminati1, G. Borghi, N. Zorzi, F. Ficorella, A. Picciotto, I. Allegretta, G. Falkenberg and C. Fiorini, *J. Instr.* **16**, P07057 (2021).
9. T. Guruswamy, L. Gades, A. Miceli, U. Patel and O. Quaranta, *IEEE Trans. Appl. Supercond.* **31**, 2101605 (2021).


## KEYWORDS

ptychographic X-ray laminography microscope, 3D X-ray chip imaging, non-destructive 3D X-ray chip imaging.

# Integrating Atom Probe Tomography and Transmission Electron Microscopy into a Single Instrument

Eric Van Cappellen[1]; Joachim Mayer[2]; Rafal E. Dunin-Borkowski[2]; Joseph Bunton[3]; Frank de Jong[4] and Hugo van Leeuwen[4].

*[1]Thermo Fisher Scientific, 5350 NE Dawson Creek Drive, Hillsboro, OR 97124, USA; [2]Ernst Ruska-Centre for Microscopy and Spectroscopy with Electrons, Research Centre Juelich, D-52425 Juelich, Germany; [3]CAMECA Instruments Inc, Atom Probe Tomography, Madison, Wisconsin, USA; [4]Thermo Fisher Scientific, Achtseweg Noord 5, 5651 GG, Eindhoven, The Netherlands.*

## INTRODUCTION

(Scanning) Transmission Electron Microscopy (S/TEM) and Atom Probe Tomography (APT) are two well-established but fundamentally different materials characterization techniques. They both offer three-dimensional characterizations at the atomic scale, however neither of them can provide complete characterization of microstructural morphology, crystallographic structure, and chemical composition.

Atomic-scale S/TEM tomography has been demonstrated by amongst others, Sara Bals et al. [1] and Yang et al. [2]. S/TEM tomography reveals the atom positions with sub-100 pm precision but has limited elemental sensitivity because image contrast is used for identification. This excludes neighboring elements in the periodic table and light elements altogether, although recent developments using (integrated) Differential Phase Contrast (i)DPC may provide promising alternatives [3]. The S/TEM tomography approach is also limited to small volumes containing just a few thousands of atoms.

Conversely APT datasets can contain millions of atoms and species sensitivity is exceptional, it can even distinguish between different isotopes. Unfortunately, atom positioning precision is limited due to the reconstruction algorithms that lack precise information on the trajectories that the ions take from the specimen to the detector.

Harvesting both S/TEM and APT data from the same sample can be done via a correlative approach where after S/TEM analysis, the needle shaped sample is then transferred to an APT and both datasets are then correlated, in the hope to get a better three-dimensional understanding of the sample [4]. In this paper a new concept is discussed in which the APT mode is integrated into a TEM column to achieve atomic-scale correlation of S/TEM and APT data.

## SCIENTIFIC AND WORKFLOW DRIVERS

The goal is to achieve Atomic Scale Analytical Tomography (ASAT [5,6]) meaning that a complete 3D representation of the specimen containing chemical, compositional, structural, and physical properties information at the atomic scale is achieved. The 3D position of each atom must be determined with sufficient precision and accuracy to determine the atomic structure of (non-)crystalline materials and visualize possible defects. The atomic (and isotopic) identities must be determined with high precision and accuracy. Chemical bond state information must also be available on the atomic scale in sufficient detail so that it can be matched to computed chemical state information. The information must cover a large enough volume to be technologically useful (millions to billions of atoms).

Using ASAT [7], the three-dimensional distributions of functional elements possibly down to the single-atom level can be determined, and simultaneously linked to atomic structures with picometer precision and electronic structures with sub-eV resolution. This will be applied to the study of structures and defects of material systems like nano-electronic components, compound solar cells or catalytically active nanoparticles. Atomic-level segregation studies of light elements such as H, Li or O to active defects and interfaces will become possible, leading to novel insights into a wide variety of structural materials, energy storage systems and functional elements. For nanoelectronics components, such as intrinsically three-dimensional nano-sheet transistors containing Si/SiGe multilayer stacks explored for the latest generations of CMOS logic [3], the volumes to be analyzed may be smaller,

but the new technology should be able to analyze local, 3D elemental intermixing, crystal structure (strain) and dopant distributions at the atomic-scale.

Experimental workflows exist in which an APT needle is first characterized in the S/TEM and then transferred to the APT where it is destructively analyzed. However, reliable S/TEM results can only be obtained from the thinnest part of the needle, which often does not contain the relevant part of the sample. Also, the standard method of reconstruction of the APT atomic positions assumes that the apex shape of the needle is hemispherical. Even in cases where this is a fairly accurate starting position, "grooving" will occur during evaporation due to the presence of dislocations, twin boundaries, stacking faults, grain boundaries or multiple phases in the sample [5,8]. This leads to an alteration of the trajectories and thus to artefacts in the final APT tomograms. Thus, S/TEM and APT datasets become less and less accurate moving away from the initial tip of the needle. In addition, the environmental exposure and long transfer times during the sample transfers could result in a significantly modified surface e.g. caused by oxidation.

## THE INTEGRATED APPROACH

A unique integrated S/TEM-APT tool is being developed by Thermo Fisher together with Cameca, in close cooperation with the Ernst Ruska Centre (ER-C) in Jülich, Germany, who will also be the first recipient of the tool. Being able to practice both techniques on the same instrument in a common environment without having to transfer or move the sample allows for sequential and quasi-instantaneous S/TEM and APT. The data acquired with either technique is acquired from the exact same sample location and can be correlated with confidence. The needle is first analyzed with S/TEM, then a few million atoms are evaporated in APT mode before being re-examined in S/TEM mode. This is then repeated until the whole useful volume is analyzed. Along the way the needle is being thinned and the true shape of the apex is being monitored. The sample remains in an ultra-high vacuum environment for the full analysis, preventing oxidation and/or contamination.

Detailed knowledge of the sample contours and the electrical field in the vicinity of the apex, as well as how these evolve over time due to evaporation, will improve APT data reconstruction, which is a prerequisite for 3D atomic resolution. One such method of measuring a low-voltage electrical field is electron holography as demonstrated by Beleggia et al. [9], and for this reason multiple bi-prisms are configured on the tool. An alternative approach is to use Differential Phase Contrast (DPC) which offers a direct assessment of the electric field through beam deflection measurements using a segmented STEM detector or a 4D-STEM detector [10]. For full 3D sample contour characterization TEM and STEM electron tomography is available and EELS is available if chemical mapping is required.

From an engineering perspective, the integration of two distinct tools into one means that the minimum requirements of both techniques need to be exceeded and combined. Transmission Electron Microscopy accelerates electrons up to 300 keV energy that are then optically guided by a magnetic field exceeding 1 T to a sample that must be vibrationally stable enough to allow for better than 80 pm spatial resolution. The atom probe, on the other hand, requires a needle-shaped sample; ultra-high vacuum in the $10^{-10}$ mbar range and a cryogenic environment below 35 K. Moreover, the needle needs to be primed in the absence of a magnetic field with a very high electrical field of about 30 V/nm and irradiated by a laser capable of injecting pulses with controlled energy of 25 nJ into the sample at a repetition rate greater than 200 kHz. The environments and requirements of both techniques could not be more divergent, and in addition will necessitate quick switching between modes (high-resolution versus field-free). These major design challenges are being addressed during the design and development of the new tool.

At the heart of the S/TEM, a new specimen chamber is being built, in which the ultra-high vacuum (UHV) level will be improved by at least an order of magnitude compared to conventional S/TEMs, including possibilities for bake-out cycles. A modified, UHV compatible sample stage is under development, which will still provide the usual five axes motion. At the same time, the sample needs to be cooled to very low cryogenic temperatures and be kept at those temperatures in a vibration-free manner to allow sub-Ångstrom resolution S/TEM. For this, an innovative solid-state Cooler (a thermal battery) is being tested which will act as an intermediary between the compressor unit and the sample. A multi-stage UHV sample loader is being designed as well, as the normal side-entry loading cannot sustain the required vacuum levels.

Integrating the APT mode in such a way that it is coincident with the electron beam also requires several additional changes to the TEM specimen chamber, such as a high voltage feedthrough to the sample and a line of sight to the sample for the laser which is used during evaporation of the sample. The atom probe detector must have a large solid angle to register the evaporated ions, but the geometrical constraints of bolting it on to a S/TEM column requires

additional ion-optics and further modifications of the specimen chamber. All these changes are incorporated in the new design of the integrated tool (see Figure 1), which is being tested.

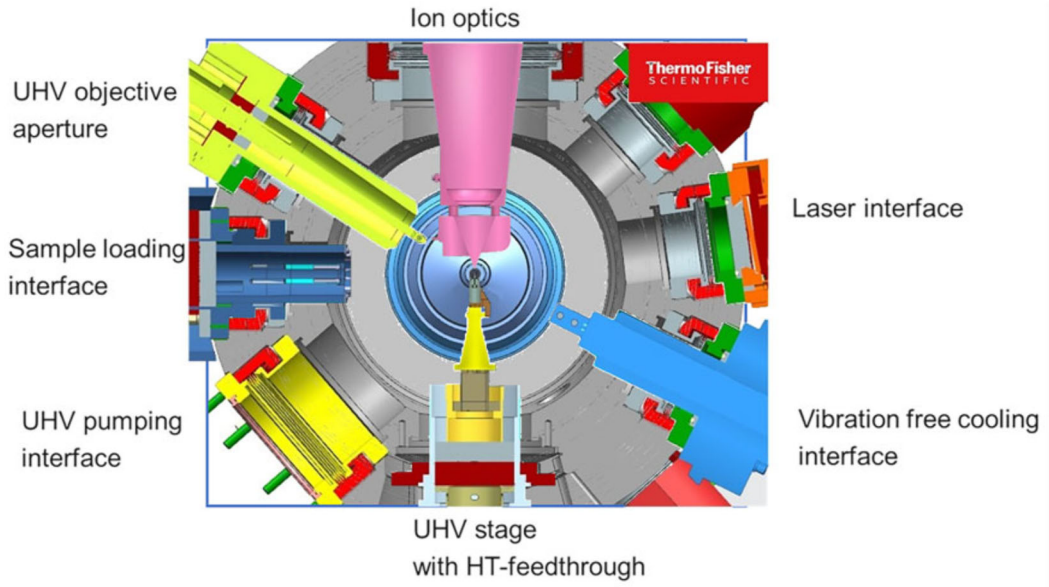


**FIGURE 1.** Layout of the UHV specimen chamber (top-down view) showing all the modules required for the integration of APT on a S/TEM.

## CONCLUSION

The integration of an Atom Probe into a Transmission Electron Microscope or the TOMO instrument as it is known will benefit from the almost complete complementarity of the S/TEM and APT techniques, which can be applied to the same object quasi-simultaneously, without transfer or move. The S/TEM mode offers high spatial resolution from a smallish sample area together with relatively modest elemental sensitivity (approximately 1 %), and the APT mode offers unrivalled elemental (isotopic) sensitivity in the part-per-million (ppm) range albeit with a poorer spatial resolution [7].

The expected synergistic gain obtained by the integrated approach lies in the fact that it will be possible to observe the shape of the apex *in-situ* and thus correct atom trajectories for greater spatial precision. The TOMO instrument will also pave the way to the determination of locations and types of larger numbers of atoms (billions in a volume of several hundred thousand cubic nm), if needed, down to each individual lattice position, in one instrument.

## REFERENCES

1. 5. S Bals et al., Current Opinion in Solid State and Materials Science **17** (2013), p. 107.
2. Y Yang et al., Nature **542** (2017), p. 75.
3. I. Alexandru et al., in: Frontiers of Characterization and Metrology for Nanoelectronics (E.M. Secula and J. A. Liddle) p. 201
4. M. Herbig et al., Ultramicroscopy **153** (2015), p 32-39
5. T. F. Kelly et al., Atomic-Scale Analytical Tomography, Cambridge University Press, 2022. ISBN: 9781316677292
6. T. Kelly – M&M 2023 A10.1.1 - Introduction to Atomic-scale Tomography
7. J. Mayer – M&M 2023 A10.1.3 - TOMO project
8. H. van Leeuwen – M&M 2023 A10.1.4 – APT on TEM
9. M. Beleggia et al., J Appl Phys **116** (2014), p. 24305.
10. Josef Zweck 2016 J. Phys.: Condens. Matter **28** 403001

## KEYWORDS

(Scanning) Transmission Electron Microscopy (S/TEM), Atom Probe Tomography (APT), Atomic Scale Analytical Tomography (ASAT), Crystal structure, defects

# Advanced Electron Microscopy-Based Metrology Approaches

A. K. Petford-Long,[1,2,3] A. McCray,[1.3] Y. Li,[1] F. Barrows,[1,3] D. B. Durham,[1] S. Guha,[4,1] C. Phatak[1,2]

*[1]Materials Science Division, Argonne National Laboratory, 9700 S. Cass Ave, Lemont, IL 60439; [2]Department of Materials Science and Engineering, Northwestern University, 2220 Campus Dr, Evanston, IL 60208; [3]Applied Physics program, Northwestern University, 2145 Sheridan Dr, Evanston, IL 60208; Pritzker School of Molecular Engineering, University of Chicago, 5640 S. Ellis Ave, Chicago, IL 60637.*

## INTRODUCTION

Advanced transmission electron microscopy (TEM) and scanning TEM (STEM) are commonly used for characterization, down to the atomic level, of the microstructure and composition of materials systems including thin films and heterostructures in which the interfaces are of particular interest. However, in addition to being able to understand microstructure and composition, electron microscopy can also be used to image electric and magnetic fields in 2D and 3D, to determine the oxidation state of the elements present via the use of electron energy loss spectroscopy, and to explore the effect of features such as defects and lattice strain. A further advantage of TEM analysis is the ability to explore the local time-dependent behavior of materials as a function of external stimuli such as applied magnetic and electric fields and temperature, and to correlate this behavior with the heterogeneity in the material under analysis. In this presentation I will illustrate some of the capabilities of advanced electron microscopy by drawing on examples related to the magnetic behavior of 2D ferromagnetic van der Waals (vdW) materials containing magnetic skyrmions lattices (of potential interest in spintronic applications), to mapping of electrostatic potentials as a function of electric fields in nanopatterned $TiO_2$, and to electrical switching in charge density waves and ferroelectric materials.

I will also discuss how the use of machine-learning and artificial intelligence have extended our ability to understand the electron microscopy data and take us beyond what could be achieved previously.

Some examples of the work that I will discuss are included below.

## RESULTS

### Temperature-Dependent Magnetic Behavior of Ferromagnetic Van der Waals Materials

Ferromagnetic vdW materials such as $Fe_3GeTe_2$ (FGT) and $CrGeTe_3$ (CGT) are of interest because they can support magnetic skyrmions, which are chiral topological magnetic excitations that could potentially be harnessed for high-density low energy skyrmionics devices [1]. The ability to harness magnetic skyrmions for applications relies on developing an understanding of the energy terms that control their magnetic behavior.

Figure 1 (left) shows a Lorentz TEM (LTEM) image of a Néel-type skyrmion lattice in an exfoliated thin film of FGT, recorded in situ in the TEM at a temperature of 180K in an out-of-plane magnetic field of 300 G. The circular features are the magnetic skyrmions. Overlaid on the image are red dots that indicate the positions of the centers of the skyrmions, identified using a convolutional neural network (CNN) that was trained on simulated LTEM images of skyrmions lattices. The magnified region also shows the overlaid Voronoi diagram, which enabled the local skyrmions lattice order, and the size of each skyrmion, to be determined. Figure 1 (right) shows the way in which the average local skyrmion lattice order changed as a function of temperature during heating and cooling in an applied

magnetic field.The use of machine learning enabled identification of more than 600,000 skyrmions in 380 images recorded at different locations, magnetic fields and temperatures. Analysis of such a large data set allowed for statistical analysis and the development of a model that determined the energy landscape in which the skyrmions sit, and thus the energy terms that control their behavior.

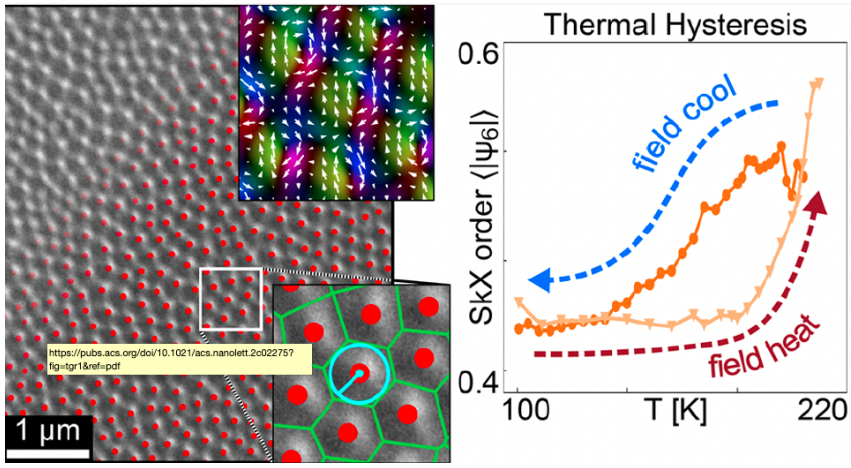


**FIGURE 1.** Left: LTEM image of skyrmions lattice in FGT at a temperature of 180 K and in an out-of-plane applied field of 300 G. Right: plots of the average skyrmions lattice order as a function of temperature during field-heating and field-cooling [2].

## Mapping Electric Fields in Resistive-Switching Oxides

Resistive-switching oxides show charge transport behavior that arises due to the interaction of a number of different mechanisms, many of which depend on the local structure including heterogeneity in the oxide material or a controlled nanostructuring. Resistive-switching materials are of interest from an applications point of view for devices based on memristive behavior, which is being exploited in neuromorphic computing applications. Central to harnessing the resistive-switching behavior is the requirement to understand how effects such as nanostructuring affect the charge transport behavior.

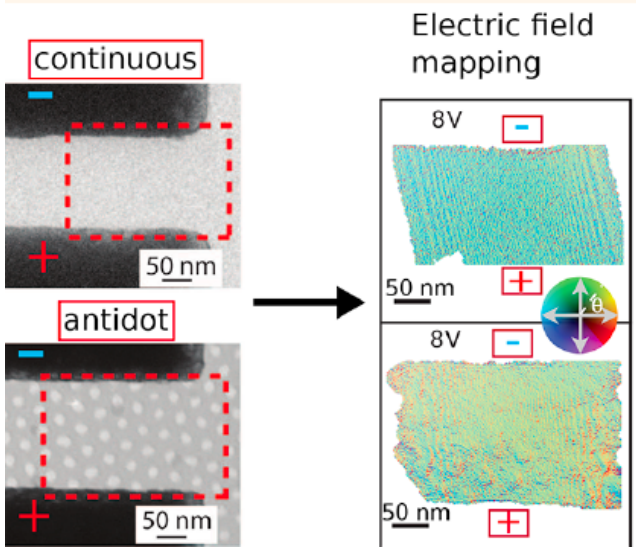


**FIGURE 2.** Left: TEM images of continuous and nanopatterned $TiO_2$ films contacted to Pt electrodes. Right: vector maps of the electric field in the regions outlined in red, during in situ biasing at an applied voltage of 8 V [3].

Figure 2 shows thin films of $TiO_2$ contacted to Pt electrodes (dark regions). The lower $TiO_2$ film has been patterned into an antidot array using a hard mask created from alumina infiltration into a self-assembled block

copolymer array. The images to the right show color vector maps of the electric field obtained from electron holography data obtained during in situ TEM biasing experiments. These data allowed us to develop a model that indicated the presence of charge accumulation and quantum interference effects arising from the nanoscale patterning.

## Visualizing Ultrafast Electrical Switching in Thin Films

Electrical fields can be used to drive switching of atomic order in materials, two examples of which are the reversal of ferroelectric domains and the crystallization/reamorphization of phase change materials, both of which can be harnessed for memory applications. As the demand for more energy-efficient microelectronics has grown, so there is an interest in exploring the electrical switching of materials at a smaller length scale and at higher speed. As for the case of $TiO_2$ discussed above, at such small length scales the effects of nanoconfinement need to be taken into consideration, as completely new electronically-driven phenomena can arise. Correlating this behavior with the local microstructure and composition is critical, and in situ TEM biasing is a valuable approach to understanding the behavior. However, going beyond this is the need to explore these phenomena at the timescales of relevance, and I will present the results of in situ ultrafast electron microscopy experiments with time resolution down to the ns regime that reveal the presence of emergent behavior that contributes to the electrically-induced switching [4].

## REFERENCES


1. H. Vakili *et al*., *J. Appl. Phys.* **130**, 070908 (2
2. A. R.C. McCray, Y. Li, R. Basnet, K. Pandey, J. Hu, D. P. Phelan, X. Ma, A. K. Petford-Long, C. Phatak, *Nano Lett.* **22**, 7804–7810 (2022).
3. F. Barrows, H. Arava, C. Zhou, P. Nealey, T. Segal-Peretz, Y. Liu, S. Bakaul, C. Phatak, A. K. Petford-Long, *ACS Nano* **15**, 12935–12944 (2021).
4. T.E. Gage, D.B. Durham, H. Liu, S. Guha, I. Arslan, C. Phatak, arXiv:2306.01171 (2023).
5. This work was supported by the U.S. Department of Energy, Office of Science, Office of Basic Energy Sciences, Materials Sciences and Engineering Division, and by the U.S. Department of Energy, Office of Science for support of microelectronics research under Contract No. DE-AC02-06CH11357. Use of the Center for Nanoscale Materials, an Office of Science user facility, was supported by the U.S. Department of Energy, Office of Science, Office of Basic Energy Sciences, under Contract No. DE-AC02-06CH11357.


## KEYWORDS

Transmission electron microscopy, in-situ experiments, nanomagnetism, charge transport behavior

# Characterization of Magnetic Textures in Materials for Spintronics-based Devices

Rafal Dunin-Borkowski

*Ernst Ruska Centre for Microscopy and Spectroscopy with Electrons*

# MRAM End of Line Magnetic Testing: From Single Bit Properties to Full Memory Qualification

Siamak Salimy[1], Antoine Chavent[1], Steven Lequeux[1], Gilles Zahnd[1], Anthony Bussiere[1], Eric Montredon[1], Isabelle Joumard[2], Aymen Fattassasoui[2], Kevin Garello[2].

1. Hprobe, 4 Rue Irène Joliot Curie, 38320 Eybens, France
2. Univ. Grenoble Alpes, CEA, CNRS, Spintec, 38000 Grenoble, France

## INTRODUCTION

Magnetic Random-Access Memories (MRAM) are emerging as a highly promising solution for embedded memory systems, including low-level caches and e-Flash, at technology nodes of 2x nm and beyond[1]. MRAM offers scalability, non-volatility, and low power consumption, thereby enhancing overall performance. Spin Transfer Torque (STT)-MRAM is currently being adopted as a replacement for eFlash (NAND) due to its ability to address functional challenges and cost escalation associated with reducing process critical dimensions in eFlash.

Moreover, MRAM has the potential to address power consumption and integration density issues encountered by Static Random Access Memory (SRAM) at single-digit technological nodes[2,3]. This is achieved through the introduction of Spin Orbit Torque (SOT) [4-5] and Voltage Control of Magnetic Anisotropy (VCMA) effects, which improve writing speed and endurance limitations of STT-MRAM.

The introduction of embedded MRAM (eMRAM) in foundries necessitates appropriate and dedicated metrology measurement methods. These methods should include magnetic field measurements to ensure magnetic specifications at the thin film level, as well as at the device and circuit levels. These tests should be combined with high-performance electrical testing, including sub-nanosecond excitations, fast bit error rates, and large endurances.

In the following, we will discuss typical MRAM testing needs and metrology that we have developed to meet these requirements. This includes fulfilling testing needs from single cells for R&D to macro level for wafer sorting in production. Additionally, we will present the field immunity procedure we are implementing for MRAM qualifications in different environments.

STT-MRAM employs a perpendicular magnetic tunnel junction (pMTJ) consisting of thin-film layers, including fixed and free magnetic layers separated by an insulator. Each layer has its electronic spin oriented up or down (Figure 1). Parallel spin orientations indicate lower resistance ('0' bit), while antiparallel orientations signify higher resistance ('1' bit). External fields or Spin Transfer Torque (STT) via electronic current can switch between states (Figure 1). A single pMTJ and transistor form a memory cell, replicated "n" times in an array to meet application needs. MRAM manufacturing shares most steps with BEOL CMOS, differing only in pMTJ placement between metallization layers.

While the operational aspect of STT-MRAM in the final product is purely electrical, the stored information is magnetic, and the programming can be initiated by electrical current, temperature, or magnetic field variations. Recognizing this, the incorporation of simultaneous magnetic and temperature considerations during electrical testing is introduced at both foundries End of Line (EoL) and during the Back-End (B-E) process. This strategic insertion of meticulously designed metrology flow with magnetic excitation to account for the physics of Magnetic Tunnel Junctions (MTJ) establishes a secure foundation to support the successful ramp-up of STT-MRAM in High Volume Manufacturing. Consequently, the designed test flow for eMRAM chips must strike a balance between cost efficiency (high throughput) and consideration of STT-MRAM specificities at each testing stage, encompassing MTJ, arrays, and the chip as a whole.

## END OF LINE MRAM TESTING

During EoL tests, MTJ test cells play a crucial role in monitoring specified control parameters (SPC) of the manufacturing process. These cells enable the extraction of various physical parameters of the MTJ through the application of an external magnetic field while probing electrically. Parameters such as Tunnel Magnetoresistance (TMR), coercive field, magnetic anisotropy, and thermal stability factor (retention parameter) are among the 25 parameters extracted. To validate Spin Transfer Torque (STT) switching under pulsed current excitation and to extract MTJ switching voltage distributions, ultra-narrow analogue pulses (ranging from 0.3 to 200 nanoseconds) are utilized in the I-V test. Approximately 20 parameters, including switching voltage, critical currents, and probability of switching, are also extracted during this process. The application of field and current excitations aims to analyze MTJ characteristics from various perspectives, including switching dynamics, write voltage, and retention. Switching dynamics assessment primarily focuses on evaluating the MTJ's ability to transition between different states under magnetic or current excitation. Write voltage testing involves applying analogue pulse voltages within the range of pulse width and amplitude similar to those used in the bit-cell transistor. Retention testing evaluates the energy barrier between the two steady states (parallel and anti-parallel) of the devices. However, implementing these testing protocols requires additional test equipment capable of handling such requirements. This includes equipment capable of generating and applying precise magnetic fields during testing, as well as instruments capable of performing fast pure analogue narrow I-V pulsed sweeps. Consequently, an extra test step is needed compared to standard End of Line testing procedures, as traditional 'CMOS-like' Automated Test Equipment (ATE) typically do not include provisions for testing under magnetic fields or performing rapid pure analogue narrow I-V pulsed sweeps. Thus, adapting the testing infrastructure to accommodate these specialized requirements becomes essential for ensuring the accurate characterization and validation of STT-MRAM devices during the manufacturing process.

### System for End of Line process control and monitoring

The system implemented for EoL parametric tests is illustrated in Fig.2. In this system, the magnetic field is generated perpendicular to the wafer surface at levels up to 700mT while probing it electrically. Hprobe has designed a test head that is docked on the top plate of production wafer probers which integrates the magnetic field generator. The magnetic generator is based on a proprietary design that enable fast field sweeping capability that the field excitation can be compatible with production throughput requirements, basically extracting the MTJ hysteresis curves in a time down to 100milliseconds. The magnetic field is generated by coils surrounding and ferromagnetic flux guide that concentrate and project the magnetic on the wafer surface (Fig.2). The field excitation is synchronized with low level of biasing current used to record the state of the resistance. At this test, both the ability of MTJ to be programmed from one state to another is controlled as well as the energy barrier quantified. Energy barrier can be modeled considering the fact that the barrier height between two states is reduced by providing an amount of energy through magnetic field. To evaluate the programming (writing) reliability of the MTJ, common test used is the Bit Error Rate (BER) test that consist in setting the MTJ into its parallel and anti-parallel tests for several million events by use of electrical narrow pulses to evaluate the corresponding error rate (Fig.3). This test can be very time consuming as the full range of pulse amplitude and pulse width are commonly verified, each with equal or more than million writing events. For this Hprobe has recently introduced a unique system that enable to execute such test to include more than 2 million writing and 2 million reading events on the MTJ in less than 3seconds (Fig.3).

## BACK-END MRAM TESTING

In the Back End process, the product embedding MRAM are tested. In this context, the electrical test is purely digital and consequently the test methods used for MRAM in EoL which are purely analogue cannot be straightly transferred. In the Back-End testing, one can consider that the product should be evaluated purely with electrical test since this is the way it should operate in the end application. However, some parameters cannot be evaluated that way or with some drawbacks. First, the energy barrier or retention test, it can be evaluated through BER that can be driven from a BIST in the chip. However, such BER will provide an average information on the retention over the entire array or clusters of the arrays and this is a time-consuming test that cannot be really fully executed at a large test coverage in HVM. Another approach, commonly used is to run a true retention test that consist of heating the wafer for some time and read-out the count of bit that are subject to unwanted switching (e.g loss of their stored information). The problem with this is that the wafers are stresses for temperature and then they basically cannot be shipped to end customer. To resolve the bottleneck of retention test on embedded MRAM chips, we implemented a new protocol of retention test using magnetic field in order to extract the energy barrier information of each of the bits of an array and

this within few seconds. The advantage of this method is that it is not altering any properties of the MTJs and is fully compatible with throughput requirements. Second, because of the sensitivity of MRAM to magnetic excitation, this sensitivity should be evaluated to ensure the chip in end application will be immune to surrounding magnetic fields. Magnetic immunity is not an issue as it can be controlled and resolved from system level architecture to increase the spacing between MRAM chip and surrounding magnets or by inserting a shielding plane to effectively reduce the magnetic field seen by the MTJs. Validating the chip is resilient to external field attacks require to insert another test in the flow (in-line or off-line, mostly depending on the market application) that consist of applying an arbitrary magnetic field vector of amplitude almost at 25 to 50% of the switching (coercive) field and having an angle that can be from 0 to 360°.

## System for Back-End Sorting Test and Magnetic Immunity

To resolve these two testing challenges, we have implemented a dedicated magnetic instrument aiming in providing, at wafer level, a 3D arbitrary magnetic field vector projected on the MRAM array embedded in the chip. The field projection is covering an area that is compatible with the array size and both field strength and angle are controlled. For the magnetic immunity purpose, the challenge is to cover all different possible sources of magnetic field present in the end applications, which is particularly important for Automotive, IoT and Wearables chips. For this, we designed a 3D magnetic field generator capable of applying a vectorial field with the XYZ components of direction controlled. The magnetic generator is integrated into a test head docked on the top plate of a wafer prober, as illustrated in Fig.3. The vectorial field is directly projected at wafer level and the test head integrates a hexapod robot used to align the generator with the electrical probe needles and the wafer under test. To calibrate and monitor the projected field on wafer, the system integrates a Field Calibration Unit (FCU) composed of a two-axis robot carrying a 3D hall sensor. The FCU can map the magnetic field in a spatial volume around the position of test. The test head is air-cooled and embeds a set of temperature sensors, controllers and safety interlocks. The magnetic instrument is driven by an electrical rack and a proprietary software interfacing with the electrical memory tester. The memory tester provides the electrical stimuli and sensing for BER tests and operates synchronously with the magnetic field projection on the wafer. The instrument is designed to reach the required level of magnetic field strength and 360° angles. Maximum out-of-plane perpendicular field is of 700mT to voluntary switch the free layer, and maximum in-plane field of 200mT. The projected area on the wafer is in the range of ~3x3mm² to ~50x50mm² depending on the hardware configuration and magnetic field requirements. The vectorial 3D magnetic generator is operating as 3D magnetic arbitrary waveform generator for both static and dynamic fields projection simulating the chip exposition in the end-application. Stress with vectorial field at controlled and variable angle can be also executed like on a rotating field pattern illustrated in Fig.4. Dynamic out of plane rotating field with constant norm of amplitude at above 100mT is plotted to simulate a vector field coming from any direction in a plane that is perpendicular to the chip surface. The system can expose the MTJ by controlling the field strength, angle of vector and duration of exposition simultaneously with BER tests.

## REFERENCES

1. K. Takeuchi, "Scaling challenges of NAND flash memory and hybrid memory system with storage class memory & NAND flash memory," *Proceedings of the IEEE 2013 Custom Integrated Circuits Conference*, 2013, pp. 1-6, doi: 10.1109/CICC.2013.6658450.

2.Abbasian, E., Birla, S. & Gholipour, M. A Comprehensive Analysis of Different SRAM Cell Topologies in 7-nm FinFET Technology. *Silicon* (2021). https://doi.org/10.1007/s12633-021-01432-6.

3. E. Rezaei, M. Donato, W. R. Patterson, A. Zaslavsky and R. I. Bahar, "Fundamental Thermal Limits on Data Retention in Low-Voltage CMOS Latches and SRAM," in *IEEE Transactions on Device and Materials Reliability*, vol. 20, no. 3, pp. 488-497, Sept. 2020, doi: 10.1109/TDMR.2020.2996627.

4. M. Gupta *et al*., "High-density SOT-MRAM technology and design specifications for the embedded domain at 5nm node," *2020 IEEE International Electron Devices Meeting (IEDM)*, 2020, pp. 24.5.1-24.5.4, doi: 10.1109/IEDM13553.2020.9372068.

5. S. Couet *et al*., "BEOL compatible high retention perpendicular SOT-MRAM device for SRAM replacement and machine learning," *2021 Symposium on VLSI Technology*, 2021, pp. 1-2.

## Keywords

MRAM, Magnetic Test, Spin Transfer Torque, Spin Orbit Torque, Parametric Test, End of Line test, Back end test, Process control and Monitoring.

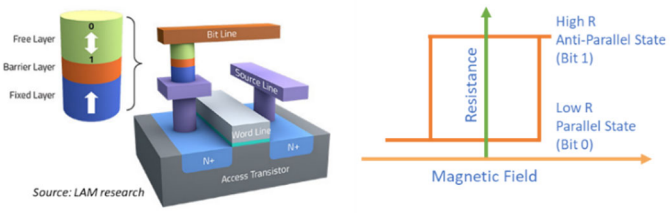


**FIGURE 1.** 1T1M (one transistor on MTJ) bit cell with MRAM magnetic tunnel junction (left) and hysteresis curve of MTJ showing parallel and anti-parallel states (right)

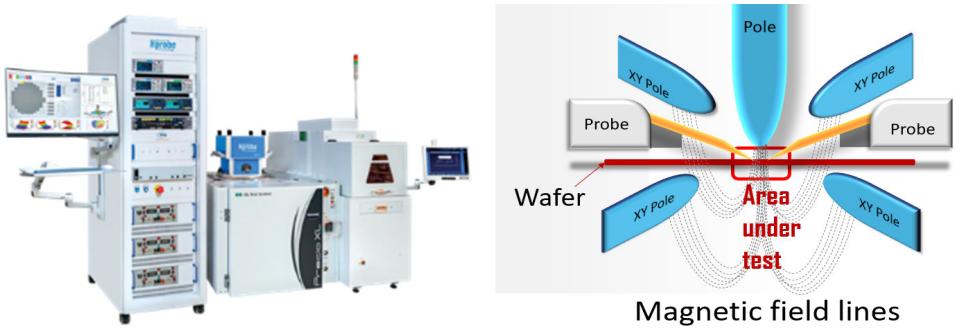


**FIGURE 2.** Hprobe Parametric Test Equipment for MRAM process control and monitoring (left) and working principle of magnetic generator field projection on wafer

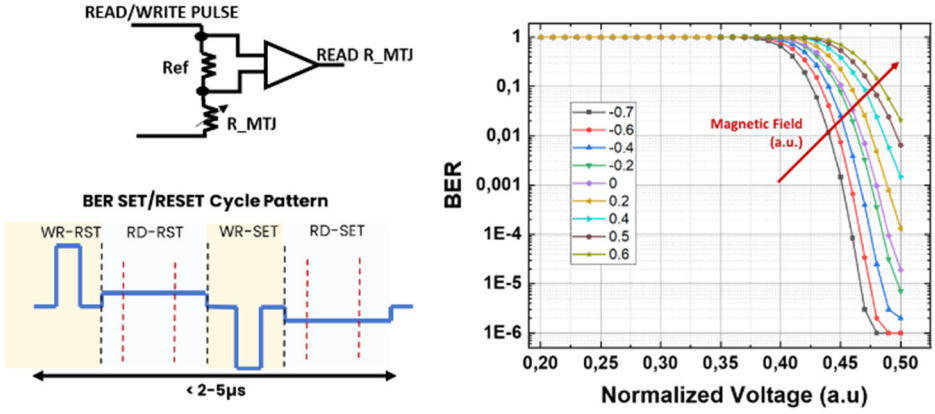


**FIGURE 3.** Bit Error Rate (BER) test architecture and corresponding signal cycles (left) and illustrative result (right)

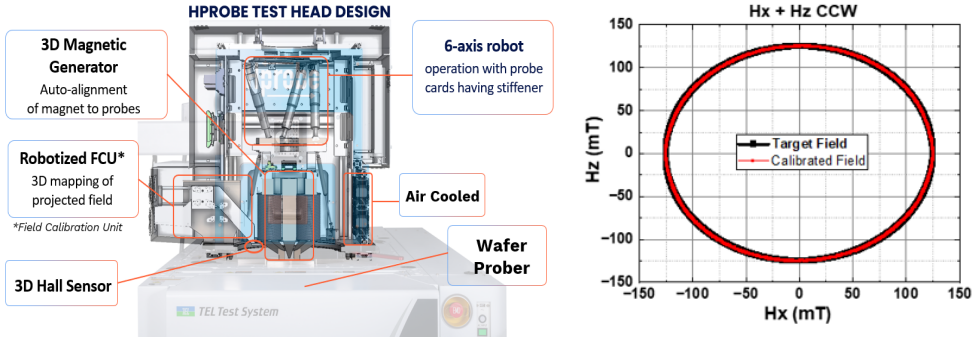


**FIGURE 4.** Cross section view of MRAM Back-End magnetic instrument (left) and illustrative angle and amplitude control of 3D vectorial field.

# Characterization of Crystal Structure and Morphology of Ultra-Thin 2D MoS2 Layers Using X-ray Metrology

Lixia Rong, Hao-Ling Tang, Luc Thomas, Hanson Kwok, Michael Phillips, Hongwen Zhou, Qinyi Fu, Lavinia E. Nistor, Jaesoo Ahn, Mahendra Pakala

*Applied Materials, Inc., 3050 Bowers Avenue, Santa Clara, CA, 95054*

## INTRODUCTION

Few-layered two-dimensional transition metal dichalcogenides (2D TMDs) are strong candidates for several applications such as high mobility channel in memory or logic devices, photovoltaics, photodetectors, and optoelectronics [1, 2]. Since high-quality ultra-thin layers are needed to take full advantage of these 2D materials, precise control of the crystallinity, morphology and thickness of these ultra-thin layers is critical. This requires a set of metrology techniques highly sensitive to these ultra-thin layers and fast enough to provide rapid feedback to help optimize deposition parameters. In this presentation, we use a combination of X-ray scattering and fluorescence metrology techniques, including grazing incidence X-ray diffraction (GI-XRD), in-plane X-ray diffraction (In-plane XRD), X-ray reflectivity (XRR) and wavelength dispersive X-ray fluorescence (WDXRF) to characterize MoS2 samples of various thicknesses. We show that this fast and non-destructive X-ray based metrology is sensitive to crystal phase, crystallite grain size, thickness, density, composition, and uniformity of the MoS2 films down to sub-nm thickness.

## RESULTS AND DISCUSSION

In this study, we analyzed 4 MoS2 films of various thicknesses deposited by atomic layer deposition (ALD) and annealed at 950°C in N2 atmosphere for 2 minutes. First, the thickness and density of the films were investigated by XRR. XRR scans the X-ray from an angle smaller than the critical angle and measures the reflected intensity at the same angle as the incident angle (specular direction). By fitting XRR data, the film thickness and density can be obtained. XRR data for the 4 MoS2 films are shown in Figure 1. The 3 thickest samples S2-4 show clear thickness fringes and can be fitted unambiguously to derive film thickness and density (shown in Table 1). Thickness values derived from XRR are in good agreement with TEM data, as shown in the inset of Figure 1 for the 21.7A film S4. While XRR is suitable for films thicker than ~10A, it becomes more challenging for thinner films which may be discontinuous and not exhibit the mirror-like surface required for high intensity specular reflection. In addition, thin films do not show thickness fringes in the measurable angular range so fitting results are not unique, leading to large error. This is the case for S1, for which XRF can be used to complement XRR.

The energy of florescence of X-rays are characteristic for each element and the intensity of fluorescence X-ray are directly related to the concentration of the element. XRF measures only the number of the atoms, and the thickness information is derived from the density of the materials. For MoS2 film, Mo-Lα (2.29 keV) and S-Kα (2.31 keV) lines are used to quantify the film thickness and composition. Due to the small energy difference between the two atoms, WDXRF is necessary since it has higher energy resolution than energy dispersive XRF (EDXRF). WDXRF intensity counts were calibrated with XRR fitting thickness for S2-4. A fundamental parameter (FP) method was used for the calibration. In FP method, the theoretical intensity calculated based on the XRR fitting thickness is correlated with the measured XRF counts. Figure 2 shows the excellent correlation between the calculated intensities and WDXRF measured counts. This correlation allows us to derive the thickness of S1 as 7A from the XRF count. XRR data are then refitted with this thickness as a self-consistency check. As shown in Figure 1, good fit is obtained for a density close to that of the thicker samples (Table 1).

WDXRF measurement shows excellent repeatability of the films: Measurements repeated 10-time show variability 1σ of less than 0.2 % for all films S1-4 between 7 and 21.7A. WDXRF technique also has faster throughput than XRR, making wafer mapping measurements possible. This is important for the within wafer uniformity check. The film uniformity measurement was conducted by 49 points WDXRF film thickness and count mapping. As shown in Figure 3 for S4, the within-wafer thickness non-uniformity 1σ is only 0.5% across the 300mm wafer. Note that there are small thickness variations with a 3-fold symmetry across the wafer which we attribute to the design of the deposition tool. Figure 4 shows WDXRF S-Kα vs. Mo-Lα counts. The good linear relationship observed indicates relative Mo vs. S composition of these films remains constant for all 4 thicknesses.

To characterize the crystalline quality of these ALD MoS2 ultra-thin films, GI-XRD and in-plane XRD were implemented with optimized measurement conditions. These techniques are preferred for ultra-thin films because they provide higher film intensity relative to Si substrate background noise than the conventional θ-2θ configuration. In GI-XRD, the incident beam is fixed at a small angle, approximately 0.5 to 1°, slightly above the critical angle (below which total reflection will occur), and the detector is moved on the 2θ circle to collect the pattern. It is important to note that during the scan, the Bragg plane does not remain at a fixed direction relative to the sample surface but instead moves as 2θ is varied. Therefore GI-XRD provides information of any existing randomly oriented lattice planes of the film (Figure 5a). For in-plane XRD configuration, the measured diffraction intensities are from the lattice planes normal to the sample surface, so the technique is more sensitive to in-plane crystallinity and grain size (Figure 5b). Aside from S1 for which diffraction is too weak, the other three samples could be measured in both GI and in-plane configurations. Figure 6 shows examples of GI-XRD 2θ and in-plane 2θχ/φ (inset) for S2 (11.7A). Diffraction peaks are consistent with polycrystalline hexagonal beta phase. Figure 7 shows the grain size derived from GI and in-plane scans for S2-4 as a function of thickness. Interestingly, grain size from GI-XRD is much smaller than that of in-plane XRD. This is because GI-XRD is sensitive to lattice planes in all 3 dimensions, so the grain size is constrained by the film thickness. By contrast, grain size from in-plane XRD reflects the in-plane crystal growth of 2D MoS2 and shows grains as large as 160A for the thicker sample S4. Note that large in-plain grains are critical for MoS2 application in memory or logic device channels, because fewer grain boundaries are associated with higher electron mobility [3]. This result shows that in-plane XRD is the preferred technique to help guide process development of 2D MoS2 ultra-thin films for device applications.

## SUMMARY

In conclusion, we show that XRR combined with WDXRF are suitable for characterization of 2D MoS2 films in a wide range of thicknesses. We also show that in-plane XRD is sensitive to MoS2 lateral grain size which is a key performance driver for 2D MoS2 based devices. This suite of X-ray based metrology techniques offers a fast, non-destructive, and sensitive methodology for in-depth characterization and optimization of ultra-thin layer 2D materials.

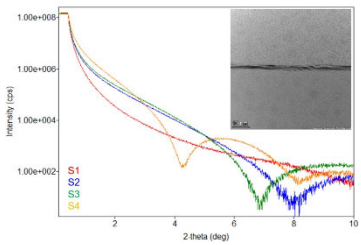


**FIGURE 1.** XRR data of 4 MoS2 films with 21.7 A film TEM image of shown in inset.

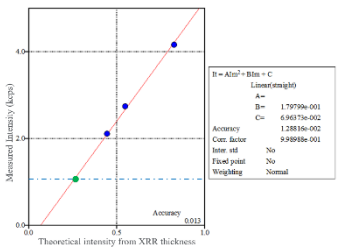


**FIGURE 2.** Fundamental parameter method calibration between calculated intensities and WDXRF measured counts.

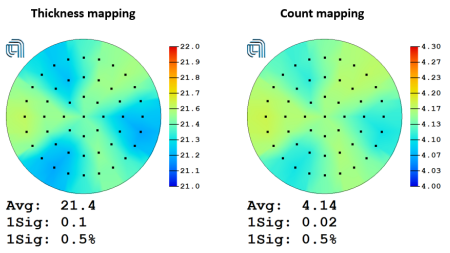


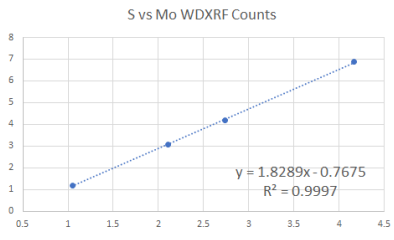

**FIGURE 3.** 49-point WDXRF thickness & count mapping of sample S4 (thickness 21.7 A) indicates good film uniformity.

**FIGURE 4.** WDXRF S-Ka & Mo-La counts good correlation shows constant composition for all 4 films.

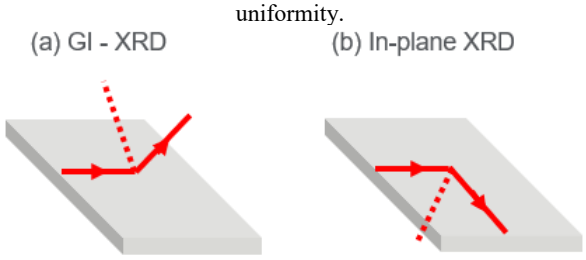


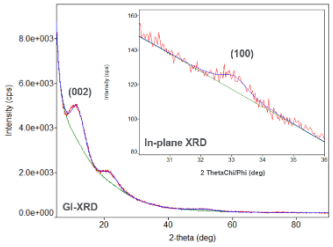


**FIGURE 5.** Schematics illustrate of the XRD measurement geometries of the MoS2 films. XRD data usually measure scatted X-ray intensity as a function of ω and/or 2θ.

**FIGURE 6.** GI-XRD 2θ scan with incident angle 0.5° for S2 (thickness 11.7A). In-plane 2θχ/φ scan with incident angle 0.35° is shown in inset.

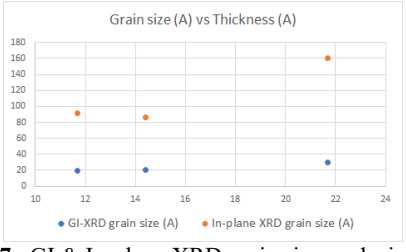


**FIGURE 7.** GI & In-plane XRD grain size analysis shows that in-plane grain size is larger and increases with 2D MoS2 film thickness.

**TABLE 1.** GI and in-plane XRD grain size, XRR fitting thickness, density and WDXRF counts of Mo-La & S-Ka

| Sample ID | GI-XRD grain size (A) (002) | In-plane XRD grain size (A) (100) | XRR fitting thickness (A) | XRR fitting density (g/cm3) | WDXRF Mo-Lα (kcps) | WDXRF S-Kα (kcps) |
|---|---|---|---|---|---|---|
| Film 1 | NA | NA | ***7.0*** | 5.9 | 1.05 | 1.19 |
| Film 2 | 19 | 92 | 11.7 | 6.0 | 2.10 | 3.06 |
| Film 3 | 21 | 86 | 14.4 | 6.2 | 2.74 | 4.20 |
| Film 4 | 30 | 161 | 21.7 | 6.1 | 4.16 | 6.87 |

## REFERENCES

1. K. F. Mak, C. Lee, J. Hone, J. Shan, and T. F. Heinz, *Phys. Rev. Lett.* 105, 136805 (2010).
2. A. Splendiani, L. Sun, Y. Zhang, T. Li, J. Kim, C. Y. Chim, G. Galli, and F. Wang, *Nano Lett.* 10, 1271 (2010).
3. R. Ganatra and Q. Zhang, *ACS Nano*, 8, 4074 (2014).

## KEYWORDS

MoS2, X-ray diffraction (XRD), X-ray reflectivity (XRR), Wavelength Dispersive X-ray fluorescence (WDXRF).

# Complementary Field-Effect Transistors (CFET): Metrology Challenges and Solutions

J. Bogdanowicz[1], A.-L. Charley[1], M. Saib[1], M. Beggiato[1], G. Lorusso[1], V. Brissonneau[1], E. Dupuy[1], R. Loo[1,5], Y. Shimura[1], A. Akula[1], H. Arimura[1], BT Chan[1], D. Zhou[1], N. Horiguchi[1], S. Biesmans[1], P. Leray[1], J. Hung[2], I. Turovets[2], S. Wei[3], P. Hönicke[4] and R. Ciesielski[4]

[1] *imec, Kapeldreef 75, 3001 Leuven, Belgium,*
[2] *Nova Ltd., 5 David Fikes St.,Rehovot 7632805, Israel*
[3] *Hitachi High-Tech Corp.,552-53, Shinkocho, Hitachinaka-shi, Ibaraki, Japan*
[4]*Physikalisch-Technische Bundesanstalt (PTB), Abbestr. 2-12, 10587 Berlin, Germany*
[5] Ghent University, Department of Solid-State Sciences, Krijgslaan 281, building S1, 9000 Ghent, Belgium

## INTRODUCTION

While the industry is transitioning from Fin Field-Effect Transistors (FETs) to nanosheet (NSH) FETs, heavy research is already being carried out to define the next transistor architecture which will allow even more functionality from the same Si area. Complementary FETs (CFETs), whereby two n- and p-NSH transistors are stacked on top of each other, seem to reach a broad consensus [1-3]. Similarly, their monolithic integration, i.e. from a single piece of Si, also appears to be the industry's preferred route. However, monolithic CFET integration comes with an unprecedented level of complexity, which makes metrology and inspection more critical but also more challenging.

In this contribution, we start with a summary of the metrology challenges implied by the complexity of monolithic CFET integration. We then investigate the solution space and highlight existing inline metrology techniques which have the potential to solve CFET's needs. Finally, we demonstrate the concrete use of some of these techniques. We conclude that, although many capabilities remain to be demonstrated, the solution space is broad such that CFET metrology is not expected to suffer from a *capability gap.* However, we foresee a heavier resort to slower solutions, which is likely to lead to a *throughput* or *capacity gap*.

## METROLOGY NEEDS

Compared to NSH transistors, the complexity of monolithic CFET integration comes from (i) the aspect ratio of these devices, (ii) the requirement of a middle dielectric isolation (MDI) between the top and bottom devices and (iii) the separate integration of the top and bottom devices. Metrology will therefore be needed to control these new processing challenges. The most critical metrology capabilities required for control of monolithic CFET integration are summarized in Fig. 1.

In a nutshell, complex material characterization is required for the complex blanket SiGe/Si multilayer and for the gate stack [Fig 1(a)]. Lateral and vertical control is necessary after the vertical fin and gate etches [Fig 1(b)]. The necessary and complex control of lateral etches is amplified by the presence of 2 SiGe materials with different Ge concentrations and a higher aspect ratio [Fig. 1(c)]. Lateral control will also be needed if a cover spacer is used to integrate the top and bottom devices separately. Finally, vertical control is required after the numerous steps of material fill and etch back, e.g. $SiO_2$ and Metal0 [Fig. 1(d)].

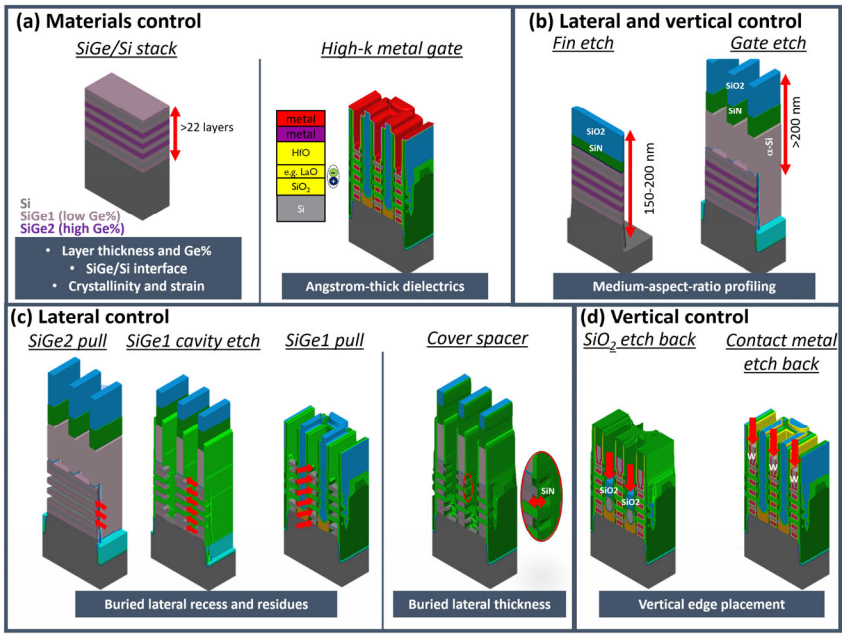


**FIGURE 1.** Summary of metrology challenges for monolithic CFET integration

## METROLOGY SOLUTIONS

Since most of the challenges presented in Fig. 1 require the extraction of information buried deep inside the structure, CFET metrology inherently belongs to the field of 3D metrology. Building on our earlier work focused on 3D logic, 3D memory and 3D interconnects [4], we propose to map the solution space for CFET metrology along two main axes, i.e. lateral resolution and probing depth (Fig. 2). Given the nanometer-scale of CFET devices and their medium aspect ratio, relevant metrology solutions for monolithic CFET integration belong to the bottom left corner indicated by a dotted box.

In the rest of this contribution, we move from the global and strategic evaluation of CFET metrology to concrete demonstrations of the capabilities of a few technologies, i.e. Optical Critical Dimension (OCD) scatterometry, EUV scatterometry/reflectometry or X-ray Fluorescence (XRF) etc, to solve the needs highlighted in Fig. 1.

Our general conclusion is that solutions exist to solve most CFET metrology challenges. However, in too many instances, slow options have to be opted for, which compromises either the speed of the feedback or the level of control. We therefore recommend more focus on a third axis, i.e. the throughput (color scale of Fig. 2), by means of both software and hardware optimizations.

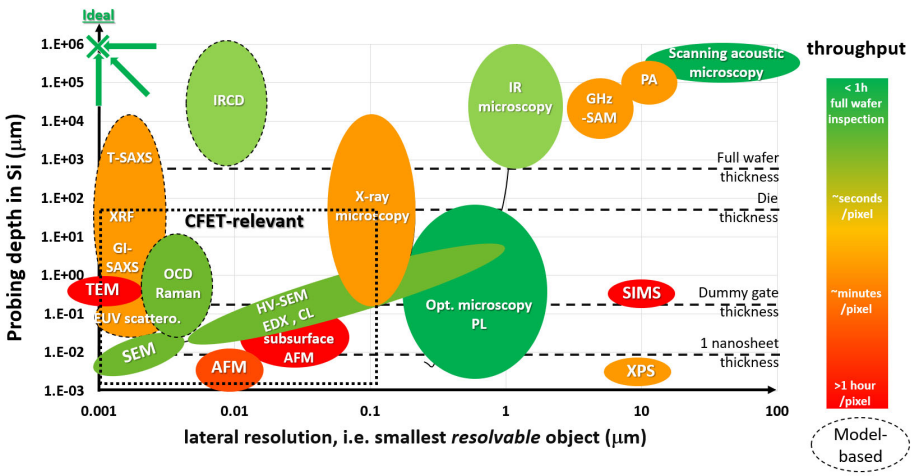


**FIGURE 2.** 3D metrology landscape and solutions relevant to CFET metrology

## REFERENCES

1. Luc van den Hove, *The endless progression of Moore's law*, Proceeding of SPIE Advanced Lithography + Patterning, PC1205301 (2022)
2. S. Liao, *Complementary Field-Effect Transistor (CFET) Demonstration at 48nm Gate Pitch for Future Logic Technology Scaling*, IEDM 2023
3. M. Radosavljević et al., *Demonstration of a Stacked CMOS Inverter at 60nm Gate Pitch with Power Via and Direct Backside Device Contacts*, M. Radosavljević, IEDM 2023
4. J. Bogdanowicz et al., *Semiconductor metrology for the 3D era*, Proc. SPIE 12496, Metrology, Inspection, and Process Control XXXVII, 1249617

## KEYWORDS

CFET, gate all around, 3D metrology

# Asymmetry of Junction Line Defect Distribution in $WS_2$-$WSe_2$ Lateral / Vertical Hetero-structures Revealed by TERS Imaging

Andrey Krayev[1], A. Edward Robinson[1], Peng Chen[2], Xidong Duan[3], Zhengwei Zhang[3], Xiangfeng Duan[4]

*1. HORIBA Scientific, 359 Bel Marin Keys Blvd, Novato, CA94949, USA (415-884-9500)*
*2. Southern University of Science and Technology, Shenzhen, China*
*3. Department of Applied Chemistry, Hunan University, China*
*4. Department of Chemistry and Biochemistry, University of California, Los Angeles, USA*

## INTRODUCTION

2D semiconductors attracted significant attention of the research community in recent years due to combination of unique optoelectronic properties and great promise in diverse applications like optoelectronics, light harvesting and quantum computing. Relative ease of vertical stacking of these Van der Waals materials and possibility of the synthesis of their lateral hetero-sctructures open new horizons in the control of the optoelectronic properties of such hybrid materials and rational engineering of new unique states like vertical or lateral interlayer excitons, defect-bound excitons, quantum localization of the excitons due to extreme mechanical strain etc. In particular, the 1D interface in lateral hetero-structures as well as the vertical multilayers comprised of different 2D semiconductors look specifically attractive in terms of rational design of optoelectronic properties of such hybrid materials. Characterization of the optical properties and chemical composition of the 1D/2D interfaces at the proper length scale, which is often of the order of few nanometers or less, becomes a crucial necessity for further progress in understanding their properties and rational device engineering.

## THE METROLOGY TECHNIQUE

In presented work we report deep-sub-diffraction-limit Raman imaging achieved by means of the tip enhanced Raman spectroscopy (TERS) of lateral and vertical hetero-structures of $WS_2$ and $WSe_2$ transferred to gold.

## Results and Discussion

Thanks to dramatically enhanced sensitivity and spatial resolution enabled by the gap mode TERS, we first observed that within 20-50 nm at the junction line in $WS_2$-$WSe_2$ lateral hetero-structures that grew on top of the bilayer $WS_2$, TERS spectra were clearly different from the core ($WSe_2$ on 2-Layer $WS_2$) vertical hetero-trilayer, showing noticeable intensity of two new peaks at ~ 290 $cm^{-1}$ and ~ 330 $cm^{-1}$. The positions of these two junction-specific peaks were strikingly reminiscent of the $A_1^1$ and $E_2$ modes correspondingly of Janus WSSe structures[1]. Formation of the Janus–type junction was a rather non-trivial, though not totally impossible hypothesis.

In order to probe it, we collected TERS maps of the junction in lateral $WS_2$-$WSe_2$ hetero-monolayers and discovered that junction-specific spectra actually occurred on the $WSe_2$ side of the lateral hetero-structure. With a

certain degree of confidence we can propose that the ~290 $cm^{-1}$ band is the second overtone of the mode at ~145 $cm^{-1}$, as the latter was also evident in the junction-specific spectra and in some cases we even observed a weak peak at ~435 $cm^{-1}$ that would be the third overtone of the 145 $cm^{-1}$ band. TERS spectra on the $WS_2$ side of the lateral $WS_2$-$WSe_2$ hetero-monolayer junction remained practically the same as the TERS spectra of the core $WS_2$.

Junction specific peaks in $WSe_2$ spectra look very similar to the longitudinal acoustic modes at M point which are associated with defects in this material. Therefore we can make the conclusion that defects at the junction in lateral $WS_2$-$Se_2$ hetero-structures are preferentially concentrated on the $WSe_2$ side.

How such asymmetry affects the electronic and optoelectronic properties of the hetero-structures remains a question for further investigation. It is clear, however that there exist important compositional differences, on the scale of nanometers, which must be understood when engineering such hetero-structures; similar variable alloying at hetero-junctions and nanometer-scale variations are seen by TERS in other systems.

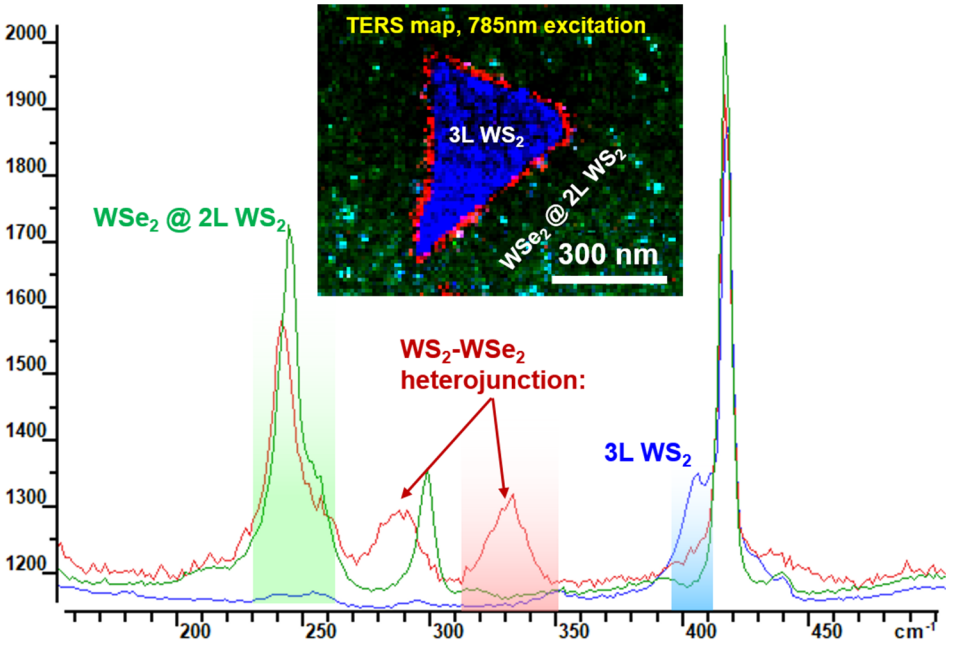


**FIGURE 1.** TERS evidence of variable composition near the lateral hetero-junction between $WS_2$ and $WSe_2$ on 2-layer $WS_2$

## REFERENCES

1. Petrić, M. M.; Kremser, M.; Barbone, M.; Qin, Y.; Sayyad, Y.; Shen, Y.; Tongay, S.; Finley, J. J.; Botello-Méndez, A. R.; Müller, K. Raman Spectrum of Janus Transition Metal Dichalcogenide Monolayers WSSe and MoSSe. Physical Review B 2021, 103 (3). https://doi.org/10.1103/PhysRevB.103.035414.

## KEYWORDS

TERS, Raman, 2D materials, TMDC heterojunctions

# Atom probe tomography using an extreme ultraviolet pulsed light source

Luis Miaja-Avila[1], Benjamin W. Caplins[1], Jacob M. Garcia[1], Ann N. Chiaramonti[1], and Norman A. Sanford[1]

[1]*National Institute of Standards and Technology, Boulder, CO, USA*

## INTRODUCTION

Atom probe tomography (APT) is a powerful materials characterization technique capable of measuring the isotopically resolved three-dimensional (3D) structure of nanoscale specimens with atomic resolution [1-3].

In laser-pulsed APT (LAPT), a nanoscale needle shaped specimen is electrically biased until just before DC field ion emission occurs. A laser pulse is then used to initiate the timed emission of ions from the specimen apex. The identity of the ions can be inferred from the time-of-flight data, while their origination location can be extracted by a combination of the location of the ion signal on the detector and the sequence of detection events. The accumulated information is then used to computationally generate a 3D "reconstruction" of the specimen. Commercially available LAPT microscopes typically use an optical pulse to trigger field ion evaporation—most commonly, the second, third, or fourth harmonic of a solid-state laser ($\sim\lambda$ = 532 nm, 355 nm, or 257 nm).

For optical pulses in the visible to near ultraviolet regions of the spectrum, the LAPT process is commonly understood to be based on transient, laser-induced heating and its efficiency will depend on such specimen-specific properties as optical absorption, heat capacity, and both thermal and electrical conductivities in the presence of a high, static electric field. The progression in LAPT instrumentation from the infrared to the deep ultraviolet wavelengths has continuously produced improved results, e.g., better mass resolution and signal-to-noise ratio in APT mass spectra. At the National Institute of Standards and Technology (NIST) we have pursued a different approach by introducing the possibility of an athermal ion emission pathway through the direct photoionization of the atoms at the specimen's apex using a pulsed extreme ultraviolet (EUV) source [4].

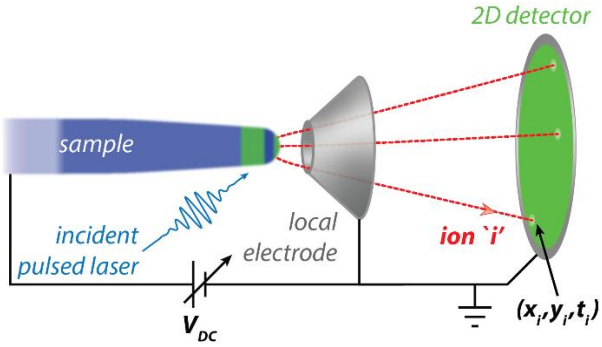


**FIGURE 1.** Schematic representation of laser-pulsed atom probe tomography.

## EUV-ASSISTED ATOM PROBE TOMOGRAPHY

The experimental setup, described in detail by Caplins et al. [5], consists of three main elements: an EUV source, a vacuum beamline, and the atom probe chamber. (1) For EUV light generation we use a Ti:Sapphire

laser system centered at 800 nm with an energy per pulse of 0.5 mJ, a repetition rate of 25 kHz, and a pulse duration of ~ 35 fs. The laser output is focused into a noble-gas filled capillary to produce EUV light through the process of high-harmonic generation [6-8]. (2) Because EUV light is strongly absorbed by all materials, including gases, the beamline must be evacuated to less than $10^{-1}$ Pa ($10^{-3}$ Torr) to avoid significant absorption losses. The elements in the vacuum beamline that connects the EUV source to the APT chamber must transmit sufficient EUV photons to trigger field ion emission from the APT specimens, block any co-propagating 800-nm light from the laser, and allow for the focusing and alignment of the EUV light to the APT specimen's apex. (3) The atom probe chamber is a commercially available LEAP 4000X-Si local electrode straight flight path atom probe tomograph (CAMECA Instruments, Madison, WI) [9]. This atom probe microscope originally came equipped with a 532 nm (green) laser, which was removed for our experiments.

With our newly developed EUV APT microscope we have demonstrated the successful collection of EUV triggered APT data on several specimens including insulators and semiconductor materials. Figure 2 presents data from $SiO_2$, GaN, and InGaN quantum wells in GaN. The $SiO_2$ mass spectra (Figure 2a) shows isotopically resolved peaks from $Si^+$ at 28 m/z, $Si^{++}$ at 14 m/z, and $O^+$ at 16 m/z. Other peaks present in the spectra belong to molecular ions such as $O_2^+$ at 32 m/z, $SiO^+$ at 44 m/z, and $SiO_2^+$ at 60 m/z [10]. Figure 2b presents the EUV APT mass spectra of GaN, a key material in the development of high-power electronics, laser diodes, and light-emitting diodes, among others. The GaN mass spectra also shows clear atomic peaks from the two Ga isotopes and nitrogen. Molecular ion peaks from $N_2$, GaN, and $N_3$ are discernable in the spectrum. Figure 2c shows the TEM image of the sample used for EUV APT, including a representation of the needle-shaped specimen liftout, and the APT 3D reconstruction of the InGaN quantum wells separated by GaN barriers on top of a InGaN buffer layer [11].

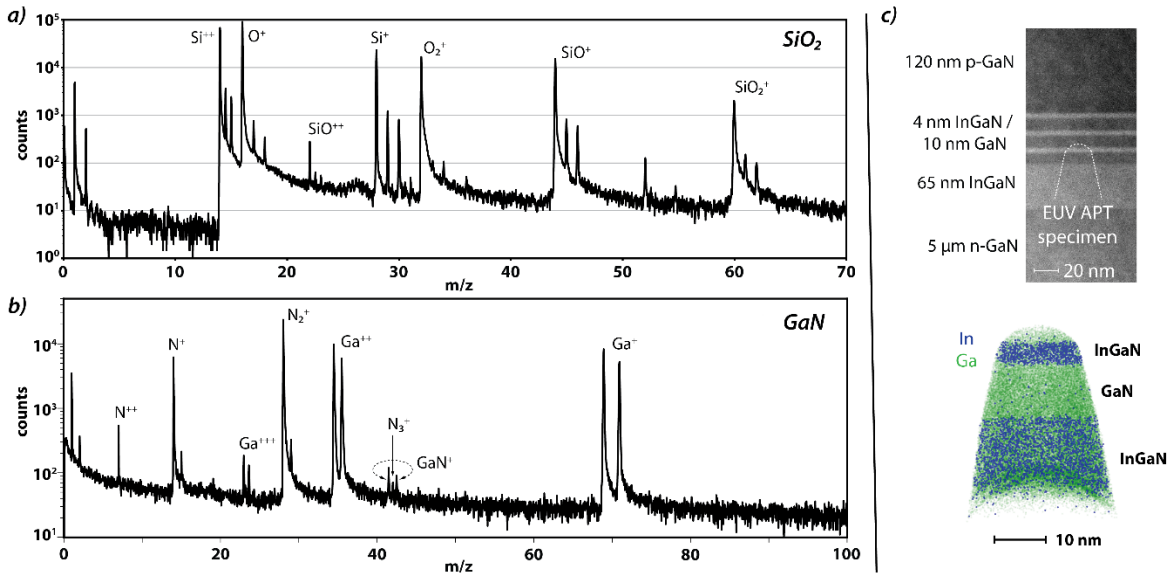


**FIGURE 2.** EUV APT mass spectra of $SiO_2$ and GaN and 3D reconstruction of InGaN quantum well specimen.

## CONCLUSION

The results presented here show that extreme ultraviolet atom probe tomography can be applied to the study of insulator and compound semiconducting samples. Continued work will help to fully understand the benefits of EUV light pulses in the development of LAPT for the field of semiconductor metrology.

## REFERENCES

1. T. Kelly and M. Miller, "Invited Review Article: Atom probe tomography," Rev. Sci. Instrum. 78, 031101 (2007)
2. D. Larson, T. Prosa, R. Ulfig, B. Geiser, and T. Kelly, Local Electrode Atom Probe Tomography (Springer, New York, 2013)

3. M. Miller and R. Forbes, Atom-Probe Tomography: The Local Electrode Atom Probe (Springer, New York, 2014)
4. N. Sanford, A. Debay, B. Gorman, D. Diercks - US Patent 9,899,197, 2018
5. B. Caplins et al., Rev. Sci. Instrum. 94, 093704 (2023)
6. J. L. Krause, K. J. Schafer, and K. C. Kulander, Phys. Rev. Lett. 68, 3535 (1992)
7. A. L'Huillier and P. Balcou, Phys. Rev. Lett. 70, 774 (1993)
8. P. B. Corkum, Phys. Rev. Lett. 71, 1994–1997 (1993)
9. Commercial instruments, equipment, or materials are identified only to adequately specify certain procedures. In no case does such an identification imply recommendation or endorsement by NIST, nor does it imply that the products identified are the best available for the purpose.
10. A. Chiaramonti et al., Microsc. Microanal. 26, 258 (2020)
11. L. Miaja-Avila et al., J. Phys. Chem. C 125, 2626 (2021)

## KEYWORDS

Atom Probe Tomography, Oxides, Semiconductors, Extreme-Ultraviolet Light

# Merging Integrated Photonics and Electron Beams: µeV-Electron-Spectroscopy and Single-Particle Heralding

A. Feist[1,2*], G. Huang[3,4], G. Arend[1,2], Y. Yang[3,4], J.-W. Henke[1,2], A. S. Raja[3,4], F. J. Kappert[1,2], R. N. Wang[3,4], H. Lourenço-Martins[1,2], Z. Qiu[3,4], J. Liu[3,4], O. Kfir[1,2], T.J. Kippenberg[3,4], and C. Ropers[1,2]

*1. Department for Ultrafast Dynamics, Max Planck Institute of Multidisciplinary Sciences, Göttingen, DE*
*2. IV. Physical Institute – Solids and Nanostructures, University of Göttingen, Göttingen, DE*
*3. Institute of Physics, Swiss Federal Institute of Technology Lausanne, Lausanne, CH*
*4. Center for Quantum Science and Engineering, EPFL, Lausanne, CH*
** Contact author: armin.feist@mpinat.mpg.de, +49(0)551 39-26820*

## INTRODUCTION

Electron microscopy is an indispensable technique providing unique insights into heterogeneous nanomaterials and integrated circuits. Beyond static imaging and spectroscopy, new methods allow for quantitative imaging of fast and high-frequency processes [1–3], and novel spectroscopies readily access nanophotonic modes [4]. Meanwhile, photon-based techniques feature capabilities largely unexplored in electron microscopes, including programmable optics, coherent spectroscopy, or quantum-enhanced imaging and sensing. Merging these two realms defines a new frontier in nanometrology and promises a novel class of light-enhanced electron microscopes. However, this requires concepts and technology to interact and detect electrons and photons at the single-particle level.

Here, we present the coupling and manipulation of electron beams with light at an unprecedented efficiency using integrated photonics. This enables continuous-wave laser-driven electron phase modulation, µeV-electron spectroscopy, and the in-situ imaging of on-chip optical modes [5]. Furthermore, we establish the generation of electron-photon pair states featuring contrast-enhanced photonic mode imaging [6]. These advances may also contribute to the in-situ metrology and characterization of functional silicon photonic devices.

## EXPERIMENT

Inside a custom-modified transmission electron microscope (TEM) [7], a continuous electron beam passes parallel to an air-cladded $Si_3N_4$ microresonator (Figs. 1a&2a). The CMOS-compatible integrated photonic platform is fabricated using the photonic Damascene process with low losses and efficient fiber-coupling, allowing for high-quality-factor resonators ($Q \sim 10^6$) [8]. Phase-matched interaction of the electrons with the evanescent field of the chip-bound optical mode provides a unique interlink between electrons and photons. Nanoscale imaging and spectroscopy are performed using an imaging energy filter (CEOS CEFID) equipped with an event-based hybrid pixel detector (ASI EM-Cheetah, Timepix3 ASIC).

### Continuous-Wave Optical Phase Modulation and µeV-Electron Spectroscopy

In the first experiment, the optically-pumped high-Q integrated photonic microresonator (~390-MHz linewidth, ~1-THz free spectral range) facilitates highly efficient continuous-wave optical phase modulation of electron beams [5]. Inelastic electron light scattering (IELS) at the coherent optical field (quasi-TM fundamental mode) produces spectral sidebands in the electron energy distribution [9,10]. At an electron energy of 115 kV, a spectral width of ~160 eV is observed for only 4 mW of optical power coupled to the microresonator (Fig. 1d).

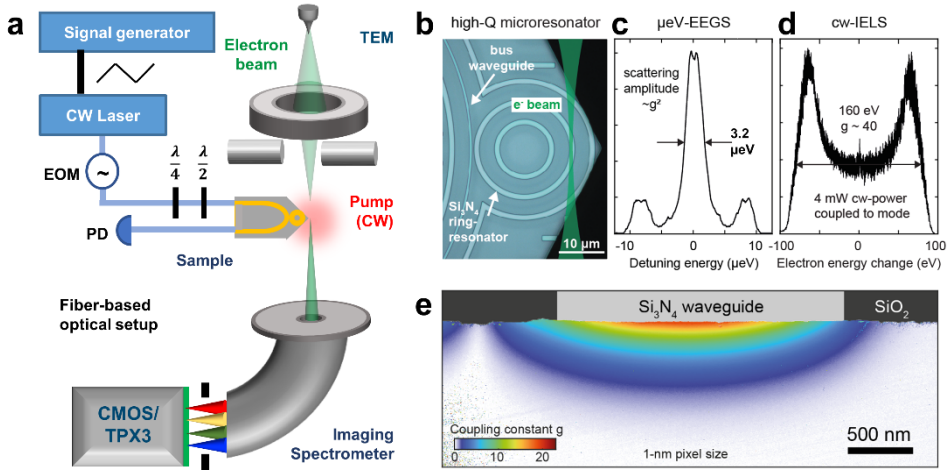


**FIGURE 1.** a) Inside a transmission electron microscope (TEM), an electron beam passes close to a CW-pumped integrated $Si_3N_4$ microresonator in aloof geometry. The laser at a wavelength of 1550 nm can be modulated in frequency and tuned in polarization. b) SEM image of the microresonator chips (side view, electron beam indicated in green) c) Electron energy gain spectroscopy (EEGS) of the resonator mode. d) Typical IELS spectrum using 4 mW of CW optical power. e) Nanometer resolved quantitative mode map reconstructed by stacked EFTEM images (0.8-eV energy slit width).

High-resolution electron energy gain spectroscopy (EEGS) spectroscopy is performed by detuning the laser frequency and recording IELS spectra with a 100-µs time binning, revealing a 3.2-µeV linewidth (Fig. 1c). Finally, the evanescent cavity field of the photonic mode is mapped by sub-eV energy-filtered imaging (Fig. 1e), showing efficient electron phase modulation even at hundredths of nanometer distance to the chip surface.

## Generation of Electron-Photon Pair States and Event-Based Spectroscopy

Secondly, using a low-current stream of electrons, spontaneous scattering at the empty cavity creates electron-photon pair states [6]. Here, the stream of single electrons interacts with the empty resonator, generating cavity photons by inelastic electron-light scattering [11]. The photons are extracted from the cavity, efficiently coupled to a bus waveguide, and detected with a single-photon avalanche diode (SPAD) (Fig. 2b). The electron-light interaction strength is mapped by scanning the focused electron beam (<25-nm focal spot size) above the resonator surface. Spectral filtering of the emission to a single optical mode reveals Ramsey fringes from two sequential transits at the resonator, as recently also observed for the corresponding stimulated interaction [12].

Event-based electron spectroscopy, using the SPAD signal for time tagging, yields time and energy-resolved correlation histograms (Fig. 2c). A strong coincidence peak appears for a loss of about 0.8 eV—the energy of the generated photons (1550-nm wavelength) (Fig. 2d). Selecting events within a narrow energy- and time-interval around this peak enables the unambiguous identification of correlated electron-photons pairs. In analogy to spontaneous parametric down-conversion, this mechanism allows for heralded single-electron or photon sources that we characterize in terms of their heralding efficiencies. In the first application, we use coincidence-gated imaging to suppress noise, thus enhancing the contrast of cathodoluminescence mode maps by two orders of magnitude (Fig. 2e,f).

## CONCLUSION

Ultimately, tailored electron-light interactions and the ability to induce correlated electron/photon states may provide new avenues in electron metrology of nanoelectronic and nanophotonic devices, including new contrast mechanisms and enhanced sensitivity. In particular, photonic integrated circuits can be imaged in situ with µeV-spectral and nanometer spatial resolution. Establishing single-particle coupling is pivotal for the evolving field of free-electron quantum optics [13], promising laser-driven electron optics and high-frequency beam modulators [14], as well as hybrid quantum technology fusing free electrons and light. Conceptually, the coherent coupling between electrons and photons may be transferred to all-integrated hybrid electronic-photonic quantum circuits, building on the recent advances in silicon-based quantum electronics [15–17].

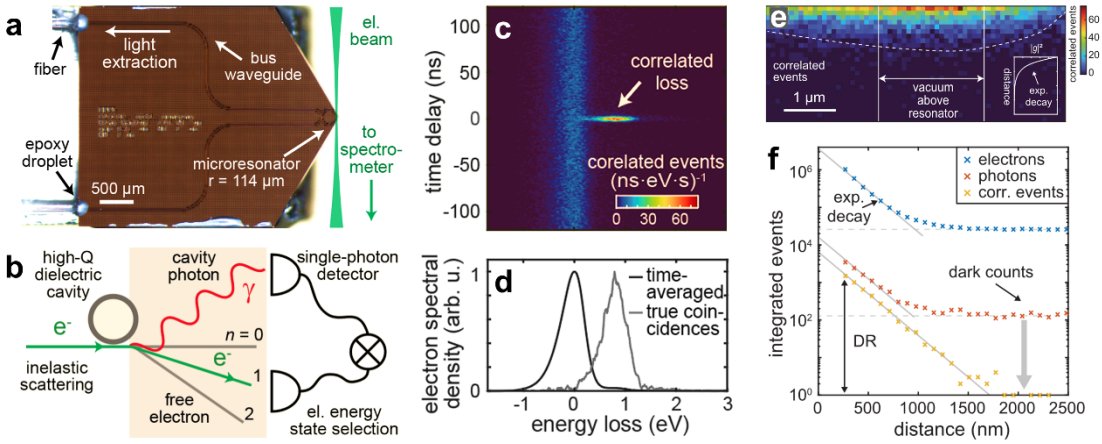


**FIGURE 2.** a) An electron beam (green, illustrated) passes a photonic-chip-based $Si_3N_4$ microresonator (SEM image). b) Spontaneous inelastic scattering at the empty cavity generates electron-photon pair states that are measured in coincidence. c) Two-dimensional correlation histogram over the electron energy and electron-photon delay. A strong energy-shifted peak at zero delay is visible over an uncorrelated background. d) Spectral distribution of the time-averaged background correlated electrons. e) A raster-scanned image of the evanescent cavity field using electron-photon pairs exhibits a strongly suppressed noise and enhanced contrast compared to the individual signal channels.

## REFERENCES


[1] P. A. Midgley and R. E. Dunin-Borkowski, Nature Mater **8**, 271 (2009).
[2] A. H. Zewail, Science **328**, 187 (2010).
[3] R. Frömter, F. Kloodt, S. Rößler, A. Frauen, P. Staeck, D. R. Cavicchia, L. Bocklage, V. Röbisch, E. Quandt, and H. P. Oepen, Applied Physics Letters **108**, 142401 (2016).
[4] A. Polman, M. Kociak, and F. J. García de Abajo, Nat. Mater. **18**, 1158 (2019).
[5] J.-W. Henke, A. S. Raja, A. Feist, G. Huang, G. Arend, Y. Yang, F. J. Kappert, R. N. Wang, M. Möller, J. Pan, J. Liu, O. Kfir, C. Ropers, and T. J. Kippenberg, Nature **600**, 653 (2021).
[6] A. Feist, G. Huang, G. Arend, Y. Yang, J.-W. Henke, A. S. Raja, F. J. Kappert, R. N. Wang, H. Lourenço-Martins, Z. Qiu, J. Liu, O. Kfir, T. J. Kippenberg, and C. Ropers, Science **377**, 777 (2022).
[7] A. Feist, N. Bach, N. Rubiano da Silva, T. Danz, M. Möller, K. E. Priebe, T. Domröse, J. G. Gatzmann, S. Rost, J. Schauss, S. Strauch, R. Bormann, M. Sivis, S. Schäfer, and C. Ropers, Ultramicroscopy **176**, 63 (2017).
[8] J. Liu, A. S. Raja, M. Karpov, B. Ghadiani, M. H. P. Pfeiffer, B. Du, N. J. Engelsen, H. Guo, M. Zervas, and T. J. Kippenberg, Optica **5**, 1347 (2018).
[9] B. Barwick, D. J. Flannigan, and A. H. Zewail, Nature **462**, 902 (2009).
[10] A. Feist, K. E. Echternkamp, J. Schauss, S. V. Yalunin, S. Schäfer, and C. Ropers, Nature **521**, 200 (2015).
[11] X. Bendaña, A. Polman, and F. J. García de Abajo, Nano Lett. **11**, 5099 (2011).
[12] K. E. Echternkamp, A. Feist, S. Schäfer, and C. Ropers, Nature Phys **12**, 1000 (2016).
[13] K. Wang, R. Dahan, S. Nehemia, O. Reinhardt, S. Tsesses, I. Kaminer, O. Kfir, H. Lourenço-Martins, A. Feist, C. Ropers, and T. J. Kippenberg, Optics & Photonics News **31**, 35 (2020).
[14] Y. Yang, J.-W. Henke, A. S. Raja, F. J. Kappert, G. Huang, G. Arend, Z. Qiu, A. Feist, R. N. Wang, A. Tusnin, A. Tikan, C. Ropers, and T. J. Kippenberg, arXiv:2307.12142.
[15] G. Feve, A. Mahe, J.-M. Berroir, T. Kontos, B. Placais, D. C. Glattli, A. Cavanna, B. Etienne, and Y. Jin, Science **316**, 1169 (2007).
[16] X. Mi, M. Benito, S. Putz, D. M. Zajac, J. M. Taylor, G. Burkard, and J. R. Petta, Nature **555**, 599 (2018).
[17] A. M. J. Zwerver, T. Krähenmann, T. F. Watson, L. Lampert, H. C. George, R. Pillarisetty, S. A. Bojarski, P. Amin, S. V. Amitonov, J. M. Boter, R. Caudillo, D. Correas-Serrano, J. P. Dehollain, G. Droulers, E. M. Henry, R. Kotlyar, M. Lodari, F. Lüthi, D. J. Michalak, B. K. Mueller, S. Neyens, J. Roberts, N. Samkharadze, G. Zheng, O. K. Zietz, G. Scappucci, M. Veldhorst, L. M. K. Vandersypen, and J. S. Clarke, Nat Electron **5**, 184 (2022).


## KEYWORDS

electron microscopy, integrated photonics, photonic device characterization, electron-photon pairs, event-based electron spectroscopy, quantum electron microscope

# Characterization of 2D transition metal dichalcogenide layers by combined TOF-SIMS and *in-situ* AFM

Rita Tilmann[1], Stefan Heiserer[2], Valentina Spampinato[1,3], Yuanyuan Shi[1,4], Jill Serron[1], Albert Minj[1], Benjamin Groven[1], Georg S. Duesberg[2], Thomas Hantschel[1], Paul A.W. van der Heide[1] and Alexis Franquet[1]

*1 IMEC, Kapeldreef 75, 3001 Leuven, Belgium*
*2 University of the Bundeswehr Munich & Center for Integrated Sensor Systems (SENS), Institute of Physics, EIT2, 85579 Neubiberg, Germany*
*3 Università degli Studi di Catania, Dipartimento di Scienze Chimiche, Viale A. Doria 6, 95125 Catania, Italy*
*4 School of Microelectronics, University of Science and Technology of China, Hefei, China*

## INTRODUCTION

Two-dimensional (2D) transition metal dichalcogenides (TMDs) with the general formula $MX_2$ (with M being a transition metal and X a chalcogen) promise to be the next-generation semiconductor platform [1–4] providing the sought-after complementary metal oxide semiconductor technology downscaling. In particular, Mo and W disulfide ($MoS_2$, $WS_2$) receive considerable attention in both scientific and industrial research communities in view of their unique chemical, thermal, electrical, and optoelectrical properties [5]. More recently noble metal transition metal dichalcogenides (NTMDs) also gained considerable attention, amongst them PtSe2 and PdSe2 being promising and most importantly air stable candidates for future nanoscale electronics applications. However, the semiconductor and its interfaces become increasingly more difficult to characterize chemically and electrically. Conventional methodologies, including scanning probe microscopies (SPM), fail to capture insight into the chemical nature of the semiconductor, albeit vital to understand its impact on the semiconductor performance. Therefore, this work presents a unique and universal *in-situ* approach combining time-of-flight secondary ion mass spectrometry (TOF-SIMS) and atomic force microscopy (AFM) to map chemical differences between regions of different morphological and topographical appearance.

## RESULTS AND DISCUSSION

Numerous studies have demonstrated the use of TOF-SIMS as an advantageous technique to determine the surface chemistry of nano scaled materials, including more complex composite materials, such as 2D layers and their heterostructures. Previous reports combined the structural information, morphology, and planar chemical composition results from (micro) Raman spectroscopy, AFM and TOF-SIMS on h-BN/graphene heterostructures to reveal the planar chemistry on a virtually atomic level [6].
The thickness of such 2D layered structures can range from bulk material of several tens of nanometers down to only monolayers. Thickness control during growth or processing of the materials is still one major concern since it is strongly correlated with the material properties, such as electrical conductivity, therefore TOF-SIMS was demonstrated as suitable technique to determine the layer number e.g. on multilayer graphene [7].
Finally, implementation of such nano scaled materials also demands for quality control of the materials surface and interface properties concerning oxidation and contamination issues. For this purpose, studies on cleaning procedures with mass selected Gas Cluster Ion Beam (GCIB) were previously reported to promote the removal of hydrocarbons adsorbed to the surface of 2D materials [8]. Another approach for the removal of polymeric residues or hydrocarbons from 2D materials was reported for in-situ annealing in the UHV atmosphere of the TOF-SIMS tool [9], coupled with

simultaneous surface chemistry control. Depth profiling can also be applied to study the chemical composition at heterostructure interfaces or at the contact surface to their growth substrate and dielectrics or contact components of a device structure. Such detailed chemical information is indispensable for the complete integration of 2D materials into functional devices.

In this contribution, we demonstrate the importance of combining TOF-SIMS and different *in-situ* AFM modes to tackle the above-mentioned challenges in 2D material quality control. As an example among others that will be discussed in the paper, we show below conductive AFM (C-AFM) [10] to characterize thin $WS_2$ layers. In this way, it is possible to map chemical differences between regions of different electrical conductivity in the 2D material, thanks to the accurate chemical information achievable with TOF-SIMS combined with the atomic resolution attainable with AFM. We found that $WS_2$ regions of lower electrical conductivity possess a larger amount of sulfur compared to regions with higher conductivity, for which oxygen is also detected. Such difference in chemical composition likely roots from the non-homogeneously terminated sapphire starting surface, altering the $WS_2$ nucleation behavior and associated defect formation between neighboring sapphire terraces [11]. These resulting sapphire terrace-dependent doping effects in the $WS_2$ hamper its electrical conductivity. Thus, we demonstrate how accurate chemical assignment at sub-micrometer lateral resolution of atomically thin 2D semiconductors is vital to achieve a more detailed understanding on how the growth behavior affects the electrical properties.

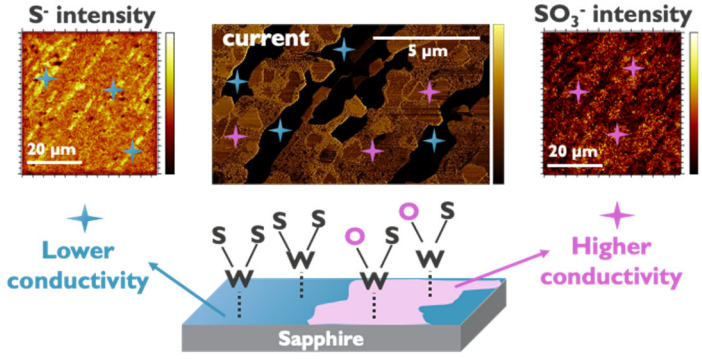


**FIGURE 1.** TOF-SIMS and C-AFM maps of $WS_2$ grown on sapphire with different surface terminations.

## REFERENCES


1. S. B. Desai, S. R. Madhvapathy, A. B. Sachid, J. P. Llinas, Q. Wang, G. H. Ahn, G. Pitner, M. J. Kim, J. Bokor, C. Hu, H.-S. P. Wong, A. Javey, *Science* 2016, 354, 99.
2. D. Akinwande, C. Huyghebaert, C.-H. Wang, M. I. Serna, S. Goossens, L.-J. Li, H.-S. P. Wong, F. H. L. Koppens, *Nature* 2019, 573, 507.
3. D. Akinwande, D. Kireev, *Nature* 2019, 576, 220.
4. N. Flöry, P. Ma, Y. Salamin, A. Emboras, T. Taniguchi, K. Watanabe, J. Leuthold, L. Novotny, *Nat. Nanotechnol*. 2020, 15, 118.
5. K. F. Mak, J. Shan, *Nat. Photonics* 2016, 10, 216.
6. H. Chou, A. Ismach, R. Ghosh, R. S. Ruoff, A. Dolocan, *Nature Communications*, 2015, 6, 7482.
7. I. H. Abidi, L. T. Weng, C. P. J. Wong, A. Tyagi, L. Gan, Y. Ding, M. Li, Z. Gao, R. Xue, M. D. Hossain, M. Zhuang, X. Ou, Z. Luo, *Chemistry of Materials*, 2018, 30, 1718.
8. B. J. Tyler, B. Brennan, H. Stec, T. Patel, L. Hao, I. S. Gilmore, A. J. Pollard, *Journal of Physical Chemistry C*, 2015,119, 17836.
9. W. Xie, L. T. Weng, K. M. Ng, C. K. Chan, C. M. Chan, *Carbon*, 2015, 94, 740.
10. Y. Shi, B. Groven, J. Serron, X. Wu, A. Nalin Mehta, A. Minj, S. Sergeant, H. Han, I. Asselberghs, D. Lin, S. Brems, C. Huyghebaert, P. Morin, I. Radu, M. Caymax, *ACS Nano* 2021, 15, 9482.
11. V. Spampinato, M. Dialameh, A. Franquet, C. Fleischmann, T. Conard, P. van der Heide, W. Vandervorst, *Anal. Chem.* 92 (2020) 11413.

## KEYWORDS

2D materials, transition metal dichalcogenides (TMDs), conductive atomic force microscopy (C-AFM), correlative microscopy, Kelvin probe force microscopy (KPFM), time-of-flight secondary ion mass spectrometry (TOF-SIMS)

# Hard X-ray Photoelectron Spectroscopy (HAXPES) in Material Development

**T. Sloboda, [1] S. Eriksson,[1] M. Lundwall,[1] P. Amann,[1,2] M. Masatake,[3] B. Krömker,[2] T. Wiell,[1] B. Gerace,[4] A. J. Yost, [4] T. Nishihara,[5] T. Hashimoto[1]**

[1] *Scienta Omicron AB, Danmarksgatan 22, 75323 Uppsala, Sweden*
[2] *Scienta Omicron GmbH, Limburger Strasse 75, 65232 Taunusstein, Germany*
[3] *Scienta Omicron Inc. 6-17-10 Minami-Oi Shinagawa-ku, 140-0013 Tokyo, Japan*
[4] *Scienta Omicron Inc. 3222 E. 1st Ave, #521, Denver, CO 80206 United States*
[5] *School of Science and Technology, Meiji University, 214-8571 Kawasaki, Japan*

*Contact author:*
*Tamara Sloboda,*
*phone: +46 18 477 66 21,*
*email: tamara.sloboda@scientaomicron.com*

## INTRODUCTION

Buried interfaces in electronic devices such as batteries, solar cells, transistors etc. are highly chemically sensitive and reliable instrumentation is necessary for material development. While X-ray photoelectron spectroscopy (XPS) is a powerful method to investigate the chemical nature of surfaces, buried interfaces occurring in device electronics are difficult to investigate, since the energies of the excited electrons are often not high enough to travel through the material and to the detector. Most electrons instead scatter inside the material bulk and this prevents their signal from being detected. During the past decades, hard X-rays have been increasingly useful in the photoelectron spectroscopy field[1] due to the higher photon energies, which increase the information depth in the material investigations.

## HAXPES AND XPS APPLICATIONS

Having access to XPS and HAXPES X-ray sources enables measurements of different core levels of the same element, including deep core levels. After excitation, electrons with enough kinetic energy escape the material and reach the detector. With an XPS source, the kinetic energy of most elements is low, thus the obtained information is very surface sensitive. However, with high energy X-rays it is possible to be both surface and bulk sensitive, as electrons stemming from deep core levels will have lower kinetic energy and contain more surface sensitive information. Similarly, electrons stemming from shallow core levels will have higher kinetic energy and contain more bulk sensitive information. This is especially valuable when detecting artefacts formed by sample exposure to different environments (e.g. air, moisture, heat, cold etc.) or by preparation steps known to induce chemical changes on the surface (e.g. sputtering). Scienta Omicron's HAXPES Lab uses a monochromatic Ga Ka metal jet source with excitation energy of 9.25 keV, therefore enabling artefact-free investigations with superior information depth, which clearly extends beyond limits of conventional XPS surface analysis. This unlocks a comprehensive and effective characterisation of your materials. Combined with a hemispherical electron analyzer with a ±30 degree acceptance angle [2], investigation of buried interfaces, operando devices and real-world samples becomes easily achievable. (Fig.1a). [3] Over the years it has proven invaluable in research of semiconductor materials in thin film electronic devices including the operando characterization of bias induced changes in chemical composition of material interfaces. Other applications include polymer materials, metal surfaces and coatings, or even food processing and pharmaceutical industry. This presentation will give an overview of HAXPES applications with a focus on buried interfaces in electronic devices.

## Detection of Buried Nanoparticles

Nanoparticles typically consist of a core surrounded by a protective shell, e.g. a passivation layer in quantum dots for optoelectronics and bioimaging. The shell thickness and chemical composition highly influence the material properties such as conductivity, particle dispersion, molecule adsorption etc. Herein, a series of PMMA coated PTFE nanoparticles was investigated, where the nominal shell thickness, D, was varied between 4.5 and 35.5 nm (Figure 1). The 'off-centre' model is defined by the transmission electron microscopy analysis. While with the standard XPS source (Al Kα) was able to detect only the particles under the thinnest shell, with the Ga Kα source the F 1s signal from PTFE was reliably detected even under 35 nm shell, when the F 1s signal is close to the detection limit. (Fig 1). As the volume fraction of PTFE particles in such core–shell structure is less than 5%, this is an excellent example of reliable detection of a light element with a typically low photoionisation cross-section using Ga metal jet as an X-ray source.

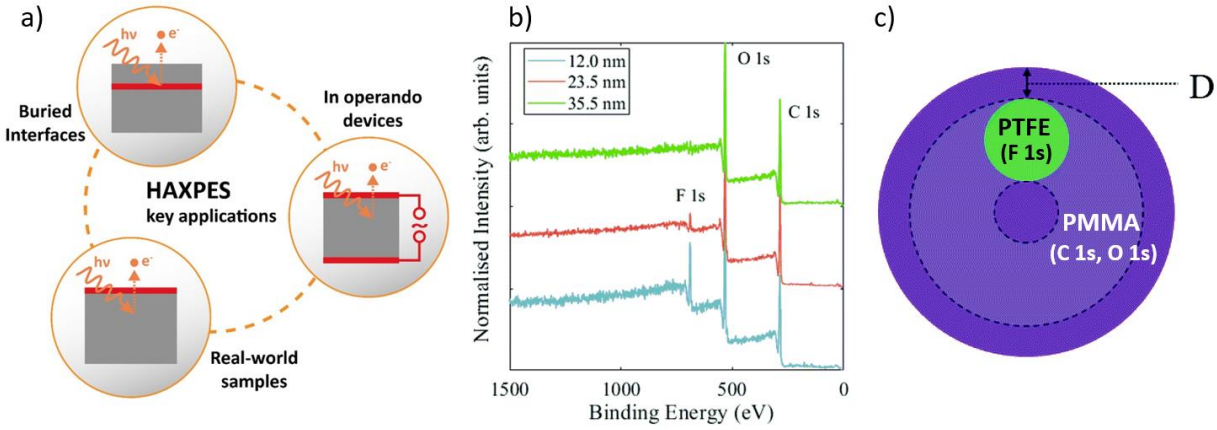


**FIGURE 1.** (a) key applications of HAXPES (b) overview spectra of a PTFE nanoparticle embedded in PMMA shell of different thickness, measured with Ga Kα source in HAXPES Lab. (c) Particle model, where the PMMA shell thickness is marked with D. [2]

## REFERENCES

[1] Kalha, J. Phys. Condens. Matter., 33 (2021) 233001.
[2] B. Spencer, Faraday Discuss., 236 (2022), 311
[3] T. Hashimoto, Vac. Surf. Sci. 64 (2021) 493.

## KEYWORDS

HAXPES, XPS, buried interfaces, bulk, semiconductors, thin films

# Analysis of Alternative Dopants for Organic Light-Emitting Diodes Layers Using a Correlative TOF-SIMS & XPS Protocol

C. Guyot[1], J.P. Barnes[1], O. Renault[1], D. Mariolle[1], T. Maindron[1]

[1]*Univ. Grenoble Alpes, CEA, Leti, F-38000 Grenoble, France*

## INTRODUCTION

Organic light-emitting diodes (OLEDs) have made significant progress since their invention in 1989 and are now widely used for display and lighting applications. There are still improvements to be made in device lifetime, efficiency and luminance to address new applications and to compete with other LED technology. One way this is being done is by exploring new structures, molecules and dopants. To facilitate these developments, there is a need to study the degradation mechanisms in the organic layers in order to attempt to improve device performance [1]. In particular it is extremely important to be able to analyze each individual layer in a thin complex multilayer OLED stack, without damaging the fragile organic layers. Thus, the degradation of the stacks can be evaluated without the risk of confusion with damage from sample preparation or analysis. This requires the use of analysis techniques with good depth-resolution and high sensitivity to small changes in chemical structure such as time of flight of secondary ion mass spectrometry (TOF-SIMS) and X-ray photoemission spectroscopy (XPS).

## STUDY OF NEW DOPANTS USING A CORRELATIVE PROTOCOL

The use of Ag to replace Ca as a dopant was recently demonstrated [2] in 2019 and has the advantage of being more air-stable and easier to handle in a production environment. We therefore decided to test Ag doped BPhen (4,7-Diphenyl-1,10-phenanthroline) to replace Ca doped BPhen in a standard OLED stack and also in a set of simplified test samples where the BPhen layer is sandwiched between two electrodes. One sample is grown with a calcium doped BPhen layer another with a silver doped BPhen layer. An undoped control sample was grown also.

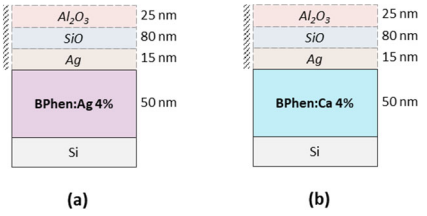


**FIGURE 1.** Structure of test samples of a doped BPhen layer sandwiched between two electrodes (a) the sample is grown with a Ca-doped BPhen layer and (b) the sample is grown with a Ag-doped BPhen layer.

In this study we use a correlative protocol to combine TOF-SIMS and XPS measurements on exactly the same sample area. Firstly the inorganic capping is removed using adhesive tape prior to sputtering with the argon cluster beam to avoid artefacts due to the very different sputter rates of inorganic and organic material. Then an argon cluster ion beam is used to sputter away material to access different depths within the layer of interest.

The sample is transferred between the two techniques in a dry $N_2$ atmosphere.

Firstly we performed TOF-SIMS mass spectrometry on the Ag doped BPhen layer to check the quality of the film deposition. A peak at a mass-to-charge ratio (m/z) of 439 is observed that could correspond to a Ag-BPhen complex. This peak was then analyzed using tandem mass spectrometry in a Physical Electronics NanoTOF II TOF-SIMS instrument. The selected peak is deviated into a collision cell where it is fragmented by collisions with argon gas atoms. The ionized fragments are then accelerated to a second time of flight detector. The spectrum shown in figure 2 shows that the peak at m/z 439 is fragmented into Ag and BPhen-$H^+$ molecular ions confirming the formation of a Ag-BPhen complex.

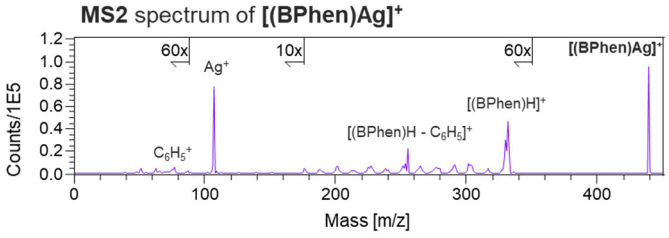


**FIGURE 2.** Tandem MS spectra of the peak at m/z 439 revealing the presence of $Ag^+$ and $BPhenH^+$ fragments

Then XPS analysis was performed on the same layers. The C 1s and N 1s spectra shown in Fig. 3 show a 0.6 eV peak shift to higher binding energy that is consistent with an n-type doping for both Ag and Ca doped films in comparison to the undoped BPhen film.

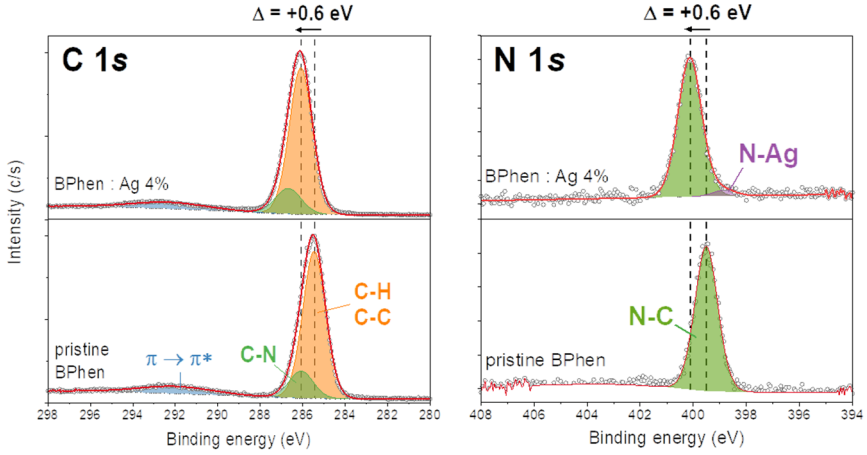


**FIGURE 3.** XPS data: high resolution C 1s and N 1s core level spectra of Ag (top), undoped (bottom) BPhen films showing a shift Shift towards higher binding energy (Δ = +0.6 eV) characteristic of n type doping

In order to assess the stability of the Ag-doped film compared to that of the Ca-doped one, both films were depth profiled after different air exposure times ranging from a few minutes to several hours. The silicon interface width in the depth profile is plotted in figure 4(a). In the case of the Ca doped films the silicon interface width increases rapidly with air exposure time. Even at a short air exposure time of 30 minutes the film has an RMS roughness of 1.25 nm (figure 5(a)), which is over four times that of the Ag doped film after the same air exposure time (it was not possible to perform the measurement at shorter exposition times as AFM was performed under air). This roughening is attributed to crystallization of the Ca-doped BPhen film. For the Ag-doped film the interface width remains constant until air exposure times greater than 40 hours. The fact that the film does not roughen before is confirmed by AFM measurements that show 0.35 nm RMS roughness after 30 minutes (figure 5(b)), and 0.36 nm after 26 hours air exposure. To investigate whether more subtle changes are occurring we used the detection of backscattered Argon clusters as this has been shown to give information on the mechanical properties of polymer films [3, 4]. Fig. 4b shows the ratio of $Ar^+_2/Ar^+_2 + Ar^+_n$ where n = 3 or 4 increases, consistent with a hardening of the film, after 4 hours of air exposure. These results confirm an improved stability of Ag-doped vs Ca doped films.

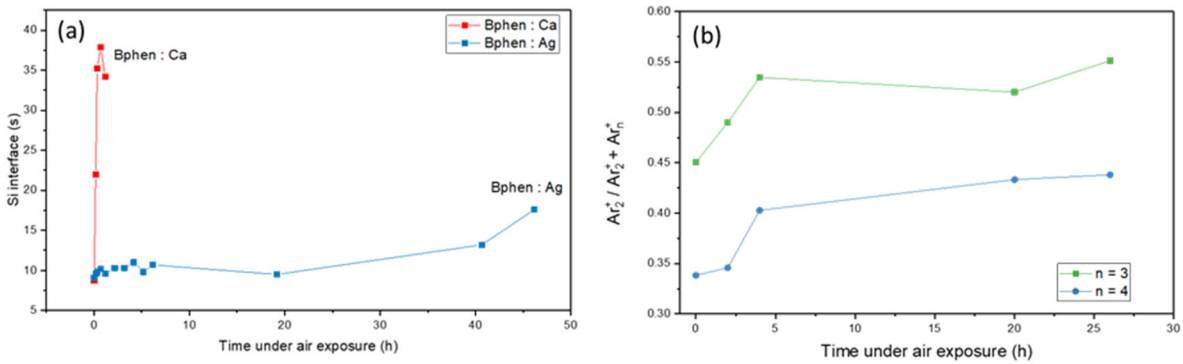


**FIGURE 4.** (a) evolution of the silicon interface width as a function of time, (b) evolution of the backscattered Argon cluster signal showing an increase in the $Ar^+_2/Ar^+_2 + Ar^+_n$ where n = 3 or 4 indicating a hardening of the layer with time.

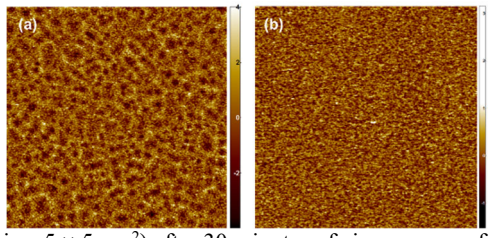


**FIGURE 5.** AFM images (field of view 5 × 5 µm$^2$) after 30 minutes of air exposure of (a) Ca doped film, RMS 1.25 nm, Z-Range 11.99 nm (b) Ag doped film, RMS 0.35 nm, Z-Range 4.68 nm

## CONCLUSIONS AND PERSPECTIVES

A correlative approach using TOF-SIMS and XPS has been used to investigate the use of Ag as an alternative dopant to Ca in the BPhen layer of an OLED device. The interest of Ag as a dopant is confirmed and work is in progress to study electrical ageing in Ag doped devices using a bevel crater approach in order to limit damage to the organic layers [5]. The air exposure experiments also highlight the importance of performing such correlative work using a vacuum or protective environment transfer system.

## ACKNOWLEDGEMENTS

This work, carried out on the Platform for NanoCharacterisation (PFNC), was supported by the “Recherches Technologiques de Base” programme of the French National Research Agency (ANR).

## REFERENCES

1. Scholz, S., et al. Chemical Reviews, **115**(16) 8449-8503 (2015)
2. Z. Bin, *Nature communications,* **10**, 866, (2019*)*
3. Poleunis, C. et al *J. Am. Soc. Mass Spectrom.* **29**, 4–7 (2018)
4. Inui N., et al *International Journal of Applied Mechanics* **08** 03 1650041 (2016)
5. Guyot et al *Surf. Int. Anal. Notes and Insights early version* https://doi.org/10.1002/sia.7277 (2023)

## KEYWORDS

OLEDs, TOF-SIMS, XPS, bevel crater, Argon cluster sputtering, tandem MS

# SPATIALLY RESOLVED CHEMICAL METROLOGY ON EUV RESIST

Komal Pandey[1], Quentin Evrard[2], Albert M. Brouwer[2], C.B. Chuang[1], Maarten van Es[1], Diederik J. Maas[1]

[1]*TNO, Stieltjesweg 1, 2628CK, Delft, The Netherlands*
[2]*University of Amsterdam, Science Park 904, 1090 GD Amsterdam, The Netherlands*

## INTRODUCTION

Over time, the semiconductor industry has pursued device scaling by adopting smaller lithographic wavelengths. With the recent shift to extreme ultraviolet (EUV) lithography, the patterning challenge has shifted to reducing the stochastic effects. Managing stochastic effects becomes highly challenging when dealing with EUV resists, which require ten times fewer photons compared to ArF systems and necessitate a thickness of less than 100 nm to produce smaller features. Random variations in photon absorption within a photoresist, the stochastic distribution of various molecular components in the resist, and the probabilistic interaction of resist molecules with photons, all collectively contribute to the emergence of stochastic effects[1]. In addition to the local variation of the critical dimension (CD), the stochastic failures may take a form of micro-bridging, broken lines, or missing or merging contacts. These failures are random, isolated, and non-repeating in nature. Traditionally, the industry has dealt with the local variation in CD by quantifying line edge/width roughness (LER/LWR) for line or space printing and local CD uniformity (LCDU) for contact or dot printing[2]. These measures are in turn major contributors to Edge Placement Error (EPE). Understanding the sources of stochastic effects, and the ability to monitor these at all stages of the resist processing, can be expected to help significantly improve EPE. The patterning process in semiconductor manufacturing can be broadly divided into two main stages (see figure 1). The first stage deals with resist patterning, encompassing various procedural steps to imprint mask patterns onto the resist. The second stage consists of additional processing steps for transferring the resist pattern onto the wafer. Quantifying above mentioned stochastic effects require adequate metrology, which is typically performed after the first stage when the pattern has been transferred into the resist. The absence of commercial metrology tools capable of assessing pattern quality already before the development step hampers our ability to identify and monitor the most critical sources of such stochastic effects. Ideally, one would want to obtain spatially resolved chemical information about the resist at each processing step during resist patterning to understand the underlying chemistry responsible for producing the final spatial patterns in resist. In this presentation, we will demonstrate the utility of infrared-atomic force microscopy (IR-AFM) in obtaining crucial chemical information at different resist processing steps. First, we focus on quantifying the molecular inhomogeneity within virgin resist using IR-AFM. Then we extend this approach to obtain a dose response curve of resist by measuring latent resist images. In view of our long term goal of introducing IR-AFM as metrology solution for assessing pattern fidelity, this work is the first step in gaining the full understanding of various photon induced chemical reactions a resist.

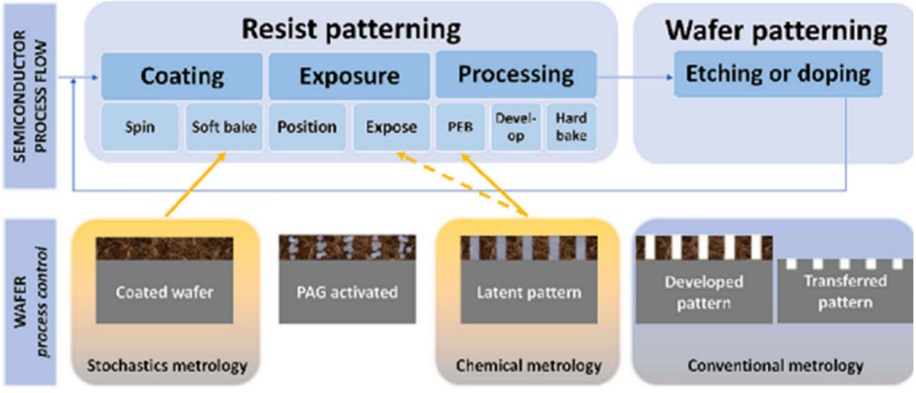


**Figure 1:** Semiconductor process flow. The two main stages, i.e., resist patterning and wafer patterning are illustrated schematically. The picture illustrates that the conventional metrology is performed only after resist patterning is done whereas IR-AFM enables metrology at earlier processing steps. This opens new opportunities for process control

## IR-AFM MEASUREMENT CONCEPT

In IR-AFM, a tunable mid-IR laser is focused on to a sharp, metal coated AFM tip. When the tip-cantilever system is brought closer to the sample, the electromagnetic field enhancement near the tip apex results in the highly localized forces acting between the tip and the sample. Essentially, the light-matter interaction underneath the tip leads to either the thermal expansion of the sample or the induction of dipoles within the sample and the tip[3,4]. Depending on the nature of the interaction forces involved, the tip experiences repulsive or attractive forces that are mechanically detected by the AFM cantilever. We used a commercial Vista One system by Molecular Vista, which is equipped with Block Engineering QCL mid-IR laser. For measuring topography, second eigen mode ($f_2$) of the cantilever is used by the AFM feedback system. The IR laser is pulsed at a frequency, $f_m$. The nonlinear nature of the tip-sample interaction forces acts as a frequency mixer and produces a response also at frequencies equal to the sum and differences of the second eigen mode of cantilever and the laser pulsed frequency. Since the laser pulsed frequency was chosen such that it is equal to the difference of the second and the first eigen mode of the cantilever, i.e., $f_m = f_2 - f_1$ , the response produced at $f_1$ is detected to record the photo-induced forces.

## RESULTS AND DISCUSSION

A resist based on organometallic compound, TinOH, was used in all the measurements presented henceforth. The tin oxo cages, forming the inorganic core of the resist, are positively charged clusters each consisting of twelve tin atoms bridged by oxygen. Butyl groups attached to each tin atom form the surface layer. The tin oxo cage has a net charge of +2, which is compensated by two hydroxide ($OH^-$) anions . Upon exposure to EUV, tin-carbon bonds break, generating radicals that react with neighboring clusters, forming cross-links. This process enables cluster agglomeration, ultimately triggering a solubility switch in the resist[5]. Figure 2 depicts the IR-AFM images taken on a 40 nm thick TinOH resist, which was spin-coated on a silicon substrate but not exposed or processed further. In our experiment, the IR-laser was initially tuned to a wavenumber of 1252 $cm^{-1}$ for scanning a 500x500 $nm^2$ region. Subsequently, the same area was scanned with the IR laser set at 1560 $cm^{-1}$, capturing both chemical and topographic images each time. Any lateral drift caused by thermal drift was mitigated by cropping all the images such that only the region common in both topography images was considered for identifying differences in the IR maps. Comparing the two collected IR maps revealed valuable insights into the chemical uniformity of the unexposed resist. As depicted by white arrows, a triangular feature, initially faint in figure 2b became notably brighter in figure 2d. The IR absorbance at 1560 $cm^{-1}$ is expected to originate from $OH^-$ ions whereas 1252 $cm^{-1}$ is attributed to the tin cluster. Overlaying the two IR maps (figure 2e) showed that different regions are highlighted at different wavenumbers, representing domains of different resist components. Power spectral density (PSD) analysis performed on topography and IR data suggests that measuring topography does not provide a complete picture of the resist inhomogeneity. While we obtained similar PSD curves for both topography measurements, the PSD curves obtained for the two IR maps differ significantly. Although the overall intensity of the images at both IR wavelengths is not significantly different, the PSD for the $OH^-$ component has much larger amplitude at low spatial frequencies. Also, the slope of the PSD curves suggests that spatial variation of the $OH^-$ ion concentration is distributed over smaller length scales (10-30 nm) in comparison to the tin-cluster (~100 nm). The interpretation of this observation is not yet immediately clear to us. It may be for example that the film contains microscopic aggregates or even small crystalline regions. The fact we are now asking these questions shows the relevance of being able to observe the resist with this detail. Any stochastic failures that we measure post resist patterning arise from the propagation of probabilistic events occurring at each processing step. In this context, our results on unexposed resist become significantly important for two reasons. Firstly, they indicate that we do not have a chemically uniform resist to start with and resist manufacturers must tune their processes to achieve desired chemical uniformity. Secondly, these results present an opportunity for the industry to delve deeper into understanding relative contributions of each process step to the final pattern quality and thereby to optimize the resist processing dependent on the observed heterogeneities.

Following the measurements on unexposed resist, the latent line space patterns were imaged using IR-AFM. The exposure step was conducted on the XIL-II beamline at Paul Scherrer Institute in Switzerland. Line space patterns of 100 nm pitch were made with EUV dose ranging from 5 $mJ/cm^2$ to 150 $mJ/cm^2$. IR-images were obtained for different exposure doses and the chemical contrast versus dose curve was plotted. Figure 2 illustrates this experiment. Three exemplary IR-maps taken at 1252 $cm^{-1}$, representing under, optimal, and over exposed situations are shown in figures 3a, 3b, and 3c, respectively. The relative positions of the dose corresponding to these IR maps are marked by dotted circles on the resist's Hurter-Driffield (H-D) curve[6], shown in figure 3e. Clearly, the chemical contrast of under exposed region is lowest and the over exposed region showed the maximum chemical contrast. Corresponding topography images are also presented in figures 3f-3h. Literature suggests that in the case of organometallic resist, increasing the photon dose leads to the homolytic cleavage of the tin-carbon bond, thereby allowing the clusters to combine[5]. Following this argument, we expect that the EUV exposed regions should be deprived of the surface layer of butyl, making a recess in the topography. The topography data collected for various doses (figure 3d) agree well with this hypothesis and a monotonic increase in the depth of the exposed region was seen. Similarly, the contrast of the IR images also increases linearly with dose (figure 3f). Note that the contrast value obtained from the IR maps show high similarity with the resist H-D curve when plotted as a function of the exposure dose. H-D curves provide information about the resist's response to the exposure dose. However, they are not independent of the process parameters, such as post-exposure bake (PEB) temperature, developer strength, development duration etc. In order to understand and eventually control the stochastic effects, isolating the impact of each process parameter on the resist behavior is necessary. The contrast curve from IR-AFM does not contain any information about PEB or development, and yet look similar to the H-D curve. Although it is too early to rule out any impact of

these parameters on TinOH response to the EUV dose, a systematic IR-AFM measurements on such latent images can provide the true chemical response of the resist towards the photon exposure.

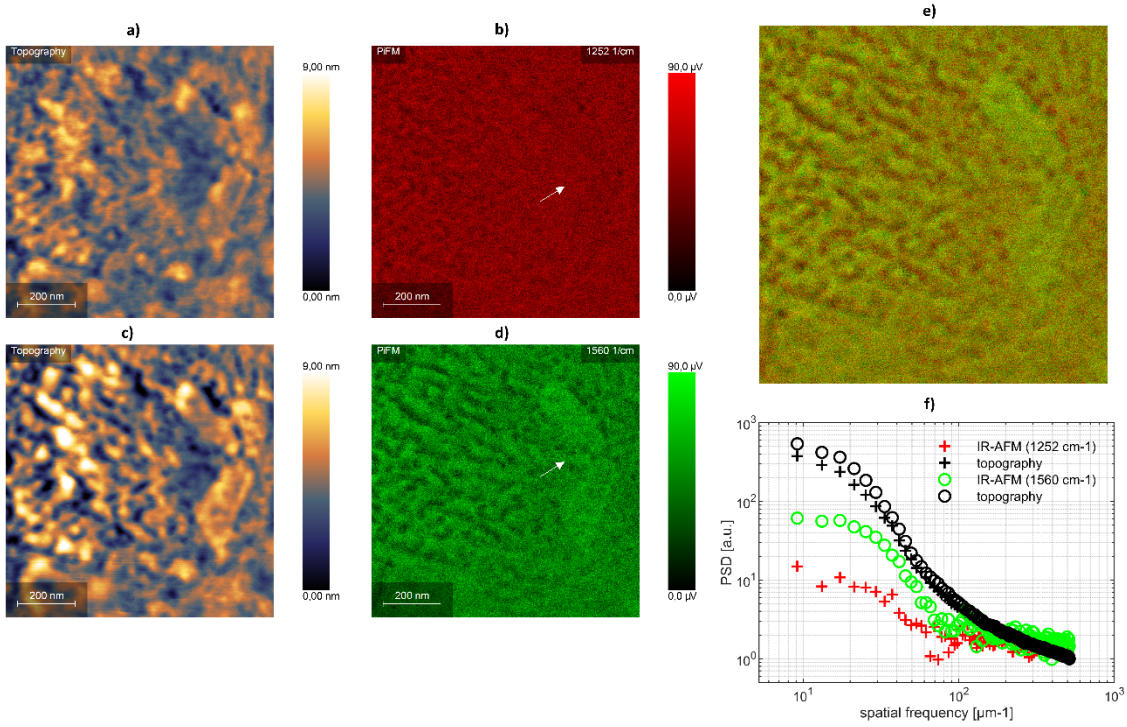


**Figure 2**: IR-AFM on unexposed TinOH: a)topography and b) IR images obtained with IR wavenumber set to 1252 $cm^{-1}$. Same area was scanned again to get c) topography and d) IR images for 1560 $cm^{-1}$ wavenumber. The two IR maps were superimposed in e) to visualize the spatial distribution of the resist components representing the two IR absorbance.

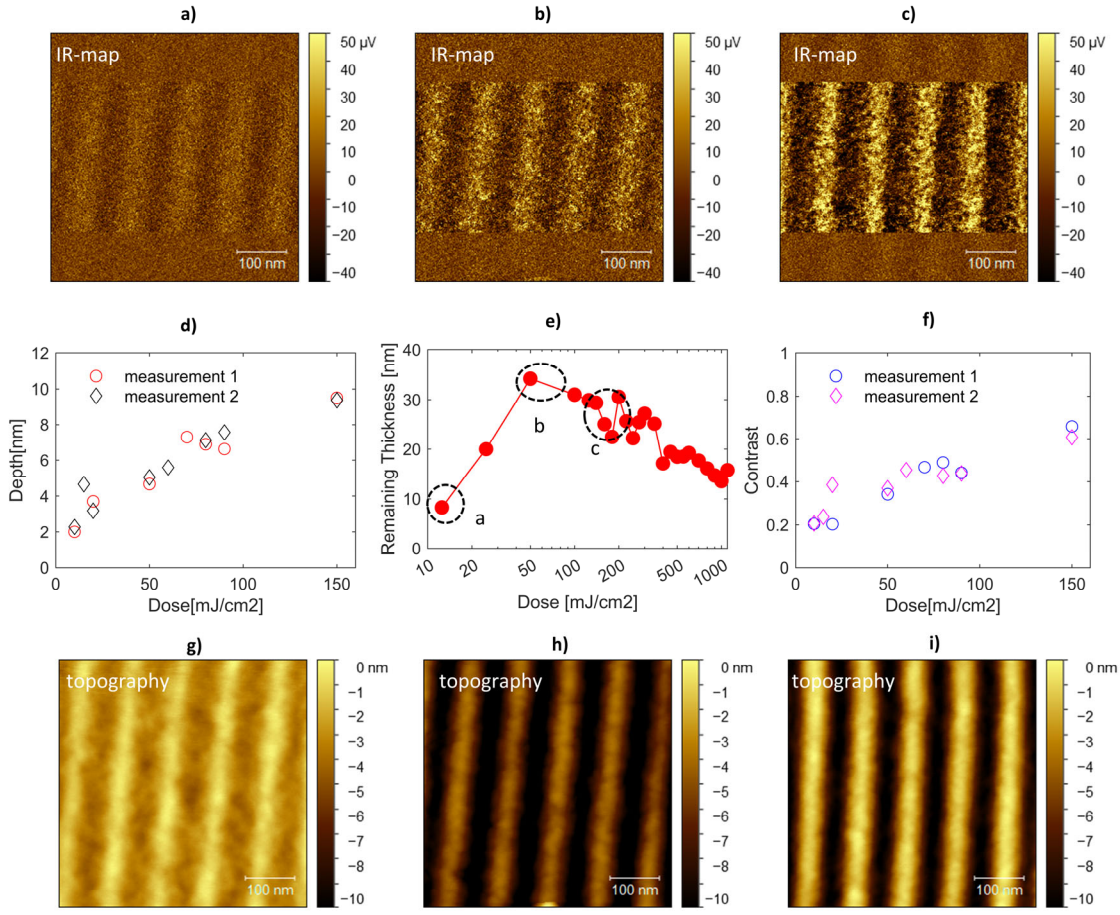


**Figure 3**: The IR-AFM experiment conducted on latent line/space patterns. The IR-maps were obtained for various dose of which the images obtained on a) an underexposed, b) optimally exposed, and c) over-exposed regions are shown here. Corresponding topography maps on the latent patterns are depicted in g), h), and i). When plotting the data for all the measured doses, a linear increase in the d) depth of the exposed region was observed, consistent with the known after-development dose-response curve for this resist depicted in e). Similarly, f) the chemical contrast as calculated from the obtained IR-maps also show a linear increase with the dose.

The measurements in any scanning probe based method are highly dependent on the quality of the tip used. Therefore, to be able to extract reliable information, the technique must provide reproducible outputs. To evaluate reproducibility, the measurements on the same sample were repeated twice, each time with a fresh tip. It goes without saying that with the tip change, the measurements parameters also change. The contrast curves obtained for the two measurement runs are plotted in figure 2f. Note that one measurement run means a series of scans taken on regions exposed with different doses. Since the order in which different regions were scanned was not same in the two measurement runs. If present, tip degradation would have impacted the contrast curve. The fact that we did not observe any significant difference in the two contrast curves encourages us to believe that the measured quantity remains reproducible despite the changing the measurement conditions. Still, tip-related artefacts are observed from time to time. We plan to cater this issue in the near future.

## Conclusion

This work demonstrates the capabilities of IR-AFM in measuring the roughness pertaining to different chemical components of the resist, and ultimately in determining the pattern quality at earlier process steps. The achievement of reproducible dose-contrast curves on latent images paves a way forward in integrating the technique as a metrology method in the semiconductor manufacturing. Apart from its utility in FAB environment, resist manufacturers and failure analysts could also benefit from metrology of resist stochastics.

## REFERENCES

(1) Shot Noise: A 100-Year History, with Applications to Lithography. *J. MicroNanolithography MEMS MOEMS* **2018**, *17* (04), 1. https://doi.org/10.1117/1.JMM.17.4.041002.

(2) Constantoudis, V.; Patsis, G. P.; Leunissen, L. H. A.; Gogolides, E. Line Edge Roughness and Critical Dimension Variation: Fractal Characterization and Comparison Using Model Functions. *J. Vac. Sci. Technol. B Microelectron. Nanometer Struct. Process. Meas. Phenom.* **2004**, *22* (4), 1974–1981. https://doi.org/10.1116/1.1776561.
(3) Nowak, D.; Morrison, W.; Wickramasinghe, H. K.; Jahng, J.; Potma, E.; Wan, L.; Ruiz, R.; Albrecht, T. R.; Schmidt, K.; Frommer, J.; Sanders, D. P.; Park, S. Nanoscale Chemical Imaging by Photoinduced Force Microscopy. *Sci. Adv.* **2016**, *2* (3), e1501571. https://doi.org/10.1126/sciadv.1501571.
(4) Jahng, J.; Kim, B.; Lee, E. S.; Potma, E. O. Quantitative Analysis of Sideband Coupling in Photoinduced Force Microscopy. *Phys. Rev. B* **2016**, *94* (19), 195407. https://doi.org/10.1103/PhysRevB.94.195407.
(5) Cardineau, B.; Del Re, R.; Marnell, M.; Al-Mashat, H.; Vockenhuber, M.; Ekinci, Y.; Sarma, C.; Freedman, D. A.; Brainard, R. L. Photolithographic Properties of Tin-Oxo Clusters Using Extreme Ultraviolet Light (13.5nm). *Microelectron. Eng.* **2014**, *127*, 44–50. https://doi.org/10.1016/j.mee.2014.04.024.
(6) J. Haitjema, Y. Zhang, M. Vockenhuber, D. Kazazis, Y. Ekinci, and A. M. Brouwer. Extreme ultraviolet patterning of tin-oxo cages. J. Micro/Nanolitho., MEMS, MOEMS, 2017, 16, 033510-033517. https://doi.org/10.1117/1.JMM.16.3.033510

## KEYWORDS

Metrology, IR-AFM, Lithography, EUV resist, latent image, stochastics

# Development of a double mirror $C_C$-$C_S$-corrector for Low-Voltage SEM

Maas, Diederik[1,2], Krielaart, Maurice[1], van Velzen, Léon[1], Kruit, Pieter[1]

[1]*Delft University of Technology, Applied Sciences, Lorentzweg 1, Delft, 2628 CJ, The Netherlands,*
[2]*Netherlands organisation of Applied Science (TNO), Stieltjesweg 1, Delft, 2628 CK, The Netherlands*

## INTRODUCTION

A long-standing challenge in Low-voltage SEM is the cancellation of the objective lens aberrations by a practical corrector. This poster reports on the development of a double mirror corrector for simultaneous correction of the chromatic ($C_C$) and spherical ($C_S$) aberration.

The imaging resolution of a LV-SEM is primarily limited by optical properties of the objective lens. To reduce the effect of this limitation, cancellation of the objective lens aberrations is required [1]. Aberration corrector concepts that rely on multipole or mirror configurations have been realised in the past [2] [3] [4] [5] [6]. However, most are either too complex for productization, or rather difficult to operate, while all have very strict tolerances on beam alignment and stability of the power supplies [7]. Recently, the development of a double mirror corrector (DMC) has started at TUD [8]. Except for the mirror pair, the DMC consists of conventional optical elements like lenses, deflectors and a stigmator. Such translates in relatively relaxed requirements on the power supplies. A condenser system and the EBE beam separator [9] inject the electron beam into the mirror cavity (**FIGURE 1FIGURE 1a**). The double reflection of the beam in the cavity provides for an easily adjustable amount of negative chromatic and spherical aberration. After reflecting of both mirrors once, the EBE beam separator deflects the beam back onto the microscope optical axis. After proper adjustment of demagnification of the DMC to the objective lens by a transfer lens (**Figure 1d**), the SEM optics is corrected for chromatic and spherical aberrations (**FIGURE 2**). Secondary aberrations are reduced by accurate alignment of the beam to the mirrors and the objective lens.

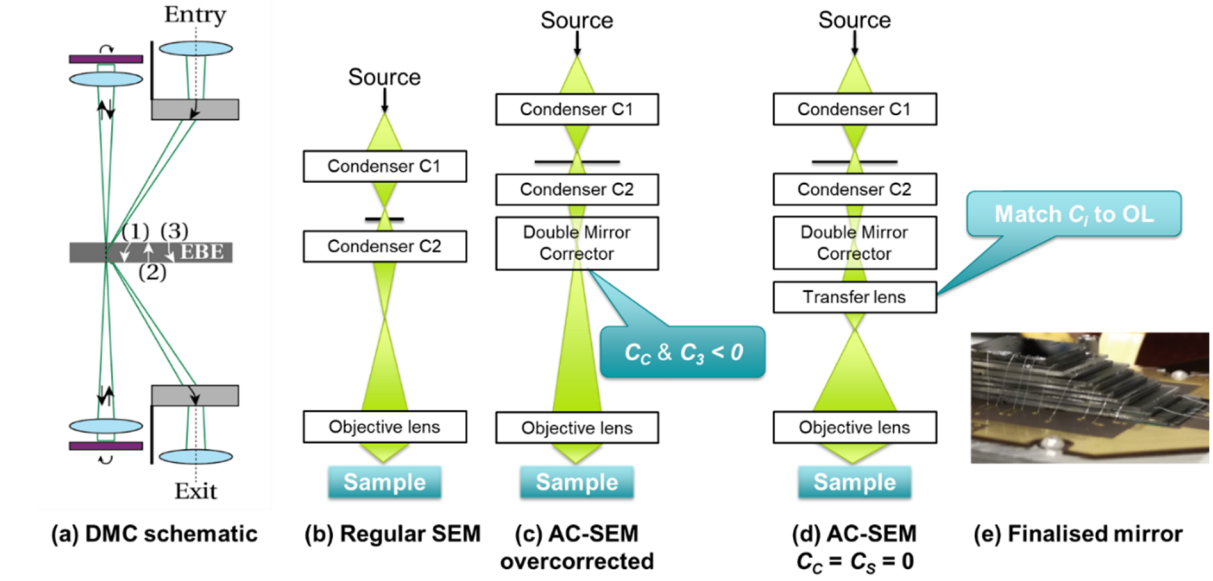


**FIGURE 1.** (a) Schematic of the double mirror corrector elements with the electron trajectory inside the DMC (b) Conventional uncorrected SEM column configuration. (c) Placement position for the DMC in the column as used to demonstrate negative aberrations by the DMC (d) Column with a transfer lens between the DMC and objective lens, enabling optimal matching of the aberrations for imaging at improved resolution. (e) Picture of a completed MEMS mirror stack.

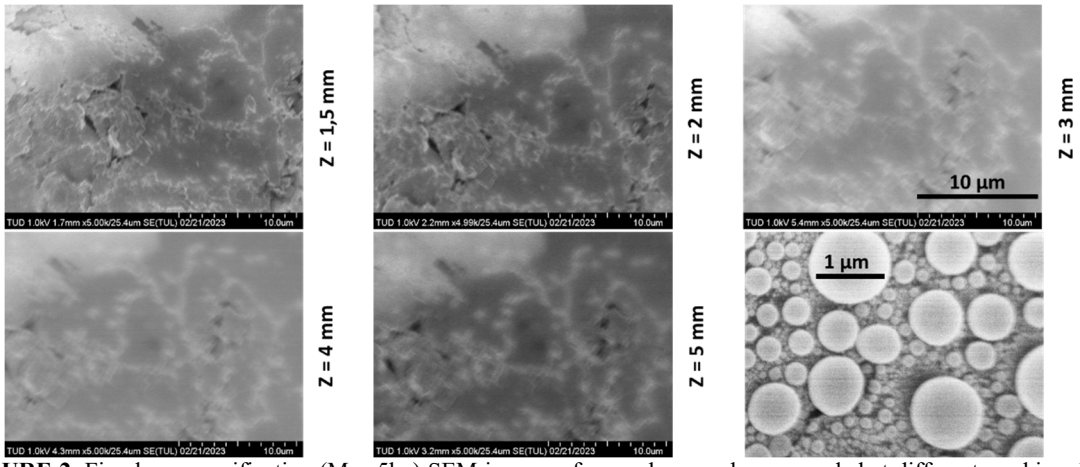


**FIGURE 2.** Five low-magnification (M = 5kx) SEM images of amorphous carbon, recorded at different working distances (WD) with the double mirror corrector at a fixed strength. The DMC overcorrects the spherical aberration for all these WD (**Figure 1FIGURE 1c**). Images are more blurred at larger WD as overcorrection is more effective for longer focal lengths. The SEM image (M = 30kx) of tin balls is recorded at WD = 1,5 using the transfer lens to better match the aberrations of the corrector and objective lens (**Figure 1FIGURE 1d**). Further optimization will improve the original SEM resolution over a factor of two [8].

## SUMMARY

This poster briefly introduces the novel elements (i.e., the EBE beam separator and the MEMS-based miniature electron mirrors (**Figure 1FIGURE 1e**). Measured aberrations are shown for a large range of mirror control voltages and transfer lens settings. Lastly, we show the latest corrected image(s) as obtained with a fully energised DMC in a modified commercial LV-SEM, operated at a beam energy of 1 keV.

## REFERENCES

[1] B. Bunday, E. Solecky, A. Vaid, A. F. Bello and X. Dai, “Metrology capabilities and needs for 7nm and 5nm logic nodes,” *Proc. SPIE,* vol. 10145, p. 101450G, 2017.

[2] J. Zach and M. Haider, “Aberration correction in a low voltage SEM by a multipole corrector,” *Nuclear Instruments and Methods in Physics Research, Section A,* vol. 363, no. 1-2, pp. 316 - 325, 1995.

[3] D. Maas, S. Mentink and S. Henstra, “Electrostatic aberration correction in low-voltage SEM,” in *Microscopy and Microanalysis*, 2003.

[4] M. Steigerwald, G. Benner, U. Mantz and D. Preikszas, “Corrected electron optics - Improved resolution and new analysis capabilities,” in *AIP Converence Proceedings*, 2009.

[5] R. R. Schroder, B. Schindler, M. Schnell, C. Hendrich, J. Wensorra, W.-S. Zhang, J. Eisele, L. Veith, J. Kammerer, M. Pfannmoller, D. Preikszas and I. Wacker, "DELTA - A Novel Ultra-Low Voltage SEM for Electron Spectroscopic Imaging," *Microscopy and Microanalysis,* vol. 24, no. S1, pp. 656-627, 2018.

[6] G. F. Lorusso, "Unavoidable renaissance of electron metrology in the age of high numerical aperture extreme ultraviolet lithography," *J. Micro/Nanopattern. Mater. Metrol.,* vol. 22, no. 2, pp. 021005-1-10, 2023.

[7] D. Joy, “The aberration corrected SEM,” in *Biological Low-Voltage Scanning Electron Microscopy*, AIP, 2007, pp. 535-542.

[8] H. Dohi and P. Kruit, "Design for an aberration corrected scanning electron microscope using miniature electron mirrors," *Ultramicroscopy,* pp. 1-23, 2018.

[9] M. A. R. Krielaart, D. J. Maas, S. V. Loginov and P. Kruit, "Miniature electron beam separator based on three stacked dipoles," *J. Appl. Phys. 127, 234904 (2020),* p. 234904, 6 June 2020.

## KEYWORDS

Charged particle optics, Aberration correction, Low-voltage SEM, electron mirror.

# The Interface Study of Photoresist/Underlayer Using Hybrid R-ray Reflectivity and X-ray Standing Wave Approach

Atul Tiwari[1], Roberto Fallica[2], Marcelo D. Ackermann[1] and Igor A. Makhotkin[1]

*1 Industrial Focus Group XUV Optics, MESA+ Institute for Nanotechnology, University of Twente, Drienerlolaan 5, 7522 NB Enschede, The Netherlands*

*2 IMEC, Kapeldreef 75, 3001 Leuven, Belgium*

## INTRODUCTION

Extreme ultraviolet lithography (EUVL) is a cutting-edge technology that uses EUV light to create fine patterns for fabricating microelectronic devices. The photoresist is a light-sensitive film whose structure changes when exposed to light, forming a patterned mask used for etching various nanostructures, including components for semiconductor devices. The photoresist plays an essential role in this lithography process. Chemically amplified resists (CARs) are a type of photoresist that was found to increase the sensitivity of the lithography process to create fine patterns[1]. This type of resist consists of three main components: i) Polymer, ii) base quencher and iii) photoacid generator (PAG). The PAG is a key element that generates acid upon EUV exposure. This acid creates chemical changes in the polymer to make it soluble in the developer solution. The role of the quencher is to prevent unwanted reactions before exposure by controlling the reactivity of photoacid.

Several spectroscopy and microscopy techniques, such as XPS and SEM, have been used to characterise photoresists, but they are lacking in-depth sensitivity to the geometry of internal structure. In the current work, hybrid x-ray reflectivity (XRR) and x-ray standing wave (XSW) approach[2] have been used to study i) the possibility of analysing the distribution of PAG across blanket photoresist and ii) to examine its migration towards the underlayer/substrate. The PAG in the photoresist samples used in this study is a Sulphur (S)-containing photoacid generator. Tracing Sulphur (S) in the PAG by measuring S fluorescence as a function of incidence angle modulated by XSW formed total external reflection mode can be helpful in achieving these objectives. The first results and their interpretation are presented in this paper.

The two main objectives of this study were: i) to observe the distribution of PAG across the photoresist thickness and ii) to examine its migration towards the underlayer/substrate after EUV exposure

## SAMPLE AND STRUCTURAL CHARACTERISATION

The model resist employed in this study was a prototype organic chemically amplified resist designed for extreme ultraviolet lithography. It consisted of a blend of a copolymer of poly(hydroxystyrene) modified with a 50% t-Butyloxycarbonyl protecting group and tert-butyl methacrylate blended with PAG and a base quencher.

The XSW was formed above the substrate at total external reflection condition. As the angle of incidence increases from zero towards the critical angle of silicon (Si), the positions position of 1st XSW antinode moves from infinity towards the sample surface. The modulated fluorescence of Sulphur by XSW movement holds information about S distribution in the film depth. The X-ray reflectivity data supports the analysis of XSW data, providing information about the electron density profile of studied films.

Different samples i) Photoresist (PR)/organic underlayer/Sub., ii) PR/SiO2/Sub. and iii) PR/Sub. were prepared on Si substrate. Two pieces of each sample were taken into study. One piece was exposed to EUV radiation,

while another piece was kept unexposed to compare the S atomic distribution before and after EUV exposure. These samples are challenging for X-ray analysis. Firstly, the photoresist layers and underlayer have low contrast, which reduces the contrast of measured XSW, therefore, complicates the analysis. Secondly, since the photoresist is designed to modify under irradiation, the possible low stability of the studied sample during the X-ray experiment may complicate data collection. We have experimentally demonstrated that in the case of PR layer irradiation with a monochromized laboratory, CuKa radiation source does not modify the structure enough to change the measured even during the 24-hour experiment. We have also seen that both XSW and XRR data show measurable modification of the internal underlayer/photoresist structure. An example of obtained optical constant profile and atomic profiles for PR on the Si sample is shown in Fig. 1. Detailed data interpretation indicated that EUV exposure induces shrinkage of the PR layer, possibly roughening of interfaces and re-distribution of S in the PR layer. We will present the obtained results, and discuss the tolerances of analysis and benefits of additional complimentary measurements.

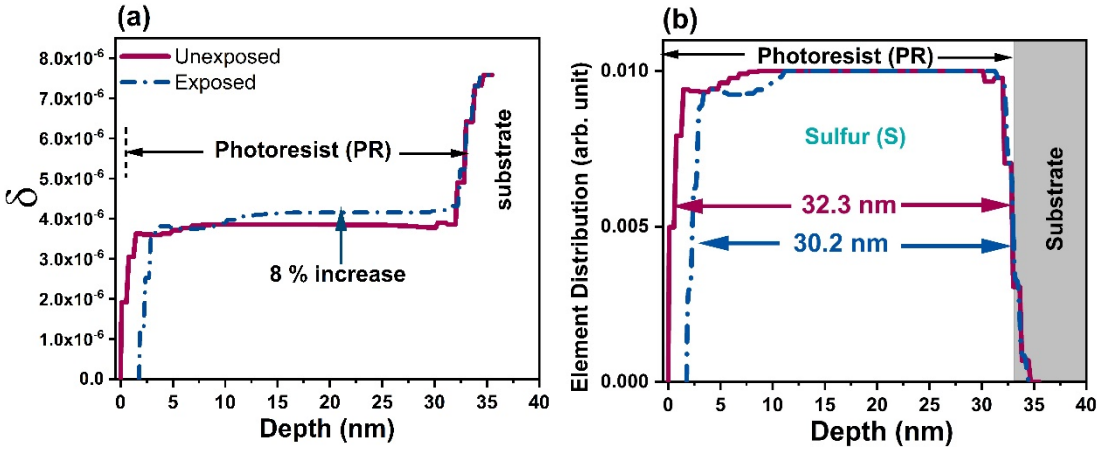


**FIGURE 1.** (a) shows the profile of the real part of optical constant decrement δ and (b) the distribution of S atoms across PR film thickness before and after exposure of sample 1 (PR on Si substrate).

## REFERENCES

1. Junarsa, I., Stoykovich, M. P., Nealey, P. F., Ma, Y., Cerrina, F. & Solak, H. H. (2005). *Journal of Vacuum Science & Technology B: Microelectronics and Nanometer Structures Processing, Measurement, and Phenomena* 23, 138-143.
2. Kondratev, O. A., Makhotkin, I. A. & Yakunin, S. N. (2022). *Applied Surface Science* 574.

## KEYWORDS

Thin Films Characterization, Photoresist, X-ray reflectivity, X-ray fluorescence, X-ray Standing Waves, Hybrid X-ray Metrology.

# Paradigm shift: conical frustum arrays for electron-beam goniometry

A. C. Madison[†], K. A. Cochrane[‡], J. S. Villarrubia[†], D. A. Westly[†], R. G. Dixson[†], C. R. Copeland[†], J. D. Gerling[‡], A. D. Brodie[‡], J. A. Liddle[†], L. P. Muray[‡], S. M. Stavis[†,*]

[†]*National Institute of Standards and Technology, Gaithersburg, Maryland 20899*
[‡]*KLA Corporation, Milpitas, California 95035*
**sstavis@nist.gov*

## INTRODUCTION

Nanoelectronic device manufacturing demands accuracy, precision, and throughput of fabrication process metrology. Scanning electron microscopy, in particular, is important for in-line monitoring of critical dimensions resulting from lithography and etch processes. However, electron-optical aberrations degrade the accuracy of critical-dimension metrology across wide imaging fields. Among several aberrations of potential concern, axial tilt of the scanning electron beam, a vectorial quantity that comprises an inclination and azimuth, shifts apparent positions and deforms intensity profiles of device features under test (Figure 1a-c). Electron-beam goniometry can address this issue by physical compensation of beam deflection or by analytical correction in a measurement function.

The current paradigm of electron-beam goniometry involves analyses of image shifts.[1-3] Defining the state of the art, measurements of a pyramidal micropit[1] show submilliradian repeatability but lack validation of accuracy and present a design constraint. For pyramidal micropits in silicon, an anisotropic etch couples the lateral and vertical dimensions, yielding a trade-off between narrower features to densely sample the imaging field and deeper features to sensitively manifest lateral shifts from electron-beam tilt. Moreover, beam tilt is only one of several aberrations, and it is unclear whether pyramidal micropits are optimal for comprehensive calibrations.

In a paradigm shift that addresses these issues, we explore conical frustum arrays as multifunctional microscopy standards, using theoretical simulations to inform our submicrometer structure design and experimental imaging parameters. This shift promises to improve accuracy, precision, and throughput in scanning electron microscopy, leveraging array standards to calibrate aberration effects[4-6] and measure electron-beam tilt across wide imaging fields.

## THEORY

Our measurement concept benefits from a straightforward geometry and shift analysis, unlike that of a pyramidal micropit.[1] For a tilt inclination $\theta$, a centroid shift $s$ occurs between the top and bottom edges of a conical frustum. For a frustum height $h$, the tilt measurement function is simply $\theta = \sin^{-1}(s/h) \approx s/h$ in the small-angle approximation. This tractable expression greatly facilitates self-calibrating goniometry and null-tilt sensing (Figure 1a-f).

Simulations of scanning electron microscopy allow a test of the limit of accuracy. To understand the random effect of electron shot noise and the systematic effect of frustum sidewall angle, we simulate micrographs across a range of imaging conditions using a physical model of electron scattering.[7-9] At a dose of 60 electrons per nm$^2$, synthetic image shifts show the feasibility of submilliradian accuracy for sidewall angles greater than approximately 40 mrad.

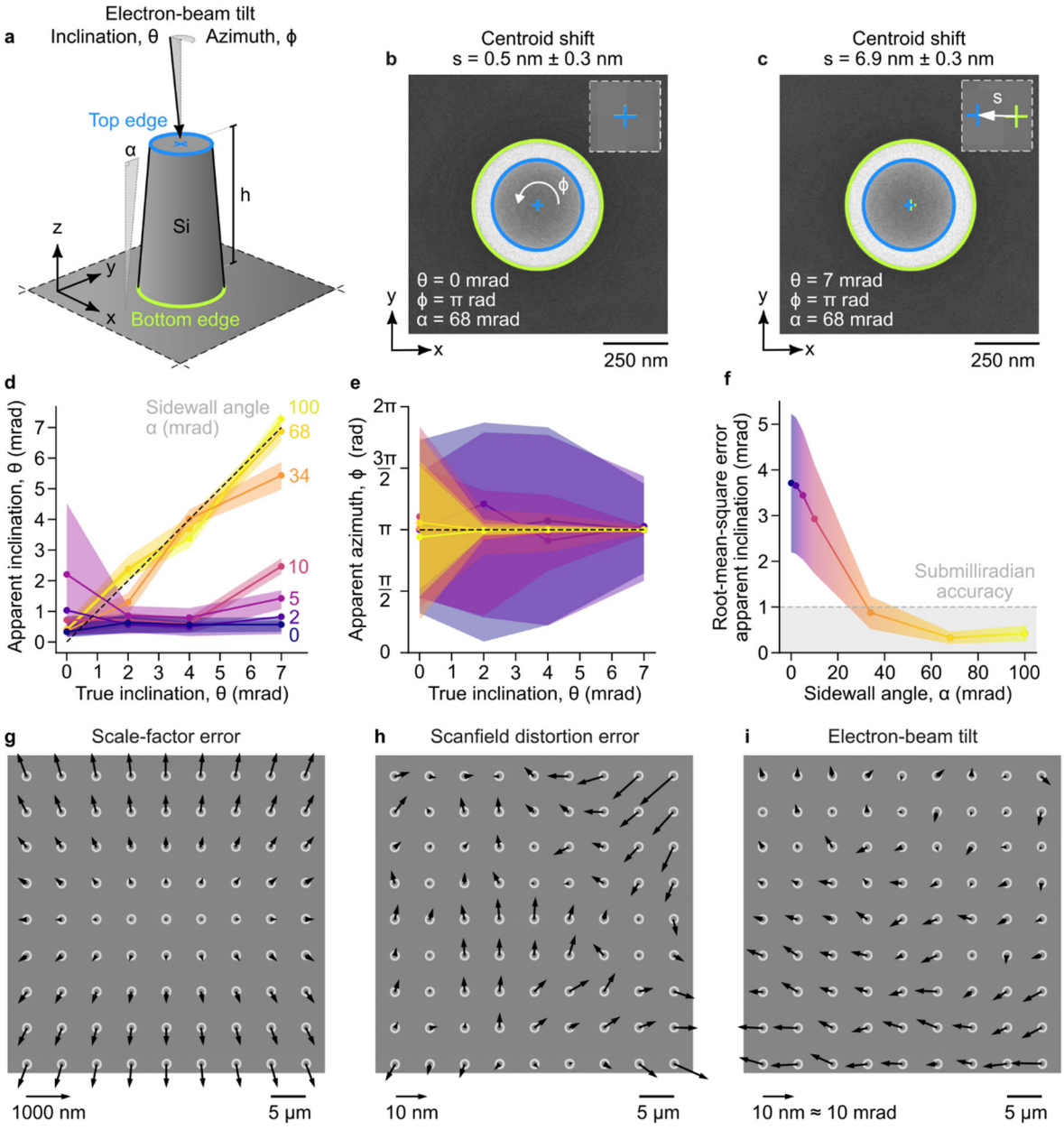


**FIGURE 1.** (a) Schematic showing a conical frustum with a sidewall angle α and an incident electron beam with a tilt inclination θ and azimuth ϕ. (b, c) Scanning electron micrographs showing synthetic images of silicon frusta, resulting from a physical model of electron scattering and emission. The frusta have top diameters of approximately 500 nm, heights of 1000 nm, and sidewall angles of 68 mrad. The electron beam has an energy of 5 keV, a Gaussian profile with a standard deviation of 3.75 nm at best focus at the midsection of the frustum, a beam divergence angle of 17 mrad, an azimuth of π rad, and an inclination of (b) 0 mrad and (c) 7 mrad. A dose of 60 electrons per $nm^2$ results in approximately Gaussian shot noise. Blue and green ellipses show the results of edge detection, indicating shifts in the (crosses) centroids of the top and bottom edges of (c). (d, e) Plots showing (d) apparent inclination and (e) apparent azimuth as a function of true inclination from simulations. Black dash lines are true values. (f) Plot showing root-mean-square errors of apparent inclination as a function of frustum sidewall angle in (d). Colorful regions around data markers in (d-f) are 68 % coverage intervals, corresponding to the random effect of electron shot noise. (g, h, i) Scanning electron micrographs showing experimental images of a silicon frustum array. The array has a pitch of 5001.71 nm ± 1.32 nm at 68 % coverage, from a traceable chain of atomic-force and super-resolution optical microscopy. Black arrows denote (g) scale-factor errors, (h) scanfield distortion errors, and (i) centroid shifts due to electron-beam tilt.

## EXPERIMENT

We fabricate submicrometer frustum arrays in silicon with a crystallographic orientation of (100) using electron-beam lithography and reactive ion etching. Our fabrication process has four main steps. First, thermal oxidation of silicon substrates yields an oxide film with a thickness of approximately 100 nm, forming a hard etch mask. Second, spin coating and patterning a negative-tone resist on the oxide mask defines circular features in square arrays. Third, a tetrafluoromethane etch of silicon oxide transfers resist features into the oxide mask. Fourth, a chlorine etch transfers oxide features into the silicon substrate, with power and duration controlling the sidewall angle and frustum height.

We characterize the resulting arrays, providing quantities that enable electron-beam goniometry. Super-resolution optical microscopy yields a traceable pitch, which deviates from the nominal value by 0.034 % under interferometric control of the lithography system.[6] Optical profilometry provides an estimate of the mean pillar height of approximately 990 nm. In combination, these quantities allow calibration of scale factor and correction of scanfield distortion, improving the accuracy of electron-beam goniometry across an imaging field width of tens of micrometers (Figure 1g-i). In this way, the frustum array enables identification and future compensation of the effects of electron-optical aberrations, which can otherwise degrade accuracy in fabrication process metrology.

## REFERENCES

1. K. Setoguchi et al., *Proceedings of SPIE* 5752, 2005.
2. X. Zhang et al., *Journal of Micro/Nanolithography MEMS and MOEMS*, 13, 2014.
3. L. Han et al., *Microscopy and Microanalysis*, 27, 2021.
4. C. R. Copeland et al., *Light: Science & Applications*, 7, 2018.
5. C. R. Copeland et al., *Nature Communications*, 12, 2021.
6. C. R. Copeland et al., *arXiv*, 2106.10221, 2021.
7. J. S. Villarrubia et al., *Proceedings of SPIE* 7638, 2010.
8. J. S. Villarrubia et al., *Ultramicroscopy*, 154, 2015.
9. J. S. Villarrubia et al., *Proceedings of SPIE* 9778, 2016.

## KEYWORDS

Scanning electron microscopy, fabrication process metrology, electron-beam tilt, electron-beam goniometry

## ACKNOWLEDGMENTS

We gratefully acknowledge Meredith Metzler for helpful comments on control of sidewall angle in our etch process.

# Automation Of Precession-Assisted Nanobeam Diffraction And 4D-STEM Measurements For Multimodal Characterization Of Semiconductor Devices

Daniel Němeček[1] and Robert Stroud[2]

[1]*TESCAN GROUP, Libušina třída 21, 62300 Brno, Czech Republic*
[2]*TESCAN GROUP, 765 Commonwealth Dr #101, Warrendale, PA 15086, USA*

Continuous development of new semiconductor devices is driven by the demand for faster data processing, faster signal transmission, greater storage capacity, and continuously decreasing power consumption. Achieving such performance improvements is dependent on increasing the density of the active elements and cutting the signal path in semiconductor devices. Consequently, semiconductor manufacturers are challenged when characterizing chemistry and morphology at specific sites on ever smaller devices. It is beneficial to employ comprehensive and complementary analytical methods, measuring chemical and structural properties as well as specimen morphology, down to the sub-nanometer scale.

4D-STEM is a powerful analytical method based on nanobeam diffraction that can resolve and characterize distribution of crystalline phases and orientations of individual grains in different layers of semiconductor devices at the nanoscale level. These analyses are critical because the electrical performance of devices depends strongly on the type and distribution of crystalline phases in the device layers. However, broader adoption of 4D-STEM techniques has been limited by complexity of experimental setups and challenges with synchronization of sample scanning by an electron beam with beam blanking, beam precession and readout of a pixelated detector. In this presentation, we will show a new approach to acquisition and processing of 4D-STEM datasets quickly and with minimal user input due to full integration of all needed hardware components with high levels of system automation and optimization algorithms for on-the-fly data processing and visualization of results.

The power of 4D-STEM characterization will be demonstrated on identification of phases in a device that contained anomalies in the GST layer that could not have been revealed by using the standardly used analytical methods such as EDX elemental mapping. Additionally, 4D-STEM measurements enhanced by electron beam precession are optimal for accurate and precise strain mapping in complex semiconductor devices. The power of precession-assisted 4D-STEM measurements, as it is implemented in the novel analytical STEM instrument, TESCAN TENSOR, will be demonstrated on the example of 2D strain mapping of a Samsung 5-nm node with both tensile and compressive strains. The strain values were calculated based on a user defined reference pattern from an unstrained region using a fully automated procedure with on-the-fly data processing, which makes accurate and precise strain measurements accessible to all operators of analytical instruments.

## KEYWORDS

Electron microscopy, 4D-STEM, beam precession, EDX mapping, phase mapping, grain orientation, strain measurement

# Self Focusing SIMS to enable Boron quantification in small Si and SiGe structures

Alexis Franquet[1], Valentina Spampinato[1,2] and Paul A.W. van der Heide[1]

*1 IMEC, Kapeldreef 75, 3001 Leuven, Belgium*
*2 Università degli Studi di Catania, Dipartimento di Scienze Chimiche, Viale A. Doria 6, 95125 Catania, Italy*

## INTRODUCTION

Next generation semiconductor devices with improved performances have forced the industry to investigate and implement new materials and new devices architectures [1]. Among the different materials that have attracted interest over the past years are strained-Ge and SiGe as these are good candidates for p-FET and n-FET (Field-effect transistor) thanks to their excellent hole and electron mobilities [1,2]. The continuous downscaling of devices and the trend toward 3D architectures, lead to the deposition, growth and integration of the different materials in more and more confined volumes (of dimensions <10 nm). Therefore, characterization methods are needed that can not only provide chemical information (for bulk composition) and high sensitivity (for dopant concentration), but also do so at a spatial resolution compatible with the devices under investigation. Secondary Ion Mass Spectrometry (SIMS) is a well-known surface analysis technique which enables to measure the distribution of elements and molecules in 1D (depth profiling), 2D (spatial imaging) and 3D (volumetric imaging) [3]. Since decades, SIMS was used in the Complementary Metal Oxide Semiconductor (CMOS) industry to derive dopant depth distributions thanks to its exceptional sensitivity and very low detection limits. This was until recently mostly done on blanket samples which turns to be irrelevant nowadays, as the properties of nano-volumetric devices are far away from the one of blanket samples. Although SIMS lacks the spatial resolution to directly probe devices from sub-10 nm technologies, it can analyze the composition of narrow trenches (<20 nm) using the concept of Self Focusing SIMS (SF-SIMS) [4].

## SELF FOCUSING – SIMS CONCEPT

A complete description of the SF-SIMS concept can be found elsewhere [4]. Briefly, the formation of a secondary ion cluster (such as AA, AB) can be due to either of the following mechanisms [5]: (1) direct emission model and (2) atomic combination model. While in the first mechanism, the origin of the detected cluster in the sample is obvious (cluster constituents bonded together in the material), one can think in the latter case about the possibility of combination above the sample surface of particles located far away in the material. However, SF-SIMS works on the principle that the formation process of secondary ion clusters, i.e., AA, AB, requires a close temporal, spatial, and even energetic overlap in the emission process of the constituents in order to have a sizeable probability for cluster ion formation [6]. Hence, 90% of the constituent particles of the formed cluster are initially first or second neighbor atoms at the sample surface, i.e., their points of origin are very close together, i.e., <0.5 nm [6]. This is illustrated by the formation of the AB cluster ion as shown in Figure 1, which can only be formed if both A and B constituents come from the same area. Hence, as the formation of a cluster AB with constituents from different regions (AA and BB) is not possible, no interfering signal is produced masking the composition to be determined. As a result, the problem of lateral resolution of the SIMS method can be overcome and the composition of films grown in confined volumes can be determined (using calibration curves based on specific clusters). In practice, the SF-SIMS is applied on multiple similar structures repeated over a large area and thus provides an average composition value. This averaging over many trenches leads to relatively large analyzed volumes, high counting statistics, and thus a "good signal/ noise ratio." This averaging over many identical features is key to statistically relevant and sensitive metrology (in particular, for process control and monitoring purposes) and a clear advantage compared to high resolution methods (like Atom Probe Tomography, Transmission Electron Microscopy / Energy Dispersive Spectroscopy)

which only measure one isolated structure and may suffer from the accidental analysis of a "defected" area (empty or not entirely filled structures, not ideal shape of the structure) as well as from sensitivity limitations in view of the small analyzed volume.

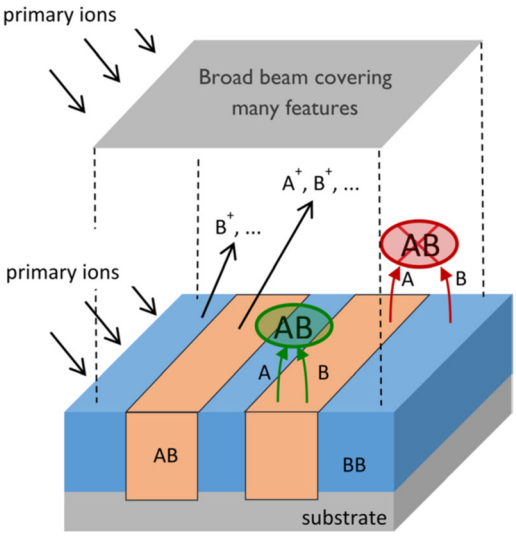


**FIGURE 1.** Schematic representation of the Self-Focusing-SIMS concept.

## RESULTS AND DISCUSSION

In our previous works [4,7], we have demonstrated that SF-SIMS can be successfully applied to accurately quantify the bulk composition of various materials grown in different types of structures of dimensions far below the SIMS lateral resolution, i.e. squares and fins of SiGe, InGaAs, InAlAs, ... In the present work, we are focusing on the use of SF-SIMS to enable Boron dopant quantification in small Si and SiGe structures.

First, SF-SIMS concept has been successfully applied to the Boron quantification of a pattern sample composed by Silicon fins (with width size ranging from 20 to 500 nm) surrounded by $SiO_2$. Careful study of the reference standards, such as B-doped Si and B-doped $SiO_2$ standards, was initially carried out in order to identify the most suitable cluster ions to use for the quantification of the Boron level. The most appropriate cluster ions were found to be $BSi_2^-$ for the Boron and $Si_3^-$ for the matrix. *In-situ* AFM was used before and after sputtering the pattern sample, to precisely extract the sputter rate of both Si and $SiO_2$ regions and correctly convert the sputter time scale into depth scale. With this approach, a Boron implant with peak concentration of ~8e20 at/cm$^3$ was found for the wide fins, and a decrease of the B concentration was observed with decreasing fin width. Moreover, the SF-SIMS approach was demonstrated to be in good agreement with standard SIMS approaches performed on the largest fins size, such as (1) Boron quantification after $SiO_2$ removal by chemical etching and (2) Boron quantification only on the fins by high lateral resolution data acquisition, albeit with some loss of sensitivity/detection limits. To benchmark the SF-SIMS approach, SIMS quantification was also performed on the $SiO_2$ region surrounding the 500 nm-wide fins and the Boron peak concentration (1.1e21 at/cm3) was found to be in good agreement with SRIM simulation.

Second, complex devices made of B doped SiGe epi dots (∅<50 nm) grown on 10 nm wide B doped Si nanowires embedded deeply below multiple layers and surrounded by Si-based material are investigated (see Figure 2 left). The SF-SIMS was applied to determine in one acquisition the Ge content in the SiGe nanodots together with the 3 different B dopant levels contained in the SiGe nanodots, the Si channel/nanowire and the Si substrate. The Ge and B quantified profiles are shown in Figure 2 right. To allow such results, multiple calibration curves using different SF-clusters were determined from the measurements of different reference samples (B doped Si, B doped $Si_xGe_y$, ...).

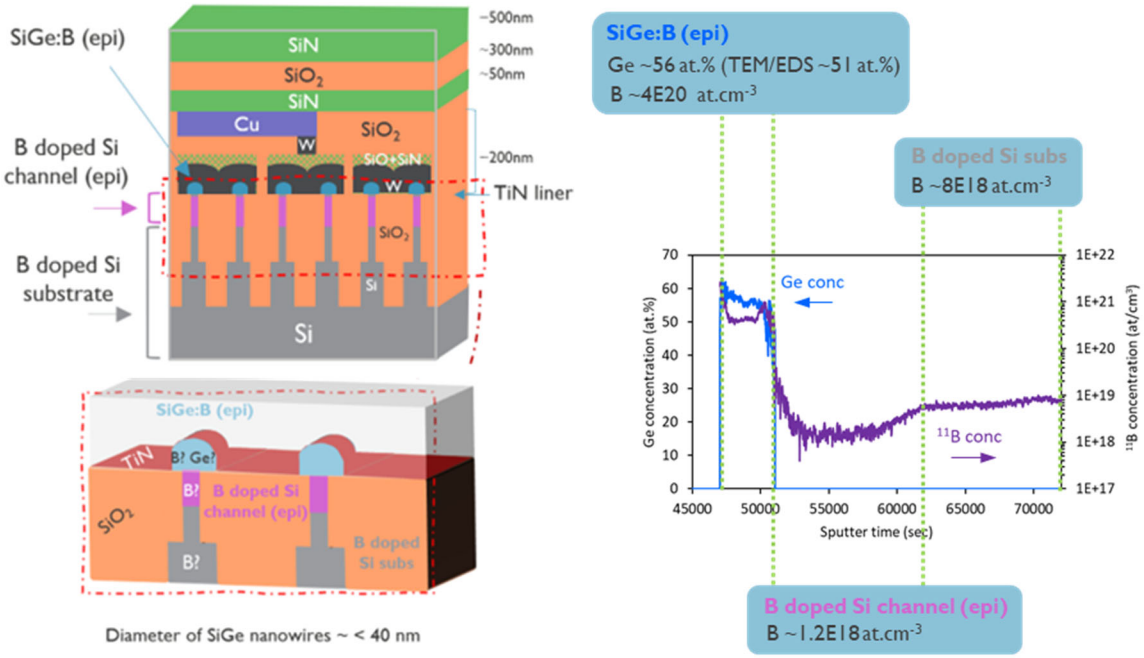


**FIGURE 2.** Schematic representation of the sample under study (left) and the corresponding Ge and B quantified SIMS profile using the SF-SIMS concept.

## REFERENCES

1. R. Chau, Process and Packaging Innovations for Moore's Law Continuation and Beyond, *IEEE IEDM Tech. Dig*., 2019, 1.1.1.
2. P. Hashemi et al., High performance PMOS with strained high-Ge-content SiGe fins for advanced logic applications, *2017 International Symposium on VLSI Technology, Systems and Application (VLSI-TSA)*, 2017, 1-2.
3. P.A.W. van der Heide, Secondary Ion Mass Spectrometry: An Introduction to Principles and Practices, *John Wiley & Sons*, 2014, ISBN: 978-1-118-48048-9.
4. A. Franquet, W. Vandervorst et al., *Applied Surface Science*, 2016, 365, 143-152.
5. H. Oechsner, *SIMS III Proceedings* (Springer-Verlag, New York), 1982, p.106.
6. J. Vlekken, K. Croes, T.-D. Wu, M. D'Olieslaeger, G. Knuyt, W.Vandervorst, and L. De Shepper, *J. Am. Soc. Mass Spectrom*. 1999, 10, 246.
7. A. Franquet, W. Vandervorst et al., *J. Vac. Sci. Technol. B*, 2016, 34(3), 03H127-1.

## KEYWORDS

Silicon Germanium, Boron, dopant, quantification, Secondary Ion Mass Spectrometry (SIMS), Self Focusing SIMS (SF-SIMS)

# Etching monitoring of advanced forksheet devices using AKONIS SIMS tool

A-S. Robbes[1], O. Dulac[1], K. Soulard[1], M. Adier[1], S. Choi[1], D. Jacobson[2], A. Merkulov[3], R. Tilmann[3], P.A.W. van der Heide[3] and A. Franquet[3]

*[1]CAMECA, 29 quai des grésillons 92622 Gennevilliers Cedex*
*[2]CAMECA Instruments Inc., 5500 Nobel Drive, Madison, WI, USA*
*[3]IMEC, Kapeldreef 75, 3001 Leuven, Belgium*

## INTRODUCTION

FinFET (Fin Field-Effect Transistor) design that has been widely adopted in the last decade to overcome some of the limitations of planar transistor technology, allowing for better control of current flow and reduced leakage. Nowadays, the most advanced manufacturers are facing a big challenge in scaling CMOS beyond FinFET to nanosheets. In the near future, they will have to overcome another fundamental change, where nanosheet devices will be combined to form complementary FETs (CFETs). IMEC recently proposed an innovative alternative architecture between the nanosheets and the CFETs, called the forksheet device which can be considered as a natural extension of the nanosheet device. Their process flow is quite similar, with only a few additional process steps in the case of the forksheet devices for which manufacturers are in need of accurate and sensitive analytical tools. The AKONIS Secondary Ion Mass Spectrometry (SIMS) tool from CAMECA has been designed to answer these customer's needs combining analytical performance and full automation. The tool is equipped with a novel ion source embedded in a redesigned ultra-low-energy primary column with seamlessly automated beam optics. It enables to reach an excellent depth resolution while keeping very high sensitivity on 80µm x 80µm OCD pads. The work here presents the forksheet etching monitoring with AKONIS SIMS tool.

## FORSHEET DEVICES: AN ALTERNATIVE BETWEEN NANOSHEET AND CFETs

The forksheet devices have been developed from exploring the limits of the nanosheet architecture. It can be considered as the next step in the natural evolution from planar to FinFET and to vertically stacked nanosheets. The nanosheet's main feature is its horizontal stacks of silicon ribbons surrounded by its current-controlling gate. Although nanosheets just entered into production in the most advanced manufacturer sites, physical limitations are already well known, and experts are working for several years now to find a way to overcome these limitations without going to CFETs which request a fundamental change in manufacturing the devices. IMEC was tasked with figuring out an alternative they called forksheet.

They found that one of the main limitations to shrinking nanosheet-based logic is keeping the separation between the two types of transistors that make up CMOS logic. The two types, NMOS and PMOS, must maintain a certain distance to limit capacitance that limit the devices' performance and power consumption. In forksheet FETs, both nFET and pFET are integrated in the same structure. A dielectric wall separates the nFET and pFET which is different from existing gate-all-around FETs, using different devices for the nFETs and pFETs.Thus, forksheet FETs allow for a tighter n-to-p spacing and reduction in area scaling.

However, from a manufacturing perspective, forksheet devices are quite complicated to process as it involves several types of dielectrics used in advanced CMOS and thus several steps that involve etching it away. The etching processes without accidentally attacking the wall is a critical step for which manufacturer are in need of accurate and sensitive analytical technique.

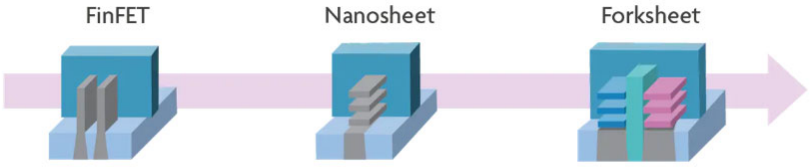


**FIGURE 1.** Natural evolution from FinFET to nanosheet, and to forksheet[1]

## AKONIS SIMS TOOL: ETCHING MONITORING OF FORSHEET DEVICES

AKONIS tool is equipped with a novel ion source embedded in a redesigned ultra-low-energy primary column with seamlessly automated beam optics. This state-of-the-art equipment enables relative standard deviations (RSD) of less than 1% for dose measurements in a broad array of customer applications in fully automated analysis mode.

AKONIS easily measures 80µm x 80µm OCD pads of forksheet devices with unrivalled analytical performance, enabling to monitor the Ge concentration variation during the etching process and give an estimation of %Ge remaining. Thanks to its superior single detection system, combined with a unique high extraction field technology, AKONIS delivers very high dynamic range with unequalled depth resolution and sensitivity. Figure 2 shows TEM images of the three samples with SiGe respectively unetched, half etched and fully etched.

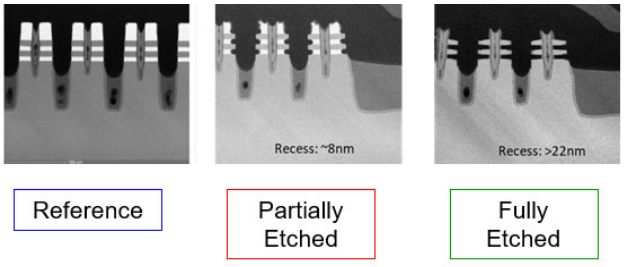


**FIGURE 2.** Three forksheet samples analyzed with SiGe respectively unetched, half etched and fully etched.

The main challenge of the analysis is to reach the best depth resolution while keeping enough signal and statistics to characterize the fully etched sample. Figure 3 depicts an overlay of the 3 profiles acquired on 80µm x 80µm OCD pads with SiGe forksheet devices respectively unetched, half etched and fully etched. The three profiles nicely show the different SiGe stacks even for the fully etched sample, only achievable thanks to the ultimate performance of AKONIS.

The %Ge remaining was estimated by calculating the integral of the Ge signal with unetched sample taken as a reference, the integral of its Ge signal being assumed to be equal to 100%Ge (see table 1).

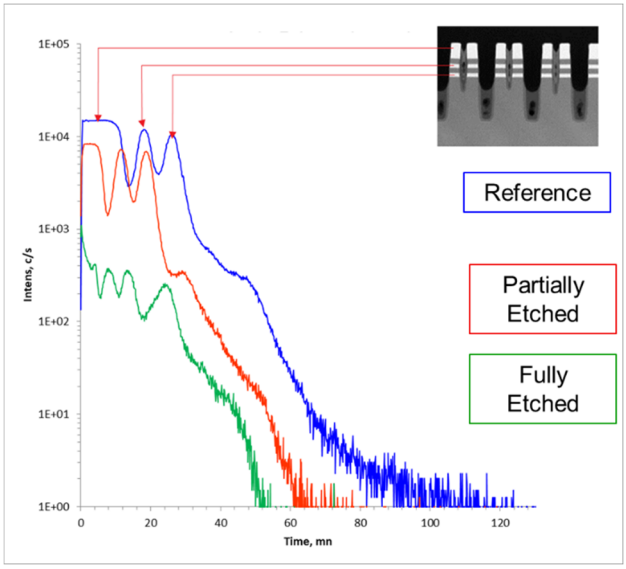


**FIGURE 3.** SIMS profiles using AKONIS @250eV impact energy on the three forksheet samples with SiGe respectively unetched, half etched and fully etched.

**TABLE 1.** Estimation of %Ge remaining for the three samples

| | Reference | Partially etched | Fully etched |
|---|---|---|---|
| Integral of the Ge signal (counts) | 1.71E+06 | 4.66E+05 | 1.02E+05 |
| Ge % | 100 | 27.2 | 5.9 |

## CONCLUSION

AKONIS outperforms other analytical systems for etching monitoring of advanced forksheet structures delivering excellent depth resolution while keeping very good sensitivity. Combining superior analytical capabilities with full automation and ease-of-use, the AKONIS SIMS tool is uniquely positioned to meet the requirement of current and future logic devices.

## REFERENCES

1. https://www.imec-int.com/en/imec-magazine/imec-magazine-december-2019/scaling-cmos-beyond-finfets-from-nanosheets-and-forksheets-to-cfets

## KEYWORDS

Forksheet, Etching, SIMS, High Volume Manufacturing support, Monitoring.

# In-situ and Ex-situ Diagnostics for Ion Measurement and Control for RF-driven Plasma Tools

A. Verma[1], T. Gilmore*[1] and D. Simpson[2]

[1]*Impedans Ltd, Chase House, City Junction Business Park, Northern Cross, Dublin, D17 AK63, Ireland*
[2]*Centre for Light Matter Interactions, School of Mathematics and Physics, Queen's University Belfast, UK*
**Email: Thomas.gilmore@impedans.com, info@impedans.com*
*Phone number: 086 183 2376*

## INTRODUCTION

Plasma-based technologies are widely used to fabricate nanoelectrodes and ultra-thin oxide films for nanoelectronics. Plasmas can provide a wide range of controllability for deposition and etching techniques. The fact that plasma is in non-thermal equilibrium allows it to be a source of highly reactive species (e.g., radicals) and energetic ions at low gas temperatures. Indeed, most anisotropic etching processes and many deposition processes are plasma based, being enabled by the directional ion bombardment and high reactivities of radicals generated in plasmas. It is evident that plasma technology at nanoscale has enabled the fabrication of the next generation of electronic devices with high data rate communications as well as high-speed operation of electronic switches. In parallel to the development in plasma process technology, it is also imperative to come up with the tools to measure and control the plasma response to create a defect-free device.

To date various kinds of diagnostic tools have been developed for in-situ and ex situ measurements of plasma parameters. Impedans Ltd. offers an umbrella of these tools to characterize plasma [1]. This talk will present a systematic study performed on a Capacitively Coupled Plasma System equipped with an ion energy analyzer "Semion" and "Octiv" VI probe on RF line. The study shows a novel non-invasive technique to measure ion flux reaching on powered electrode using the Octiv V-I probe. Ion flux (defined as number of ions impacting a surface per unit time) is a key parameter to control process repeatability and hence the properties of the deposited films [2]. The study provides a relation between intrinsic plasma parameters (ion flux, energy) and external parameters such as RF power which will be useful in the absence of any direct measurement facility. Further these results will be supported with direct measurements made using RFEA to check the sanity of the V-I probe measurements.

## EXPERIMENTAL SETUP

A 13.56 RF CCP chamber was used in the study with plasma produced using Argon gas at different pressure and RF power. The schematic of the experiment is shown in Fig. 1. The chamber consists of two parallel electrodes (each diameter 30 cm); one powered and one grounded with separation of 5.8 cm. The placement of Octiv in RF line between the matching network and powered electrode is also shown. The Octiv is an advanced V-I probe from Impedans which can measure all the RF parameters (power, voltage, current, phase, plasma impedance, harmonics) along with live ion flux amount reaching on the powered electrode. The Impedans made Semion RFEA is a multi-grid system capable of measuring ion flux and ion energy distribution functions of positive and negative ions in plasma. For this experiment, it was placed on the powered electrode as shown in Fig 1.

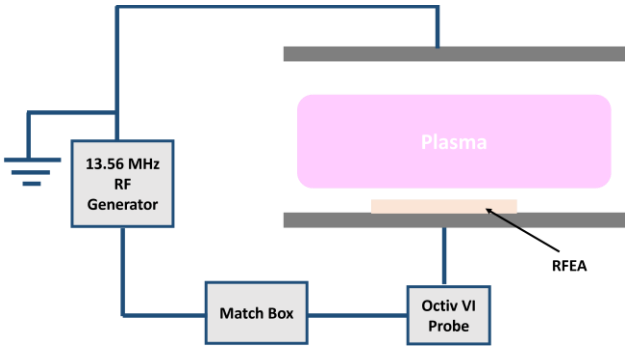


**Figure 1.** Experimental setup of the study – a CCP chamber equipped with Octiv VI probe and Semion RFEA diagnostics tools.

## RESULTS AND DISCUSSIONS

During the experiments RF power varied from 25 to 250 W and pressure range of 0.3 to 3 Pa were exploited. Keeping the RF power fixed at 100 W, Octiv and RFEA measurements were made at different pressures and shown in Fig. 2. It is seen that both the tools measure similar trends in ion flux behavior. As the pressure increases from 0.3 Pa to 3 Pa, ion flux increases which is due to the increase in plasma density with power as evident by Langmuir probe measurements too. Fig. 2 additionally has a pressure correction for the RFEA measurements.

As we know, ion energies are a function of plasma and sheath potential which is highly dependent on pressure, so it is remarkable to match the ion flux profiles over such a wide range of pressure. Octiv takes advantage of simultaneous measurement of voltage ($V$), current ($I$), phase ($\theta$) and also of the DC self-bias developed at the powered electrode and the ion flux is estimated using the formula below [3].

$$J_i = \frac{VICos\theta - I^2R_0 - Ik_p}{1.4VA}$$

Here, $R_0$ is the series resistance of the circuit between the measurement point and the electrode. $k$p is a pressure dependent quantity that accounts for any voltage drop on the resistance of the bulk plasma. $A$ is the electrode area. For the plasma system with densities $10^{11}$ cm$^{-3}$ and electron temperature of few eV, the above formula simplifies to the following.

$$J_i = \frac{ICos\theta}{1.4A}$$

The ion flux measured by Octiv is slightly outnumbered by the value measured using Semion. However, such a difference is expected because the Octiv measurements are sensitive to its placement, the closer it is placed to the electrode better is the measurements. A voltage transformation was applied to correct Octiv measurements and seen a better matching between the two diagnostics. Detailed experimental observations and measurement results will be shown at the conference.

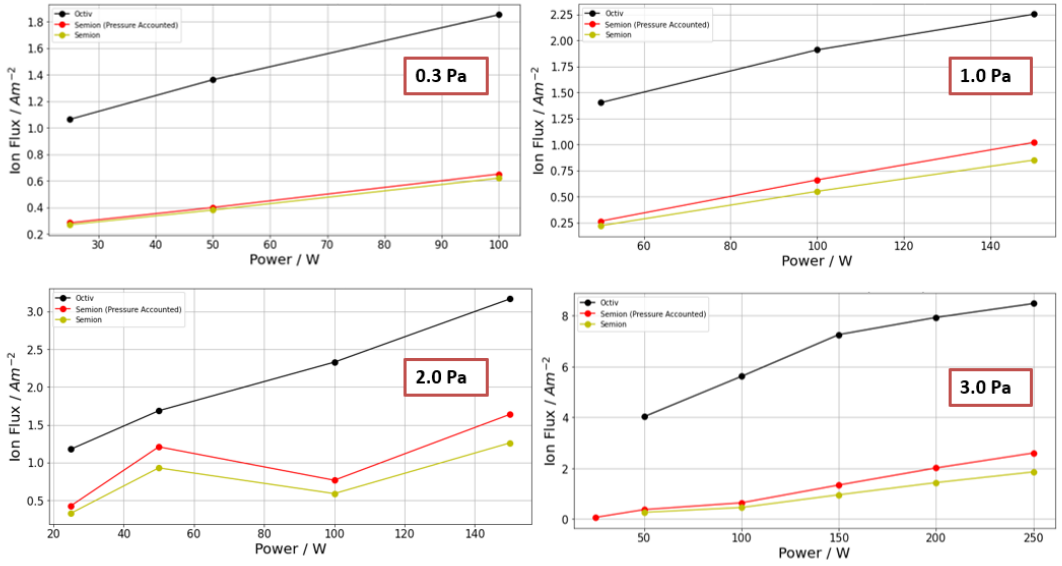


**Figure 2**. The ion flux measurement with Octiv and Semion as a function of power and shows here at multiple pressures.

## REFERENCES

1. Impedans Ltd, Dublin, Ireland [www.impedans.com]
2. A. Michelmore et al, *ACS Appl. Mater. Interfaces* **5**, 5387–5391(2013).
2. Octiv User guide Resources | Impedans.

## KEYWORDS

Capacitively Coupled Plasma, ion flux measurement, retarding field ion energy analyzer, V-I probe

# Improving Self-Focusing SIMS On Hybrid SIMS Instruments – Instrumental Aspects and Method Development

T. Grehl[1*], S. Kayser[1], J. Zakel[1], D. Rading[1], A. Pirkl[1], H. Arlinghaus[1], V. Spampinato[2,3], A. Franquet[2]

*(1) IONTOF GmbH, 48149 Muenster, Germany*
*(2) MCA, IMEC, Kapeldreef 75, 3001 Leuven, Belgium*
*(3) Università degli Studi di Catania, Dipartimento di Scienze Chimiche, Viale A. Doria 6, 95125 Catania, Italy*

## INTRODUCTION

To boost the performances of the next generation transistors, new materials and device architectures have been investigated in the semiconductor industries[1]. In this context, strained-Ge and SiGe channel FET's have received high interest due to their excellent hole mobility[2] and recently obtained results have encouraged the semiconductor device industry to incorporate them in its latest FinFET technology[3,4]. As a consequence, characterization techniques have to provide chemical information and high sensitivity with a spatial resolution compatible with the device structure of down to 10 nm.

During the last years we demonstrated that the improved mass resolution of the Hybrid SIMS[5] instrument, which integrated the Orbitrap™ mass analyzer into a SIMS instrument, has been extremely beneficial for advanced semiconductor structure analysis. Especially the application of the so-called Self-Focusing SIMS (SF-SIMS)[6,7] approach opened up new possibilities for the analysis of next generation devices.

Despite the very encouraging first results it also becomes clear that, depending on the individual analytical conditions, the Orbitrap mass analyzer can suffer from oversteering and saturation effects. These effects limited the repeatability, absolute quantification and matching to other analytical techniques. To overcome this limitation, we developed a unique adaptive injection system for the Orbitrap mass analyzer. The new system automatically adapts the number of injections (i.e., Orbitrap spectra per frame) or number of pixels within the field of view to avoid oversteering and saturation effects in real time.

In this presentation we will explain the working principle, apply the new adaptive ion injection system to different sample systems and report the advances for the measurement repeatability, the quantification and the matching to other analytical techniques.

## RESULTS AND DISCUSSION

The SF-SIMS approach utilizes the effect in Secondary Ion Mass Spectrometry that heteroatomic cluster ion signals are only observed in SIMS spectra, if their atomic constituents colocalize (cf. figure 1). This renders an elegant way to prove coexistence of certain atoms in small structures even if the instrumental capabilities like sensitivity and lateral resolution are insufficient for resolving these features directly.

However, in time-of-flight SIMS instruments for some sample systems the analysis is hampered by mass interferences of the clusters of interest with background ions from the sample matrix due to insufficient mass resolving power. This deteriorates the detection limits, and in some cases even renders an analysis impossible.

An Orbitrap analyzer is employed in Hybrid SIMS instruments as additional detection system. This helps to substantially increase the mass resolving power by more than an order of magnitude and successfully mass separate

* Presenting author: thomas.grehl@iontof.com, phone: +49 251-1622-321

clusters and background signals. Furthermore, the intermediate trapping of ions in the curved linear trap, built in to the Orbitrap system, even allows to use (quasi-)DC ion beams for the analysis. This increases the fraction of generated sputtered material that is subjected to mass analysis leading to improved analytical sensitivity.

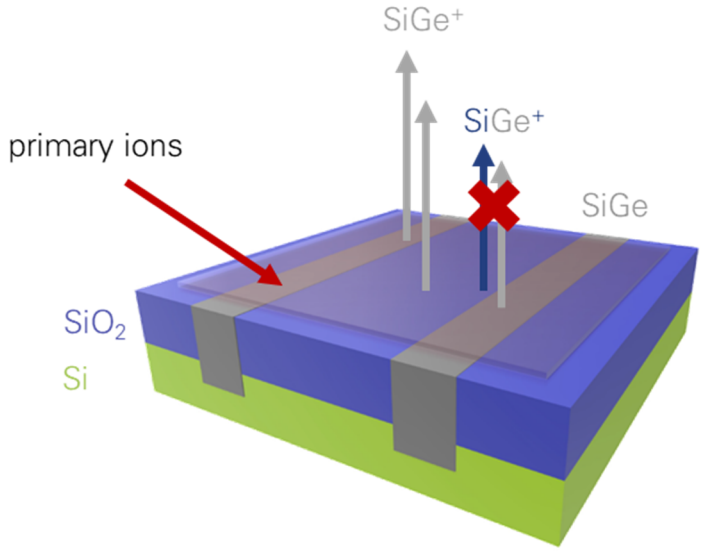


**FIGURE 1.** Principle of the Self-Focusing SIMS approach. Heteroatomic cluster ions can only be formed, if the constituents colocalize on the sample.

As a drawback the much higher secondary ion signal intensity from the (quasi-)DC primary ion beam can easily lead to saturation of the Orbitrap detector, if the primary ion current is not precisely optimized in advance.

To solve this, we implemented a dedicated software algorithm termed Adaptive Ion Injection System, which automatically reduces the number of secondary ions per spectrum, if the measured total signal intensity comes close to the saturation limit of the detector. This can be achieved by splitting up the injection to the Orbitrap into multiple parts as illustrated in figure 2. As the intensity rises and reaches a certain threshold (here 1E7 a.u.), a second injection is triggered reducing the number of ions per Orbitrap spectrum by a factor of 2. The intensity of the datapoint will then be the sum of the intensities of both Orbitrap spectra. As the intensity increases further, a third injection per datapoint is performed, and so on.

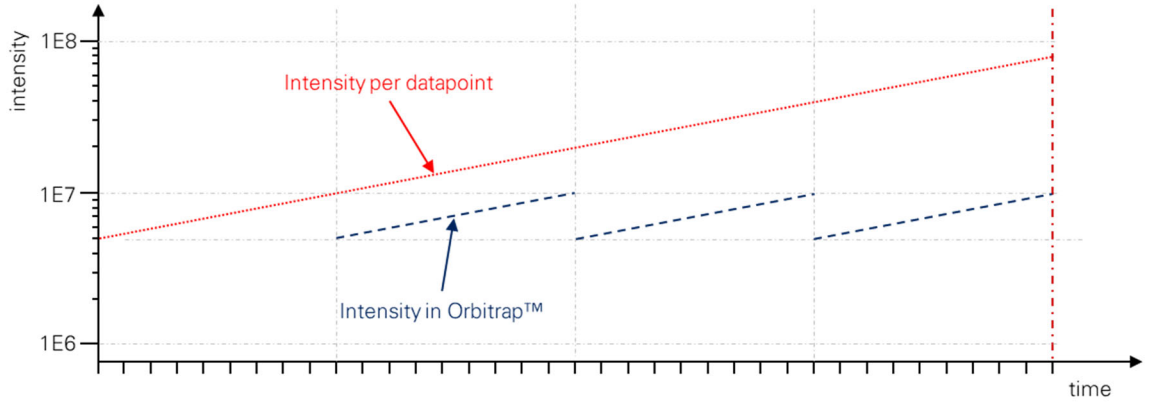


**FIGURE 2.** Principle Adaptive Ion Injection System.

Applying this approach to an analytical standard (here Si:InGaAs) shows that avoiding saturation is crucial for obtaining reliable quantitative results (cf. figure 3). As a direct consequence of the superior mass resolving power a better limit of detection is obtained for this sample with the Orbitrap analyzer compared to the classical TOF-SIMS approach.

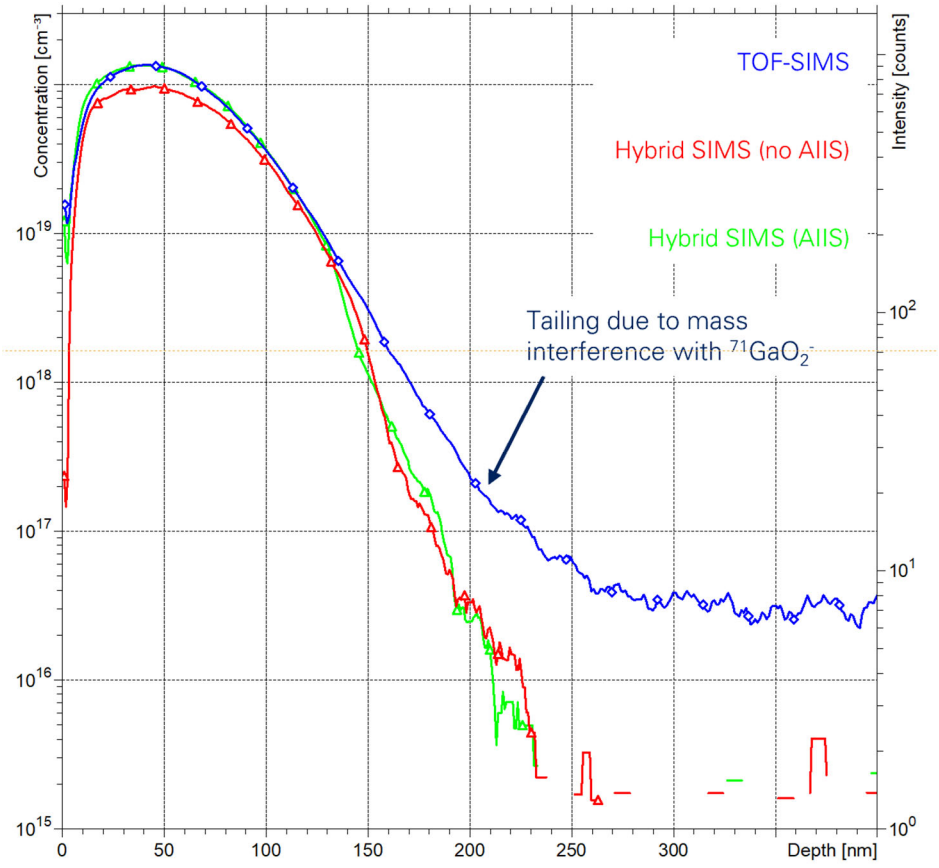


**FIGURE 3.** Comparison of depth profiles from an analytical standard implant sample (Si:InGaAs) acquired with Hybrid SIMS instrument and standard TOF-SIMS instrument. Plotted here is only the $AsSi^-$ signal.

## REFERENCES


1. S. Datta, Electrochem. Soc. Interface 22 41 (2013).
2. J. Mitard et al., Jap. J. Appl. Phys. 50 04DC17-1 (2011).
3. M.J.H. van Dal et al., IEEE International Electron Devices Meeting (IEDM) 23.5.1- 23.5.4 (2012).
4. R. Pillarisetty, Nature 479 324 (2011).
5. MK Passarelli, A Pirkl, et al., Nature Methods, 14, 1175–1183 (2017)
6. A. Franquet et al., Applied Surface Science 365, 143-152 (2016).
7. A. Franquet et al., J. Vac. Sci. Technol. B 34(3), May/Jun (2016).


## KEYWORDS

Secondary Ion Mass Spectrometry (SIMS), Self-focusing SIMS, Hybrid SIMS, Silicon Germanium

# Towards a better understanding of GaN based HEMT electrical response thanks to XPS, nano-Auger and STEM-EDX multi-technique approach

K. Gaffar[*1], S. Béchu[1], G. Patriarche[2], M. Bouttemy[1]

[1] *Institut Lavoisier de Versailles, UVSQ, Université Paris-Saclay, CNRS, UMR 8180, 45 avenue des Etats-Unis, 78035 Versailles CEDEX, France*
[2]*C2N, Université Paris-Saclay, CNRS, Palaiseau, France*

**Corresponding Author E-mail: kirene.gaffar@cnrs.fr; Phone: +33 601233035*

## INTRODUCTION

Outstanding progress has been noticed in Gallium Nitride (GaN) based power electronic devices for the last decades[1]. In particular, studies have demonstrated the excellent potential of GaN-based High Electron Mobility Transistor (HEMT), delivering high voltage, high current, and high-frequency performance, not only for military but also land-based applications[2]. GaN-based HEMTs' attractiveness is therefore established but this technology still faces long-term reliability issues, for which interface mastering has been identified as a key lever. Interface properties and quality are usually studied through electrical characterizations. These techniques are easy to use and enable to identify gate leakages, defects and trapping effects that can be correlated to the overall device behavior[3,4]. Nevertheless, complementary chemical characterization has proved to be very helpful in further understanding and localizing the faulty zone[5]. In particular, detection of defects, whether they are structural, physical (cavity, interdiffusion, oxide..) or electrical (polarization, doping, …) gives insights into the origin and degradation mechanism of the electrical response. In the microelectronic field, the most common chemical and structural characterization techniques employed are SIMS[6] (Secondary Ion Mass Spectroscopy), XPS[7] (X-ray photoemission spectroscopy), AES[5] (Auger Electron Spectroscopy) and STEM-EDX[8] (Transmission Electron Microscopy/ Energy Dispersive X-ray Spectroscopy). Their capabilities have been illustrated on many semi-conductors and applications, but the majority of studies report on the analysis of simple stacks and not on the final device. The reason is simple: the device consists of a complex architecture of nanometric layers of semi-conductors, nitrides and metals, besides on isolating substrates (generally SiC or sapphire) and few techniques are adapted for analyzing such challenging objects. In previous papers, we have demonstrated the great potentiality of Auger nano-probes (nano-Auger) to bring chemical information at the deca-nanometer scale and a direct access to buried interfaces on cross-sections [9]. This technique is thus a good candidate to complement STEM-EDX analyses which cannot inform about the chemical bonding. In the specific case of GaN devices, we are developing a dedicated analytical methodology to enable nano-Auger analyses. Indeed, the feasibility of such analyses is conditioned by tackling major issues: the poor conductivity of such samples and their preparation (surface chemical state preservation). The originality of the present approach lies in the realization of Auger analyses on FIB (Focused Ion Beam) lamellas, as for STEM-EDX analyses, enabling to correlate results acquired in the same regions of the transistor, and, subsequently, to electrical performances. First feedback will be presented and discussed. XPS is also considered in this multi-technique approach to refine Auger quantification by adjusting sensitivity factors with respect to the different compounds' nature but also to increment a spectral database of Auger spectra (X-AES). However, using common Al k-alpha X-ray sources, GaN compounds quantification is not obvious due to the unfortunate overlapping between N 1s photopeak and Ga $L_2M_{4,5}M_{4,5}$ Auger transition. The scrupulous decomposition procedure of this spectral region we developed, based on the NLLSF (Non-Linear Least Square Fitting) of N 1s and Ga-$L_2M_{4,5}M_{4,5}$ reference spectra, will be depicted.

## Multi-technique Approach: Correlation Between Chemical, Structural and Electric Characterization of HEMTs

Although XPS and AES are both surface-sensitive techniques, the high spatial resolution (around 12nm) provided by the Auger nano-probe enables the access on cross-sections to each layer of the HEMT structure and to buried interfaces. It offers thus the possibility to bring complementary information to STEM-EDX structural and elemental analysis, such as oxidation states (Metal-Oxygen bonds) or contaminants detection. To overcome inherent limitation of the Auger analyses, especially charging effects, a novel approach is considered here by performing Auger analysis on FIB Lamellas. Another advantage lies in the fact that the same objects could be analysed both in Auger and STEM-EDX. Yet, the feasibility and compatibility of such a correlative approach requires the optimization of the lamella to respect both specifications of the two techniques in terms of thickness and surface state (Ga implantation, amorphization, carbon adventitious contamination), especially for Auger. Indeed, for Auger analyses, lamellas configuration (one or two points attachment on the TEM grid) and thickness are essential parameters to focus on to limit charge accumulation on the surface and reduce drifting troubles. The Auger electron beam is focused on very localized areas for several acquisition hours leading to surface heating and drifting issues, and finally the damage of the lamella. Not only sample preparation but also mounting is not so easy: carbon or copper tapes used to fix the grids are subject to severe degradation under UHV (loss of conductivity) and also unavoidably contaminate the surface while ion gun sputtering is employed for surface cleaning. Issues with electron beam exposition time and surface contamination are not as prejudicial for faster TEM analyses and for which the beam passes through the entire thickness. The optimal configuration will be discussed and preliminary results of the multi-technique approach will be presented. Another major point is to evaluate Gallium incorporation inherent to FIB preparation within the subsurface to deliver a quantification of GaN-based components without this artefact. This quantification will be optimized thanks to XPS analyses of similar layers giving a point of reference and, for GaN compounds, the specific decomposition procedure of XPS spectra described.

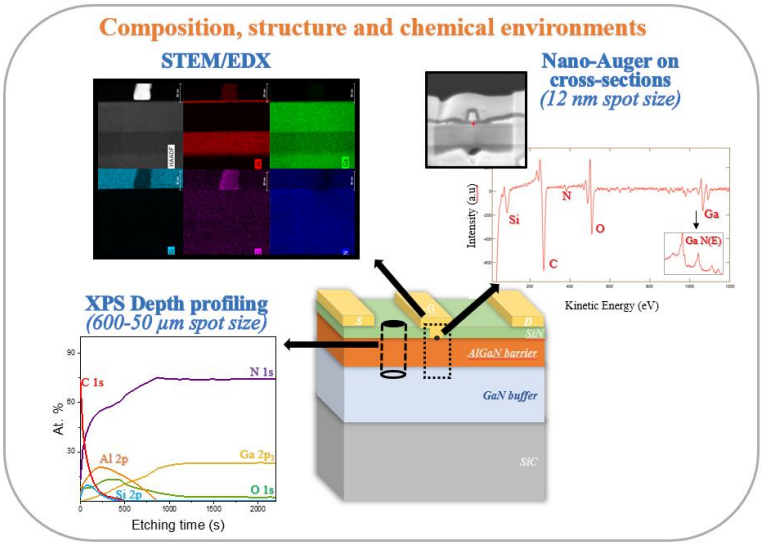


**FIGURE 1**. Overview of the multi-technique methodology employed for GaN devices characterization.

## X-Ray Methodology Development For An Advanced GaN-based material Quantification

If the added value of completing commonly used STEM-EDX on transistors cross-sections with spectroscopy techniques is obvious, the direct interpretation of XPS and Auger analyses is not straightforward. The analysis of GaN materials by XPS (Al source) requires the separation of overlapping N 1s /Ga-LMM contributions and remains a challenge. As the access to the ultimate composition of any GaN-based structure is conditioned by the fitting procedure to ensure a reliable nitrogen content determination, a study combining the X-Auger electron spectroscopy (X-AES) transitions simultaneously obtained with the X-ray photoemission spectroscopy (XPS) photopeaks using the Al Kα source has been carried out. In HEMT transistor cases, the depth probed by the XPS (≈ 10 nm) can be higher than the structures' multilayer thicknesses[7] and, as previously described, Ga $L_2M_{4.5}M_{4.5}$ transition and nitrogen N 1s photopeak overlap. Thus, access to the ultimate composition of the HEMT structure may become a difficult

process leading to erroneous information. The fitting method developed in this study for XPS data allows the modeling of Ga $L_2M_{4.5}M_{4.5}$ (~ 395 eV) and Ga $L_3M_{4.5}M_{4.5}$ (~ 420 eV) X-AES transitions including N 1s photopeak (~ 398 eV) using oxidized/deoxidized gallium-based references (III-V binary alloys) to determine the gallium and nitrogen contributions in GaN based-materials. This new procedure consists of using the higher energy Auger line (Ga $L_3M_{4.5}M_{4.5}$) to find and fix the right fitting parameters on the lower energy transition where the overlap between nitrogen and gallium occurs. To reach buried interfaces, modifications induced by sputtering while depth profiling have been studied for developing a strong and universal methodology for processing XPS data of GaN components. The consistency and reliability of the method have been verified by calculating representative gallium ratios and comparing compositions to additional STEM-EDX analysis. For quantification on direct or differentiated Auger spectra, the upstream determination of the different layers' composition using representative reference samples in XPS and STEM-EDX is crucial to determine Relative Sensibility Factors (RSFs) as these factors condition the Auger quantification accuracy. The replication of the X-AES fitting protocol to Auger spectra (e-AES) is also considered but implies the adaptation of the XPS fitting method on Auger spectra, as the generated spectra from the electron source will differ from the one acquired with an X-ray source in many aspects, especially when it comes to background subtraction.

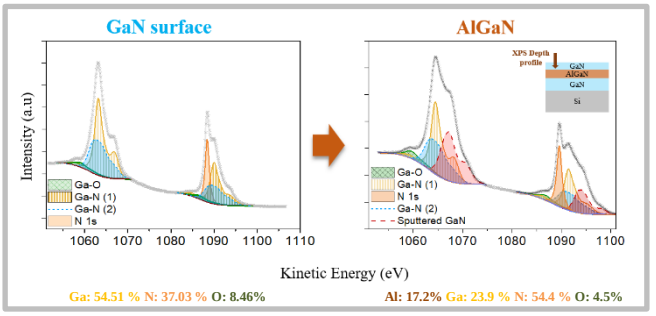


**FIGURE 2.** Decomposition of Ga-LMM/N 1s region for GaN-based materials quantification using Al Kα source. Illustration on GaN and AlGaN.

## Conclusion

This multi-technique approach using XPS / Auger / STEM-EDX tools not only provides access to elemental compositions but also to key information on chemical environments, especially after each determinant technological step during device fabrication. It allows the correlation between localized surface trapping mechanisms to chemical states at different interfaces for a complete diagnosis. Thus, HEMT devices' poor electrical performances such as current collapsing or gate leakage will be linked with the device's chemical and structural properties, improving the understanding of HEMT's performance degradation.

## REFERENCES


1. Eastman, L. F. *et al.* Progress in high-power, high frequency AlGaN/GaN HEMTs. *Phys. Status Solidi Appl. Res.* **194**, 433–438 (2002).
2. C. Xie and A. Pavio, "Development of GaN HEMT based high power high efficiency distributed power amplifier for military applications," in Proc. IEEE Military Comm. Conf., Oct. 2007.
3. Vigneshwara Raja, P., Nallatamby, J.-C., DasGupta, N. & DasGupta, A. Trapping effects on AlGaN/GaN HEMT characteristics. *Solid. State. Electron.* **176**, 107929 (2021).
4. Harrouche, K. *et al.* Low Trapping Effects and High Electron Confinement in Short AlN/GaN-On-SiC HEMTs by Means of a Thin AlGaN Back Barrier. *Micromachines* **14**, 291 (2023).
5. Ofuonye, B. *et al.* Electrical and microstructural properties of thermally annealed Ni/Au and Ni/Pt/Au Schottky contacts on AlGaN/GaN heterostructures. *Semicond. Sci. Technol.* **29**, 095005 (2014).
6. Mimila-Arroyo, J., Jomard, F. & Chevallier, J. Improvement of AlGaN/GaN/Si high electron mobility heterostructure performance by hydrogenation. *Appl. Phys. Lett.* **102**, (2013).
7. Bourlier, Y. *et al.* In-depth analysis of InAlN/GaN HEMT heterostructure after annealing using angle-resolved X-ray photoelectron spectroscopy. *Surf. Interface Anal.* (2020) doi:10.1002/sia.6857.
8. Naresh-Kumar,G. *et al.* Multicharacterization approach for studying InAl(Ga)N/Al(Ga)N/GaN heterostructures for high electron mobility transistors. *AIP Advances.* **4**, 127101 (2014)
9. Yadav, P. K. *et al.* Investigation of SiGe/Si heterostructures using state-of-the-art Auger Nanoprobes. in *IOP Conference Series: Materials Science and Engineering* vol. 41 (2012)


## KEYWORDS

GaN technology, HEMT, Characterization, Multi-technique, Interface

# EBIC Mapping of Threshold Voltage Distribution During Device Turn-on in SiC MOSFETs

Greg M. Johnson [1], Andreas Rummel[2], Heiko Stegmann[3]

*1 Carl Zeiss Microscopy, Dublin, CA, 2 Kliendiek Nanotechnik, Reutlingen, Germany, 3 Carl Zeiss Microscopy GmbH, Munich, Germany*

## INTRODUCTION

Power semiconductor devices are increasingly important to the electrification of society. Fully understanding the health of devices will aid in yield management. Fully understanding how the device turns on will aid in device improvement and modeling. This work examined the use of Electron Beam Induced Current in the examination of a cross-sectioned, commercially available SiC MOSFET.

## PROCEDURE

A commercially available SiC MOSFET device was cross-sectioned with a a Crossbeam 350 FIB-SEM instrument. A beveled cross-section was cut across 21 gates in the central area of the device with the focused Ga+ ion beam (Ga-FIB). The sample was milled with an untitled stage such that a "wedge", or window of a beveled section, was prepared in the sample. As such the windows was about 10 microns long and of a depth greater than the N-type, "Current Spreading Layer" (CSL) of the device. Then the sample was examined with Electron Beam Induced Current in a Kleindiek Nanotechnik PS8 Prober Shuttle with an EBIC amplifier. Figure 1 shows both the experimental setup with nanoprobes (left image) and these preliminary results (right image). The probe was able to access the emitter junctions of the device by simply touching the top surface. Thus, when the electron beam scans the sample, charge carriers are acted upon by the electric field(s) in the sample, and an EBIC current is detected at the needle. The EBIC scans were at 2 kV, where the secondary electron image (SEI) has been overlaid with white from the EBIC image. Here we see a nice delineation of the depletion zones between the P-well and the N-type Current Spreading Layer (CSL) of the device.

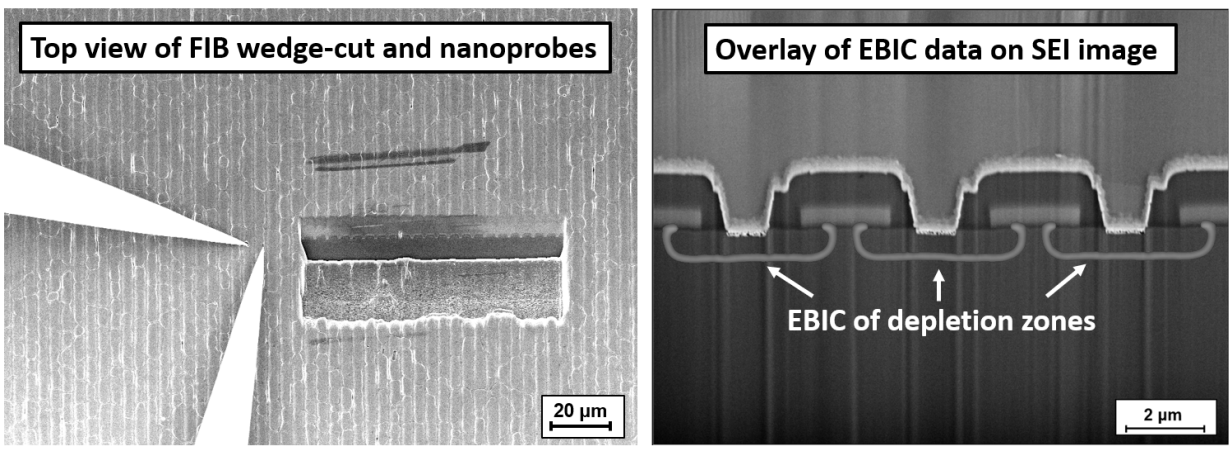


**FIGURE 1.** Views of cross section and EBIC results on as-cut sample imaged with one probe. Left image shows a low-mag view of the FIB wedge-cut made into the device, with probes touching the top surface. Right: EBIC data highlights depletion zones reaching underneath the gates.

## RESULTS WITH GATE BIAS

An additional set of experiments was undertaken to explore the effect of gate bias on the devices of this cross section. Figure 2 depicts this technique. One probe was applied to the poly of one exposed gate, and because of the "fishbone" structure of these gates, any bias applied to one exposed gate feature is seen on all of them. Additional scans at 0 to 6 V bias were now applied.

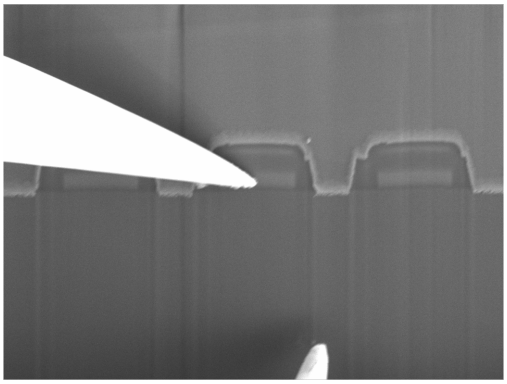

**FIGURE 2.** View of two probes placed on the cross section of the device. The top probe was in contact with the gate array, and applied a static bias and was varied from +0.0 V to +6.0 V, in increasing steps of 1 V. The bottom probe was in contact with the bulk, and measured the EBIC current.

The full set of EBIC scans are now featured in Figure 3. One thing to note is that the images portray the ray, black-and-white data as originally provided by the system. It may have been tempting to provide a low-bit or monochrome color map which hides the electrical data from the system, but this treatment shows the true noise present in the analysis. But from these slides, one may see that at 0 V, the same depletion zone as seen in Figure 1 is again seen. One may even detect a slight "shadow" from the probe tip, by comparing this image to the SEI one in Figure 2. Now, as the voltage is slowly increased, the depletion zone for this *p/n* junction gradually disappears, then one may see the zones between this N+ and P-well regions of the sample, and then they, too fade away.

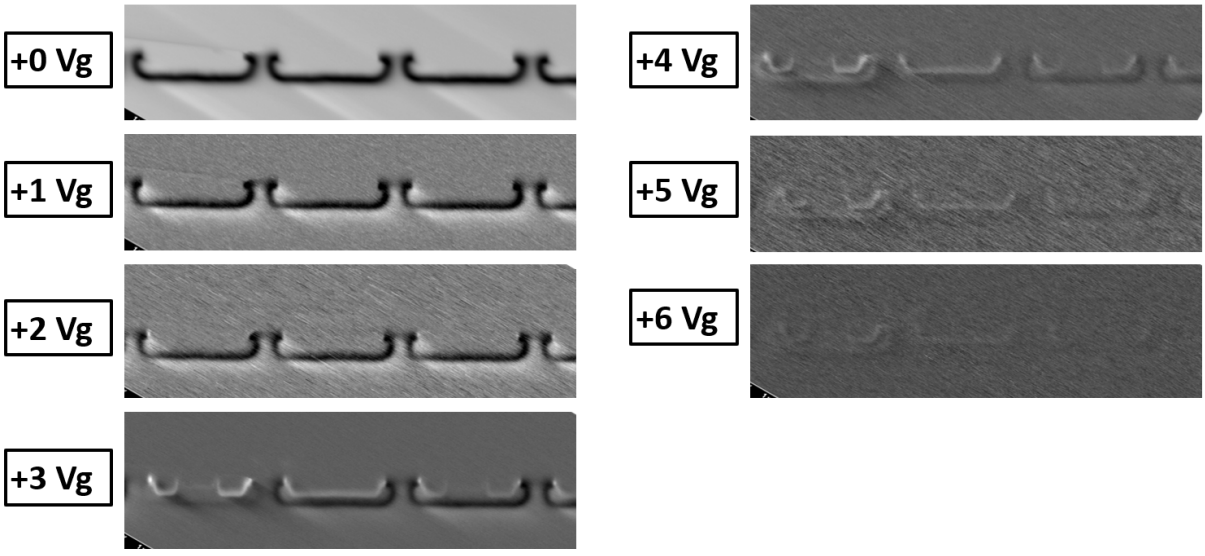


**FIGURE 3.** View of a series of EBIC measurements on three nearby devices in the field of view. As the gate voltage increases, the depletion zone between the P-well and N regions disappears, indicating inversion of the channel. Eventually at higher gates, no depletion zones are observed.

## CONCLUSIONS

This analysis has successfully mapped the depletion zones of a SiC MOSFET, in-situ, and thus given a unique insight as to the operation and turn-on of the device. Given that the data are provided in an image form, this work may rightfully claim to map the threshold voltage distribution across the sectioned area.
Furthermore, given that these EBIC analyses directly image the electric fields in the sample, and that these go to zero (no EBIC; no field), this analysis provides unique insight, perhaps a paradigm shift, in how current travels across the thickness of the device. Typically, the current path is drawn as an upside-down "L", where the current has to sneak along laterally, until it goes under the gate, and then, it can travel across the thickness of the device. But if there were no electric fields, then the carriers would be free to travel from top to bottom. These results will need further discussion and confirmation. Although it should be noted that a similar treatment on Si-based IGBT devices have found the same result.

## REFERENCES

[1] J. R. Beall and J. L. Jamiter, "EBIC - A valuable tool for semiconductor evaluation and failure analysis," *Proc. 15th International Reliability Physics Symposium*, pp. 61-69, 1977.
[2] G. Johnson, H. Stegmann, T. Rodgers, A. Rummel, D. Mello, M. Kuball and F. Hitzel, "In-situ Junction Analysis in SiC (and GaN)," *Proc. ISTFA 2023*, 2023.
[3] H. Stegmann, G. Johnson and A. Rummel, "Combining Three-dimensional FIB-SEM Imaging and EBIC to Characterize Power Semiconductor Junctions," *Proc. ISTFA 2023*, 2023.
[4] M. Cantoni und L. Holzer,"Advances in 3D focused ion beam tomography," *MRS Bulletin*, Bd. 39, Nr. 4, p. 354–360, 2014.

## KEYWORDS

EBIC, junction, SiC, Power, device, nanoprobing

# Coming of Age of Computational SEM

Benjamin D. Bunday, Shari Klotzkin, Douglas Patriarche, Yvette Ball
AMAG nanometro, Schenectady, NY, 12303, USA, E-mail: ben.bunday@amagnm.com

## ABSTRACT

SEM (scanning electron microscopy) systems have been the main workhorse of CD metrology for advanced semiconductor nodes for almost three decades. While the community has achieved a basic understanding of a SEM's general behaviors for analyzing many sample types and applications, the systematic isolation of SEM signal parameters with respect to all the varying parameters in both tool and sample has been elusive, experimentally. Computational SEM, a quantitatively informed simulation approach to optimization of the output SEM signals, will be presented as a more precise and useful method to assist with such characterizations.

Several application studies will be shown in this work as examples of how computational SEM can be applied to many different practical fab SEM measurement situations. The first two involve HV-SEM (fig 1), which has recently become a mainstream fab tool for measurement of HAR holes and trenches in VNAND lines and which is currently using see-through SEM imaging to detect the bottom layer registration to calibrate overlay (fig 2). Such work is time-consuming and expensive in terms of tool time, and such solutions can be very dependent on the exact measurement situation; simulation support for such roles can save much tool time, achieve more conclusive results, and avoid confusion resulting from experimentation using poorly characterized samples. Another case study will apply typical CD-SEM imaging to Cu CMP (fig 3) samples showing that signal signatures of interest for detecting dishing and copper thickness should be observable, and, with simulation support, could be analyzed quantitatively. A last case study will apply computational methods to demonstrate how the detection of different defects in an advanced complex ONO stack and how the ability to estimations of signal to noise ratio (SNR) are affected by choice of DI-SEM beam conditions. (fig 4).

DOE (design of experiments) SEM simulation studies concerning these different cases will be performed using SimuSEM software based on NIST's JMONSEL [1-2] which is a first-principles Monte Carlo electron scattering physics engine that has been well validated for over ten years as quantitatively accurate. AMAG SimuSEM, with a user-friendly GUI version, [3-4] makes JMONSEL usable and mass-producible by converting it into a virtual tool calculator, a computational SEM with DOE capabilities. This work will also demonstrate the quantitative accuracy of the model solutions, comparing simulated results to real HV-SEM images of HAR holes [5]. The work will conclude with quantitative results of HAR Hole and VNAND HV-SEM, CD SEM imaging of Cu CMP, and defects in an ONO stack that demonstrate the importance of computational SEM for improving SEM usefulness, productivity, and value for future SEM applications in-line.

## REFERENCES

[1] J.S. Villarrubia, A.E.Vladár, B.Ming, R.J.Kline, D.F.Sunday, J.S.Chawla, and S.List, "Scanning electron microscope measurement of width and shape of 10 nm patterned lines using a JMONSEL-modeled library," Ultramicroscopy 154 (2015) 15. http://dx.doi.org/10.1016/j.ultramic.2015.01.004

[2] Bunday, B., Mukhtar, M., Quoi, K., Thiel, B., and Malloy, M. "Simulating Massively Parallel Electron Beam Inspection for sub-20 nm Defects". Proceedings of *SPIE* Vol. 9424, 94240J (2015).

[3] Bunday, Benjamin D., Klotzkin, S., Patriarche, D., Mukhtar, M., Maruyama, K., Kang, SK, Yamazaki, Y. "Simulating process subtleties in SEM imaging". Proceedings of *SPIE* Volume 12053, Metrology, Inspection, and Process Control XXXVI; 120530A (2022) https://doi.org/10.1117/12.2615753.

[4] Bunday, Benjamin D. "Metrology test artifact availability improvement", Proceedings of *SPIE* Volume 12053, Metrology, Inspection, and Process Control XXXVI; 120531C (2022) https://doi.org/10.1117/12.2615726 .

[5] Bunday, Benjamin D. "Metrology test artifact availability improvement", Proceedings of *SPIE* Volume 12053, Metrology, Inspection, and Process Control XXXVI; 120531C (2022) https://doi.org/10.1117/12.2615726 .

**KEY WORDS:** CD-SEM, DI-SEM, HV-SEM, JMONSEL, computational SEM, virtual SEM, Monte Carlo simulation

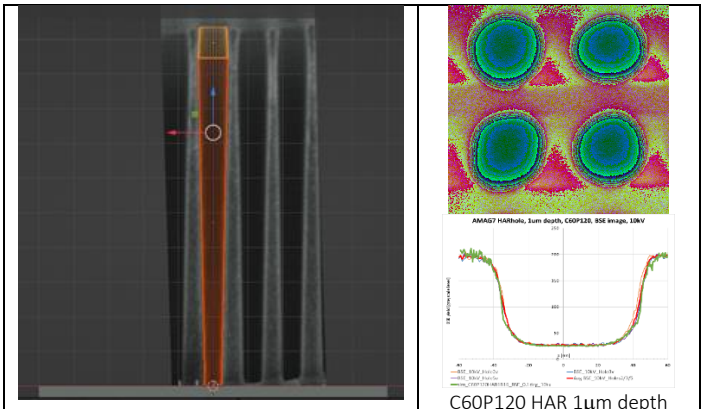


Fig 1. Left: XSEM image of AMAG7 HARhole test features, with 2-cone model for hole profile. Top right: Magnified views of the NGR5000 HV-SEM images of 1um depth AMAG7 HARhole features in SiO2 on Si, with stretched color scales to highlight the details of the very dim signal from the hole bottoms. Bottom Right: SEM signal linescans from experimental image plotted with four simulation trials where the parameters of the feature converge to very close fit to the experimental result, demonstrating a regressive solution is achievable for matching the simulated hole to physical data to attain a model-based solution for measurement.

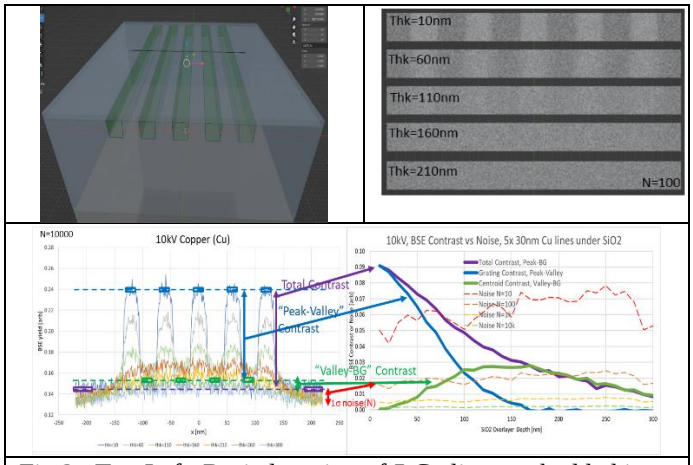


Fig 2. Top Left: Buried grating of 5 Cu lines embedded in SiO2, with 30 nm CD, 60 nm pitch and 30 nm depth. The lines are trapezoidal fills of oxide with 2° sidewall angle as shown. The overlayer is an oxide film which is defined to be looped within the simulation to different thicknesses so an entire DOE of buried grating depths can be run. Top right: Simulated images of the buried copper grating through different SiO2 film thicknesses at 10 keV beam. Bottom: SNR analysis showing detectability of buried grating from the simulated data down to 160 nm depth under oxide.

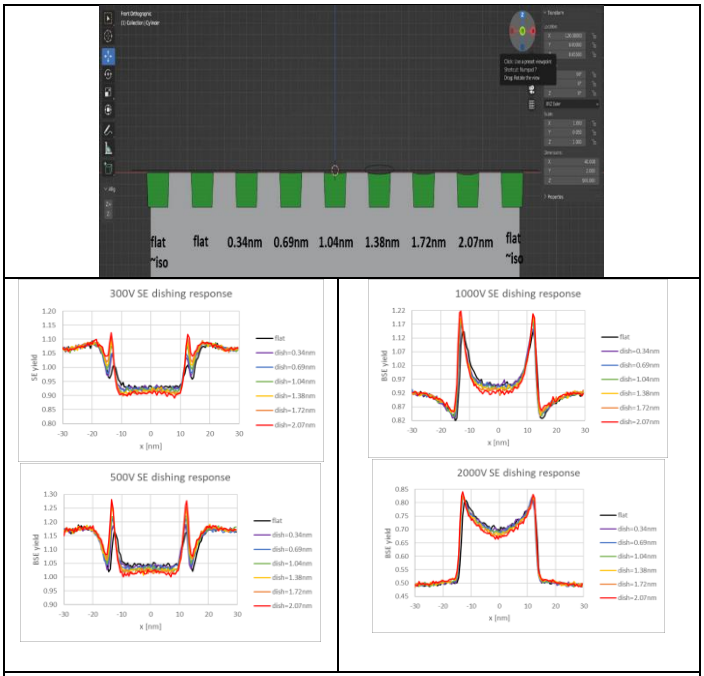


Fig 3. Top: Cu CMP dishing test structure with dialed dishing amounts. Grating is 60nm pitch, 30nm wide, 30nm deep Cu lines, 88° SWA, in trenches in SiO2.Bottom: Many different beam conditions are simulated in the study and the SE responses at 300V thru 2000V beams demonstrate significant sensitivity to the dishing.

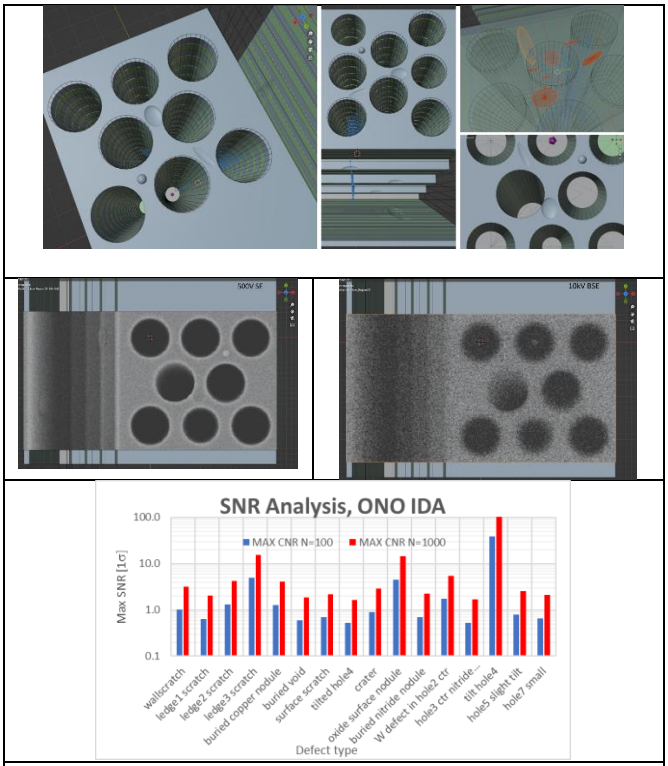


Fig 4. Top: Intentional defect array in ONO stack showing many different surface and buried defects. Top: Image gallery. Middle: two example images showing detection of various defects. Bottom: SNR analysis showing defect detectability.

# Effective pupil apodization in digital holographic microscopy

T. Cromwijk[1,2], M. Noordam[1,2], S. Witte[1,2], J. F. de Boer[2], A. den Boef [3]

[1]*Department of Physics and Astronomy, and LaserLaB, Vrije Universiteit, The Netherlands*
[2]*Advanced Research Center for Nanolithography (ARCNL), The Netherlands*
[3]*ASML Netherlands B.V., The Netherlands*

## INTRODUCTION

In semiconductor industry, optical wafer metrology is a key in the manufacturing process of integrated circuits. A crucial step during the fabrication is measuring the lateral alignment with respect to the previous wafer layer in the multilayer stack. This metrology step is called overlay metrology and is of importance for tuning the fabrication process and detecting problematic wafers early[1]. Detecting misalignment in the overlapping structures (overlay errors) requires sub-nm metrology precision. To keep up with shrinking devices as stated by Moore's law, a major development in overlay metrology is required. Therefore, we present dark-field Digital Holographic Microscopy (df-DHM) as a promising new technique for overlay metrology. We measure overlay on advanced semiconductor targets using a diffraction-based overlay (DBO) metrology technique[2]. Here the intensity difference between +1st and -1st diffraction orders, coming from two biased overlapping gratings, scales linearly with the overlay error. DHM distinguishes itself from other microscopy techniques by digitally recording the object as a hologram using a reference beam[3] (Fig. 1). The object image can be reconstructed from the hologram using fast Fourier transform techniques. The retrieved complex field gives access to amplitude and phase information which allows us to correct for imperfections in the imaging system. For example, defocus, illumination spot inhomogeneities, spurious apodization and lens aberrations can be corrected with dedicated computational imaging algorithms.

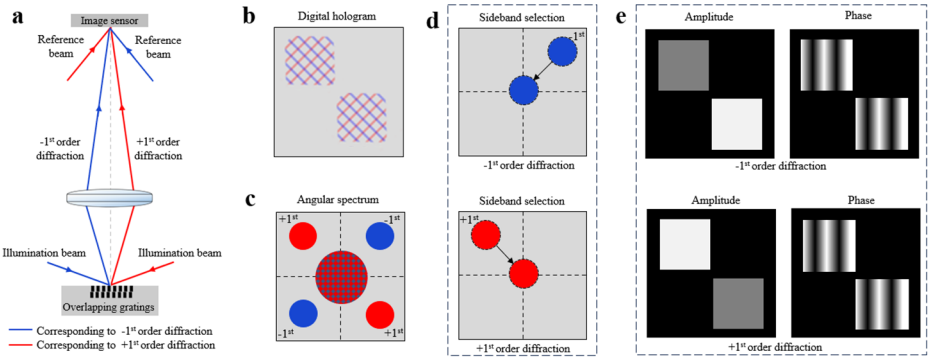


**FIGURE 1.** Schematic illustration of off-axis holographic recording and processing concept. **a** Schematics of the dark-field off-axis digital holography microscopy concept. **b** Recorded digital hologram with two overlapping interference patterns of the +1st and -1st diffraction orders. **c** The angular spectrum of the digital hologram retrieved by performing an 2D-FFT back-propagating to the pupil plane. **d** Selecting the sidebands and translating them to the center of the pupil plane. **e** Reconstructed object fields via inverse FFT of the selected sideband, resulting in the retrieval of the object amplitude and phase information.

## COHERENT ARTIFACTS

The coherent imaging conditions in our microscope introduce coherent imaging artifacts which limit the metrology performance. The Coherent Transfer Function (CFT) of the imaging system creates oscillating edge

transitions in the retrieved image, degrading the imaging quality. The oscillating behavior, i.e. Gibbs ringing, is a result of a sharp cut-off in the exit pupil plane, which is forward-propagated to the image. Gibbs ringing results in spurious oscillations in the high frequency region like the edges of a metrology target. Ringing not only leads to degradation of the image quality but also increases the optical crosstalk (light leakage) from surrounding structures into the metrology target. Optical crosstalk into the Region-of-Interest of the overlay target directly results in an incorrect overlay measurement. Therefore, suppression of these coherent imaging effects is required. We present computational apodization of the optical field in the exit pupil of the lens as a potential solution to mitigate these coherent imaging effects. Furthermore, we present experimental results of the influence of the imaging lens surface roughness on the apodization effectiveness. Finally, we will quantify the apodization effectiveness by the amount of optical crosstalk.

## DIGITAL PUPIL APODIZATION

Apodization functions can suppress the side lobs of a point spread function which effectively reduces ringing effects and optical crosstalk from surrounding structures at the expense of resolution. In our df-DHM concept we apply pupil apodization, as shown in Fig. 2. Via a Fourier transform the field is propagated to the pupil plane. The pupil plane is then multiplied with an apodization window. For our investigation we will use cosine-sum window functions that will moderate the effect of the CTF and reduce crosstalk noise by smoothing the higher frequencies of the measured hologram. After apodization the field is back-propagated to the image plane with an inverse Fourier transform.

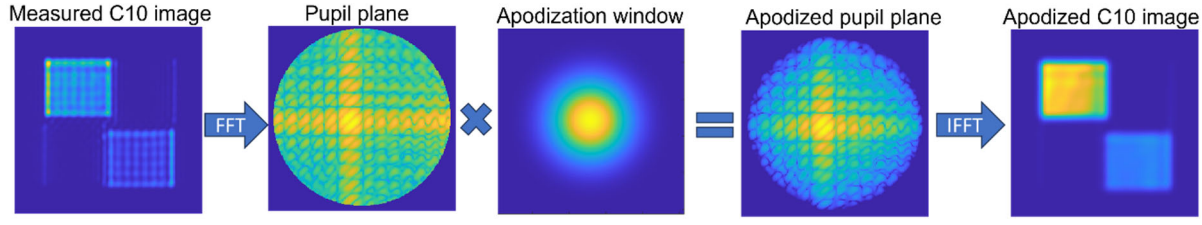


**FIGURE 2.** Concept of pupil plane apodization on a measured 10 x 10 µm overlay target, where the pupil plane is multiplied with an apodization window in the Fourier plane and then back-propagated to the image plane again.

The quantitative effect of pupil apodization is shown in Fig. 3. Here, a 10 x 10 µm overlay target is measured at a wavelength of 532 nm. The normalized intensity cross sections of an unapodized (Fig. 3a) and an apodized pupil plane (Fig. 3b) are shown in Fig. 3c.

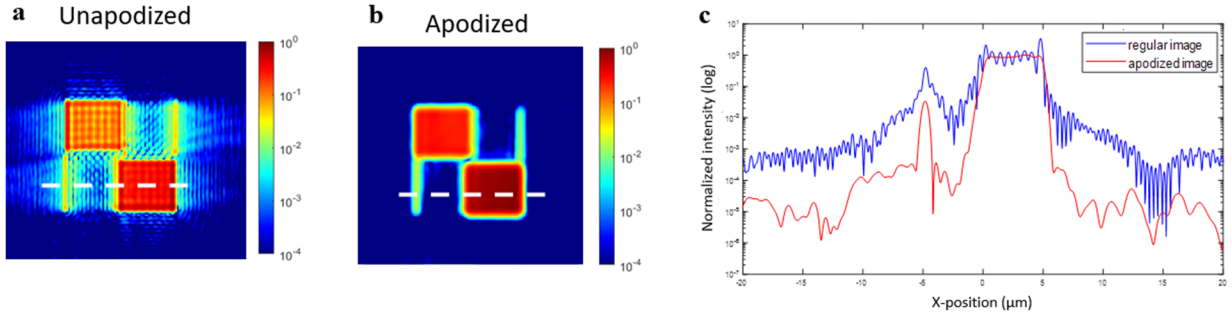


**FIGURE 3.** Effect of pupil apodization on a 10 x 10 µm overlay target.

After apodization the intensity is smoothened on the surface of the metrology target and the coherent ringing effect is completely suppressed. Furthermore, the noise level outside the target reduces from approximately $10^{-3}$ to $10^{-5}$. In order to reach the required sub-nm overlay accuracy, the noise levels should be suppressed to approximately $10^{-7}$ normalized intensity levels.

## LENS ROUGHNESS LIMITATIONS

In previous studies, simulations showed that apodization could suppress normalized intensity levels to the order of $10^{-11}$ [4]. However, lens surface roughness results in a weak coherent speckle background in the retrieved image. Lens-induced light scattering therefore limits the effectiveness of pupil apodization in DHM. In this study, the roughness of the used imaging lens is approximately 10 nm RMS, resulting in normalized intensity levels of $10^{-5}$. To reach the required $10^{-7}$ normalized intensity levels, the expect to lens roughness to be reduced to approximately 1 nm RMS.

## CONCLUSION

In conclusion, we have experimentally demonstrated the effectiveness of digital pupil apodization in our df-DHM imaging system to mitigate the coherent imaging artifacts as Gibbs ringing and optical crosstalk. Furthermore, surface roughness of the objective will be the key design parameter to minimize coherent cross-talk. To reach the sub-nm precision of OV metrology we must push the capabilities of computational imaging methods and DHM well beyond their existing boundaries. The effective pupil apodization proves to be a great step toward the realization of a DHM OV metrology tool.

## REFERENCES

1. T. C. Tin et al, *IEEE Access* **9**, 65418-65439 (2021).
2. P. Leray et al, *Proceedings of SPIE Advanced Lithography,* (2008)
3. M. Kim, *SPIE Reviews* **1**, 8005 (2008)
4. C Messinis et al, *Optics Continuum* **5**, (2022)

## KEYWORDS

Semiconductor metrology, digital holographic microscopy, digital apodization, lens roughness, computational imaging

# Polarization Sensitive Digital Holographic Microscopy

M. L. Noordam [1, 2], T. Cromwijk[1,2] , J. F. de Boer[2] , and A. J. den Boef [1, 2, 3]

[1]*Advanced Research Center for Nanolithography (ARCNL), Science Park 106, 1098 XG Amsterdam, The Netherlands*
[2]*Department of Physics and Astronomy, and LaserLaB, Vrije Universiteit, De Boelelaan 1081, 1081 HV Amsterdam, The Netherlands*
[3]*ASML Netherlands B.V., De Run 6501, 5504 DR Veldhoven, The Netherlands*

## INTRODUCTION

The ongoing trend in semiconductor industry to fabricate integrated circuits with smaller feature sizes, emphasized by the recent introduction of new lithography processes using extreme ultraviolet light, underscores the necessity for a new generation of metrology tools. Recently, dark-field digital holographic microscopy (df-DHM) has been proposed to tackle the challenges of increasing circuit complexity [1]. df-DHM builds on diffraction-based overlay (DBO) metrology tools, characterizing the overlay (OV) by measuring the difference between the $+1^{ste}$ and $-1^{ste}$ order diffraction of a DBO target [2].

DHM uses the interference signal between the $+1^{ste}$ and $-1^{ste}$ diffraction orders with two reference beams at different angles of incidence, respectively. Employing fast Fourier transform (FFT) techniques for computational selection of the distinct interference patterns, yields amplitude and phase information for both diffraction orders. These simultaneously retrieved complex fields allow for computational correction of imperfections in the imaging system [3].

Since DHM uses interference between the DBO diffraction signal and a reference beam the overlay measurements are dependent on the polarization states of the beams, i.e., an error in the polarization state in either the illumination or reference beam can influence the extracted OV values. Furthermore, polarization information of the diffracted beam can also be used to retrieve OV values [4]. To investigate and correct for the polarization dependence of OV measurements using DHM we propose a novel technique not only probing the complex fields of the $+1^{ste}$ and $-1^{ste}$ orders but also simultaneously probing the state of polarization (SOP) without any additional measurements.

## METHODS

### Experimental setup

The polarization sensitive df-DHM technique is based on the interference between the diffraction signal beam and two orthogonally polarized reference beams for both the +1ste and -1ste diffraction orders, totaling four reference beams. The separation in the angle of incidence between the total of four reference beams, as sketched in fig. 1, generates an interference pattern on the image sensor consisting of four different spatial frequencies. Using computational FFT techniques the interference patterns originating from the four reference beams can be individually selected. This results in four complex valued images constructed from a single measurement. Now, the intensity and phase profile of both diffraction orders is measured for two orthogonal reference beam polarizations in a single measurement. To demonstrate this novel technique, we focus in the next sections on the measurement of both orthogonal polarizations for only one of the two diffraction orders.

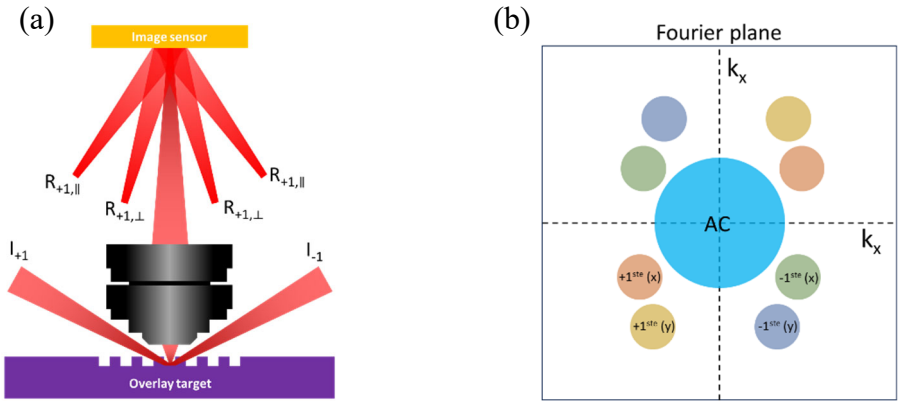


**FIGURE 1.** (a) Sketch of the optical setup. The +1$^{ste}$ and -1$^{ste}$ order diffracted light from the OV target is collected by a single objective and interfered with two orthogonal reference beams for each diffraction order on the image sensor. (b) Drawing of the spatial frequency domain representation of the detected signals.

## Calibration of the polarization state

The polarization state of a light field can be described by the Johnes vector, $\begin{pmatrix} |E_x|e^{i\phi_x} \\ |E_y|e^{i\phi_y} \end{pmatrix}$. From the Johnes vector the orientation of the fast axis of the light with respect to the x-axis can be calculated as $\theta = \arctan\left(\frac{|E_y|}{|E_x|}\right)$. The circularity of the light can be calculated as $\phi = \phi_x - \phi_y$. Because of our holographic imaging technique, we can extract the intensity as well as the phase information. From the measured interference pattern, we can separate two components: $E_{+1}E_{r_x} = \begin{pmatrix} |E_{rx}||E_{+1,x}|e^{i(\phi_x+\phi_{rx})} \\ 0 \end{pmatrix}$ and $E_{+1}E_{r_y} = \begin{pmatrix} 0 \\ |E_{ry}||E_{+1,y}|e^{i(\phi_y+\phi_{ry})} \end{pmatrix}$, see fig. 2. To extract the polarization angles, $\theta$ and $\phi$, the intensity and phase difference between the orthogonal polarized reference beams need to be calibrated first. The intensity ratio, $A_r = \frac{|E_{rx}|}{|E_{ry}|} = \frac{\sqrt{I_{rx}}}{\sqrt{I_{ry}}}$, can be extracted from a simple measurement of the intensity of the individual reference beams. The calibration of the phase difference between the reference beams, $\phi_r = \phi_{rx} - \phi_{ry}$, appears to be more complex due the fact that the reference beams are orthogonally polarized. However, we observe a small contribution of interference between the orthogonal polarized reference beams, see the inset of fig. 2. This interference signal is originating from the z component of the electric field due to the different angle of incidences with respect to the image sensor. Using the similar DHM techniques we can computationally select the spatial frequency of the interference between the reference beams and reconstruct the phase difference between the reference beams.

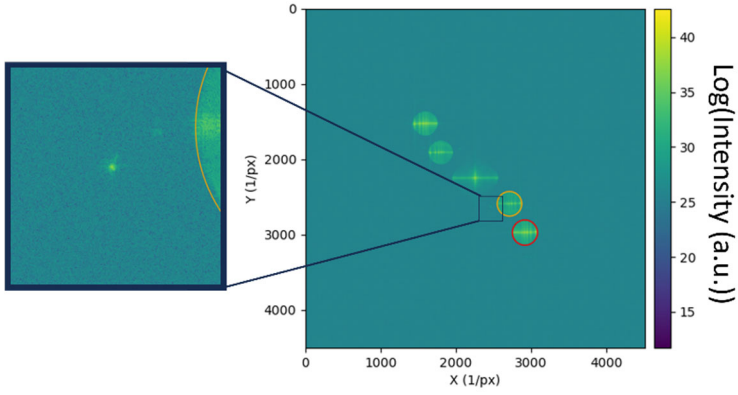


**FIGURE 2.** False logarithmic color plot of the FFT transformed measured image in the spatial frequency domain. The orange and red circle indicate the spatial frequency domain of the two orthogonal polarized diffraction signals. The inset shows the contribution of the interference between the orthogonally polarized reference beams.

## RESULTS

Figure 3 shows the calculated polarization state from a DHM measurement of a 16 µm by 16 µm OV target for an illumination beam with an arbitrary polarization state. In fig. 3(a) the total diffracted intensity, summed up for the two orthogonal polarizations, is displayed. In fig. 3(b) and fig. 3(c) the orientation of the fast axis, θ, and the circularity of the light, ϕ, are shown respectively. From fig. 3 a constant θ and ϕ can be observed over the OV target where outside the target θ and ϕ are arbitrary. Although, further analysis and different illumination polarizations are needed to achieve a full understanding of the polarizing effects of the OV target.

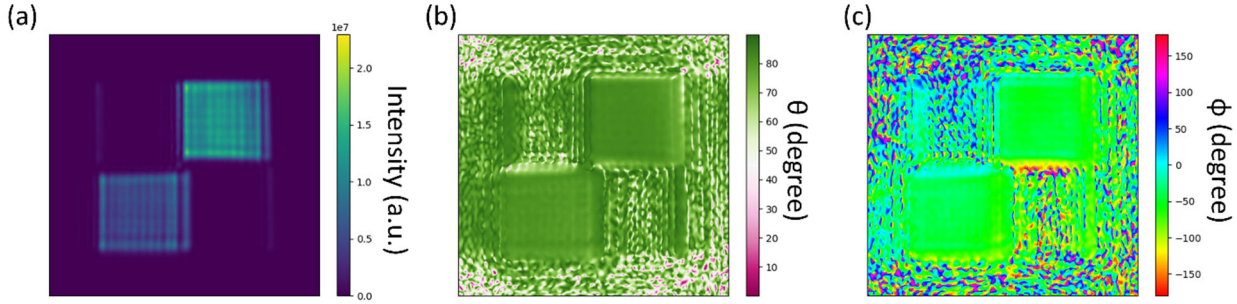


**FIGURE 3.** Polarization sensitive DHM measurement of a 16 µm by 16 µm OV target. (a) False color plot of the total diffracted intensity. (b) False color plot of the calculated orientation of the fast axis of the light with respect to the x-axis, θ. (c) False color plot of the calculated circularity of the light, ϕ.

## OUTLOOK

This work experimentally demonstrates polarization sensitive DHM measurements on an OV target. Here, we characterize the orientation of the fast axis and the circularity of the light together with the total diffraction intensity in a single measurement. Next steps to advance the progression of this work involves polarization sensitive measurements of multiple OV targets with different set OV values for different incoming polarization states. In this way we can quantify the polarization sensitivity characteristics on DHM overlay measurements. Furthermore, we plan to implement polarization dependent noise reduction to improve the quality and robustness of DHM as an overlay characterization tool.

## REFERENCES

1. Messinis, Christos, et al. "Diffraction-based overlay metrology using angular-multiplexed acquisition of dark-field digital holograms." *Optics Express* 28.25 (2020)
2. den Boef, Arie J. "Optical wafer metrology sensors for process-robust CD and overlay control in semiconductor device manufacturing" *Surf. Topogr.: Metrol. Prop.* 4 023001 (2016)
3. van Gardingen-Cromwijk, Tamar, et al. "Field-position dependent apodization in dark-field digital holographic microscopy for semiconductor metrology." *Optics Express* 31.1 (2023)
4. Chen, Xiuguo, et al. "Multi-spectral snapshot diffraction-based overlay metrology." *Optics Letters* 48.13 (2023)

## KEYWORDS

semiconductor metrology, digital holographic microscopy, Overlay, computational imaging, polarization

# Combining In-Line Atomic Force Microscopy and Scatterometry for Metrology of 3D Holographic Patterns In Roll-to-Roll Nanoscale Manufacturing

Barbara Groh[1], Kwon Sang Lee[1], Shashank Venkatesan[2], Luis Arturo Aguirre[1], Sofia Frey[1], Liam G. Connolly[3], Michael Baldea[2], Chih-Hao Chang[1] and Michael Cullinan[1]

*[1]Walker Department of Mechanical Engineering*
*University of Texas at Austin*
*[2]McKetta Department of Chemical Engineering*
*University of Texas at Austin*
*[3]Microsystems and Nanotechnology Division, Physical Measurement Laboratory*
*National Institute of Standards and Technology*

## INTRODUCTION

Roll-to-roll manufacturing at the nanoscale faces many challenges in precision control and overlay before it will be able to fulfill its potential as a continuous, high-throughput, low-cost fabrication technique [1]. These challenges include web instabilities like flutter, warping, twisting, slipping, wrinkling, and stretching [2], [3] which create a substrate that is difficult to control and monitor to the extent that is necessary for micro/nano production. Current technology reliably patterns single-layer features onto the flexible webs, but overlay between multilayer products remains out of reach [4]. By leveraging the ability to make precise structures that only require a single exposure using near-field interference lithography, such challenges can be averted [5].

However, evaluating 3D nanoscale structures on a flexible, moving substrate creates metrology challenges that require robust and flexible multiscale techniques. By pairing precise in-line atomic force microscope (AFM) metrology at the individual feature level with larger scale optical and scatterometry based measurements, we can execute holistic evaluation of the manufactured pattern. To this end, we aim to leverage machine learning techniques to integrate multiscale real-time metrology data which would enable real-time process control through feedback and fault detection.

## HOLOGRAPHIC PATTERN MANUFACTURING

The samples currently used for conceptual testing of the proposed manufacturing methods are made in a batch-to-batch process based on the final manufacturing design. A diagram of the proposed manufacturing system can be seen in Figure 1 (left) and features a conformal nanostructured optical mask loop interacting with the photoresist-covered substrate web. The polydimethylsiloxane (PDMS) mask is aligned with the substrate and exposed to an ultraviolet (UV) light source to create the near-field holographic structures within the thick layer of photoresist. An example of the resulting pattern can be found in Figure 1 (right), although refinement to the process and manufacturing environment is necessary to improve pattern quality. Also, further inverse modeling of the structures can be used to create a mask that produces 3D structures with desired properties or geometry

## MULTISCALE METROLOGY

The 3D holographic structures created by the system require metrology at multiple scales to ensure high quality features across the span of the entire web. Metrology goals include topographical imaging of the pattern at the individual feature level, assessment of the quality of the periodic internal structure of the pattern, and measurement of the material properties of the exposed resist.

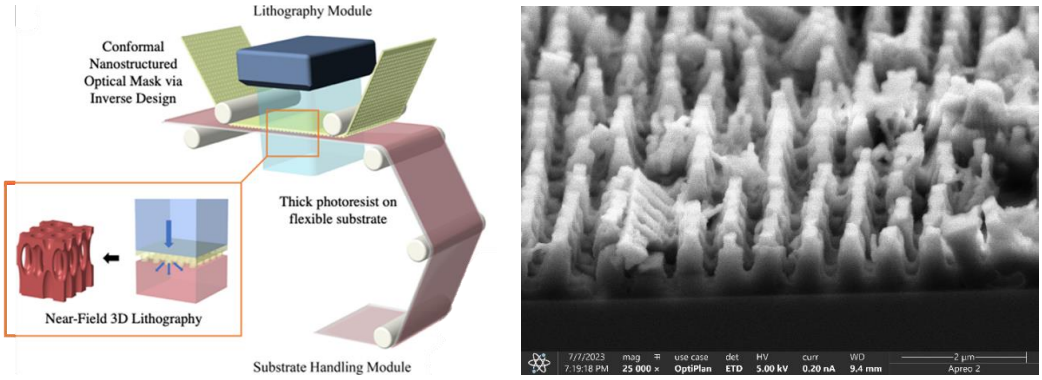


**FIGURE 1.** (Left) Diagram of proposed 3D holographic pattern manufacturing system. (Right) SEM image of 3D holographic lithography pattern.

## Feature Scale Metrology: Atomic Force Microscopy System

The existing AFM metrology tool is capable of in-line metrology of R2R samples [6]. It consists of a single-chip, micro-electro-mechanical system (MEMS)-based AFM mounted to a flexure-based gantry system as seen in Figure 2 (left) [1], [6], [7]. The single-chip AFM (sc-AFM) contains full actuation for taking a scan within a 20 µm by 20 µm area and the gantry allows the AFM chip to be suspended above the web and maintains the position of the AFM relative to the moving web. This, in combination with a flexure system stabilizing and actuating the gantry, allows the web to move continuously and the AFM to move with it for the length of the scan. The flexure-mounted AFM system can then lift and reset position to take another moving scan. This system is known as the nanopositioning subsystem for the remainder of this paper. This subsystem is actuated in the XZ plane by voice coil linear motors driving a pair of biaxial double parallelogram flexures with a gantry suspending the AFM in between. The x-axis allows for the AFM to move in tandem with the moving web for the duration of the scan while the z-axis motion regulates the approaching and disengaging actions of the probe. The flexure-gantry system is pictured in Fig. 2 (left).

Testing of AFM imaging with moving scans is still underway, but static scans of samples made using the holographic interference lithography process can be seen in Fig. 2 (right). This figure shows an sc-AFM scan of a 60 mJ/cm$^2$ exposed sample with an un-sharpened tip (radius > 100 nm) and demonstrates the device's ability to detect defects including missing features and pattern collapse. Physical limitations of the flexure nanopositioning system and AFM scan throughput results in limited sampling ability at this scale. Additionally, the scan location cannot be repositioned relative to the width of the web. Therefore, this metrology technique can only provide topographic and material property data at a relatively low sampling rate, generally under 100 µm$^2$ every 10-20 seconds. To assess the entire web, larger-scale metrology is needed.

## Web-Scale Metrology: Scatterometry

Where AFM will provide periodic sampling of individual feature-scale characterization, scatterometry will provide continuous feedback across the entire web. Additionally, the use of optical modeling of the ideal physical system and comparison to the real-time measurements will create the opportunity to characterize the internal periodic structure. The periodic nature of the pattern will result in predictable reflectance. These characteristics are dependent on both the wavelength of light used for detection and the sample structure. Experimental scatterometry results can be seen in Figure 3 (left), where samples produced more damped reflectance amplitudes and longer periods at higher dosages. By monitoring the modulation phase and amplitude, it is possible to determine over or under exposure, which is further indicative of internal pattern defects that affect the reflectance spectra.

The experimental data can then be compared to an optical model performed using finite-difference time-domain (FDTD) methods [8]. The 3D holographic interference pattern created by the optical model is then used to create a binary model of the shape created in the photoresist. A transfer-matrix method (TMM) simulation is then performed on the binary resist model to generate a reflectance spectra model [9].

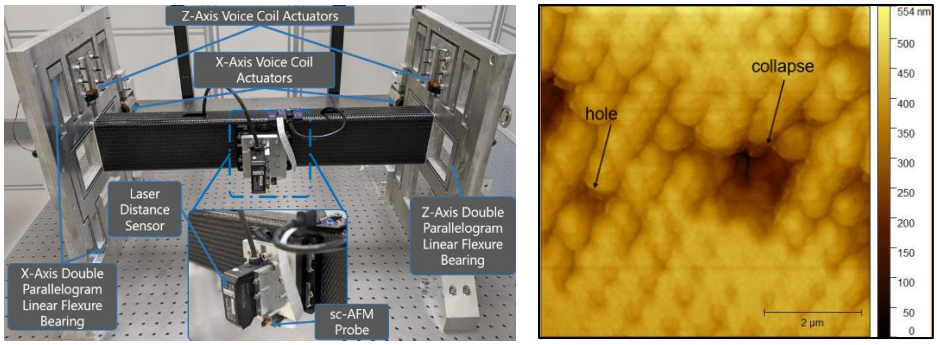


**FIGURE 2.** (Left) The double-parallelogram and gantry of the nanopositioning system with view of sc-AFM mounting subsystem. (Right) Static sc-AFM scan of 60 mJ/cm$^2$ exposed sample with local defects highlighted.

Figure 3 (right) shows an example comparison between the simulated reflectance spectra and the experimental data. In this figure, the internal structure of the pattern most significantly affects the period of the spectral modulation. The models were able to achieve period matching within 2% error. The phase shift notable within the figure is due to differences in photoresist thickness, which is not yet accounted for in the model. Using the model comparison, changes in the period of reflectance modulation can be used to indicate imperfections in the internal structure of the pattern as well as provide exposure dosage information. Reviewing areas of concern indicated by the scatterometry measurements with the AFM metrology system can provide more detailed characterization of manufacturing imperfections to allow for robust quality control.

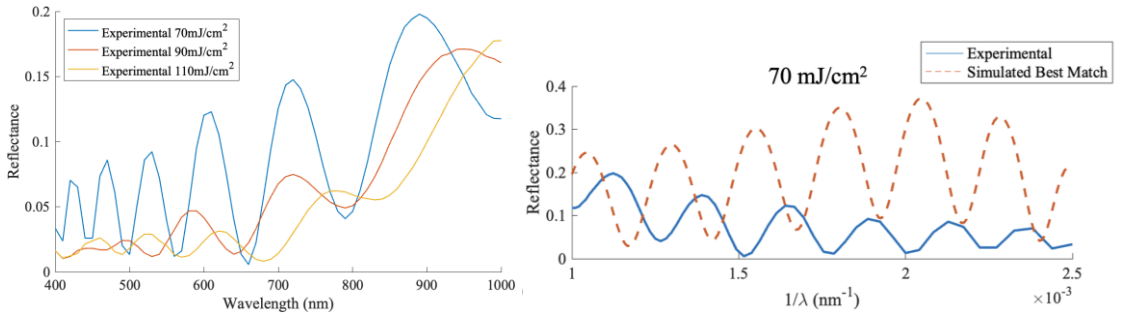


**FIGURE 3.** (Left) Reflectance measurements of fabricated samples with 70, 90, and 110 mJ/cm$^2$ exposure dose versus wavelength. (Right) Best-match reflectance spectra between experimental results and simulation.

## MACHINE LEARNING-BASED DATA FUSION

The pair of aforementioned metrology techniques create a multiscale, multifrequency, multimodal (i.e., using disparate sensing modes) set of measurements to combine into useful process control information. These challenges arise from the significant difference in scale and scan speed of the AFM system in relation to scatterometry. A 10 by 10-micron AFM image is many thousands of times smaller than the spot size of the scatterometry module across the width of the web, and can only capture images at a rate well below 1 Hertz. This type of multidimensional analysis creates a collection of scaling challenges that would require expert evaluation to extrapolate useful relationships, which may be automated by machine learning-based data fusion techniques. [10].

Fortunately, the fairly successful implementation of Machine Learning algorithms (specifically Deep Learning-based) for modelling biological systems [10], for in-situ 3D printing process evaluations [11], etc., create the foundations for our analysis of such multimodal data. High resolution, low speed AFM scans, if independently used, enable characterization of local defects and can be evaluated with image processing schemes. The higher speed, lower resolution scatterometry data would provide insights into web-wide uniformity, product porosity, the presence of periodic defects such as those due to faulty masks, etc. We shall explore the use of generative models such as Generative Adversarial Networks (GANs) to compensate for the dearth of high-resolution AFM image data due to their ability to generate realistic high-resolution images by learning the underlying probability distribution corresponding to the training data, which in this case shall be the AFM scans [12]. Scatterometry signals can be

converted to images which would then enable the use of a Convolutional Neural Network (CNN) to fuse the AFM and scatterometry data, at appropriate frequencies [11].

## REFERENCES

[1] L. G. Connolly, A. Cheng, J. Garcia, and M. A. Cullinan, "A ROLL-TO-ROLL SYSTEM FOR IN-LINE, TIP BASED NANOMETROLOGY OF PATTERNED MATERIALS AND DEVICES".
[2] J. Deng and L. Liu, "Introducting Rolled-Up Nanotechnology for Advanced Energy Storage Devices," *Advance Energy Materials*, vol. 6, no. 23, Jul. 2016.
[3] Y. B. Chang, S. J. Fox, D. G. Liley, and P. M. Moretti, "Aerodynamics of moving belts, tapes, and webs," *American Society of Mechanical Engineers, Design Engineering Division (Publication) DE*, 1991.
[4] P. Pandya, "Precision Systems for Conformable, Capillary-Driven, Continuous, Roll-to-Roll Nanoimprint Lithography," presented at the ASPE 36th Annual Meeting, Minneapolis, MN, Nov. 04, 2021.
[5] I.-T. Chen, E. Schappell, X. Zhang, and C.-H. Chang, "Continuous roll-to-roll patterning of three-dimensional periodic nanostructures," *Microsyst Nanoeng*, vol. 6, no. 1, p. 22, Apr. 2020, doi: 10.1038/s41378-020-0133-7.
[6] L. G. Connolly, T.-F. Yao, A. Chang, and M. Cullinan, "A tip-based metrology framework for real-time process feedback of roll-to-roll fabricated nanopatterned structures," *Precision Engineering*, vol. 57, pp. 137–148, May 2019, doi: 10.1016/j.precisioneng.2019.04.001.
[7] L. G. Connolly, "Enabling Hybrid Process Metrology in Roll-to-Roll Nanomanufacturing," Dissertation, University of Texas at Austin, Austin, 2022.
[8] Kane Yee, "Numerical solution of initial boundary value problems involving maxwell's equations in isotropic media," *IEEE Trans. Antennas Propagat.*, vol. 14, no. 3, pp. 302–307, May 1966, doi: 10.1109/TAP.1966.1138693.
[9] A. Yariv and P. Yeh, *Opticl Waves in Crystals: Propagation and Control of Lasere Radiation*. John Wiley & Sons, Inc., 1984.
[10] S. R. Stahlschmidt, B. Ulfenborg, and J. Synnergren, "Multimodal deep learning for biomedical data fusion: a review," *Briefings in Bioinformatics*, vol. 23, no. 2, p. bbab569, Mar. 2022, doi: 10.1093/bib/bbab569.
[11] J. Li, Q. Zhou, L. Cao, Y. Wang, and J. Hu, "A convolutional neural network-based multi-sensor fusion approach for in-situ quality monitoring of selective laser melting," *Journal of Manufacturing Systems*, vol. 64, pp. 429–442, Jul. 2022, doi: 10.1016/j.jmsy.2022.07.007.
[12] I. Goodfellow *et al.*, "Generative adversarial networks," *Commun. ACM*, vol. 63, no. 11, pp. 139–144, Oct. 2020, doi: 10.1145/3422622.

## KEYWORDS

Atomic Force Microscopy, roll-to-roll, in-line metrology, multimodal machine learning, scatterometry

# Dark Uncertainty in Hybrid Metrology for Semiconductor Manufacturing

Ronald G. Dixson*, Adam L. Pintar, R. Joseph Kline,
Thomas A. Germer, John S. Villarrubia, and Samuel M. Stavis†

*National Institute of Standards and Technology, Gaithersburg, Maryland 20899*
**ronald.dixson@nist.gov, †samuel.stavis@nist.gov*

## INTRODUCTION

The basic purpose of estimating uncertainty is to quantify confidence and guide decisions. An underestimate of uncertainty results in overconfidence, which can misguide decisions and lead to serious consequences. Uncertainty underestimates often come to light in comparisons of measurement results from different methods and laboratories. Thompson and Ellison[1] observed this common problem in a statistical meta-analysis of measurement results from the field of analytical chemistry, describing the excess variability by the term dark uncertainty.

Ideally, an evaluation of uncertainty captures all sources of error, so that the resulting estimate corresponds to the total uncertainty. In reality, the total uncertainty often exceeds the uncertainty estimate by an amount corresponding to the dark uncertainty, which can have multiple sources. We illustrate this concept in Figure 1. Any unknown error can be dark. However, unknown systematic effects, such as method bias, are particularly problematic.

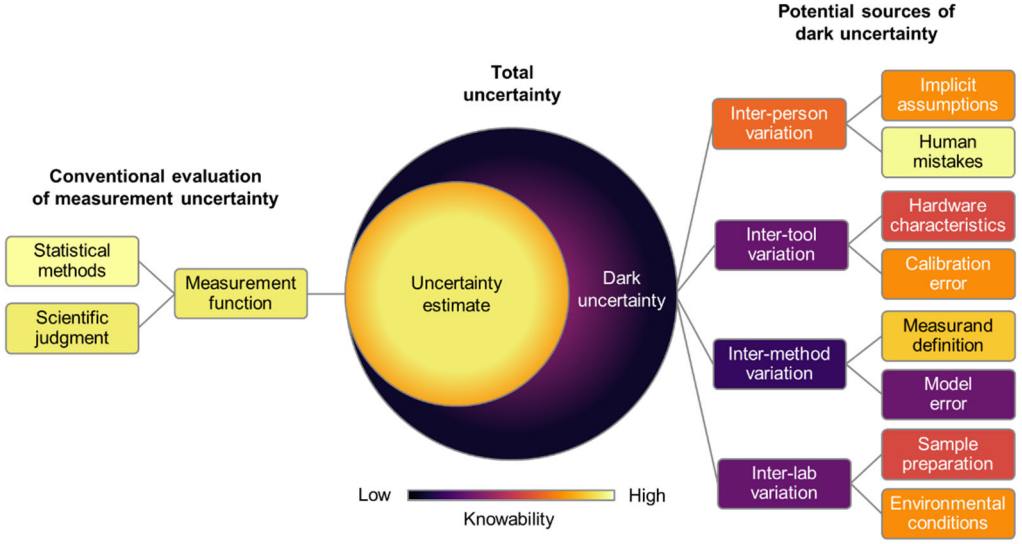


**FIGURE 1.** Schematic showing a conventional evaluation of measurement uncertainty, which provides an uncertainty estimate. This estimate is much smaller than the total uncertainty, with dark uncertainty resulting from underlying categories of root sources. The color code indicates an approximation of knowability.

We propose that dark uncertainty in linewidth metrology is a critical problem for semiconductor manufacturing. Technology roadmaps for this venture have set a target uncertainty of ± 0.2 nm at 95 % coverage by the year 2025.[2]

This challenge has motivated the use of hybrid metrology to reduce uncertainty by combining results from different methods. Previous studies have acknowledged the necessity of combining consistent results[3] but have not addressed the prevalence of inconsistent results or the effect of combining inconsistent results.[4]

Multiple methods of linewidth metrology have supported semiconductor manufacturing. Optical imaging microscopy,[5] scanning electron microscopy (SEM),[6] electrical resistance linewidth metrology[7,8], atomic force microscopy (AFM)[9], scatterometry[10], also known as optical critical-dimension (OCD), and X-ray scattering[11] have all been relevant. Two prevalent methods for high-volume manufacturing (HVM) are critical-dimension SEM (CD-SEM) and OCD. Critical-dimension small-angle X-ray scattering (CD-SAXS) is growing in importance, and critical-dimension AFM (CD-AFM) remains relevant.[12]

We illuminate dark uncertainty among three methods for linewidth metrology, using a Bayesian hierarchical model that is similar to that of the National Institute of Standards and Technology (NIST) Consensus Builder.[13] The top level of the hierarchy is inter-method variability, and the bottom level of the hierarchy is intra-method uncertainty, with estimation per the Guide to the Expression of Uncertainty in Measurement (GUM).[14] Such a model quantifies the dark uncertainty as a standard deviation and the consensus uncertainty as a coverage interval. Two limitations are worth noting—the dark uncertainty is a metric of the overall comparison that is unassignable to any particular method, and errors that may occur in a common mode among different methods remain dark.

## LINEWIDTH DARK UNCERTAINTY

We apply our Bayesian hierarchical model to analyze a representative comparison of linewidth measurement results of approximately 13 nm by SEM, TEM, and CD-SAXS,[15] assuming that the corresponding coverage intervals account for any sampling non-equivalence. We use the values of middle linewidth and 95 % coverage intervals from Villarrubia *et al*.[15] This statistical analysis estimates a dark uncertainty of 0.5 nm and a consensus uncertainty of ± 0.8 nm at 95 % coverage. We compare the TEM, SEM, CD-SAXS, and consensus results in Figure 2.

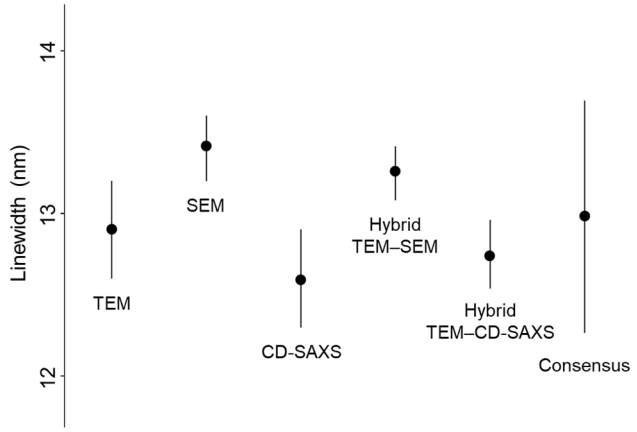


**FIGURE 2.** Plot comparing mean values and 95 % coverage intervals resulting from transmission electron microscopy (TEM), scanning electron microscopy (SEM), and critical-dimension small-angle X-ray scattering (CD-SAXS). Different uncertainty analyses lead to a wide range of coverage intervals.

In a cautionary tale for hybrid metrology, we implement a corresponding Bayesian statistical analysis. We treat TEM as a reference method, using the TEM result as prior information first for the SEM result and then for the CD-SAXS result. The hybrid analyses weight and average the results, outputting coverage intervals that are smaller than the input coverage intervals. The hybrid uncertainty is up to five times smaller than the consensus uncertainty.

Contrary to hybrid metrology and due to dark uncertainty, the combination of inconsistent results, such as TEM and SEM, should increase rather than decrease the coverage interval. Even if two methods are consistent, such as TEM and CD-SAXS, assuming coverage of all sources of uncertainty is perilous for a small sample size. The hybrid TEM–CD-SAXS result differs more from the SEM result than the original TEM result because of the smaller SEM coverage interval, and is also inconsistent with both the hybrid TEM–SEM result and the SEM result. The hybrid TEM–CD-SAXS result ignores a source of dark uncertainty that becomes evident only in light of the SEM result.

The coverage interval for the consensus result is larger than any of the individual coverage intervals, because it explicitly recognizes inconsistency of the measurement results. The consensus result is then consistent with all three individual results due to this larger coverage interval. Calculation of the consensus result from only two of the three individual results would further widen the coverage interval due to the smaller sample size and fewer degrees of freedom, which would remain consistent with all three of the individual results.

In conclusion, we begin to illuminate dark uncertainty in linewidth metrology for semiconductor manufacturing. Considering a target uncertainty of 0.2 nm at 95 % coverage by the year 2025, dark uncertainty ranging from 0.1 nm to 1.0 nm is a critical issue. Amplifying this issue, the growing popularity of hybrid metrology promotes the naive combination of inconsistent results in an attempt to reduce uncertainty, yielding underestimates of total uncertainty that can misguide decisions.

## REFERENCES


1. M. Thompson. and S. L. R. Ellison, Dark uncertainty. *Accreditation and Quality Assurance*, **16**, 483-487 (2011).
2. IEEE International Roadmap for Devices and Systems—Metrology, IEEE (2022).
3. N. F. Zhang *et al*., *Applied Optics*, **51**, 6196-6206 (2012).
4. N. G. Orji *et al*., *Nature Electronics*, **1**, 532-547 (2018).
5. D. Nyyssonen and R. D. Larrabee, *Journal of Research of the National Bureau of Standards*, **92**, 187-204 (1987).
6. M. T. Postek and D. C. Joy, *Journal of Research of the National Bureau of Standards*, **92**, 205-228 (1987).
7. D. Yen, *Proceedings of SPIE*, **342**, 73-81 (1982).
8. L. W. Linholm, R. A. Allen, and M. W. Cresswell, *Proceedings of SPIE*, **10274**, 1027407 (1994).
9. Y. Martin and H. K. Wickramasinghe, *Applied Physics Letters* **64**, 2498-2500 (1994).
10. C. Raymond, *Proceedings of SPIE*, **10294**, 1029408 (1999).
11. R. L. Jones *et al*., *Applied Physics Letters*, **83**, 4059 (2003).
12. B. Bunday *et al*., *Proceedings of SPIE*, **10585**, 105850I-1 (2018).
13. NIST Consensus Builder. https://consensus.nist.gov/app/nicob
14. Evaluation of Measurement Data – *Guide the Expression of Uncertainty Measurement*. JCGM 100 (2008).
15. J. S. Villarrubia *et al*., *Ultramicroscopy*, **154**, p. 15-28 (2015).


## KEYWORDS

metrology, uncertainty, dark uncertainty, inter-method comparisons

# GaN/InGaN µLEDs Study by Cathodoluminescence and Photo-Sensitive Kelvin Probe Force Microscopy

Palmerina González-Izquierdo*, Névine Rochat, Davide Zoccarato, Fabian Rol, Julia Simon, Patrick Le Maitre, Marion Volpert, Matthew Charles, Matthieu Lafossas, Simona Torrengo, Narciso Gambacorti and Łukasz Borowik*

*Univ. Grenoble Alpes, CEA, Leti, F-38000 Grenoble, France*

## INTRODUCTION

The rapid advancement of microscale technologies has led to the emergence of µ-LEDs as a prominent contender in various applications such as display technology, augmented and virtual reality, optogenetics, and more.(1) However, as these light-emitting wonders continue to shrink in size, a critical challenge emerges - the impact of sidewall defects on efficiency and performance, particularly as the perimeter-to-surface ratio increases.(2) This study delves into this multifaceted challenge, employing advanced analytical techniques with nanometric resolution: cathodoluminescence (CL) and photo-sensitive Kelvin Probe Force Microscopy (KPFM). CL provides valuable insights into radiative recombination processes, allowing a deeper understanding of how sidewall defects affect overall µ-LED performance. Moreover, employing CL at two different acceleration voltages enables a targeted exploration of defect-induced processes in various regions of the µ-LED structure. In parallel, photo-sensitive KPFM measures surface photovoltage (SPV), a parameter intricately linked to critical factors affecting device performance, like recombination, transfer and trapping of charge carriers.(3) The comparative analysis of results obtained through these techniques offers valuable insights into the interplay between defect-induced processes and performance degradation near LED edges. Furthermore, this study investigates the dependence of light emission on epi-LED square and circular mesa structures of various sizes using CL. By performing measurements at room temperature (RT) and 10 K (where defect-related energy states are inactive), we can decouple the contributions of light extraction efficiency (LEE) and internal quantum efficiency (IQE) to the external quantum efficiency (EQE). Our findings shed light on the interplay between IQE and LEE as a function of LED size and geometry, paving the way for efficient miniaturization of LEDs.

## Influence of shape and size on GaN/InGaN µLED light emission

Initially, we studied the dependence of light emission in micro epi-LED mesa structures with different widths (2.5, 5, 7.5 and 10 µm) and geometries (square and circular). Fig. 1 shows the CL integrated intensity maps of the square mesas (circular mesas maps not shown here) at RT, 10 K (LT) and the ratio between both maps. Surprisingly, we found an intermediate size with optimal light emission (Fig. 2a). At RT, these maps show the EQE, which depends on IQE and LEE on the form: $EQE = IQE \cdot LEE$. Consequently, the non-linear relationship between EQE and the perimeter-to-surface ratio may be attributed to a competition between these two factors. To distinguish between IQE and LEE, we conducted LT measurements, where light emission is primarily influenced by LEE, given that approaching 0 K leads to the "freezing" of defect levels and IQE tends to 1. Finally, we obtained the I(RT)/I(LT) ratio in order to follow the evolution of IQE with the epi-LED size and shape. The results show that the LEE decreases with size and shows a different trend for square and circular geometries (Fig. 2b) and non-radiative recombination on the mesa edges (which is greater for LEDs whose distance from the center to the edge is shorter or near the minority carrier diffusion length). These findings illustrate the importance of understanding the relationship of IQE and LEE with respect to LED size and geometry in the path towards µLED array design.

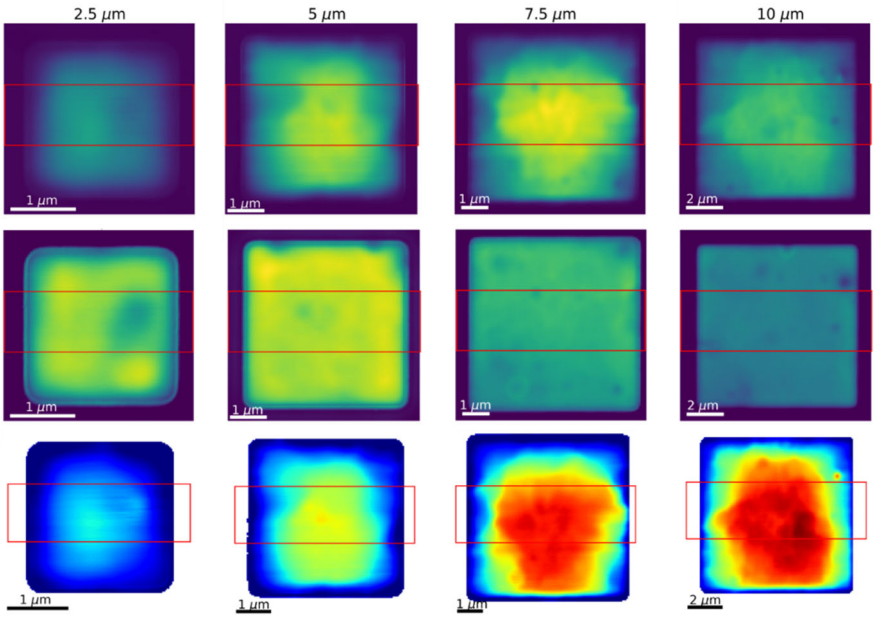


**FIGURE 1.** Integrated MQW cathodoluminescence intensity (*I*) maps at RT (1st row), LT (2nd row) and *I(RT)/I(LT)* (3rd row) for four square epi-LED mesas with different widths (2.5, 5, 7.5 and 10 µm). Each row of maps is normalized to the maximum value within the series.

a) c)

b)

**FIGURE 2.** Normalized maximum (filled markers) and mean value (empty markers) over the central area of the mesas (marked as red rectangles in Fig. 1) for square (red square markers) and circular (blue circular markers) epi-LEDs. a) *I(RT)*, b) *I(LT)*, c) *I(RT)/I(LT)*.

## GaN/InGaN LEDs sidewall defects analysis by Cathodoluminescence and photo-sensitive Kelvin probe force microscopy

In this second part of the study, we investigated the impact of sidewall defects on a GaN/InGaN epitaxial LED using CL and photo-sensitive KPFM. Utilizing CL at two distinct excitation energies, we were able to independently analyze the top p-GaN layer and the InGaN quantum well structures (QWS) within the mesa. Our findings revealed a reduction in the GaN near-band-edge (NBE) and InGaN QW peak intensities, coupled with an increase in yellow luminescence (YL) as we approached the mesa's edge (results not shown here). These changes were attributed to the presence of sidewall defects formed during the etching process. Conversely, when specifically examining the top p-GaN layer, the GaN NBE peak remained consistent throughout the entire measured area of the mesa, including the vicinity of the edge. The lack of variability near the edge suggested that sidewall defects may not significantly impact this layer. However, it is plausible that any potential sidewall effects are masked due to the pre-existing significant defects in this layer, a characteristic often observed in Mg-doped GaN.(4)

In the context of complementary photo-sensitive KPFM measurements, we observed a generated surface photo-voltage (SPV) on the vicinity of the edge of a mesa of 1 $mm^2$ (Fig. 3a, b). This SPV originates from the generation of electron-hole pairs and subsequent hole transfer towards the mesa surface through quantum tunneling. Notably,

the observed decay of the SPV, taking tens of seconds, was remarkably slow when compared to the reported radiative carrier lifetimes of GaN/InGaN QWs.(5) We associated this slow SPV decay with the presence of charge traps on the surface. This decay is better fit by a double exponential decay, indicating the presence of at least 2 charge de-trapping mechanisms. Furthermore, the SPV and the obtained time decay constants are uniform across the entire studied mesa area (Fig. 3 c, d, e), indicating that the charge trapping observed by photo-sensitive KPFM is not related to sidewall defects. It aligns, however, with the CL data examining the top p-GaN layer, suggesting possible trapping related to Mg doping. The hypothesis of charge trapping was further supported by the KPFM measurements at 10 K (not shown here). These findings contribute critical insights into defect-induced processes and their role in device performance, particularly in the vicinity of LED edges.

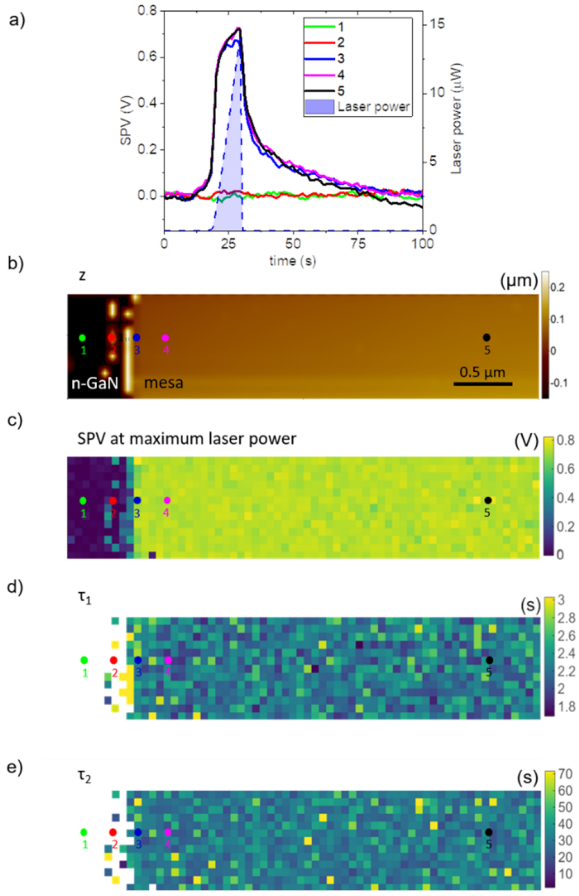


**FIGURE 3.** a) SPV at different points (marked with dots in b-e) in the vicinity of the edge of a 1 $mm^2$ epi-LED, b) topography measured by AFM, c) SPV under maximum laser power map and c, d) time decay constant maps resulting from the double exponential decay fit. Image size: 4 x 0.8 $\mu m^2$, 64 x 13 $px^2$.

## REFERENCES


1. Parbrook PJ, Corbett B, Han J, Seong TY. *Laser & Photonics Reviews*. 2021;15(5):2000133.
2. Olivier F, Daami A, Licitra C, Templier F. *Appl Phys Lett*. 2017 Jul 10;111(2):022104.
3. González-Izquierdo P, Rochat N, Charles M, Sochacki T, Borowik Ł. J *Phys Chem C*. 2023 Jun 24;
4. Kumar A, Yi W, Uzuhashi J, Ohkubo T, Chen J, Sekiguchi T, et al. *Journal of Applied Physics*. 2020 Aug14;128(6):065701.
5. Reklaitis I, Kudžma R, Miasojedovas S, Vitta P, Žukauskas A, Tomašiūnas R, et al. *J Electron Mater*. 2016 Jul 1;45(7):3290-9.


## KEYWORDS

µ-LEDs, GaN, InGaN, Kelvin probe force microscopy, charge trapping, sidewall defects.

# 3D corner residue monitoring for CFET gate patterning using CD-SEM

Wei Sun[1], Emmanuel Dupuy[2], Il Gyo Koo[2], BT Chan[2], Gian Lorusso[2], Janusz Bogdanowicz[2], Anne-Laure Charley[2], Jef Geypen[2], Patrick Carolan[2], Kei Sakai[1], Zhenghan Li[1], Miki Isawa[1]

*1 Hitachi High-Tech Corp.,552-53, Shinkocho, Hitachinaka-shi, Ibaraki, Japan*
*2 IMEC, Kapeldreef 75, 3001 Leuven, Belgium*

## INTRODUCTION

The transistor architecture of complementary FET (CFET) is attractive to continue device scaling for technology nodes beyond 1 nm. CFET principle consists in stacking nMOS and pMOS transistors vertically to gain area and reduce the device footprint. The vertical integration involves complex manufacturing processes, like high aspect ratio (HAR) patterning in nanosheet (NSH), gate, spacer, and contact modules [1-2]. For the gate, the challenges lie in gate profile/CD control, NSH erosion and 3D corner residues at the bottom of gates and NSH [3]. Currently, the residue check mainly relies on top-view scanning transmission electron microscope (STEM). A high-throughput, in-line metrology technique is required for mass measurements. In this work, we demonstrate a CD-SEM measurement solution to quantify the residues after HAR gate patterning for CFET. An algorithm was developed, and an index called corner roundness (R) was used to estimate the amount of residues. We measured the R value using CD-SEM and STEM images for two contacted poly pitches (CPP). R values obtained from CD-SEM and STEM images had the same trend, which indicates that CD-SEM is feasible to quantify the residues for CFET etching process monitoring.

## METHODOLOGY

To quantify the residues at the bottom corner of the tall gate and NSH with an e-beam tool, we need to detect the electron signal variation corresponding to the residue variation. As the tall gate (300nm with hard mask) and tight gate pitch (CPP=50nm) makes the aspect ratio of the CFET trenches over 9, most of the secondary electrons (SEs) and backscattered electrons (BSEs), generated by scanning electrons with energies from several hundreds of electronvolts to a few kiloelectronvolts at the bottom area, have difficulty to escape from the bottom when they take off with angles larger than 10 degrees. On the other hand, only the electrons with small take off angles may escape from the bottom without collision with the sidewall and finally be detected. To examine which portion of the electron signal is sensitive to the residue variation, Monte Carlo simulations were performed to obtain the line-profiles. Here, the residue extension was changed from 10 nm to 0 nm (without residue), as the cross-section shown in Fig. 2(a). Fig. 2(b) shows the normalized SE line-profiles between two gates using the primary electrons of 800 eV. The SE signal intensity near the bottom area was smaller than 1% of the top signal intensity, so that the residue variation was difficult to be detected. Fig. 2(c) shows the BSE line-profiles which are detected by an annular detector with angular range of 0~15 degrees. It is obvious to see that the profile varied with changing the residue extension. These simulation results indicate that it is possible to distinguish the residue variation by detecting the BSEs with smaller take off angles.

Fig. 3 shows the top-view of the CFET after HAR gate patterning. The corner with right angle becomes curvilinear due to the existence of residues. We developed an algorithm to define the curvilinear level of the corner, which is called corner roundness (R). R is defined by the minimum distance from the cross point of the detected line edges to the detected corner edge. The threshold can be tuned to catch the line edges and corner edge.

## RESULTS AND FUTURE WORKS

To verify the feasibility of quantifying residues by a CD-SEM (GT2000, Hitachi), the top-view STEM images showed in Fig.4 (a) and (b) and the CD-SEM images in Fig. 4(c) and (d) for CPP of 50 nm and 60 nm were acquired at the same location for comparison. As shown in Fig.4(e), a difference is that the CD-SEM viewed and scanned from the top of the gate with hard mask while the top-view STEM viewed and scanned near the bottom part of the gate and nanosheet (NSH) after milling off the top part of the gate. From the STEM images, we can see that the four corners surrounded by the gate and the NSH become curvilinear because of the existence of residues. Note that the bright contrast around each bottom area is due to the thinly deposited tungsten in lamella preparation. Although the contrast of the CD-SEM images is different from the top-view STEM images, we still can observe the curvilinear corners from the BSE images. Fig. 5 shows the R values measured from the top-view STEM images and the CD-SEM images using the algorithm described above. By comparing the R values for CPP of 50 nm and 60 nm, it is seen that the CD-SEM and the top-view STEM had a same trend but with an offset value. The offset can be attributed to the height difference of the gate, the difference in image contrast, and the tool differences. This result indicates that the CD-SEM is feasible to quantify the residues and we can benefit from its high sampling capability and high throughput for the CFET etching process monitoring.

As the complexity in developing 3D structured CFET, the sidewall geometry of the HAR gate or the NSH could also give influence on the R value. The CD-SEM measurement performance and robustness for different etching conditions are being evaluated via more samples and wafers.

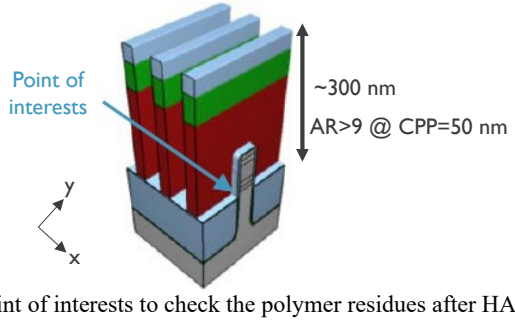


**FIGURE 1.** Point of interests to check the polymer residues after HAR gate patterning.

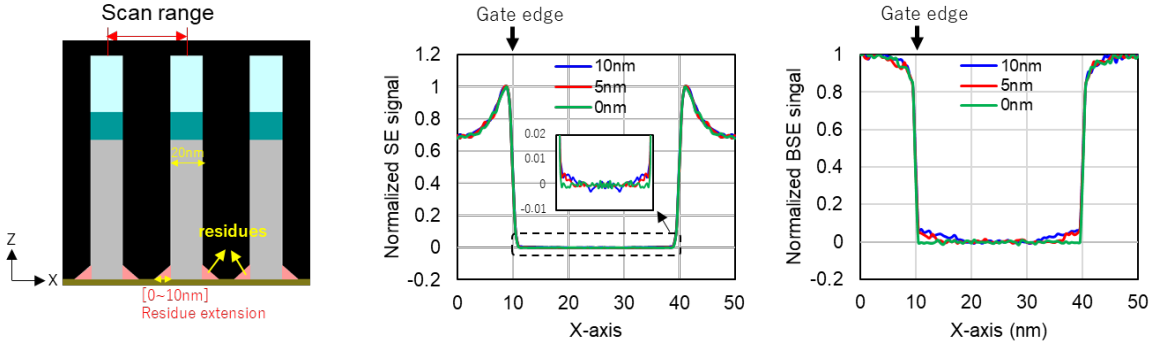


(a) (b) (c)

**FIGURE 2.** (a) Cross-section of the simulation model. Simulated (b) SE and (c) BSE line-profiles for the residue extension length of 10, 5, and 0 nm.

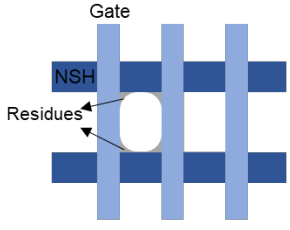


**FIGURE 3.** (a) Top view of the CFET after HAR gate patterning. (b) The algorithm for corner roundness measurement.

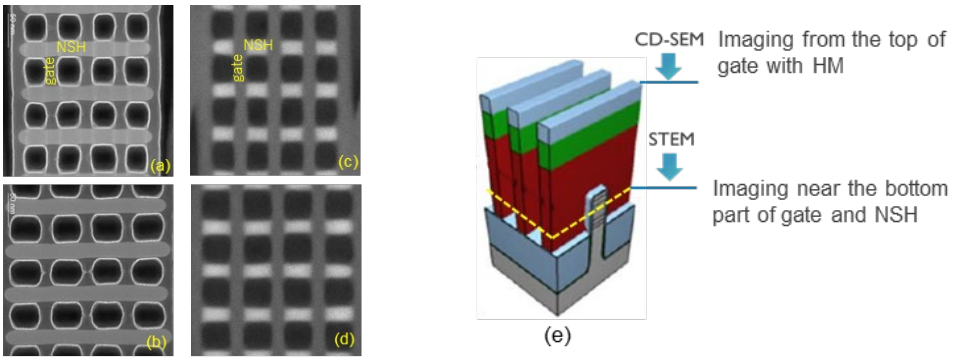


**FIGURE 4.** (a) and (b) STEM images for CPP of 50 nm and 60 nm. (c) and (d) CD-SEM images for CPP of 50 nm and 60 nm. (d) Schematic for the different view position of the CD-SEM and the top-view STEM.

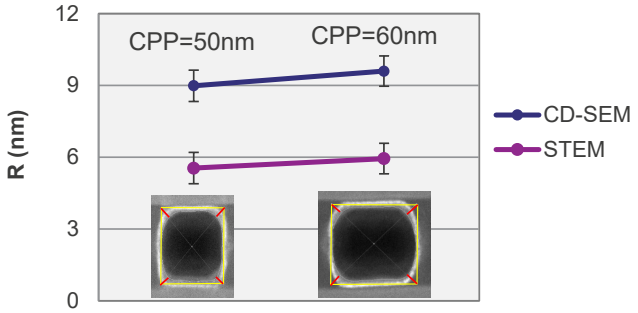


**FIGURE 5.** Comparison of the R values of STEM and CD-SEM images.

## REFERENCES

1. N. Horiguchi et al., Proc. SPIE, **PC1205608**, (2022).
2. D. Radisic et al., Proc. SPIE, **12499** (2023).
3. E. Dupuy et al, PESM conference, Grenoble, France (2023)

## KEYWORDS

CFET, CD-SEM, residues, in-line metrology

# Fluorescence-guided sub-micron optical photothermal infrared spectroscopy (O-PTIR) for the localization and identification of defects and contaminants

Eoghan Dillon and Michael K. F. Lo

*Photothermal Spectroscopy Corp. 325 Chapala Street, Santa Barbara, CA, 93101.*

## INTRODUCTION

Contamination analysis of modern microelectronics poses a great challenge due to their small feature sizes and chemical complexities. For contaminants larger than 100 µm, conventional analytical techniques, such as Fourier-transformed infrared microspectroscopy (FT-IR), would generally provide acceptable results. Each compound has a unique infrared absorption profile, thus allowing identities fingerprinting, which could be readily aided by searching against large spectral libraries. Despite these benefits, the rough spatial resolution due to its long probing wavelength (the same microns-length infrared illumination) severely limits its utility for analysing smaller contamination spots. Recent publications have established the O-PTIR technique as a novel, effective solution for contamination feature sizes smaller than 10 µm [1-3]. This non-contact, reflection-mode operated technique provides sub-micron spatial resolution, free of auto-fluorescence contribution, while still outputting infrared band shapes comparable to ideal transmission mode FT-IR spectra, which enable direct spectral identification with conventional commercially available infrared databases [1-3].

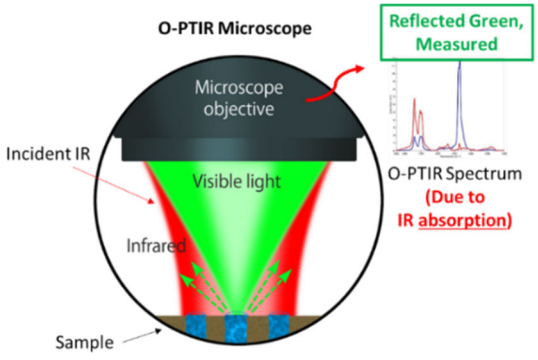


**FIGURE 1.** Operation principle of O-PTIR and the formation of O-PTIR spectra

The technique enables collection of infrared spectra with Raman-like spatial resolution but without the influence of auto-fluorescence. This novel technique employs a "pump-probe" excitation-detection mechanism, where the pump makes up of the pulsed infrared laser illuminating the specimen surface; simultaneously, a second, constant wave laser in visible wavelength would impinge in the same space to sense localized absorption-induced photothermal effect. In essence, the spatial resolution of the analysis would be in the diffraction limited spot size of the visible laser, which is typically 532 nm, thus leading to a theoretical spatial resolution of ~500 nm [1].

Auto-fluorescence imaging is a feature that is particularly helpful for quickly locating regions of interests when the visible image of the contaminated surface may be quite dark in color, with little to no optical contrast. Auto-fluorescence refers to the emission upon excitation of the molecule itself without being tagged by an external fluorophore. Since many foreign organic contaminants already possess strong auto-fluorescence under the illumination

of visible light, we can collect high quality fluorescence images directly from these FA/contamination specimens without tagging of fluorophore-based fluorescent probes. These auto fluorescence images can then be easily used to localize regions for subsequent O-PTIR analysis.

## ANALYSIS OF NON-WETTING SOLDER BUMP

The novel combination of O-PTIR spectroscopy and fluorescence imaging fully demonstrates the possibility of surveying ROI with co-located fluorescence microscopy prior to acquiring O-PTIR spectra. Under the fluorescence image in Fig. 5-B, the chemical boundaries of the components in ROI becomes readily distinguishable. O-PTIR spectra could then help identifying the unknown chemical composition (Fig. 5-D). Here, the contrasts in the fluorescence image have similarities to the O-PTIR image taken at 1732 $cm^{-1}$ (Fig. 5-C); both images would show the epoxy-based underfill adjacent to the ROI has a brown hue (orange marker) and contrast to the purple untainted underfill (gray marker) further away. These observations are supported by the heightened carboxylic acid-related absorption around 1680 $cm^{-1}$ in the ROI. These observations suggest the presence of extraneous species in the underfill near the contamination zone. As a positive control, polyimide-based solder mask is known to give out strong auto-fluorescence [5]. As expected, the polyimide-based solder mask (blue spectra) shows high contrast to the underfill, thus further confirming the immense value of combining co-located fluorescence imaging and O-PTIR spectroscopy towards a targeted and focused analysis of a complex mixture. The ability to visually assessing the ROI rapidly without knowing the sample's chemistry is highly advantageous in expediting unknown identification. It is not necessary to collect O-PTIR images to highlight localized heterogeneities prior to spectral collection. Since all O-PTIR spectra would not be affected by fluorescence, initial fluorescence image screening before collecting O-PTIR spectra from the region of interest could significantly improve the quality and efficiency of contamination and failure analysis. This new capability confirms that O-PTIR spectroscopy can collect high quality infrared spectra of strongly auto-fluorescent material.

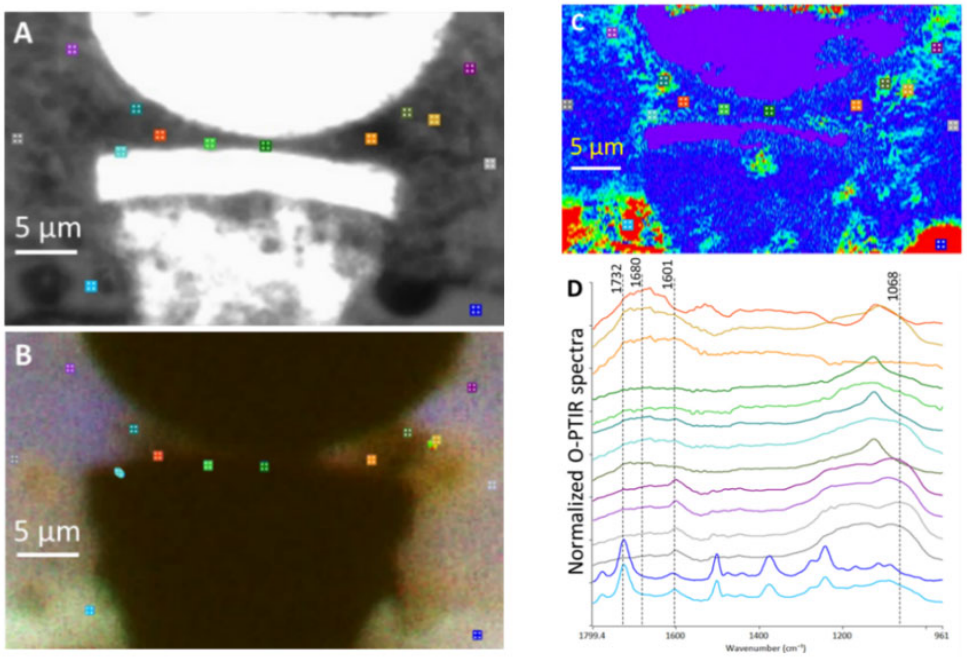


**Figure 2.** The co-located fluorescence concept toward a rapid analysis of an unknown. A) Optical image of a non-wetting solder bump provided by Photothermal Spectroscopy Corp (PSC), which fails to connect with the aluminum pad; (B) co-located overlaid fluorescence images taken as, blue: ex@497 nm, em@535 nm; green: ex@578 nm, em@641 nm; red: ex@628 nm, em@692 nm excitation/emission filters; (C) comparative O-PTIR image collected at 1732 $cm^{-1}$; (D) corresponding O-PTIR spectra taken from marker locations

## REFERENCES

1. M. Kansiz et al., *Microscopy Today*, 2020, vol. 28, no. 3, pp. 26–36.
2. M. Lo, M. Kansiz, E. Dillon, J. Anderson, C. Marcott. *2021 IEEE International Symposium on the Physical and Failure Analysis of Integrated Circuits (IPFA),* July 2021, 136.
3. S. Zulkifli, B. Zee, M. Lo, *2022 IEEE International Symposium on the Physical and Failure Analysis of Integrated Circuits (IPFA),* July 2022, 20.

## KEYWORDS

Infrared, O-PTIR, sub-micron, fluorescence, contamination, Raman.

# Crystal Orientation Quantification In Less Than 10 Seconds

D. Lopez[1], L.Grieger[2], M. Van der Haar[2], and D. Beckers[2]

*1Malvern Panalytical Inc., 2400 Computer Drive, Westborough, MA, 10581, United States*
*2Malvern Panalytical B.V., Lelyweg 1, 7600AA Almelo, The Netherlands*

## INTRODUCTION

We present here work on the orientation determination of bulk crystals for several different steps of manufacturing (cutting, grinding, end control) towards a finalized wafer. X-ray diffraction is one of the basic analytical methods that is routinely utilized for both materials research and quality control processing. It is non-destructive and offers high precision and accuracy in lattice orientation measurements.

The classic orientation method via rocking curves at different azimuthal angles is a widely used method that yields results in 10-20 minutes for near vicinal crystals. The productivity loss with such slow systems is addressed in this work. Here we presented a method 2 orders of magnitude faster (Figure 1). Offcut magnitude precision is evaluated to 0.003° 1σ and automation options range from manual to fully fab compliant to encapsulate the needs of both research and industry. Additionally, dimensional metrology for wafer shape control is available (Figure 2). This is a strong improvement in methods compared to current industrial standards, enabling control of each individual wafer at a throughput of more than 1 million wafers per automated wafer tool per year at single point per wafer. In this range of new technologies, ranging from benchtop to work floor sized installations, a powerful solution for the HVPE specific problem of quantification of lattice plane tilting can be found. Also, orientation is possible in an ultra-fast manner for ingots and boules, along with a variety of stages and attachments allowing precise orientation transfer to sawing equipment or in an equivalent manner for grinding processes.

Another use further downstream is seen in the orientation before lithography e.g. for laser diodes where cleaving is necessary or MOSFET trench orientation. Here the precise knowledge of the crystallographic directions aligns the device boundaries with the crystal unit cell orientation having direct implications to yield and process uniformity[1]. The suite of instruments contains further features like rocking curve functionality, 300mm mapping (Figure 3) and many more which shall be shown in individual use cases.

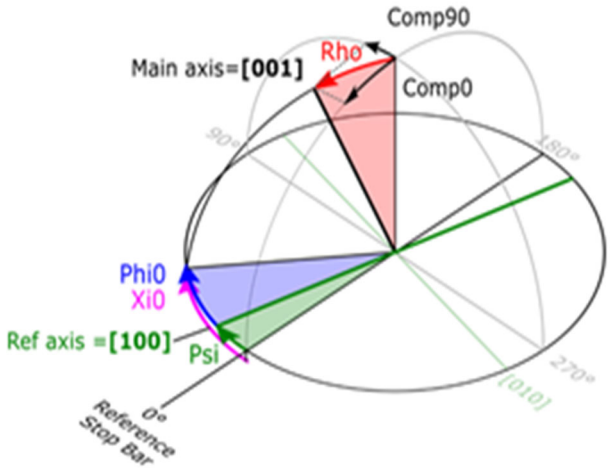


**FIGURE 1.** Graphical representation of measured quantities of the azimuthal scan method.

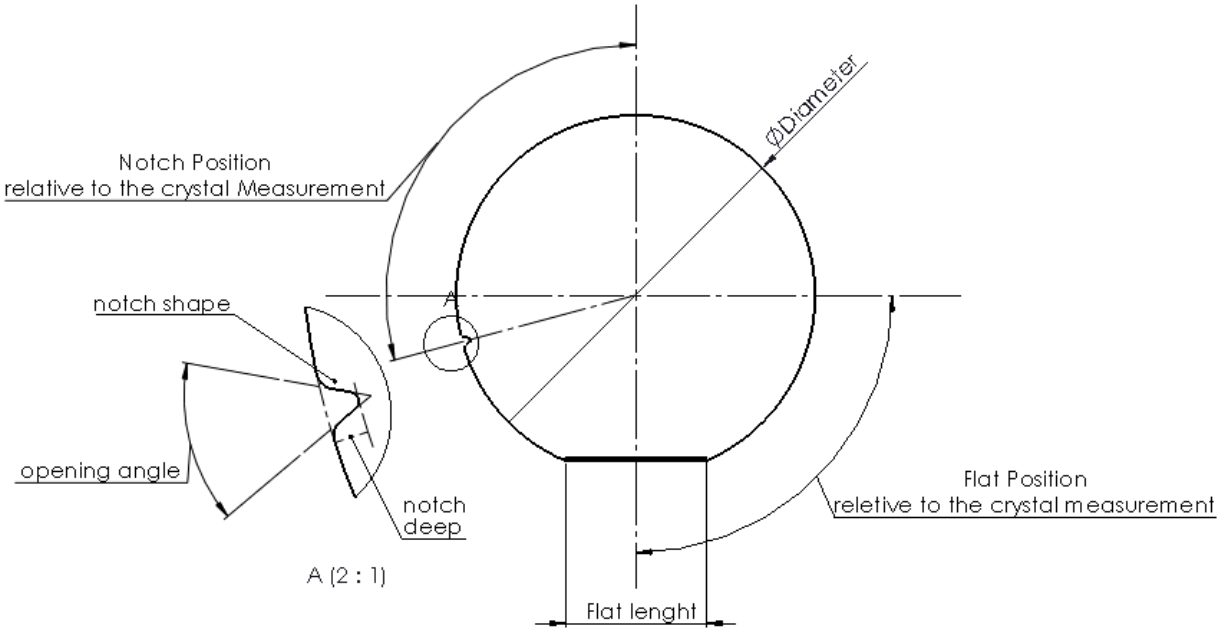


**FIGURE 2.** Wafer characteristic measurements available on systems with equipped optical sensors.

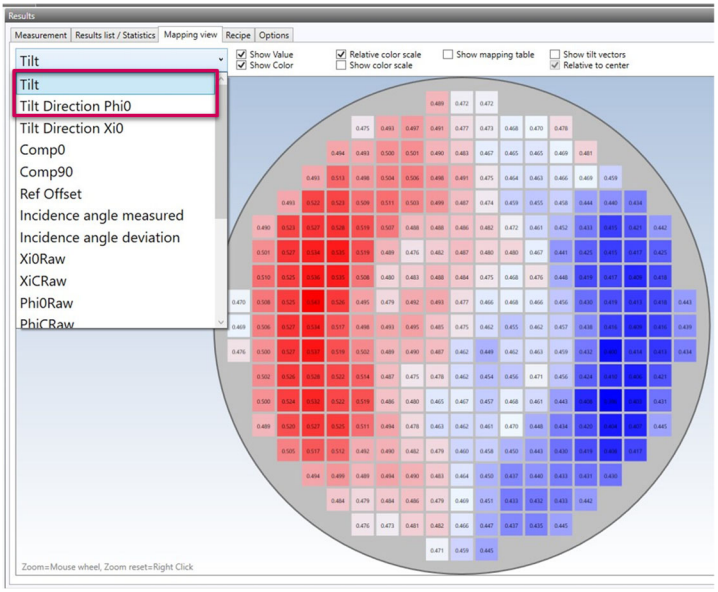


**FIGURE 3.** Surface tilt corrected measurement of lattice tilt (100 mm HVPE GaN).

## REFERENCES

1. Kosugi et al. 2017 Jpn. J. Appl. Phys. 56

## KEYWORDS

HVPE, MOSFET, orientation, single crystal, tilt, x-ray diffraction

# Instrument Development for Spectroscopic Ellipsometry and Diffractometry in the EUV

S. L. Moffitt[1], B. M. Barnes[1], T. A. Germer[1], S. Grantham[1], E. L. Shirley[1], M. Y. Sohn[1], D. F. Sunday[2], and C. Tarrio[1]

*1. Physical Measurement Laboratory, National Institute of Standards and Technology, Gaithersburg, MD, 20899, USA*
*2. Material Measurement Laboratory, National Institute of Standards and Technology, Gaithersburg, MD, 20899, USA*

## INTRODUCTION

Semiconductor devices are noted for ever-decreasing dimensions, and for becoming more and more complex. While scanning probe microscopy can still resolve the smallest features, it does not have the throughput for high-volume characterization of full wafers. Instead, optical scatterometry, operating at wavelengths in the visible and deep ultraviolet (DUV), has the throughput needed for process control. State-of-the-art visible and ultraviolet scatterometry should be acceptable through at least 2026, but five years from now, no known optical solutions exist for metrology[1].

We are currently developing a new scatterometry tool that will utilize the extreme ultraviolet (EUV). Shorter wavelength, higher energy photons will enable both the improved spatial resolution and elemental sensitivity needed to extend optics-based high-volume characterization of patterned wafers for the foreseeable future. The instrument will include two different types of measurements, spectroscopic ellipsometry and diffractometry. The first measurement will require the development of all-reflective optics to enable ellipsometry in the 50 nm to 150 nm wavelength range. All materials are strongly absorbing in this wavelength range, meaning that the technique will be surface sensitive, measuring only the top few nm of samples. The second measurement will concentrate on the 10 nm to 50 nm wavelength range. These shorter wavelengths will allow deeper penetration into samples as well as measurements above and below atomic absorption edges. The latter will enhance our ability to determine the dimensions of a specific material within multi-material samples, which reduces ambiguities in feature dimensions.

Initial development will be done at the Synchrotron Ultraviolet Radiation Facility (SURF III), an electron storage ring on the campus of the National Institute of Standards and Technology (NIST). The tool will then be attached to a laser-based high-harmonic-generation (HHG) source that is compact enough to be installed in a NIST laboratory and potentially within a fab facility.

## INSTRUMENT DESIGN CONSIDERATIONS

### Spectroscopic Ellipsometry

A conventional ellipsometer consists of a light source, polarization-state generator (PSG), sample stage, polarization-state analyzer (PSA), and detector. Both the PSG and PSA consist of a polarizer and wave plate, which are enabled through transmissive optics. Absorption at EUV wavelengths prevents the use of transmissive optics, a significant roadblock in the development of EUV ellipsometry. Recently, T. A. Germer has determined that reflective optics can be designed to enable effective PSG and PSAs in the 50 nm to 150 nm wavelength range[2]. Using multiple grazing-incidence mirrors (Fig. 1) it is possible to introduce both polarization and phase shifts to an incident beam.

A four-mirror system can be rotated about the optical axis to introduce a variable phase shift without deviating the beam.

Fig. 1D shows the results of rigorous coupled wave analysis simulations[3] for a binary silicon grating consisting of 10 nm wide, 100 nm tall lines with a 50 nm pitch on a silicon substrate (see illustration in Fig. 1C). The incident angle for the simulations was 65°, with the grating vector in the plane of incidence. The optical constants, $n$ and $k$, for silicon were taken from Palik [4]. The results shown are the normalized Mueller matrix elements $m_{01}$ = -cos 2Ψ, $m_{22}$ =sin 2Ψ cos Δ, and $m_{23}$ =sin 2Ψ sin Δ, where Ψ and Δ are the ellipsometric amplitude and phase parameters, respectively. While most traditional ellipsometry measurements are limited to approximately 5 eV in photon energy (250 nm wavelength), Fig. 1D shows significant structure out to almost 30 eV (40 nm). It is anticipated that extending ellipsometry to these much shorter wavelengths will enhance the ability for scatterometry to better measure details of the structure shape.

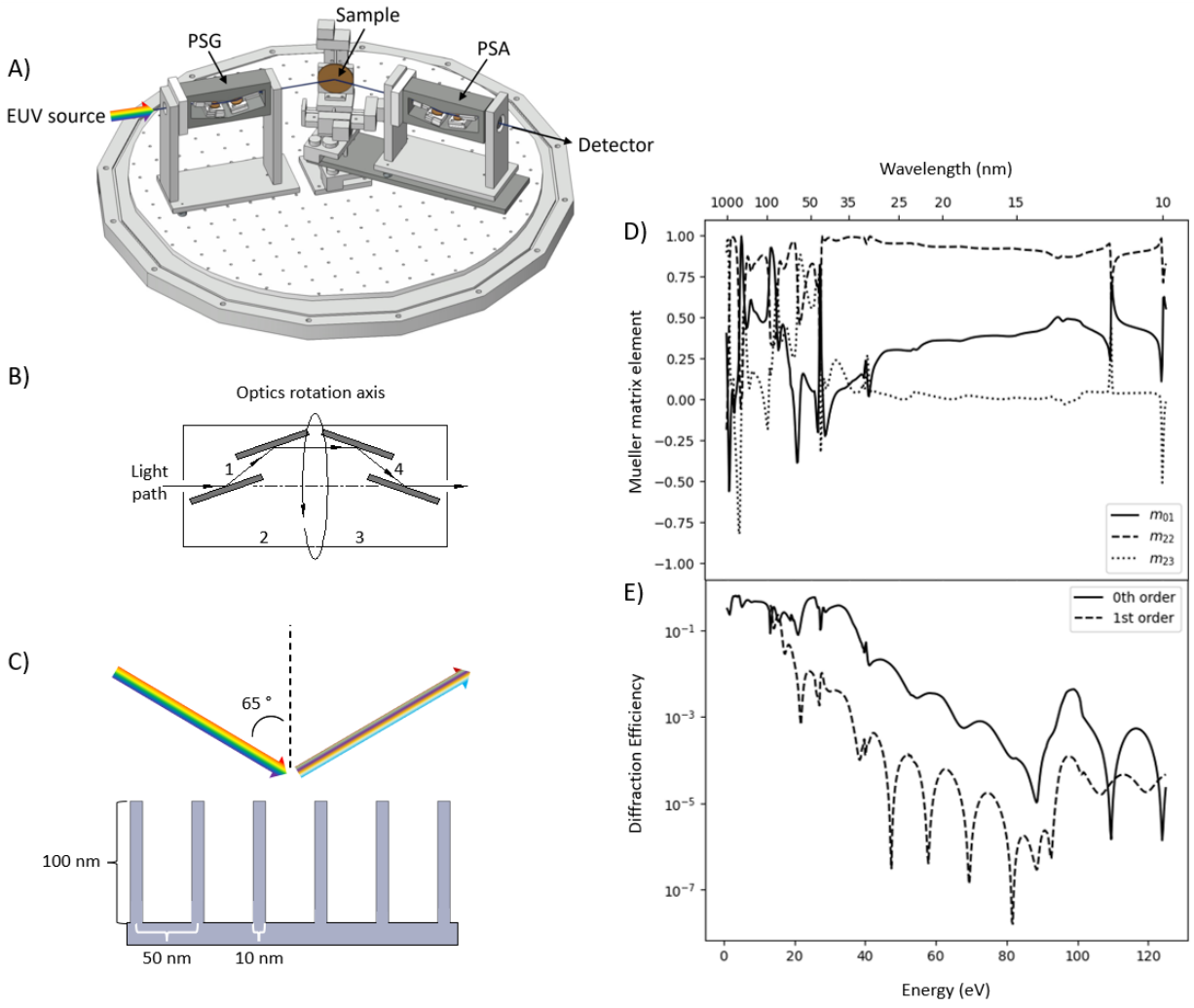


Fig. 1 A) Instrument design for spectroscopic ellipsometer. B) Schematic of the four-bounce reflective optics system which enables PSG and PSA for EUV wavelengths. C) 100 nm high, 50 nm pitch, 10 nm wide silicon lines with 90° side-wall angle, evaluated at 65° angle of incidence in a normal mounting configuration (grating vector in plan of reflection). D) Three curves corresponding to 3 unique ellipsometric parameters, $m_{01}$, $m_{22}$, and $m_{23}$, which are simulated by assuming the model shown in C. E) Diffraction efficiency simulated assuming the structure shown in C.

## Diffractometry

In conventional scatterometry, the pitch of the periodic features is much shorter than the incident wavelengths which yields reflectivity from the sample. Similarly, EUV spectroscopic ellipsometry will also utilize the reflection, or $0^{th}$ order, from these periodic structures, even though higher orders of diffraction are generated by the shorter EUV wavelengths, as shown in Fig. 1E. Reports in the literature of EUV or soft x-ray scatterometry provide insight into periodic device structures through analyses of measured changes in diffracted intensities as functions of photon energy and incident angle, without substantial control of polarization states[5,6]. In this project, the diffraction-based approach is denoted as diffractometry and will primarily be employed in the 5 nm to 50 nm wavelength range.

A major goal of the project is to determine how diffractometry can complement spectroscopic ellipsometry. These techniques are expected to be complementary as the greater transparency of materials at shorter wavelengths enables embedded features to be characterized. Comparisons shall be made between sets of device dimensions and uncertainties from separate EUV diffractometry and EUV spectroscopic ellipsometry experiments. In addition, this work will explore augmenting EUV spectroscopic ellipsometry analysis using information from diffractive order(s) to harness materials-specific changes with wavelength. Elemental sensitivity of diffractometry measurements can be achieved by harnessing the sharp changes in scattering efficiency which occur around atomic transition edge energies. There is an abundance of atomic transition edge energies in the 50 nm to 5 nm wavelength range for semiconductor materials.

## Light sources

The initial proof-of-concept will be demonstrated on beamline 3 of SURF III at NIST. SURF III is a well-established, stable light source which is ideal for the development of EUV metrology[7]. Because SURF III is a single-magnet storage ring, the irradiance can be calculated with less than 1 % uncertainty. Beamline 3 is equipped with a monochromator capable staying on-blaze in both grazing-incidence and normal-incidence configurations[8]. As such, beamline 3 can achieve efficient wavelength selection between 5 nm and 400 nm.

While SURF III will be a key step in the development of the technique, a synchrotron source is not conducive to facilitating in-line chip inspection. Thus, the second phase of the work will involve changing the light source of the measurement system to a commercial HHG laser system. HHG sources are table-top devices capable of generating spatially and temporally coherent EUV light, making these systems potentially suitable for EUV scatterometry.

## REFERENCES


(1) IEEE. *The International Roadmap for Devices and Semiconductors*; 2022 Edition: Metrology Tables File; 2022.
(2) Germer, T. A. Mueller Matrix Ellipsometer, U.S. patent application 18/218,692, filed July 6, 2023.
(3) pySCATMECH. https://pages.nist.gov/pySCATMECH/index.html.
(4) Palik, E. D. *Handbook of Optical Constants of Solids*; Academic Press: Boston, 1985; Vol. 1.
(5) Herrero, A. F.; Pflüger, M.; Puls, J.; Scholze, F.; Soltwisch, V. Uncertainties in the Reconstruction of Nanostructures in EUV Scatterometry and Grazing Incidence Small-Angle X-Ray Scattering. *Opt. Express* **2021**, *29* (22), 35580. https://doi.org/10.1364/OE.430416.
(6) Porter, C. L.; Coenen, T.; Geypen, N.; Scholz, S.; Van Rijswijk, L.; Nienhuys, H.-K.; Ploegmakers, J.; Reinink, J.; Cramer, H.; Van Laarhoven, R.; O'Dwyer, D.; Smorenburg, P.; Invernizzi, A.; et. al., M. Soft X-Ray: Novel Metrology for 3D Profilometry and Device Pitch Overlay. In *Metrology, Inspection, and Process Control XXXVII*; Robinson, J. C., Sendelbach, M. J., Eds.; SPIE: San Jose, United States, 2023; p 50. https://doi.org/10.1117/12.2658495.
(7) Arp, U.; Clark, C.; Deng, L.; Faradzhev, N.; Farrell, A.; Furst, M.; Grantham, S.; Hagley, E.; Hill, S.; Lucatorto, T.; Shaw, P.-S.; Tarrio, C.; Vest, R. SURF III: A Flexible Synchrotron Radiation Source for Radiometry and Research. *Nucl. Instrum. Methods Phys. Res. Sect. Accel. Spectrometers Detect. Assoc. Equip.* **2011**, *649* (1), 12–14. https://doi.org/10.1016/j.nima.2010.11.078.
(8) Hunter, W. R.; Williams, R. T.; Rife, J. C.; Kirkland, J. P.; Kabler, M. N. A Grating/Crystal Monochromator for the Spectral Range 5 eV to 5 keV. *Nucl. Instrum. Methods Phys. Res. Sect. Accel. Spectrometers Detect. Assoc. Equip.* **1982**, No. 1–2, 141–153.

## ACKLOWLEDGEMENT

This work was performed with funding from the CHIPS Metrology Program, part of CHIPS for America, National Institute of Standards and Technology, U.S. Department of Commerce.

## KEYWORDS

Scatterometry; Ellipsometry; Diffractometry; Extreme ultraviolet; Process control; Optical critical dimension

# Defect Localization in metallization on Advanced Packages Using Magnetic Imaging

T. Venkatesan[1,2,] Nesco Lettsome[1], Jeet Patel[1], Solomon Saul[1], Fred Cawthorne[1], Fred Wellstood[1], Steve Garrahan[1] and Henri J Lezec[3]

*[1]Neocera Magma LLC, 10000 Virginia Manor Road, Beltsville MD 20705*
*[2]CQRT, Department of Physics and Astronomy, University of Oklahoma, Norma OK 73019*
*[3]Physical Measurements Laboratory, NIST Gaithersburg, 100 Bureau Dr., Gaithersburg, MD 20899*

## INTRODUCTION

Advanced packaging is the fastest growing segment of the semiconductor industry, and the increased number of layers of metallization and ground planes makes conventional techniques for locating failures truly challenging. Most of the techniques based on photons, electrons, and heat suffer from significant loss of signal to the surface layers as the complexity of the advanced packages increase. The only two exceptions are x-ray and magnetic field-based imaging which can penetrate most of the materials used in the industry and can give information from deep layers. In our talk/ poster we will discuss the various advances we have made in the field of magnetic field imaging.

## DEPTH INFORMATION FROM MAGNETIC FIELD IMAGING

The magnetic field imaging system from Neocera Magma is a scanning system with two magnetic sensors- a superconducting quantum interference device (SQUID) and a giant magneto resistive (GMR) sensor. These devices are scanned over the sample, and they sense the Z component of the magnetic field generated by the currents in the circuit below. This is best illustrated with in Figure 1 below, where a multi-chip module (MCM) is powered between two of the pins and the resultant magnetic field is imaged by the SQUID which then gets Fourier transformed to give the actual current path. Blue represents field pointing down, red field pointing up and white represents zero field.

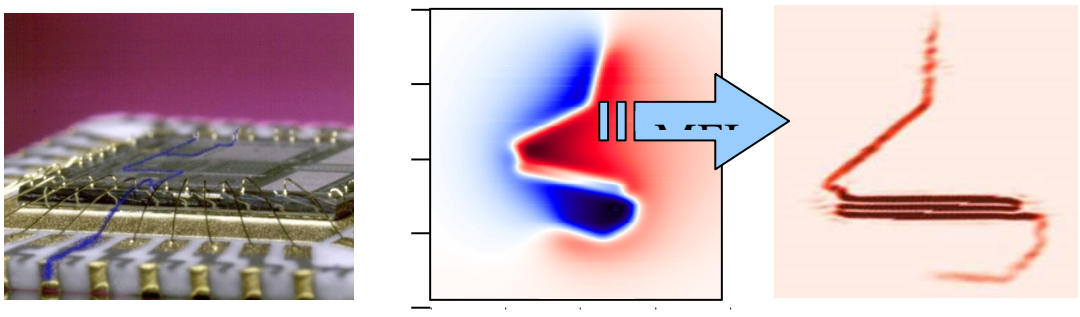

**FIGURE 1.** The powered MCM sample, resultant magnetic field image and the current profile after inversion.

If one looks at the current image one sees variations in the current intensity and spatial resolution. This is a consequence of the Z dependence of the current path which in this MCM jumps across 4 layers. The further

the layer is from the sensor lower the intensity and spatial resolution. This information can be mathematically convolved to get depth information. The characteristics of the sensors are summarized below:

| Measured Parameter | GMR Sensor (Wafer level scanning) | SQUID Sensor (Package level scanning) |
|---|---|---|
| Spatial resolution | 250-500 nm | 2 μm |
| Current sensitivity | 5 μA @2 μm | 500 nA @ 333 μm |
| Current sensitivity | 100mA@100mm | 1.5 μA @ 1000 μm |
| Maximum Depth | 100 mm | 10 mm |

For example, in an advanced package with 160 layers and a thickness of 1.5mm, one can localize a short at a depth of 600 microns with a Z resolution better than 5 microns. The SQUID because of its sensitivity can detect a fault at a depth of greater than1mm utilizing a current of 1.5 μA. The GMR sensor on the other hand requires at least 10 μA at 10 μm distance but has a spatial resolution of less than 250nm. Both these sensors can detect all faults- shorts, leakages, resistive opens, and dead opens.

## Magnetic Imaging for Front End Metrology

When one is looking at wafer level metrology there is a need to be totally noninvasive. The current required for magnetic field imaging must be generated in the metallization without any physical contacts. We will discuss various strategies to create currents in floating metal lines (non-grounded) without physical contact. As of today, we have imaged micron sized cracks in metal lines using this technique and we will report our further progress at this workshop.

## REFERENCES

1. Antonio Orozco, Elena Talanova, Alex Jeffers, Florencia Rusli, Bernice Zee, Wen Qiu, Syahirah MD, Zulkifli Allen Gu, Juan Atkinson Mora, Non-Destructive 3D Failure Analysis Workflow for Electrical Failure Analysis in Complex 2.5D-Based Devices Combining 3D Magnetic Field Imaging and 3D X-Ray Microscopy, Proceedings of ISTFA (2018)
2. Antonio Orozco, Florencia Rusli, Christopher Rowlett, Bernice Zee, Wen Qiu, and Fang-Jie Foo, 3D Fault Isolation in 2.5D Device comprising High Bandwidth Memory (HBM) Stacks and Processor Unit Using 3D Magnetic Field Imaging, Proceedings of ISTFA (2016)
3. Antonio Orozco, Elena Talanova, Alfred B. Cawthorne, Lee Knauss, Thirumalai Venkatesan, Fault Isolation of Circuit Defects Using Comparative Magnetic Field Imaging, US **Patent number:** 7019521

## KEYWORDS

Magnetic field imaging, Failure analysis, Advanced packaging, Wafer level metallization, faults in metallization, front end metrology

# DUV-Vis-NIR OCD Metrology for BCD Semiconductor Manufacturing Yield Enhancements

Jeffrey W. Roberts[*§], John C. Lam[*], Nikolaos Pallikarakis[*], Kostas Florios[*], Marco Colli[†‡], Matteo Lombardo[†] and Marcello Ravasio[†]

** n&k Technology, San Jose, CA, USA, † STMicroelectronics, Agrate Brianza MB, Italy*

§ *jroberts@nandk.com*, ‡ *marco.colli@st.com*

## DEEP TRENCH ISOLATION (DTI) FOR BCD DEVICES

Bipolar-CMOS-DMOS (BCD) devices require advanced metrology for their Deep Trench Isolation (DTI) structures, which provide electrical separation between circuit blocks. The primary need is to monitor post-etch trench depth and bottom width. While cross-section imaging is viable, it is time consuming and destructive. Alternatively, scatterometry systems that perform Optical Critical Dimension (OCD) measurements are fast and non-destructive.

Measurements of etch depth and trench widths are standard outputs for OCD systems, but the large DTI dimensions lead to sensitivity problems. However, new algorithms can enable measurements, when accompanied with optical data sensitive to the critical parameters. Fitting this description, the n&k OptiPrime-CD couples advanced modeling with a wide spectral range (190-1000nm), covering the Deep-Ultraviolet (DUV) to Near-Infrared (NIR). Figure 1 shows a cross-section SEM image and the corresponding OCD model schematic of a typical DTI structure.

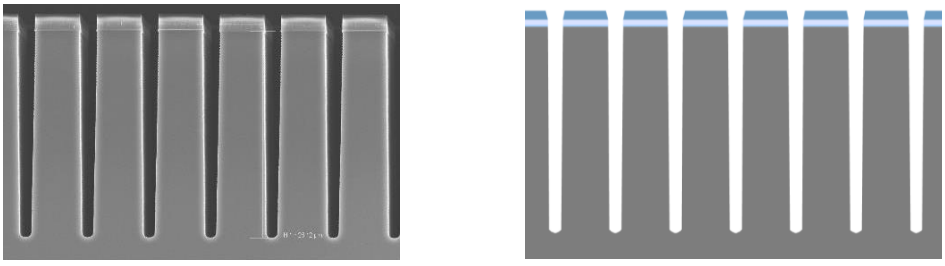

**FIGURE 1.** Deep Trench Isolation (DTI) cross-section SEM image (left) and cross-section schematic of OCD model (right). Structure has 8µm pitch, 26µm depth, 2µm top width, 1.5-1.8µm bottom width and film stack: Oxide/Poly-Si/Nitride/Oxide/Si.

## MEASUREMENTS USING THE N&K OPTIPRIME-CD

The n&k OptiPrime-CD, with polarized reflectance optics, collects two unique spectra, Rs and Rp. Measurement results are based on fitting the data to an analytical model, using Rigorous Coupled Wave Analysis (RCWA) [1-3] or a Scalar formulation. The system incorporates Forouhi-Bloomer dispersion equations [4-7] to model film properties utilized in the OCD models.

With the RCWA method [1,2], Maxwell's equations in the grating region can be transformed into finding the eigenvalues of the matrix: $A = B_x - E$, where $B_x = K_x^2$ for s-polarization, $B_x = EK_xE^{-1}K_x$ for p-polarization and $E$ is the matrix formed by the permittivity harmonic components ($\varepsilon_i$), with the $i, j$ elements equal to $\varepsilon_{i-j}$. $K_x$ is a diagonal matrix with the elements equal to $k_{xi}/k_0$. $k_{xi}$ is the wave vector of i-th diffraction order in the x direction, and $k_0$ is the wave number in free space. With this, using the boundary conditions at the surface and bottom of the grating, we can calculate the corresponding reflectance and transmittance. In addition to the classic RCWA, we implemented a formulation improvement that skips solving the eigenvalue problem without sacrificing rigor, based on the Cayley–Hamilton theorem [8]. Thus, we reduce computation time without sacrificing accuracy.

In the DTI structure with 8µm pitch, the measured reflectance is not fully coherent, resulting in inaccurate RCWA-calculated reflectance. To supplement RCWA, we utilize an approximate method suitable for modeling 1D structures, known as Scalar. In the Scalar model, the pattern is divided into features, with the reflectance of each feature calculated independently in a plane-wave approximation. The combined reflectance accounts for interference between features while ignoring diffraction. This approach [9, 10] allows for both coherent and incoherent formulations. In addition, one can integrate the Scalar waveguide model with RCWA and introduce a coherence parameter to blend the two models for better data fitting. These Scalar methods contrast with the multilayer thin film method known as MBIR [11]. Figure 2 illustrates calculated spectra from both models for a typical DTI measurement point. A mixed RCWA and Scalar model is required to achieve accurate data fitting for an 8µm pitch structure.

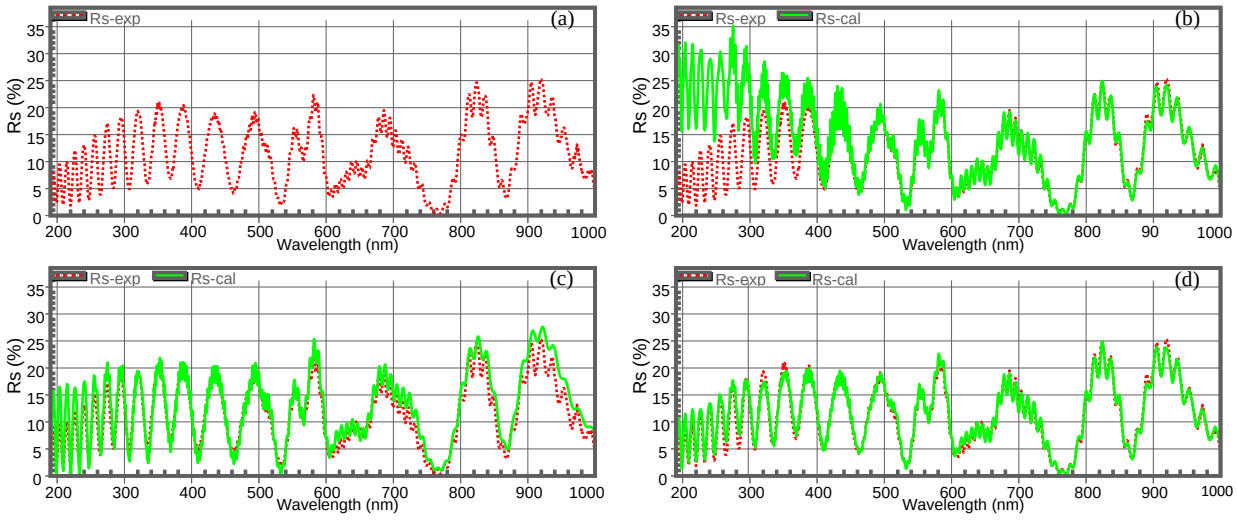


**FIGURE 2.** a-Upper Left) Experimental Rs spectra, b-Upper-Right) Calculated and experimental spectra from RCWA only, c-Lower Left) Scalar only, and d-Lower-Right) A mixed RCWA and Scalar model.

## DTI MEASUREMENT RESULTS

Typical data from the DTI structure, seen in Figure 2, showcases sensitivity to the critical components of the structure. Smaller features, the high frequency oscillations in the wavelength region from 500-1000nm, correspond to the depth and bottom width. Results are obtained with a mixed model of RCWA and Scalar, as required to best fit the experimental data. Measurements include trench depth, bottom width, top width and film thickness.

The measurement has been tested with a large set of wafers, which were processed under different conditions to produce variations in bottom width. According to cross-section SEM results, the range in bottom width is about +/-15% (1.4µm-1.9µm) for the sample set. Results are evaluated for quality in several ways: 1) Correlation with the nominal conditions and cross-section SEM, 2) Realistic mapping uniformity, and 3) Reproducibility tests.

With a single model applied to all samples, there is a clear match with the intended conditions and the measurement results. Figure 3 shows a good correlation with cross-section SEM. Mapping results, as exemplified in Figure 4, show typical center to edge wafer uniformity for the bottom width and trench depth, without any significant outliers. Finally, reproducibility tests demonstrate the measurement precision. This test is done by measuring the same site 10 times with sample load/unload between measurements. Trench depth has a 1σ standard deviation of 0.0002µm (0.001%), and bottom width has a 1σ standard deviation of 0.0012µm (0.073%). The reproducibility results are well within the process control limits. Under all conditions, the measurement results meet the process control requirements for accuracy and stability.

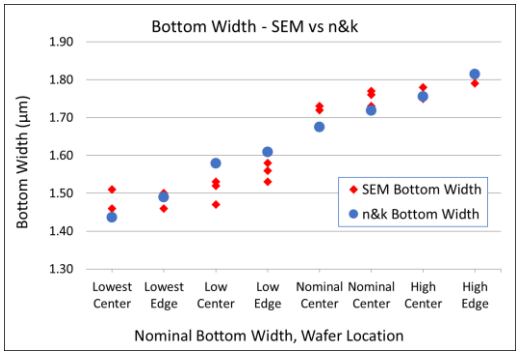


**FIGURE 3.** Correlation between cross-section SEM and n&k OptiPrime-CD for bottom width, using four samples with process variations, measured at the wafer center and edge.

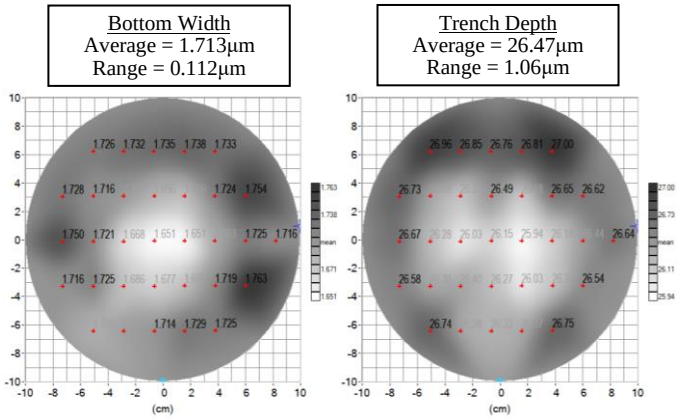


**FIGURE 4.** Mapping Uniformity Results for a wafer with nominal process conditions. bottom width (left) and trench depth (right) show typical process variations.

## ACKNOWLEDGMENT

The authors would like to thank Dr. Rahim Forouhi for his contributions and guidance.

## REFERENCES

1. M. Moharam, D. Pommet, E. Grann, and T. Gaylord, "Stable implementation of the rigorous coupled-wave analysis for surface-relief gratings: enhanced transmittance matrix approach," J. Opt. Soc. Am. A , vol. 12, pp. 1077-1086, 1995.
2. M. Moharam, E. Grann, D. Pommet, and T. Gaylord, "Formulation for stable and efficient implementation of the rigorous coupled-wave analysis of binary gratings," J. Opt. Soc. Am. A, vol. 12, pp. 1068-1076, 1995.
3. A. Gray et al., "Innovative Application of the RCWA Method for the Ultra-Sensitive Transmittance-Based CD Measurements on Phase-Shift Masks," 23rd European Mask and Lithography Conference, Grenoble, France, 2007, pp. 1-9.
4. A. R. Forouhi and I. Bloomer, "Optical dispersion equations for metals applicable to the Far-IR through EUV spectral range," J. Phys. Commun., Vol. 5, 2021, 025002.
5. A. R. Forouhi and I. Bloomer, "Optical Dispersion Relations for Amorphous Semiconductors and Amorphous Dielectrics," Phys Rev B Condens Matter., vol 34, Nov. 1986, pp. 7018-7026.
6. A. R. Forouhi and I. Bloomer, "Optical properties of crystalline semiconductors and dielectrics," Phys Rev B Condens Matter, vol 38, Jul 1988, pp. 1865-1874.
7. A. R. Forouhi and I. Bloomer, "New dispersion equations for insulators and semiconductors valid throughout radio-waves to extreme ultraviolet spectral range", J. Phys. Commun., vol. 3, no. 3, 2019.
8. J. Li et al., "Efficient Implementation of Rigorous Coupled-Wave Analysis for Analyzing Binary Gratings," in IEEE Antennas and Wireless Propagation Letters, vol. 19, no. 12, pp. 2132-2135, Dec. 2020.
9. G. Li, P. Walsh and A. R. Forouhi, "Method and Apparatus for Examining Features on Semi-Transparent Substrates," U.S. Patent 6,891,628 B2, May 10, 2005.
10. G. Li , S. Chen and P. Walsh., "Optical determination of pattern feature parameters using a scalar model having effective optical properties", U.S. Patent 7,212,293 B1, May 1, 2007.
11. C. Zhang, S. Liu, T. Shi, and Z. Tang, "Improved model-based infrared reflectrometry for measuring deep trench structures," J. Opt. Soc. Am. A, vol. 26, 2009, pp. 2327-2335.

## KEYWORDS

Bipolar-CMOS-DMOS (BCD), OCD metrology, critical dimensions, scatterometry, DTI, process control, RCWA, Scalar

# Nanoscale 3D X-Ray Imaging of Integrated Circuits using a Hybrid Electron/X-Ray Microscope

Nathan Nakamura[1,2], Joseph W. Fowler[1,2], Zachary H. Levine[3], Paul Szypryt[1,2], and Daniel S. Swetz[1]

[1] *National Institute of Standards and Technology, Boulder, Colorado 80305, USA*
[2] *Department of Physics, University of Colorado, Boulder, Colorado 80309, USA*
[3] *National Institute of Standards and Technology, Gaithersburg, Maryland 20899, USA*

## INTRODUCTION

Modern nanoelectronics contain many close-packed, nanoscale, subsurface features of multiple material compositions spanning planar chip areas. Integrated circuit (IC) features sizes are continuously being pushed to smaller scales and being packaged in increasingly complex 3D architectures. This structural complexity has greatly improved the capabilities of modern ICs and will continue to improve capabilities in the future. However, this complexity has also made high fidelity characterization of IC interiors difficult, presenting a challenge for essential diagnostics such as failure analysis, defect detection, and verification of supply chain security. 3D x-ray imaging is a powerful tool for characterization of buried features, as methods like x-ray computed tomography (CT) can provide information regarding the size and shape of subsurface features.[1] However, current instrument capabilities lag behind semiconductor fabrication capabilities, and do not achieve the spatial resolution, scanning speed, or elemental sensitivity to fully characterize modern nanoelectronics. At sub-200 nm spatial resolutions, synchrotron imaging techniques are the state-of-the-art,[2] but such methods are not readily accessible. It is advantageous to have nanoscale 3D imaging capabilities in a compact, laboratory-scale instrument. Current laboratory-scale instruments with sub-200 nm resolution rely on the use of x-ray focusing optics, which become increasingly inefficient at higher x-ray energies. This results in an upper bound on the x-ray energy which can be used while still achieving practical measurement times, limiting samples in laboratory systems to thin or low-Z materials. To support the metrology needs of modern nanoelectronics, laboratory-scale instruments capable of imaging on thick or higher Z materials are needed.

We have developed a 3D x-ray imaging instrument based on ultra-high geometric magnification, which can achieve nanoscale spatial resolution without the use of x-ray optics. The instrument combines the electron beam of a scanning electron microscope (SEM) with a metal thin film target layer deposited directly onto the sample of interest (Fig. 1). The electron beam generates a nanoscale x-ray spot in this target layer, with the energy and flux of the resultant x-rays dependent on the electron beam accelerating voltage and beam current. Coupling the sample and target layers allows the x-ray source to be held within micrometers of the sample, creating high geometric magnification while keeping the x-ray detector relatively close to the source. This improves the solid angle coverage and x-ray flux at the detector plane. A proof-of-concept of this approach to x-ray CT has successfully imaged Cu features in an IC fabricated at the 130 nm technology node, demonstrating nanoscale imaging capabilities.

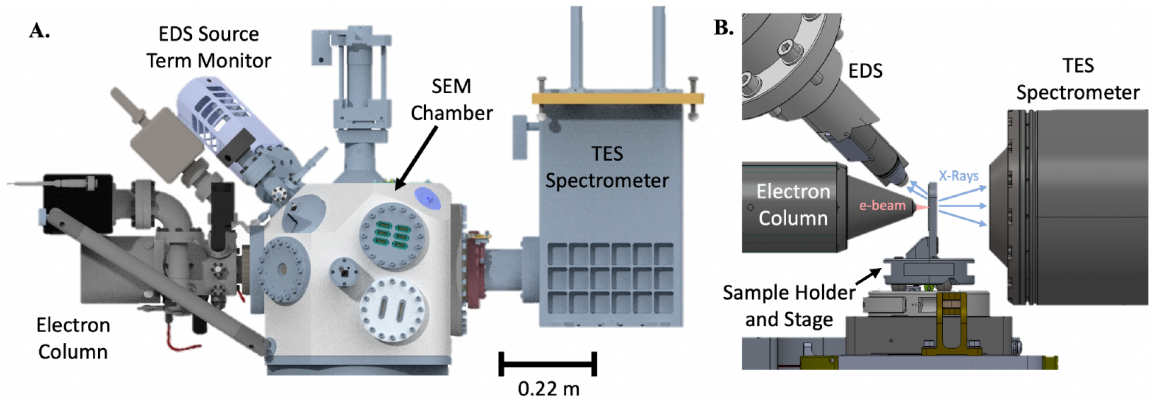


**FIGURE 1.** (A) Instrument overview, consisting of an electron column, energy dispersive spectroscopy (EDS) detector, SEM chamber, and transition-edge sensor (TES) spectrometer. A TES is a type of energy-resolving x-ray detector and was used for the proof-of-concept demonstration, but the instrument is compatible with other x-ray detectors. (B) View inside the SEM chamber, showing the electron beam incident on a sample in the sample holder and generated x-rays going to the TES and EDS detectors.

## NANOSCALE 3D IMAGING OF INTEGRATED CIRCUITS

The design file for the demonstration IC is shown for comparison with the resulting reconstructed image but was not used to guide the reconstruction (Fig. 2A). A 240-pixel transition-edge sensor (TES) spectrometer was used, and provides high energy resolution and suitable collection efficiency.[3] In Figure 2B, a reconstruction of multiple IC wiring and via layers is shown, with the energy-resolving capabilities of the TES spectrometer used to select only for photons in the 9.1 keV to 10.1 keV band. This band is dominated by the Pt Lα fluorescence line, and thus originates mostly in the Pt target used for this data collection. All expected features are clearly resolved, demonstrating the nanoscale spatial resolution of the instrument. In Figure 2C, a reconstruction including both the 9.1 keV to 10.1 keV and 5.4 keV to 6.4 keV energy bands is shown. The lower energy band enhances contrast for non-Cu features. The resulting reconstruction shows higher contrast for the first via layer relative to other wiring and via layers, indicating the presence of non-Cu vias in the IC. These results demonstrated the promise of combining a focused electron beam, high system magnification, and energy-resolved x-ray detection for nanoscale x-ray tomography. Additional explanation of the prototype instrument and tomographic results can be found in Ref. 4 and Ref. 5.

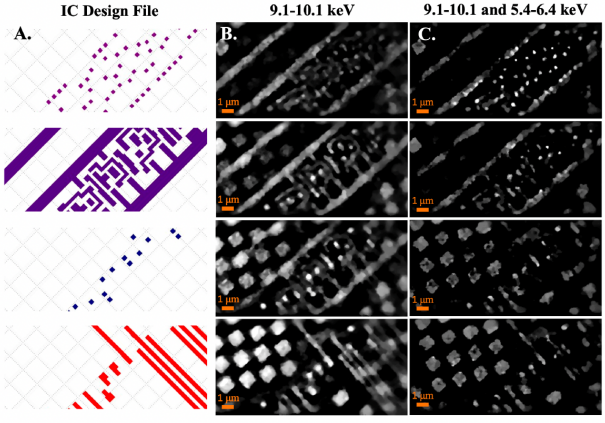


**FIGURE 2.** (A) The design file for the demonstration IC, showing 4 of the wiring and via layers imaged. (B) Reconstruction using only the 9.1-10.1 keV energy band, which contains the Pt Lα fluorescence line originating in the target material. (C) Reconstruction using the 9.1-10.1 keV and 5.4-6.4 keV energy bands. Inclusion of the lower energy band enhances contrast for non-Cu features. The large diamond shaped features in the reconstructed images are chemical-mechanical polishing (CMP) fill, which is an IC feature added for thermal and mechanical stability but is not included in the design file.

## FUTURE OUTLOOK

The approach to x-ray nanotomography presented here has a promising future, with a path towards improved imaging speed, spatial resolution, and spectral imaging capabilities. The first generation of the tool achieves spatial resolution comparable to state-of-the-art commercial x-ray imaging instruments operating at similar x-ray energies, with additional capabilities for spectral imaging. Upgrades to the system electron beam, target design, and detector technology will result in vastly improved capabilities, improving imaging speed by orders of magnitude and pushing the spatial resolution to the order of tens of nanometers. In the future, the electron column will be improved to increase the achievable current in an approximately 100 nm spot size from less than 10 nA to hundreds of nanoamperes. Additionally, a combination of higher pixel count TES spectrometers and commercial megapixel detectors based on hybrid photon counting technology will dramatically increase the collection efficiency and thus the imaging speed.[6,7] The electron beam parameters and x-ray detection used can be easily adjusted, thus allowing the instrument to be optimized for imaging speed, spatial resolution, or spectral capabilities to fit a given imaging goal. A description of this optimization and expected future capabilities is discussed in Ref. 8.

## CONCLUSION

We have developed an instrument for nanoscale, 3D x-ray imaging of ICs capable of achieving sub-200 nm spatial resolution in a proof-of-concept measurement. Features in a Cu-$SiO_2$ IC fabricated at the 130 nm technology node were imaged and compared to the design file to demonstrate imaging capabilities. The path forward to improved performance does not depend on the performance of x-ray optics, but rather on realistic improvements to the electron source and x-ray detection used. The end goal of the fully developed tool is an x-ray nanotomography instrument that will advance nanoelectronics characterization, capable of providing information on nanoscale features size, shape, and composition across large planar chip areas.

## REFERENCES


1. P. J. Withers et al., *Nature Reviews Methods Primers* **1**, 18 (2021).
2. M. Holler et al., *Nature* **2**, 464-470 (2019).
3. J. N. Ullom and D. A. Bennet, *Superconductor Science and Technology* **28**, 084003 (2015).
4. N. Nakamura et al., *arXiv*, https://arxiv.org/abs/2212.10591 (2023).
5. Z. H. Levine et al., *Microsystems & Nanoengineering* **9**, 47 (2023).
6. P. Szypryt et al., *IEEE Transactions on Applied Superconductivity* **33**, 1-5 (2023).
7. A. Forster et al., *Philosophical Transactions of the Royal Society A* **377**, 20180241 (2019).
8. N. Nakamura et al., *2023 IEEE Physical Assurance and Inspection of Electronics (PAINE)*, 1-7 (2023).


## KEYWORDS

Nanoscale, X-Ray Tomography, Nanotomography, Integrated Circuits, 3D Imaging

# Pushing the Speed and Resolution Limits of 3D X-ray for In-Line Metrology in Wafer Level Integration and Offline Defect Characterization

S.H. Lau, Sheraz Gul, Jeff Gelb, Tianzhu Qin, Sylvia Lewis, Wenbing Yun

*Sigray Inc, 1590 Solano Way, Suite A, Concord, CA 94520*
*shlau@sigray.com*

## INTRODUCTION

High-speed and large-capacity communication, such as 5G, Internet of Things (IoT) and AI, require High Performance Computing (HPC) utilizing high-performance processors and high-bandwidth memory. Therefore, semiconductor devices and packages are increasingly migrating towards 3D stacking with new approaches in connectivity and bonding. Pitch scaling of vertical interconnection is a crucial development aspect for advanced chiplet integration and wafer level integration. Micro-bump has fulfilled the demand for vertical interconnection in 3D integration; however, it is facing the limitation of scaling below 10 µm pitch due to reliability concerns and the alignment limitation with thermal compression bonding. Cu-Cu hybrid bonding can alternate the vertical interconnection, where the technology is now getting matured for Wafer-to-Wafer (W2W) integration. This introduces significant challenges for inline defect inspection and offline failure analysis techniques.

Primarily, 3D stacking and wafer bonding result in optically opaque systems that require approaches such as X-rays to see through multiple layers of buried structures for defect detection. However, with the continual shrinkage in device features in 3DHI (3D Heterogeneous Integration) as e.g., microbumps are scheduled to shrink to <10 µm diameter and TSVs interconnects are scaling to single digit micrometers, non-destructive techniques are facing a technological brick wall. This includes 3D X-ray approaches, which need to have higher resolution than currently available in order to meet the evolving requirements. Furthermore, the acquisition time for sub-one micron imaging using conventional X-ray tomography even at a single location within a large 300 mm wafer may take hours or is outright impossible.

To address these metrology gaps, we have developed two complementary groundbreaking 3D X-ray inspection tools for:

1. In line Metrology for Wafer Level Integration, providing rapid inspection of 300 mm wafers during wafer level packaging and bonding, and which can resolve various 3D defects to 0.5 µm resolution automatically and in as little as 2-3 minutes per inspection site. This tool will also address chiplet inspection and board level FA, such as PCB at high resolution.

2. Offline High Resolution 3D X-ray Microscopes (XRM) in Failure Analysis of 3DHI Packages. The system delivers true 300 nm spatial resolution (<50 nm voxel) for characterizing sub-micron defects in microbumps, delamination, voids, interfacial cracks and RDL that cannot be seen and measured by existing XRMs.

## IN LINE METROLOGY WITH 3D X-RAY

While 3D X-ray Tools or X-ray Microscopes (XRMs) have been the traditional non-destructive imaging tools in Failure Analysis labs, they typically can only achieve 1 µm or coarser resolution with smaller packages. [1] While sub-micron resolution has been demonstrated, these are only possible with very small and thin packages or samples which have been sectioned into < 1 mm diameter in size. But as sample size increases to several cm, such as a 300

mm wafer, high resolution imaging is normally not attempted. This is because acquisition times are far too long (typically hours), images are noisy and are filled with beam hardening artifacts (with bands and streaks), or analysis requirements are simply beyond the capabilities of the instrument. It is also for many such reasons that 3D X-ray tools with sub-micron resolution are unfavored for deployment as in-line metrology for wafer level packaging of ICs.

We have developed a novel approach in 3D X-ray for large planar samples, such as a 300 mm wafers, where Wafer Level Integration Defects can be detected at a spatial resolution down to 0.5 µm and free from the typical beam hardening artifacts. Using machine learning analysis methods, it is also demonstrated to characterize non-wets in micro-bumps (Fig 1), Cu-Cu hybrid bonds at very fine pitch, TSV defects (Fig 2), and misalignment, all within a few minutes per site anywhere in a 300 mm wafer. Results correlating wet vs non wets and good vs bad Cu-Cu hybrid joints were validated using SEM physical cross section.

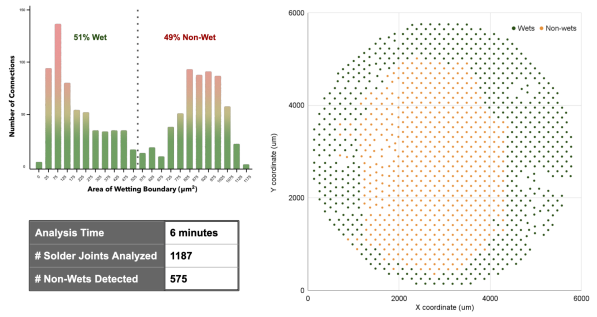


**FIGURE** 1. Machine learning routine identifies non-wets in ~1200 microbumps, collected in a single inspection scan.

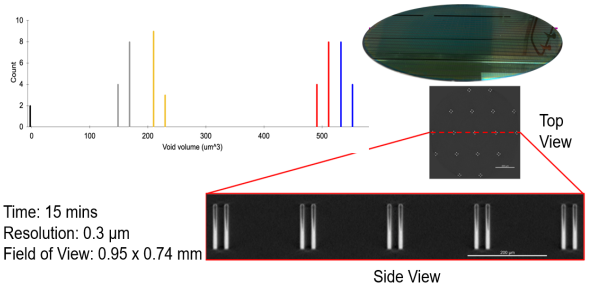


**FIGURE 2**. High-resolution cross-sectional characterization of voids in through-silicon vias (TSVs).

## 300 nm Spatial Resolution Offline 3D X-ray Tool for Failure Analysis

In PFA for advanced packages, current gaps in non-destructive 3D imaging are primarily due to insufficient resolution for resolving sub-micron defects and the lack of contrast to uncover defects within low Z materials. These low Z defects in advanced packages include sidewall delamination between Si die, underfill, and cracks or voids in the underfill, redistribution layers, inorganic substrate, or silicon. Because feature sizes are shrinking at a rapid pace with 3DHI, many of these defects cannot be detected even with the state-of-the-art XRMs (X-ray microscopes) and are quickly rendering many of these commercial instruments to be obsolete.

To keep pace with advances in packaging, we have developed a breakthrough tool with 300 nm spatial resolution (Fig 3) to identify the defects in FA that are increasingly challenging to characterize. These include:

- Submicron defects
- Delamination
- Cracks at organic interface, silicon defects or cracks (Fig 4)

The non-destructive 3D X-ray technologies presented here represent the next-generation of X-ray inspection, where flexibility and scalability are of paramount importance. These high-resolution imaging systems produce significantly higher clarity results, which deliver reliable image quality with each inspection. When paired with modern machine-learning and automated data analysis approaches, these 3D X-ray instruments provide the highest level of detection sensitivity with robust, operator-independent reliability for next-generation process lines and FA labs alike.

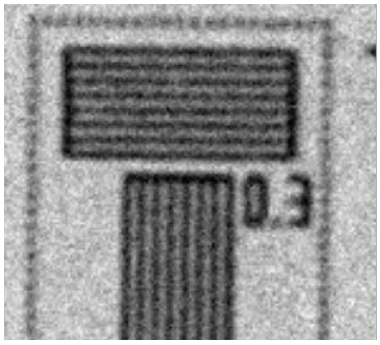


**FIGURE 3.** Resolution proof: 300 nm

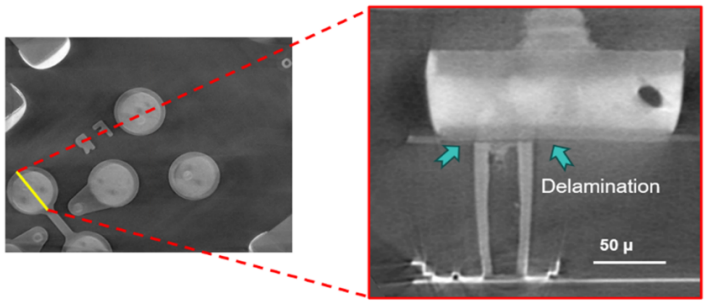


**FIGURE 4.** Delamination at interface above the TSV at 0.25 um voxel

## References

1. C.Y. Liu, et al. “High resolution 3D X-ray microscopy for streamlined failure analysis workflow”, IEEE IPFA Conference Proceedings, 2016

2. S.H. Lau et.al.,” Decoupling Sub-micron Resolution and Speed from Sample Size in 3D X-ray Imaging” IPFA 2022.

3. S.H. Lau et al.,” Characterizing Sub-micron 3D Defects from Intact Advanced Packages to Wafer Level Packaging using a Suite of Novel 3D X-ray Tools at Down to 0.3 µm Spatial Resolution” EPTC 2023

## Keywords

3D X-ray Metrology, Wafer Level Integration, Failure Analysis, Hybrid Bonds

# Dopant and Thin Film Metrology using Laboratory-Based Micro-XRF in the Low Z and Low Energy Range

Benjamin Stripe, Frances Y. Su, Michael Lun, Tinchi Leung, Ian Spink, Sylvia Lewis, Wenbing Yun

*Sigray, Inc.*
*1590 Solano Way, Suite A*
*Concord, CA, United States*

## INTRODUCTION

In front-end wafer production, the measurement of ultrathin films and elementals dosages is critical to processes for transistor manufacturing. In particular, the measurement of high dielectric constant materials, such as $HfO_2$ and $Al_2O_3$, are important to prevent dielectric breakdown in transistors. Quantification of other channel materials such as GaAs and Ge are also important for the development of ever-smaller transistors. Metrology methods that are non-destructive, precise, and have high spatial resolution will be integral to pushing the forefront of semiconductor technology. Laboratory-based x-ray fluorescence is uniquely suited to this application. Sigray has developed the AttoMap-310 micro-XRF system as a laboratory-based system that has small spot size (<10 μm) and a patented high-brightness source that has high brightness and tunable excitation energy. The tunability of x-ray energies allows the AttoMap-310 to detect elements in the range of Al down to B, as well as elements from Si to U. The new vacuum chamber design is uniquely suited to the nondestructive measurement of elements with low-energy lines including low Z elements, and useful for materials and thin-film metrology on test pads in advanced IC manufacturing.

### Patented System Design Enables Increased Sensitivity

The Sigray AttoMap-310 is an x-ray fluorescence tool, in which x-rays are focused onto a sample, which can be rastered relative to the x-ray beam. In x-ray fluorescence, x-rays from the x-ray source interact with the sample matter, knocking out inner shell electrons in the sample elements. The atom relaxes and a higher shell electron ejects a photon of a characteristic energy to take the place of the ejected electron. The characteristic photons that are emitted from the sample are captured by a detector that can determine the energy of the incoming photon. Element identification and quantification (equivalent film thickness or atomic dose) can then be done by determining the element based on the characteristic peak energy and measuring the peak amplitude. Compared to particle bombardment techniques, x-ray excitation has substantially higher signal-to-noise ratio due to lower Bremsstrahlung background. When compared to SEM-EDS, micro-XRF can have orders of magnitude higher detection sensitivity.

Three primary innovations define the AttoMap-310: 1) a high-brightness multi-target x-ray source, including a patented SiC anode that is optimized for low-Z element excitation; 2) monocapillary optics that maximize fluorescence cross-sections and enable small spots (5-25 μm), and 3) a vacuum chamber that achieves vacuum pressures down to E-5 Torr. Fluorescence efficiency, or fluorescence cross-sections, can be maximized with the excitation energy for an element that is just above the absorption edge of the element of interest. Table 1 shows the fluorescence cross-section (Barns/atom) depending on the excitation energy of the anode material commonly used in the AttoMap-310. For example, Al, which has an absorption edge of 1.6 keV, cross-section using the Si (1.7 keV) target is an order of magnitude higher than if one were to use a Cu (8.0 keV) target and another order of magnitude higher than if one were to use the Mo (17.4 keV) target. Tuning the anode energy can therefore increase the sensitivity

to an element by orders of magnitude. An added benefit of our patented Si anode is that it will minimize fluorescence of Si substrates, which can interfere with detection of elements such as Al, Mg, or Zr.

**TABLE 1.** Fluorescence cross-section of elements depending on excitation anode and corresponding energy. Units are given in Barns/atom.

| Element | Si Target (1.7 keV) | Mo Target (2.7 keV) | Cu Target (8.0 keV) | Mo Target (17.4 keV) |
|---|---|---|---|---|
| C | 15 [K-line] | 6.5 [K-line] | 0.2 [K-line] | - |
| N | 45 [K-line] | 21 [K-line] | 0.7 [K-line] | - |
| O | 119 [K-line] | 55 [K-line] | 1.9 [K-line] | 0.1 [K-line] |
| F | 275 [K-line] | 128 [K-line] | 4.8 [K-line] | 0.4 [K-line] |
| Mg | 1193 [K-line] | 983 [K-line] | 44 [K-line] | 4.1 [K-line] |
| Al | 3367 [K-line] | 1676 [K-line] | 79 [K-line] | 7.6 [K-line] |
| Ti | 60 [L-line] | 28.5 [L-line] | 2853 [K-line] | 329 [K-line] |
| Co | 886 [L-line] | 428 [L-line] | 9493 [K-line] | 1206 [K-line] |
| Ni | 1236 [L-line] | 600 [L-line] | 19 [L-line] | 1492 [K-line] |
| Ga | 2564 [L-line] | 1266 [L-line] | 41 [L-line] | 2604 [K-line] |
| Ge | 3318 [L-line] | 1648 [L-line] | 54 [L-line] | 3061 [K-line] |
| Zr | - | 6306 [L-line] | 278 [L-line] | 30.9 [L-line] |
| La | - | - | 2963 [L-line] | 333 [L-line] |
| Hf | 11347 [M-line] | 7876 [M-line] | 375 [M-line] | 1874 [L-line] |

Sigray's monocapillary x-ray optics enable spots down to 5 μm. The large working distance ~40 um for standard optics allows the silicon drift detector (SDD), which detects the fluorescence x-rays, to be placed close to the sample surface, increasing the acceptance angle and therefore number of x-rays that can be detected. Since acceptance angle varies inversely with the square of the distance from the sample, optimizing the distance of the SDD can improve sensitivity up to an order of magnitude. The large working distance of the optic also allows samples to be placed at an angle with respect to the x-ray beam. The AttoMap-310's unique design includes a rotation stage for the sample as well as the SDD, which users can use to optimize sample and detector geometries for best sensitivity. Rotation of the sample or detector can also help to avoid and identify diffraction peaks common in single crystal silicon. Finally, the vacuum chamber design prevents attenuation of low-energy x-rays in air, increasing sensitivity to low-energy x-rays and removing lines from air such as Ar, which can interfere with detection of Ag.

## Low Z Element Metrology Results

The AttoMap-310 has been used to analyze composition, equivalent film thickness of flat thin films. Figure 1 shows results from a laddered series of samples with Ge doping prepared by a third party. Sigray's patented SiC anode was used to excite the sample and the x-ray spot size was ~25 μm. Sample measurements were performed under vacuum conditions in the range of E-3 Torr. Two measurements were made for each sample type to confirm that the results were consistent. Figure 1a shows the difference in peak height of the Ge L-alpha peak (1.2 keV) across the set of laddered samples. An increase in the peak height can be seen across Samples 1 through 4 as well as when compared to an undoped Si sample. Figure 1b demonstrates excellent linearity of the Ge content of the samples, showing dosage can be easily quantified with a few known standards.

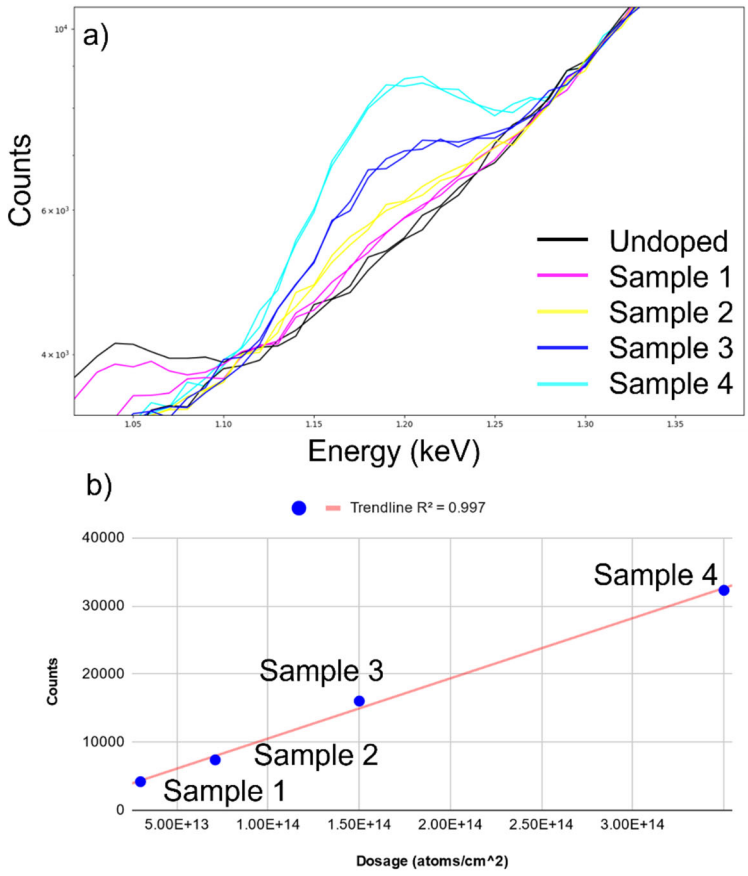


**FIGURE 1.** a) Spectral peak of the Ge L-alpha line for a ladder with doses in the range from undoped to 3.5 E14 atoms/cm$^2$. Samples 1 through 4 have increasing dosage of Ge in the sample. The lowest dosage sample (Sample 1) contains 3.0 E13 atoms/cm$^2$. b) Plot of fitted Ge counts vs dosage (provided by third party) fitted with a linear regression showing 99.7% linearity.

## KEYWORDS

MicroXRF, equivalent thin film thickness, dose, low Z, vacuum chamber

# New Development of X-ray Assisted Device Alteration (XADA) for Circuit Debugging: A Solution for Backside Power Delivery (BPD)

Sylvia Lewis, Benjamin Stripe, Frances Su, Michael Lun, Quoc Nguyen, Mark Cordier, Stuart Coleman, S.H. Lau, Wenbing Yun

*Sigray, Inc., 1590 Solano Way, Suite A, Concord CA 94520*
*slewis@sigray.com*

## Introduction

Backside power delivery (BPD) is widely anticipated by the semiconductor industry to be a pivotal development, enabling more efficient power delivery due to reduced resistance and significant improvements to transistor density (20-30% cell area reduction). The big three major IC manufacturers (Intel, TSMC, and Samsung) have all announced their intent to implement BPD by their next nodes.

The challenge with BPD is that existing circuit debugging / marginal fault isolation techniques such as LADA (laser assisted device alteration) will become obsolete. LADA has become a well-known standard approach, in which the silicon backside of the device is thinned such that it is transmissive to a laser (e.g. 1064nm wavelength). A tester then electrically stimulates a device and a laser generates photo carriers in the device, which can trip a passing device to a fail condition (or conversely, from a fail into a pass condition). Significant development in LADA has enabled spot sizes of 100-200nm, thus enabling it to isolate a small area of transistor cells.

Because LADA requires backside silicon thinning, the shift to BPD in which power rails are placed on the backside means this approach will no longer work. NIR is not sufficiently transmissive through silicon, let alone layers of copper power rails. Thus circuit debugging needs a dramatically new approach to address emerging BPD schemes.

One of the most promising approaches is using X-rays instead of NIR in a newly developed approach called X-ray Assisted Device Alteration (XADA). Because X-rays are sufficiently transmissive to copper and silicon, little to no sample preparation (e.g., backside thinning) is required and the intact device can be probed. However, there have been significant concerns about the viability of X-rays that have restrained the enthusiasm for its potential, including whether they are *too* transmissive (thus not interacting sufficiently with the sample) and whether they permanently alter the device [2]. Here we will present a completed XADA prototype and present results of the system, validating its usefulness for BPD devices.

## System Overview

Sigray has developed an X-ray Assisted Device Alteration tool simply named Sigray XADA™ (Fig. 1B) in partnership with Intel [1]. The system can achieve a spot size of <2.5 µm spot size with a high flux of >2.5e$^5$ ph/s/µm$^2$ with x-rays of operating energies between 5 to 9 keV. The system was designed using Sigray's patented x-ray component technologies of an ultrahigh brightness x-ray source and high efficiency x-ray imaging optics. To ensure the maximum flexibility of the tool, a large and flexible tester area was designed with large cable runs so

that a tester can go in and out without needing to disconnect the cables. The software enables an externally supplied triggering voltage pulse to advance the stage in a rastering pattern to spatially localize the fault.

## Feasibility Demonstration

Prior to the release of the Sigray XADA™, Sigray collaborated with Dr. William Lo of NVIDIA to perform baseline tests on the feasibility of X-rays for fault isolation and presented these results at ISTFA 2022 [2]. The preliminary results were performed in a Sigray AttoMap™ tool, which is an ultrahigh resolution microXRF system sold for geological, biological (metallomics), and semiconductor dopant/residue research applications (Fig. 1A). Sigray AttoMap™ uses similar critical components (Sigray x-ray source and x-ray optics) as the XADA tool, but is limited in its ability to accommodate testers and its stability/repeatability to enable moving toward submicron resolution. The results with AttoMap™ indicated a minor, but perceptible, VT shift on a 5nm FinFET test vehicle. A follow-on experiment conducted and presented by Dr. Lo at a 2023 ISTFA user group used a series of inverters and buffers in a 5nm test chip with large separations between transistors (50 µm) to ensure the x-rays were only perturbing one transistor. The pulse out of the device was compared to the input pulse to determine the delay using a high bandwidth oscilloscope. A 3-4ps timing delay was seen, with a delay persistence of >10 minutes (Fig. 2A).

This study was then followed up with an Intel collaboration. In this, a preliminary baseline test was performed to demonstrate an x-ray induced change of the switching time of a single CMOS inverter in a chain (Fig. 2B), similar to the NVIDIA study. The delay was shown to scale with x-ray exposure time linearly (Fig. 2B). This was followed by a real-world example in which the device had a known failure at a worldline-to-ground short in an SRAM cell. The device was rastered using Sigray XADA™ (Fig. 1B) at 2.4 µm step sizes over a 30 x 60 µm region and using a spot size of ~5 µm. Because x-rays produce persistent effects in datasets, the workaround solution was to use variable raster directions to successfully localize the fault (Fig. 2C) [1].

## Future Directions

During our presentation, we will discuss additional developments planned for XADA, including potential roadmaps toward submicron spot sizes and additional updates on experimental validation.


**FIGURE 1.** Left (1A): Sigray AttoMap™ used for initial feasibility tests with Dr. William Lo (NVIDIA). Right (1B): Sigray XADA™ used for additional feasibility tests in collaboration with Intel.

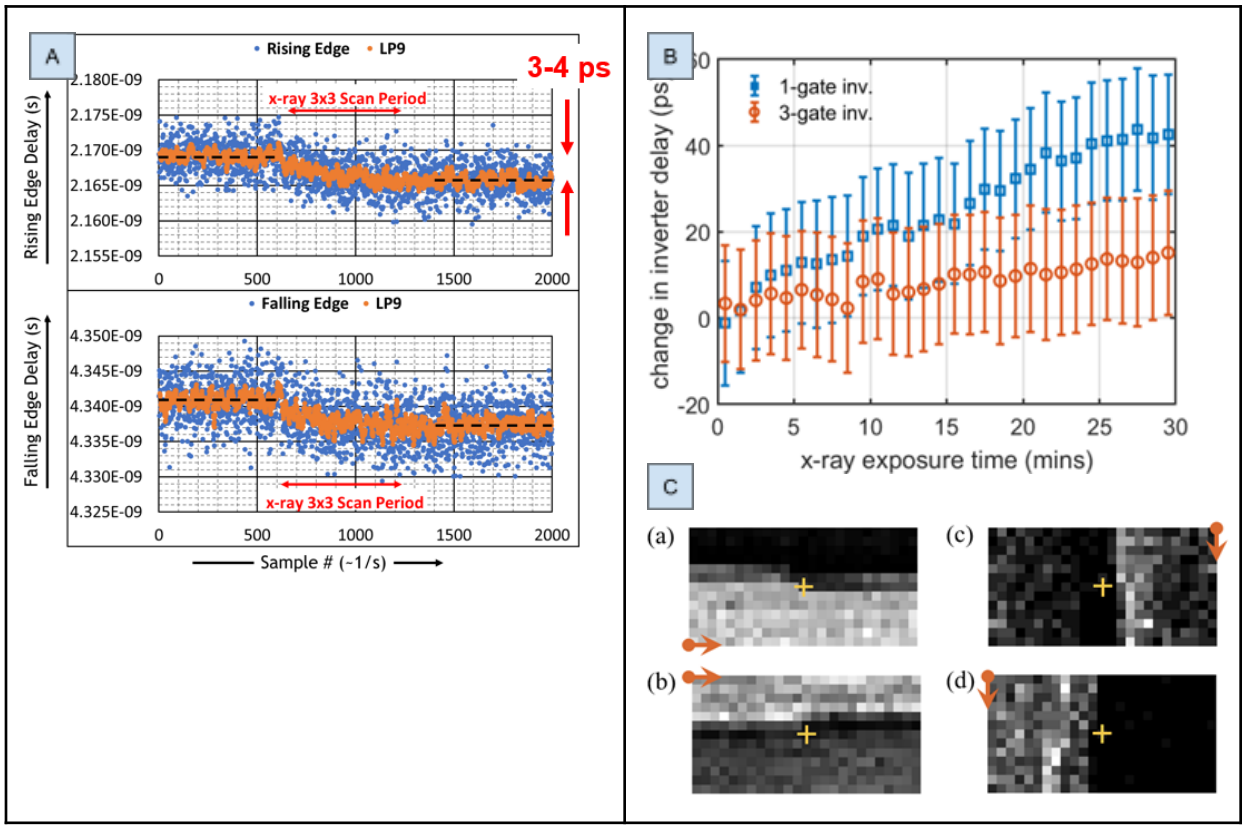


**FIGURE 2.** Left (2A): Results obtained with Sigray AttoMap™ on a 5nm DUT devised by Dr. Lo at NVIDIA. Right (2B): Changes in a single CMOS inverter , showing that delay scales with x-ray exposure time. Right (2C): Variable angle rastering enabled isolation of a physical defect (short) located at the yellow crosshairs. White pixels correspond to more failing tests and black pixels to fewer.

## References

1. KC Celio, et al. Laboratory X-ray Assisted Device Alteration for Fault Isolation and Post-Silicon Debug. *IRPS* (2024).
2. W Lo, et al. Device Alteration Using a Scanning X-ray Microscope. *ISTFA* (2022).

## Keywords

X-ray, Fault Isolation, LADA, XADA, Circuit Debugging, Laser Voltage Probing, SDL, Marginal Failure, Backside Power Delivery (BPD)

# Solving the Metrology Challenges of High Aspect Ratio Features Using 3D Tomography

Shawn Sallis*[,1], Tian Lian[1], Jin Zhang[1], Ying Gao[1], Osman Sorkhabi[1]

*1. Lam Research Corporation, 4400 Cushing Parkway, Fremont, California 94538*

## INTRODUCTION

The production and scaling of 3D NAND architectures presents unique challenges due to the presence of high aspect ratio (HAR) features. In contrast to 2D NAND which relies primarily on lithographic patterning for scaling and yield, 3D NAND relies more on control of the deposition and etch processes.[1] The production of high quality HAR features presents unique challenges to both deposition and etch processes.[2] Etching of HAR features can suffer from a variety of process errors such as incomplete etch, bowing, twisting, tilting, and CD variation which must be detected and controlled over the entire depth of the feature to produce high quality reliable devices. Adjusting the etch process to control these problems requires the ability to detect and quantify them in full 3D over large enough areas to obtain statistically significant results. Such detection and quantification requirements present a significant metrology challenge primarily due to the need to acquire nanometer scale information over large continuous volumes that are on the scale of micrometers.

## CURRENT CHALLENGES

Delayering and XSEM are two of the most common approaches to overcoming these challenges but have significant drawbacks in addition to their destructive nature. Issues with cleaving accuracy and image processing limit the reliability of XSEM, it inherently lacks the ability to produce full 3D profiles and is generally restricted to small sample sizes. Delayering can be used to reconstruct a 3D profile, but it can't provide 3D profile information for the same hole from top to bottom. It also requires a large footprint which limits the ability to track process variations across the wafer. Recently Critical-Dimension Small-Angle X-ray Scattering (CD-SAXS) has emerged as a non-destructive large sample volume technique for measuring HAR features. It can provide averaged 3D profile information of thousands of holes.

## NEW APPROACH TO 3D TOMOGRAPHY

FIB/SEM based 3D tomography (3DT) is a promising new technique that provides unique information that is not available through the other techniques mentioned here. 3DT can provide full 3D reconstructions of volumes with dimensions on the order of a few microns in the X, Y, and Z directions with sub-nanometer resolution in all dimensions. A volume of that size can contain several hundred features of interest giving access to a statistically significant sample while preserving information on hole-to-hole variation. 3DT reconstruction and visualization provides valuable information such as hole profiles, centroid, proximity, and bottom etch viewing making it extremely valuable for diagnosing etch issues. This will improve speed to solution and productivity for 3D NAND processes especially as those processes scale to larger stack sizes.

## CONCLUSION

Although 3DT is destructive and relatively time consuming, it still provides information that XSEM/delaying and CD-SAXS cannot. Cross-referencing 3DT with CD-SAXS is another way to solve metrology challenges with improved speed to solution. Using 3DT hole profile results as input for a CD-SAXS profile model helps to validate the accuracy of the CD-SAXS profile model and expedite the turnaround time. Once a CD-SAXS model is validated with 3DT data, CD-SAXS can be used as an alternative and non-destructive solution to monitor CD profile with much faster measurement time and a larger sampling plan. In this way 3DT and CD-SAXS can be used as complimentary techniques that can dramatically improve speed to solution for HAR etch processes.

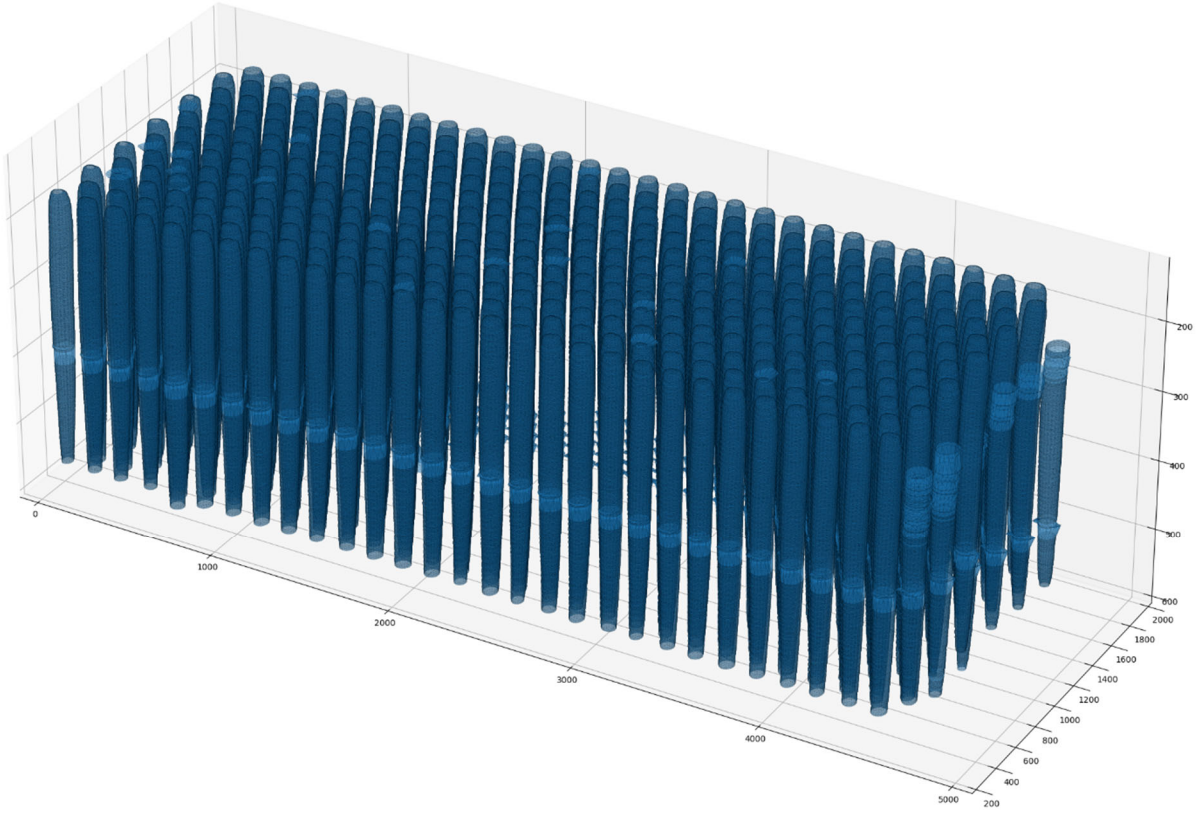


**FIGURE 1.** 3D reconstruction of ~4um by ~2um by ~5um section of ATR80 sample containing ~350 channels. The depth was compressed by a factor of 10 to improve visibility of the HAR features.

## REFERENCES

1. Y. Li and K. N. Quader, "NAND Flash Memory: Challenges and Opportunities," in *Computer*, vol. 46, no. 8, pp. 23-29, August 2013, doi: 10.1109/MC.2013.190.
2. Singh, H. ***Overcoming challenges in 3D NAND volume manufacturing***. Solid State Technol. 2017,60, 18–21.

## KEYWORDS

HAR, High Aspect Ratio, Tomography, CD-SAXS, Reconstruction, FIB, SEM

# Extreme Brightness X-ray Sources for Semiconductor Metrology

J. Hållstedt, E. Espes, G. Gopakumar, D. Nilsson, T. Dreier,
B. A. M. Hansson, L. Kjellberg, N. Kumar Iyer

*Excillum AB, Jan Stenbecks Torg 17, 164 40 Kista, Sweden*
*Email: julius.hallstedt@excillum.com, Tel: +46 708105888*

## INTRODUCTION

In the pursuit of both 'More Moore' and 'More than Moore', the interest in the semiconductor community for improved X-ray source technology has been intensified due to the fact that many of the traditional optical or electron based metrology methods are not capable of delivering the information needed in the semiconductor manufacturing. [1]. New materials and smaller dimensions combined with 3D stacking creates the need to measure very small and buried structures and material properties. Proposed solutions involve a variety of techniques including X-ray based methods, however a main problem with most of these is the very low throughput and/or or low resolution. This is due to the fact that conventional X-ray tubes are very limited in brightness limiting the usable flux for many metrology applications.

The limitation in brightness of a conventional X-ray tube is illustrated in Fig 1a, showing that X-rays are generated when highly energetic electrons are stopped in a solid metal anode. The fundamental limit for the X-ray power generated from a given spot size is when the electron beam power is so high that it locally melts the anode. A novel method of overcoming this problem is by using a liquid as metal anode MetalJet [2]. The MetalJet technology solves the thermal limit by replacing the traditional anode by a thin high-speed jet of liquid metal (see Figure 1b). Melting of the anode is thereby no longer a problem as it is already molten, and significantly (currently about 10x) higher e-beam power densities can be applied.

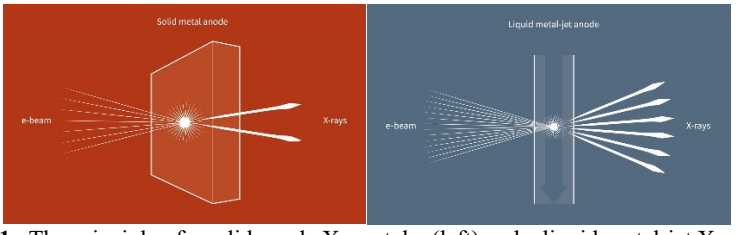


**FIGURE 1.** The principle of a solid anode X-ray tube (left) and a liquid-metal-jet X-ray tube (right).

## HIGH BRIGHTNESS METALJET XRAY SOURCE

Figure 2 illustrates the commercially available E1+ MetalJet X-ray source head which is rather similar to a traditional open tube X-ray source with main difference that anode is replaced by a MetalJet target as described above. The MetalJet is formed by ejecting a ~200 µm diameter liquid metal through nozzle into the high vacuum chamber. One key requirement to achieve 24/7 operation is that the liquid-metal-alloy can be 100% recirculated. For these sources a closed loop system is used, where the metal is recirculated to the nozzle after cooling it down again.

Presently, the maximum power is 1000 W resulting in an approximately apparent 30µm round X-ray spot. The current generation of sources use either a mainly gallium-based alloy or an alloy which also contain significant amounts of indium. The gallium Kα line is at 9.2 keV, which makes it an attractive high-brightness replacement of copper Kα at 8.0 keV. The indium Kα is at 24.2 keV making it an attractive high-brightness

replacement of silver Kα at 22.2 keV. The maximum acceleration voltage up to 160kV enabling a wide bremsstrahlung spectrum for e.g. ultra high-speed X-ray imaging or advanced optics based X-ray microscopy.

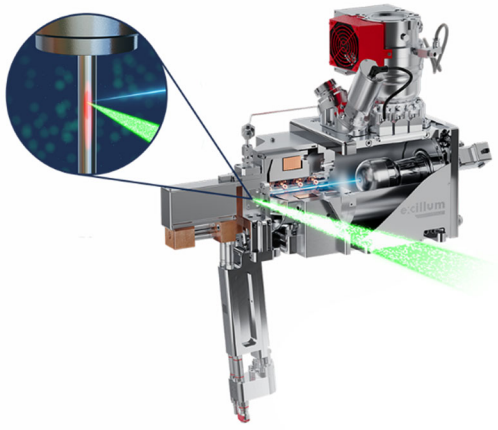

**FIGURE 2.** The E1+ MetalJet source head with inset illustrating the liquid-metal-jet/electron beam interaction point and corresponding X-ray emission shown as the green cone beam.

## APPLICATIONS - X-RAY IMAGING

MetalJet E1+ enables extreme speed CT inspection of battery cells for example PC, cell phones or electric vehicles. Full CT scans in less than 1 second is possible and allow full 3D reconstruction of the cell and possibility to characterize e.g. anode-cathode overhang to improve yield and quality.

Another application of MetalJet which allow the highest available resolution in lab-based X-ray microscopes is achieved by using zone-plate based projection microscopes. Such microscopes, however, typically use Cu Kα radiation which is not so well suited to see copper structures in silicon due to poor contrast between copper and silicon. As illustrated by Fig. 3, Kα emission of gallium used in MetalJet sources is just above the K-absorption edge of copper, which is better suited to create a sufficient contrast between copper and silicon. First, X-ray microscopy instrument using the MetalJet for Cu interconnect inspection was recently presented.

## APPLICATIONS – SCATTERING AND DIFFRACTION

Applications like X-ray reflectivity (XRR), High resolution X-ray diffraction (HRXRD) and critical dimension small angle X-ray Scattering (CD-SAXS) are being increasingly used to improve yield and detect non-conformities early in the processing. As the requirements increase more focus is put on improving the X-Ray source. For transmission geometries a MetalJet source with Indium rich target material can generate a very intense 24 keV X-ray beam ideal for penetrating the wafer while keeping good interaction with the layer structures of interest. Reflection geometry applications a gallium target enable very bright 9 keV beams with possibility to both achieve high degree of monochromatizating and collimation needed to investigate the epitaxial structures.

## REFERENCES

1. M. Lapedus, 'Can We Measure Next-Gen FinFETs?', *Semiconductor engineering,* Nov 21 2016
2. H. M. Hertz et al, 'Method and apparatus for generating x-ray or euv radiation' Patent US20020015473 *

## KEYWORDS

X-ray, tube, source, microfocus, metaljet, liquid-metal-jet, gallium, indium, microscopy, imaging, CD-SAXS, metrology, XRR, XRD, HRXRD

# Nanofocus X-ray source for improved resolution in advanced packaging metrology

T. Dreier, J. Hållstedt, E. Espes, G. Gopakumar,
D. Nilsson, B. A. M. Hansson, L. Kjellberg

*Excillum AB, Jan Stenbecks Torg 17, 164 40 Kista, Sweden*
*Email: till.dreier@excillum.com*

## INTRODUCTION

In the pursuit of 'More Moore' and 'More than Moore', the interest in X-ray source technology has been intensified since many of the traditional methods to measure and control semiconductor manufacturing such as optical or electron-based metrology methods are running out of steam. Heterogeneous integration for advanced packaging offers the possibility to optimize and increase performance of devices. As the dimensions of the electrical connects are significantly reduced in size and pitch enables more connects and faster communication. At the same time this puts increased demand on the resolution of the metrology tool as critical defect dimensions are getting smaller down to sub-µm level. The proposed solutions are mainly based on X-ray imaging techniques as X-rays can measure the internal structure of devices non-destructively. However, a main challenge is the resolution and throughput of these methods with the X-ray source being the main bottle neck. This is due to the fact that conventional X-ray tubes are limited in minimum X-ray spot size and electron beam power load. Leading to too slow measurement at too low resolution.

## EXTREME RESOLUTION DIAMOND TRANMISSION TARGET X-RAY SOURCE

The Excillum NanoTube N3 is based on cutting edge electron beam optics and the latest tungsten-diamond transmission target technology. Automatic e-beam focusing, and astigmatism correction ensures that the smallest possible, truly round spot is consistently achieved during 24/7 operation. With this the NanoTube N3 enables industry-leading performance down to 150 nm resolution in geometric-magnification X-ray imaging systems up to 160 kV. The NanoTube N3 also has the unique feature of internally measuring and reporting the current spot size. In addition, the design of the diamond transmission target, extreme control of the electron beam power density and advanced cooling and thermal design results in extreme stability as well as possibility to push the boundaries for X-ray performance over long exposures. This enables speed, stability and unprecedented true resolution of down to 150 nm lines and spaces as illustrated in Figure 1.

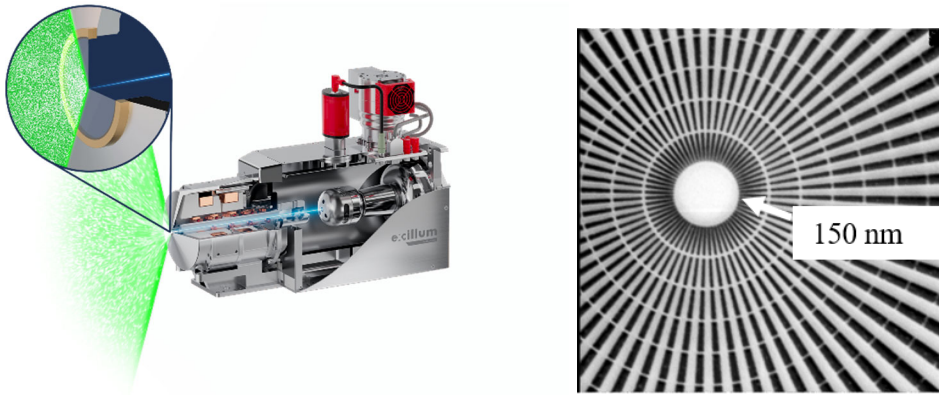


**FIGURE 1.** The N3 Nanotube Xray source (left). With inset illustrating the diamond transmission target/electron beam interaction point and corresponding X-ray emission shown as the green cone beam. Siemens star test structure (right) illustrating that 150 nm lines and spaces (innermost ring) resolution is possible in all directions.

## Advanced packaging example

In advanced packaging, a challenging example is detection of defects in e.g. High Bandwidth Memory (HBM) bumps. Here, critical defects can be of sub micrometer size which put extreme requirements on the resolution of the system. With a Nano-CT setup we illustrate the performance capability of the Nanotube N3 showing the possibility to characterize micro-bumps and through silicon vias (TSV) in great detail as illustrated in figures 2 and 3. In Figure 3, a zoom in of the slice highlights the 16µm HBM bumps with several defects visible. This illustrates the possibility of the N3 to empower electronics inspection tools in advanced packaging to increase quality and improve yield.

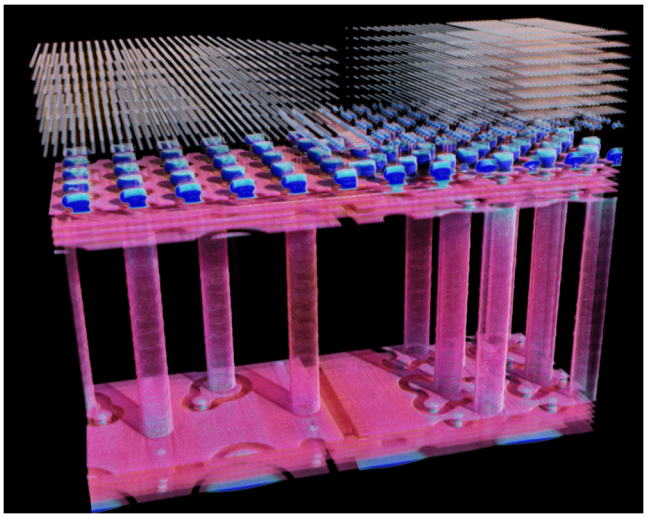

**FIGURE 2.** 3D render of the reconstructed volume of an overview scan of a GPU with bonded memory module

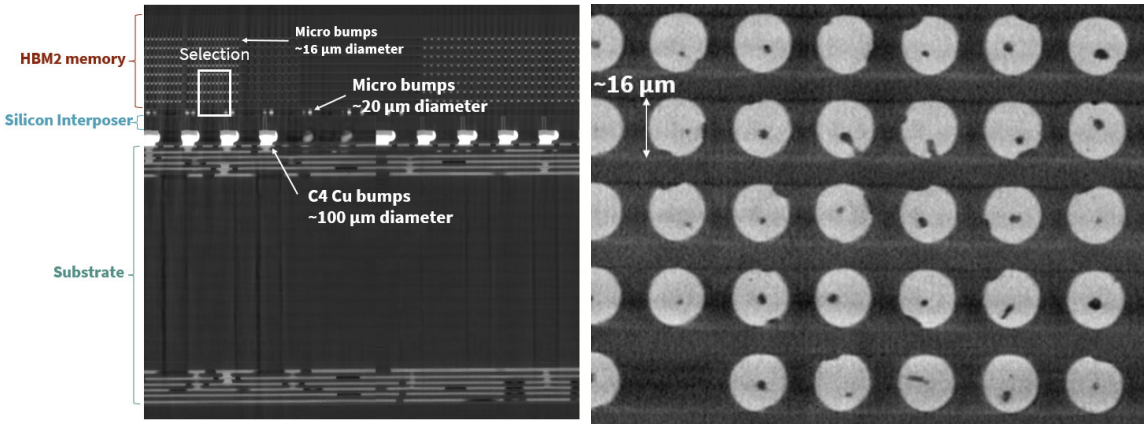


**FIGURE 3.** Slice through the volume and slice from a high-resolution scan of one layer of HBM bumps with voids.

## KEYWORDS

Nano-CT, laminography, advanced packaging, heterogenous integration, X-ray tube, metrology, high resolution

# Advancing High-Density 3D NAND TEM Sample Preparation with Ultrafast fs-Laser Milling in FIB-SEM-Laser Systems

Arun Prabha[1], Cheryl Hartfield[2]
[1]*Carl Zeiss Pte Ltd 80 Bendemeer Road, #10-01, Singapore 339949*
[2] *Carl Zeiss Microscopy, LLC 5300 Central Pkwy, Dublin, CA 94568, United States*
*cheryl.hartfield@zeiss.com*

## INTRODUCTION

Monitoring the processes involved in the fabrication of 3D NAND flash memory devices requires a detailed analysis of critical dimensions across multiple layers within the memory cell stack. Given the susceptibility of the 3D NAND channel to deformities, particularly as the aspect ratio of the channel increases, process characterization becomes critical. High-resolution planar TEM serves as a precise method for evaluating crucial parameters such as channel structure, circularity, layer thickness etc. However, as 3D NAND channels continue to shrink and the number of memory layers surpasses 300, planar TEM sample preparation becomes increasingly challenging and time-consuming.

To address these challenges, the authors developed a novel solution using a femtosecond laser-integrated FIB-SEM system, also known as a LaserFIB [1, 2]. This novel approach enables rapid and efficient TEM sample preparation, subsequently enhancing the characterization of 3D NAND channels with an increased number of data points.

## METHOD

### *A. Introduction to fs-laser integrated FIB-SEM*

While focused ion beam scanning electron microscopes (FIB-SEM) offer nm-scale imaging and analytics capabilities along with site-specific access to subsurface regions, their milling rates are limited to (40 x 40 x 40) $\mu m^3$ /h [3]. This limitation poses a challenge for large-volume material processing and analysis, especially for TEM sample preparation. The introduction of a fs-laser ablation system integrated with the FIB-SEM instrument addresses this issue by significantly reducing the milling time to seconds for large-area lift-outs. This enables lift out of large areas of 3D NAND stacks ranging up to 100 µm for lamella prep.

### *B. The 3D NAND planar TEM sample preparation process*

Unlike conventional FIB-SEM preparation workflows for TEM samples, this new method starts by using a fs-laser instead of an ion beam for targeted large trench milling preceding the sample lift out. The region of interest targeting is guided by SEM navigation and visualization for placing ablation patterns. Initially, a trench measuring 120 µm in length, 50 µm in width, and 50 µm in depth is created adjacent to the 3D NAND memory stack by laser ablation. This laser-based trench formation typically consumes up to an hour in Ga FIB systems and is achieved in just 5 minutes using the laser with the help of a preset recipe. Subsequently, the sample moves from the laser ablation chamber to the FIB chamber, where protective depositions for the lamella are applied using the focused ion beam. As the laser milling enables a large lift-out sample volume, many lamellae can be placed on the laser-prepared bulk lift-out sample. In the example shown in Figure 1, 18 lamella are created at 18 different memory layers which are equally distanced from each other. An additional lamella is prepared within the bulk Si for zone-axis alignment in TEM imaging. After completing the protective depositions for all 19 lamella sites, the subsequent steps of lamella preparation closely mirror those involved in conventional TEM sample preparation, following the typical FIB steps of U-cutting the sample, lifting out the chunk in situ with attachment to a copper grid, and the requisite lamella thinning processes.

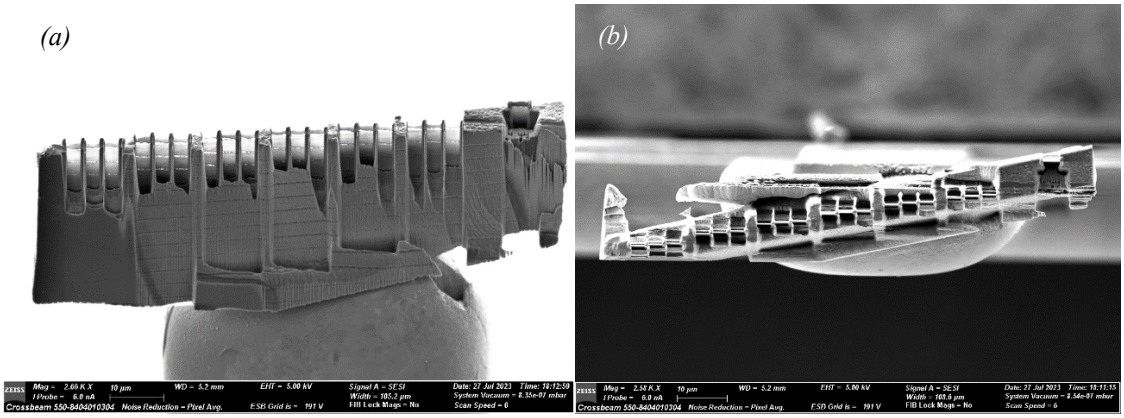


*Figure 1a is a tilted SEM image showing the TEM sample after final thinning. Figure 1b is a top down view of the completed sample. There are 18 + 1 open trenches representing 18 memory layers and the far-right trench is the silicon substrate that is used for zone-axis alignment in TEM imaging.*

The development of fs-laser-based planar TEM sample preparation for 3D NAND devices represents a significant advancement in the field of process characterization. The key advantage is the ability to prepare large-area bulk samples. This capability allows for the fabrication of multiple lamellas from a single bulk sample, significantly reducing cycle time per lamella and thus generating more data in a shorter period as detailed in Table 1. Instead of 19 iterations of lift-out (one for each of the 19 lamellae), this approach only requires a single lift-out of the large chunk, significantly contributing to the time savings. The femtosecond laser approach does not affect the integrity of intricate 3D NAND structures, enabling more accurate and reliable TEM characterization.

*Table 1 – TEM sample preparation time savings using integrated fs-laser FIB-SEM workflow vs conventional workflow*

| | **Conventional TEM sample prep** | **TEM sample prep with laser** |
|---|---|---|
| Quantity of lamella prepared | 1 | 18 |
| Total preparation time | 1.5 hr | 5 hr |
| Average cycle time per lamella | 1.5 hr | 16.6 min |

The implementation of fs-laser-based TEM sample preparation for 3D NAND devices will undoubtedly have a profound impact on the development of next-generation memory technologies. By facilitating accurate and efficient TEM analysis, this method will accelerate the advancement of device performance, reliability, and manufacturability.

## REFERENCES

1. Kaestner, M., et al. *Novel workflow for high-resolution imaging of structures in advanced 3D and fan-out packages*. in *CSTIC*. 2019. China: IEEE.
2. Tordoff, B., et al., *The LaserFIB: new application opportunities combining a high-performance FIB-SEM with femtosecond laser processing in an integrated second chamber.* Appl Microsc, 2020. **50**(1): p. 24.
3. Randolph, S.J., et al., *In situ femtosecond pulse laser ablation for large volume 3D analysis in scanning electron microscope systems.* Journal of Vacuum Science & Technology B, 2018. **36**(6).

## KEYWORDS

3D NAND, process characterization, TEM lamella, fs-laser FIB-SEM

## MEZZANINE FLOOR

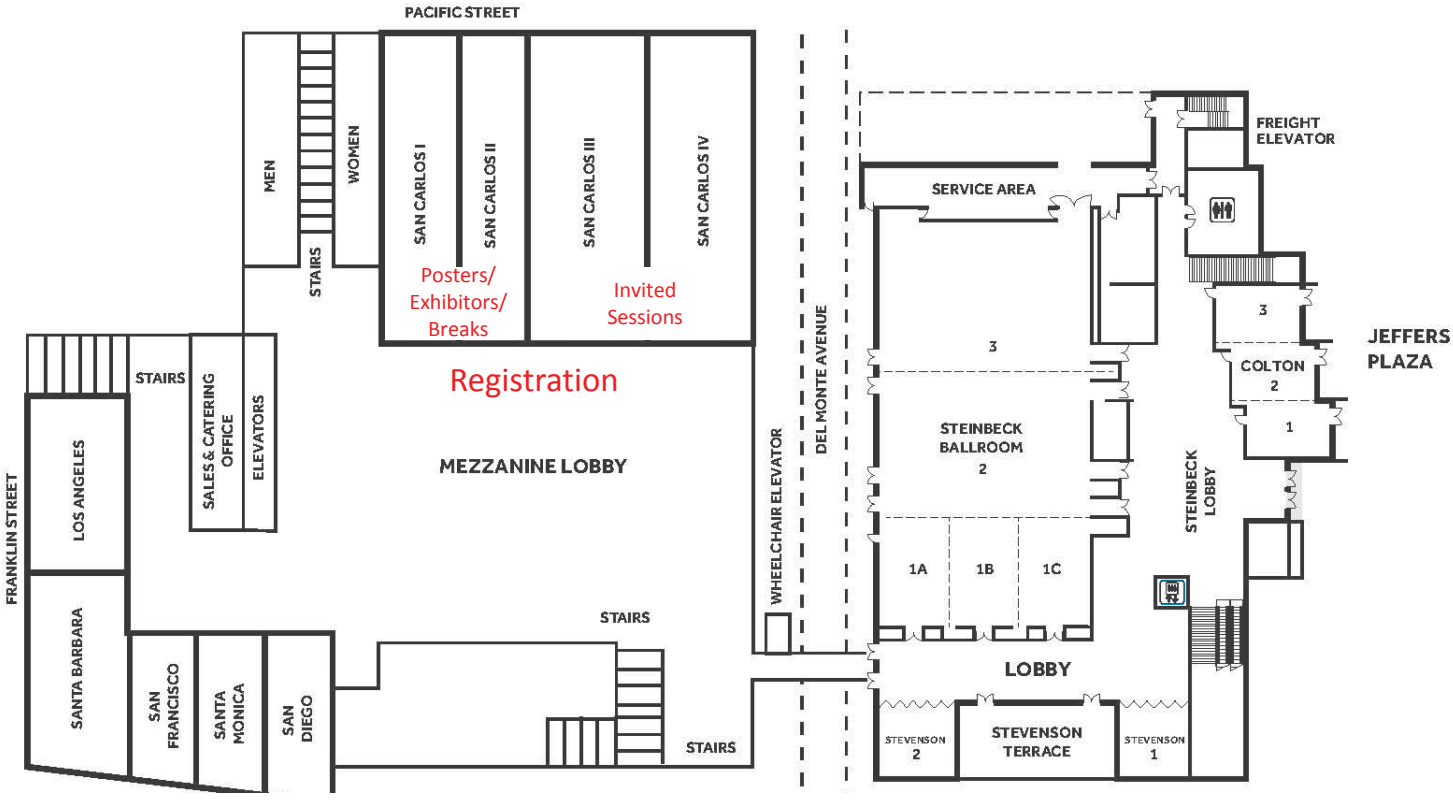


## TENTH FLOOR

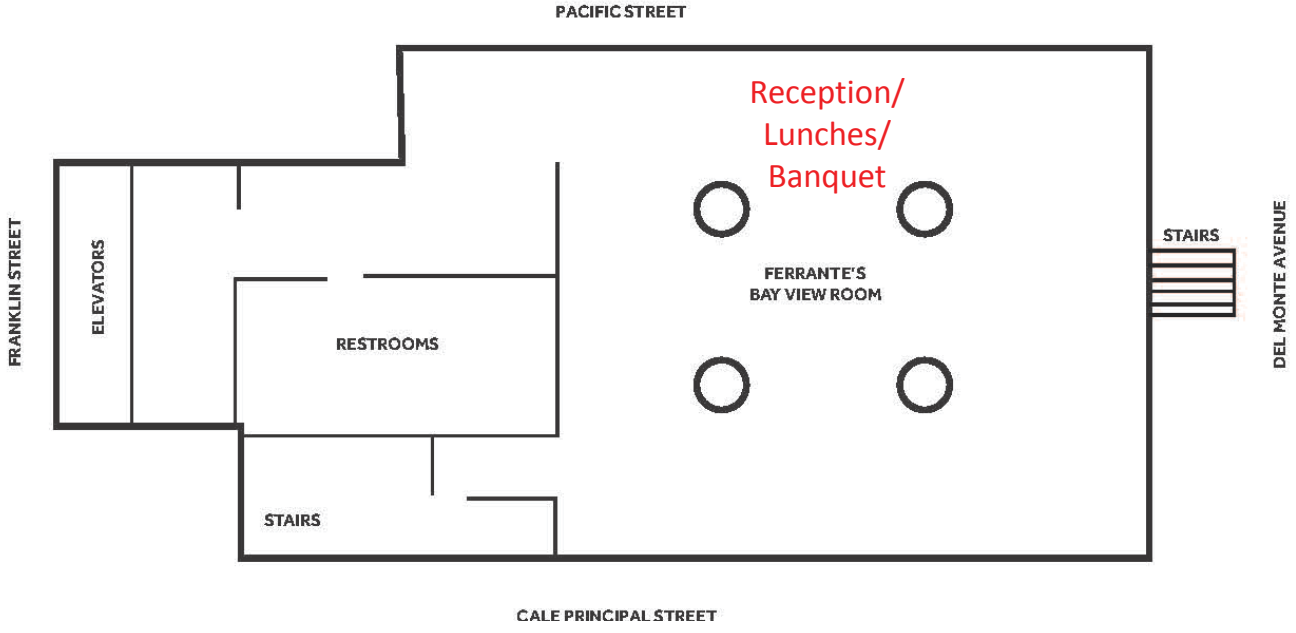

# Program at a Glance

| | Morning | AM Sessions | PM Sessions | Evening |
|---|---|---|---|---|
| **Tuesday** Apr. 16th | **7:00** Registration / Attendee Check-in | **9:00** Conference Opening<br>**9:15** Plenary<br>**11:15** Emerging Materials and Devices | **1:45** CHIPS Act & Industry Trends<br>**3:45** Microscopies: New Developments in Chemical/Property Characterization | **5:15** Poster Session<br>**7:00** Banquet |
| **Wednesday** Apr. 17th | **7:45** Registration / Attendee Check-in | **8:30** Advanced Packaging<br>**10:30** New Developments in Chemical/ Electrical Characterization | **1:00** Patterning Metrology<br>**3:00** Advanced Manufacturing Metrology – Defects | **4:30** Poster Session |
| **Thursday** Apr. 18th | **8:00** Registration / Attendee Check-in | **8:30** Plenary<br>**9:15 AM** EUV and Advanced Patterning<br>**11:15** Tomographies: New Developments in 3D Analysis | **2:45** Spintronics-Based Devices | |